Probing Quasihole and Edge Excitations of Atomic and Photonic Fractional Quantum Hall Systems
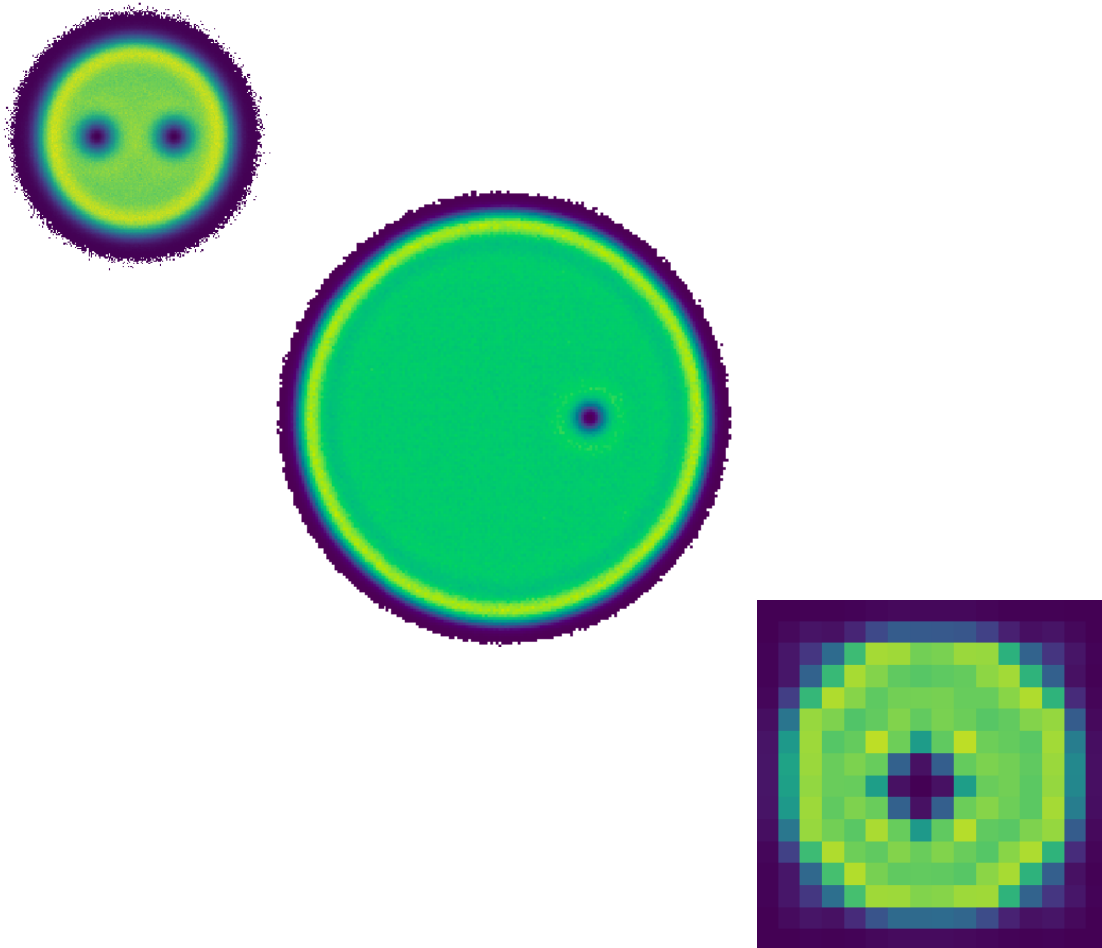
Elia Macaluso

Probing Quasihole and Edge Excitations of Atomic and Photonic Fractional Quantum Hall Systems

Elia Macaluso

A dissertation submitted to the
Dipartimento di Fisica
Università di Trento

In fulfilment of the requirements for the Degree of
Philosophiæ Doctor in Physics

Under the Supervision of
Dr. Iacopo Carusotto

Dottorato di Ricerca XXXII Ciclo
January 27th, 2020

Supervisor:

Dr. Iacopo Carusotto

Members of the committee:

Prof. Philipp Hauke - Università di Trento

Dr. Christof Weitenberg - Universität Hamburg

Prof. Oded Zilberberg - ETH Zürich

Contents

Introduction.

The discovery of the fractional quantum Hall effect for two-dimensional electron gases immersed in a strong orthogonal magnetic field represents a cornerstone of modern physics. The states responsible for the appearance of the fractional quantum Hall effect have been found to be part of a whole new class of phases of matter, characterized by an internal order with unprecedented properties and known as topological order. This kind of internal order is indeed very different from any other order of matter previously found in nature, as it cannot be associated with any symmetry (or breaking of a symmetry) and, as a consequence, it cannot be described within Landau's theory of phase transitions. This fact opened up a completely new territory for physical studies, paving the way towards many of the current hot topics in physics, such as topological phases of matter, topological order and topological quantum computing.

As it happens for most topologically-ordered phases, fractional quantum Hall states are breeding ground for the observation of many exotic physical phenomena. Important examples include the appearance of degenerate ground states when the system in placed on a space with non-trivial topology (e.g., on a torus), the existence of chiral gapless edge excitations which unidirectionally propagate without suffering of back-scattering processes, and the possibility of hosting elementary excitations, known as quasiparticles and quasiholes, carrying fractional charge and anyonic statistics. The fact that the standard classification of quantum particles into bosons and fermions can be eluded in two spatial dimensions is known since the 70's. However, it was only with the advent of the fractional quantum Hall effect that anyons (this is the name of the exotic objects breaking the paradigmatic boson-fermion dichotomy) stopped to be a mere mathematical concept to become a physical reality which can be studied in actual experiments. Although the scientific community has always had great interest towards the physics of anyons, they consolidated their importance only when Kitaev proposed to use them as building blocks for fault-tolerant quantum computers. Kitaev's groundbreaking idea made theoretical and experimental studies of anyons more widespread and intense, and nowadays several existing platforms are expected to host anyons as emergent excitations on top of a quantum state. However, it is important to stress that the unambiguous demonstration of their statistical properties is still the matter of an intense debate.

Even though for years since their discovery fractional quantum Hall states have been studied only in electronic systems, the recent advances made in the domains of quantum simulators and artificial gauge fields opened the possibility to realize bosonic analogs of these states in platforms based on ultracold atoms and photons. Reaching the appropriate conditions for the simulation of the fractional quantum Hall effect with neutral particles (such as atoms and photons) has required decades of both theoretical and experimental efforts and passed through the implementation of many topological models at the single-particle level. However, we strongly believe that the stage is set finally and that bosonic fractional quantum Hall states will be realized soon in different set-ups. Motivated by this fact, we dedicate this Thesis to the study of the edge and quasihole excitations of bosonic fractional quantum Hall states with the goal of guiding near future experiments towards exciting discoveries such as the observation of anyons.

In the first part of the Thesis we focus our attention on the behavior of the edge excitations of the bosonic $\nu = 1/2$ Laughlin state (a paradigmatic wave function for the fractional quantum Hall effect) in the presence of cylindrically symmetric hard-wall confining potentials. With respect

to electronic devices, atomic and photonic platforms offers indeed a more precise control on the external potential confining the systems, as confirmed by the recent realization of flat-bottomed traps for ultracold atoms and by the flexibility in designing optical cavities. At the same time, most of the theoretical works in this direction have considered harmonic confinements, for which the edge states have been found to display the standard chiral Luttinger liquid behavior, leaving the field open for our analysis of new physics beyond the Luttinger paradigm.

In the second part we propose a novel method to probe the statistical properties of the quasihole excitations on top of a fractional quantum Hall state. As compared to the previous proposals, it does not rely on any form of interference and it has the undeniable advantage of requiring only the measurements of density-related observables. As we have already mentioned, although the existence of anyons have been theoretically predicted long time ago, it still lacks a clear-cut experimental evidence and this motivated people working with ultracold atoms and photons to push their systems into the fractional quantum Hall regime. However, while there exist plenty of proposals for the detection of anyons in solid-state systems (mostly based on interferometric schemes in which currents are injected into the system and anyons travel along its edges), in the present literature the number of detection schemes applicable in ultracold atomic and/or photonic set-ups is much smaller and they are typically as demanding as those proposed in the electronic context.

Finally, in the last part of the Thesis we move to the lattice counterparts of the fractional quantum Hall states, the so-called fractional Chern insulators. Still with the purpose of paving the way for future experimental studies with quantum simulators, we focus our attention of the simplest bosonic version of these states and, in particular, on the properties of its quasihole excitations. Although this topic has already been the subject of intense studies, most of the previous works were limited either to system sizes which are too small to host anyonic excitations, or to unphysical conditions, such as periodic geometries and non-local Hamiltonians. Our study investigates for the first time the properties of genuine quasihole excitations in experimentally relevant situations.

The detailed outline of the Thesis is the following:

Part I. In this first part we review the main concepts which are required to understand and appreciate the results reported in the second half of this Thesis.

We start by reviewing the main properties of anyons, explaining why they only appear in two spatial dimensions and their possible application in topological quantum computers (**Chapter 1.**). After that we report the basis aspects of the fractional quantum Hall effect, with a particular focus on the possibility to observe it in lattice systems, but also in atomic and photonic quantum simulators (**Chapter 2.**). Then we present two paradigmatic wave functions of the fractional quantum Hall effect, i.e. the so-called Laughlin (**Chapter 3.**) and the Moore-Read states (**Chapter 4.**). Finally, we introduce the Jack polynomials formalism by emphasizing how it can be used to construct trial wave functions for the description of the excitations of the Laughlin state (**Chapter 5.**).

Part II. We collect and discuss all the original results we have obtained for the edge and quasihole excitations of atomic and photonic fractional quantum Hall systems. In particular:

Chapter 6. We make use of exact diagonalization calculations to characterize the behavior of $\nu = 1/2$ bosonic fractional quantum Hall droplets in the presence of cylindrically symmetric hard-wall potentials. This kind of confinements are found to produce many-body energy spectra which strongly deviates from the standard chiral Luttinger liquid description of the edge modes of a fractional quantum Hall state. At the same time, we provide evidence of a one-to-one correspondence between Jack polynomial wave functions and numerically obtained Hamiltonian eigenstates. This Chapter in based on the publications Macaluso and Carusotto [2017] and Macaluso and Carusotto [2018].

Chapter 7. By considering a generic quantum many-body state presenting anyonic excitations spatially arranged in such a way that their positions can be exchanged through rigid rotations, we establish a mathematical link between the statistical properties of the anyons and the matrix elements of the angular-momentum and the rotation operators in the (possibly

degenerate) ground-state manifold. Then we restrict ourselves to the quasihole excitations on top of fractional quantum Hall states defined in the lowest Landau level. This allows us to related the Abelian part of the quasihole anyonic statistics to density-related quantities such as the mean square radius of the fractional quantum Hall cloud or the profiles of the density depletions describing the quasihole excitations. To conclude we corroborate our theoretical results by means of Monte Carlo calculations for the quasihole excitations of both the Laughlin and the Moore-Read state. The main findings of this Chapter were published in Umucalılar et al. [2018] and in Macaluso et al. [2019a].

Chapter 8. We employ a Tree Tensor Network technique to investigate the properties of the quasihole excitations above a bosonic fractional Chern insulator state at filling $\nu = 1/2$, in the specific case of the Harper-Hofstadter model with hard-core interactions and (experimentally relevant) open boundary conditions. As a first step, we observe the fractional charge characterizing such excitations and its robustness against the details of the impurity potentials used to create and localize them. Then we numerically characterize the quasihole statistical properties, by applying a discretized version of the expression obtained in the previous Chapter for fractional quantum Hall states in continuum geometries. The main results of this Chapter were included in Macaluso et al. [2019b].

Part I

Review of the relevant literature

Chapter 1

Anyons.

$\mathcal{P}$article statistics is at the heart of many-body physics since the early days of quantum mechanics. From a theoretical point of view, the key concepts to define particle statistics are the adiabatic motion of one particle around another, hereafter the braiding, and the adiabatic exchange of particle positions.

In three spatial dimensions (3D), the particle exchange allows one to classify quantum particles into bosons and fermions, according to the symmetry property of their many-body wave functions. In particular, bosonic (resp. fermionic) many-body wave functions must be globally symmetric (resp. anti-symmetric) in the particle coordinates, meaning that they take an overall $+$ (resp. $-$) sign upon particle exchange. At this point we cannot fail to emphasize the fundamental role played by the wave-function symmetry, which is the root of many physical phenomena ranging from the stabilization of neutron stars to Bose-Einstein condensation.

At the same time, it is known since the 70's that the standard classification into bosons and fermions breaks down in two spatial dimensions (2D), where exotic objects, named anyons by Wilczek [1982b], can exist [Leinaas and Myrheim, 1977, Wilczek, 1982a, Halperin, 1984, Arovas et al., 1984, Wu, 1984, Stern, 2008]. In 2D the effect of particle exchange (resp. of braiding) on the many-body wave functions is indeed a generic phase factor $e^{i\varphi_{\rm st}}$ (resp. $e^{i\varphi_{\rm br}} = e^{i2\varphi_{\rm st}}$), where the statistical phase $\varphi_{\rm st}$ can take any values in $[0, 2\pi)$. While bosons and fermions are characterized by $\varphi_{\rm st} = 0$ and $\varphi_{\rm st} = \pi$, respectively, Abelian anyons have statistical phase $\varphi_{\rm st} = \alpha\pi$, with α a non-integer number. This already fascinating scenario is further enriched in the presence of a topologically degenerate ground state. In this case the statistical phase factor is replaced by non-commuting unitary transformations acting on the ground-state manifold and anyons are said to be non-Abelian [Moore and Read, 1991, Read and Green, 2000, Ivanov, 2001, Read and Rezayi, 1999].

Since the very first theoretical works investigating them, anyons have always been at the center of intense studies. However, they became one of the holy grails of modern condensed-matter physics only at the beginning of the 21st century, when Kitaev [2003] proposed to used them as building blocks for fault-tolerant quantum computers [Nayak et al., 2008]. That said, it is important to stress that, although several existing platforms are expected to host anyons as emergent quasiparticle excitations of a quantum many-body system, the unambiguous experimental demonstration of their properties is still a matter of intense debate [Willett et al., 2009, Mourik et al., 2012].

1.1   Particle statistics in 2D

In order to illustrate the different statistical properties of quantum particles in three and two spatial dimensions we will follow the intuitive reasoning reported in Goerbig [2009].

Let us consider a particle A which adiabatically moves around another identical particle B, along a closed path $\mathcal{C}$ lying in the (x, y) plane [see Fig. 1.1 a)]. We further assume that the path $\mathcal{C}$ is sufficiently far away from particle B and that both particles A and B are sufficiently localized
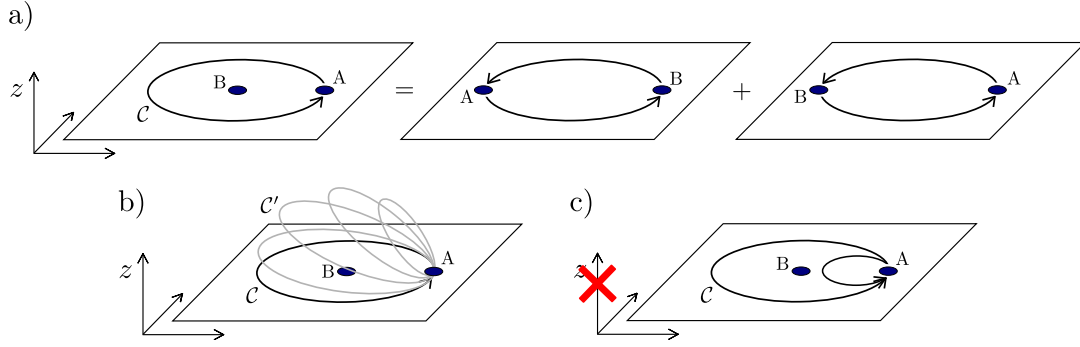
Figure 1.1: a) Equivalence between the braiding of particle A around particle B (on the left) and two consecutive exchanges of the particle positions (on the right). b) In 3D one can elevate the path $\mathcal{C}$ followed by particle A in the braiding process in the z direction, by keeping fixed the position of A, and then shrink it into a single point without passing by B. c) In 2D the path $\mathcal{C}$ cannot be smoothly deformed into the point-like path coinciding with the position of A, since they belong to two different homotopy classes.

so that we can neglect correction due to the overlap between their wave functions. At this point we can note that such a braiding process $\mathcal{R}$, in which particle A encircles particle B, is equivalent (apart from a topologically irrelevant translation in the (x, y) plane) to two successive exchange processes $\mathcal{E}$, in which one exchanges the position of A and B [see Fig. 1.1 a)]. Therefore, by expressing this equivalence in terms of the operators associated with $\mathcal{R}$ and $\mathcal{E}$, we obtain

$$\boxed{\hat{\mathcal{E}}^2 = \hat{\mathcal{R}}} \qquad \text{or} \qquad \boxed{\hat{\mathcal{E}} = \pm\sqrt{\hat{\mathcal{R}}}}, \tag{1.1}$$

modulo a translation.

As a first step, let us show what happens in 3D: Due to the presence of the third dimension (the one extending in the z direction), we can elevate the closed path $\mathcal{C}$ by keeping the position of particle A fixed in the (x, y) plane, as shown in Fig. 1.1 b). We denote this new (elevated) path $\mathcal{C}'$. At this point we can shrink the path $\mathcal{C}'$ into a single point, corresponding to the position of particle A, without passing by the position of particle B [see Fig. 1.1 b)]. We call this final (point-like) path $\mathcal{C}''$. Now it is important to recall that a quantum-mechanical braiding (or exchange) process does not specify any particular path that particle A has to follow in order to define the particle statistics. Moreover, from a topological point of view, all paths which can be smoothly deformed into each other define a homotopy class. As a consequence, we can interpret Eq. (1.1) as an equation for homotopy classes, for which a simple translation and a smooth deformation of the path are completely irrelevant. We can further observe the simple point-like path $\mathcal{C}''$, coinciding with the position of particle A, is then in the same homotopy class as the "original" path $\mathcal{C}$, and that the braiding process along $\mathcal{C}''$ can be formally described by $\hat{\mathcal{R}}(\mathcal{C}'') = \mathbb{1}$, where $\mathbb{1}$ is the identity operator.

Now, since for all paths in the same homotopy class $\hat{\mathcal{R}}$ must be the same, we can conclude that in 3D the braiding process can be described by

$$\hat{\mathcal{R}} \equiv \hat{\mathcal{R}}(\mathcal{C}) = \hat{\mathcal{R}}(\mathcal{C}'') = \mathbb{1}, \tag{1.2}$$

and so if we exchange twice the particle coordinates we have

$$\hat{\mathcal{E}}^2 = \mathbb{1}. \tag{1.3}$$

Suppose now to have two identical particles described by the wave function $\psi(\mathbf{r}_1, \mathbf{r}_2)$. The above equation tells us that if we apply twice the quantum-mechanical exchange operator $\hat{\mathcal{E}}$ on the two-particle state described by $\psi(\mathbf{r}_1, \mathbf{r}_2)$ we end with the initial state, i.e.

$$\hat{\mathcal{E}}^2 \psi(\mathbf{r}_1, \mathbf{r}_2) = \mathbb{1}\,\psi(\mathbf{r}_1, \mathbf{r}_2) = \psi(\mathbf{r}_1, \mathbf{r}_2). \tag{1.4}$$

We also know that, since we are considering identical particles, all probabilities must be the same if particle coordinates are exchanged. In other words $|\psi(\mathbf{r}_1, \mathbf{r}_2)|^2 = |\psi(\mathbf{r}_2, \mathbf{r}_1)|^2$ and therefore, upon exchange, the two wave functions can differ by at most a phase factor, namely

$$\psi(\mathbf{r}_1, \mathbf{r}_2) = \hat{\mathcal{E}}\,\psi(\mathbf{r}_2, \mathbf{r}_1) = e^{i\varphi_{\text{st}}}\,\psi(\mathbf{r}_2, \mathbf{r}_1). \tag{1.5}$$

Finally, if we put together Eqs. (1.4) and (1.5), we obtain the condition

$$e^{i2\varphi_{\text{st}}} = 1, \tag{1.6}$$

which gives two possibilities for the statistical phase φ_{st}, namely $\varphi_{\text{st}} = 0, \pi$. This is exactly the above-mentioned standard classification of particles, according to which in 3D all quantum particles are either bosons ($\varphi_{\text{st}} = 0$) or fermions ($\varphi_{\text{st}} = \pi$).

However in 2D we can not prove that $\hat{\mathcal{E}}^2 = \mathbb{1}$. On the contrary, the above topological argument yields a completely different result. In particular, since we do not have any third dimension to elevate the closed path, we can not shrink a path $\mathcal{C}$ enclosing the second particle B into a single point coinciding with the position of A, without passing by B itself. Therefore in 2D the point-like path $\mathcal{C}''$ and the "original" path $\mathcal{C}$ are elements of two different homotopy classes. The former represents the homotopy class of those paths which do not enclose any other particle, while the latter belongs to the homotopy class of those paths which start in A and enclose only the particle B [1] [see Fig. 1.1 c)]. From an algebraic point of view, this means that the exchange processes are no longer described by 1 and -1 (or equivalently by $\varphi_{\text{st}} = 0$ and $\varphi_{\text{st}} = \pi$), and the particle classification in terms of bosons and fermions is no longer valid. What is still true is that as long as we consider identical particles their wave function must satisfy $|\psi(\mathbf{r}_1, \mathbf{r}_2)|^2 = |\psi(\mathbf{r}_2, \mathbf{r}_1)|^2$. Therefore, in the simplest case of a non-generate ground state, the commutation relation

$$\psi(\mathbf{r}_1, \mathbf{r}_2) = e^{i\varphi_{\text{st}}} \psi(\mathbf{r}_2, \mathbf{r}_1) \qquad \text{with} \qquad \varphi_{\text{st}} = 0, \pi \tag{1.7}$$

for bosons and fermions, respectively, generalize to

$$\boxed{\psi(\mathbf{r}_1, \mathbf{r}_2) = e^{i\varphi_{\text{st}}} \psi(\mathbf{r}_2, \mathbf{r}_1) \qquad \text{with} \qquad \varphi_{\text{st}} \in [0, 2\pi)} \tag{1.8}$$

where $\varphi_{\text{st}} = 0$ and $\varphi_{\text{st}} = \pi$ still describe bosons and fermions, while all other values of φ_{st} describe (Abelian) anyons.

1.2   Abelian and non-Abelian anyons

In the previous section we showed that in 2D quantum particles can be characterized by a statistical phase which can take any value in the interval $[0, 2\pi)$. However in doing that we assumed, for a given set of the particles coordinates, the presence of a single (non-degenerate) state. As we will see, although the existence of particles breaking the standard classification into bosons and fermion is already exciting, it is when one relaxes this non-degeneracy assumption that really surprising phenomena can happen.

In the presence of a m-fold degenerate ground-state manifold indeed, the exchange operator $\hat{\mathcal{E}}$ is not described by a phase factor, but it is rather a $m \times m$ unitary matrix acting on the ground-state space. Therefore, if our state is initially described by ψ_a, we will express the effect of particle exchange as

$$\boxed{\psi_a \mapsto \sum_b M_{ab}\, \psi_b} \ . \tag{1.9}$$

Note that in principle one has a matrix M for each pair of particles [2]. If all these matrices commute among each other, then anyons are again Abelian. On the contrary, if these matrices do not commute [see Fig. 1.2], particles are said to be non-Abelian anyons and their braiding (or exchange) can induce non-trivial rotations within the ground-state manifold.

The origin of different statistical properties of particles in two and three dimensions can be also understood within the mathematical framework of group theory. While in 3D the braiding (or exchange) processes among N indistinguishable objects can be described in terms of the elements of the permutation group S_N, in 2D these processes are related with the elements of another group: the braid group B_N. This difference was first pointed out by Leinaas and Myrheim [1977] and by Wilczek [1982a] and it leads to the possibility of observing exotic statistical properties when particles are confined in 2D. Indeed, while S_N has only two one-dimensional irreducible representations (corresponding to bosons and fermions), for B_N there is an infinite number of

---

[1] In general, if we deal with more than two particles, the homotopy classes are described by the (integer) number of particles enclosed by the paths in each class.

[2] Actually not all of them are linearly independent, but this subtlety is not important in the present context.
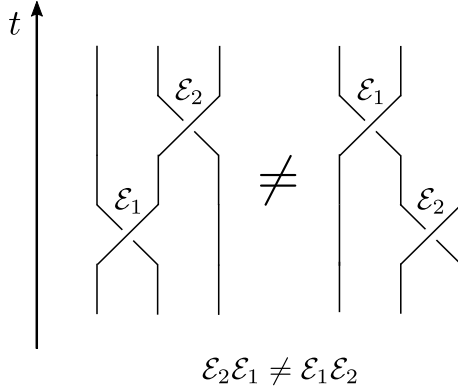
$$\mathcal{E}_2\mathcal{E}_1 \neq \mathcal{E}_1\mathcal{E}_2$$

Figure 1.2: Graphic representation of particle exchanges in 2D, described by the elements of the braid group, where $\mathcal{E}_i$ denotes the exchange of particles at position i and $i + 1$. The fact that $\mathcal{E}_2\mathcal{E}_1 \neq \mathcal{E}_1\mathcal{E}_2$ indicates particles as non-Abelian anyons.

them, each of those corresponds to a different kind of Abelian anyons [3]. Moreover, the braid group B_N also have (non-trivial) higher-dimensional irreducible representations, which (not surprisingly at this point) describe particles with non-Abelian statistics.

For a given set of anyons the effect of braiding (or exchanging) them is not the only interesting thing to look at. Indeed when one brings two anyons close together, they can be considered as a single object which can also be an anyon. The properties of the new composite object are specified by the so-called fusion rules. For the case of Abelian anyons the fusion rules are trivial. To be precise, for the fusion of n Abelian anyons of statistical phase $\alpha\pi$, only a single outcome is possible: a new particle with $\varphi_{\mathrm{st}} = n^2\alpha\pi$. Non-Abelian anyons can fuse in multiple ways instead and these different possibilities are usually called fusion channels. To understand this last point one can think that anyons carry a topological quantum number and, as two spin $1/2$ particles can combine to form either a spin 0 or a spin 1 particle, they can combine these quantities in different ways.

The fusion of two anyons is usually expressed as

$$\boxed{\phi_a \times \phi_b = \sum_c N_{ab}^c \, \phi_c} \, , \tag{1.10}$$

which means that a particle of species a fuses with a particle of species b and the result of this process is a particle of species c if $N_{ab}^c \neq 0$. In this language, Abelian anyons are characterized by $N_{ab}^c \neq 0$ for only one value of c and $N_{ab}^{c'} = 0$ for all $c' \neq c$. For non-Abelian anyons instead, there is at least one a, b couple for which there are multiple fusion channels c with $N_{ab}^c \neq 0$.

As discussed in Nayak et al. [2008], the existence of multiple fusion channels reflects the presence of degenerate states for a given set of the anyon coordinates, and in turn the possibility to have particle with non-Abelian statistical properties. We will make extensive use of this fact in Chapter 7, where we discuss a novel method to experimentally probe anyonic statistics.

To conclude we would like to rapidly recall the fusion rules for a particular anyonic model, i.e. the one of Ising anyons [Preskill, 1998, Nayak et al., 2008]. This model has three different kind of anyons, typically denoted as $\mathbb{1}$, σ and ψ, which satisfy the following fusion rules:

$$\begin{aligned} \sigma \times \sigma &= \mathbb{1} + \psi, \qquad \sigma \times \psi = \sigma, \qquad \psi \times \psi = \mathbb{1}, \\ a \times \mathbb{1} &= a \quad \text{for} \quad a = \mathbb{1}, \sigma, \psi. \end{aligned} \tag{1.11}$$

As we can see from the above expressions two σ particles can fuse to form either a $\mathbb{1}$ particle or a ψ particle. Even though this is only one of the possible anyonic models which can be found in the literature (another famous one is represented by the so-called Fibonacci anyons), it will be of crucial importance in the analysis of the Moore-Read state, which can support elementary excitations obeying the fusion rules in Eq. (1.11), as we will see Chapter 4.

---

[3]Note that there are infinitely many different ways to chose φ_{st} in $[0, 2\pi)$.

1.3 Topological quantum computation

Despite being very interesting objects in and of themselves, anyons (especially the non-Abelian ones) consolidated their central role in modern condensed-matter physics only when Kitaev [2003] proposed to use them as qubits and to take advantage of their topological nature to build quantum computers robust against external perturbations. Without entering into details (a full treatment of topological quantum computing goes far beyond the scope of this Chapter), we would like to give you the main idea behind the proposal of Kitaev [2003].

In general, in order to perform quantum computation one must be able to initialize a given many-qubit state, to perform an arbitrary series of unitary operations on such a state, and to measure the final state of the qubits. Let see how this can be done with non-Abelian anyons.

The first peculiarity of (anyon-based) topological quantum computers is that each qubit is made of several well-separated anyons, making it a non-local entity whose states ($|0\rangle$ or $|1\rangle$) are given by two different values of topological quantum number associated with the set of anyons forming it. In the previous example of Ising anyons each qubit is formed by two σ particles, and it is in the $|0\rangle$ state or in the $|1\rangle$ state if the σ particles fuse to $\mathbb{1}$ or to ψ, respectively.

The initialization process then requires the creation of anyons in specific fusion channels[4]. Note that if we assume to be able to perform measurements and unitary operations on the qubits (we explain in a second how to do that), the initialization of any given state is somehow trivial. In this case indeed we can create the anyons, without taking care of the fusion channels in which they are, measure the topological quantum numbers associated to them and finally, once we know in which fusion channels the anyons are, perform the suitable unitary operations to put them in the desired initial state.

Once we have initialized our set of qubits, controlled unitary operations can be performed by braiding the anyons in a suitable way, and here it is where topology comes into play. As we have learned, the effect of braiding does not depend on the detail of the path followed by the anyons (provided that anyons are far enough from each other). Therefore the unitary operations performed in this way will be immune to the unitary errors, as they only depend on the topology of the anyon trajectories and not on their specific geometry or dynamics. On top of that, no local perturbation can have non-zero matrix elements among different states in the ground-state manifold, as discussed in Nayak et al. [2008], and this makes our qubits almost immune to decoherence.

Once we have performed the sequence of unitary transformation representing our quantum software, there are several ways to measure the state of the qubits. In Nayak et al. [2008] for instance, the authors discuss two techniques: The first relies on the fact that bringing two anyons close to each other modifies the energy of the many-body state hosting them in a fusion-channel-dependent way. The second one is instead based on Aharonov-Bohm-type interference measurements.

In Chapter 7 we will show that, for the anyonic excitations of many-body states defined the lowest Landau level, the different fusion channels can be identified through simple density-profile measurements, making this protocol particularly appealing for ultracold atomic and photonic experiments [Macaluso et al., 2019a].

1.4 Adiabatic theorem for degenerate ground states

We have seen that the key concepts to study the statistical properties of anyons are the braiding and the exchange of two or more of them. However, we did not present the theoretical framework which allows one to mathematically treat these processes in a rigorous way. This is what we will do in the following.

As we have already mentioned, anyons have been predicted to appear as elementary excitations on top of a quantum many-body state, which we can reasonably assume to be the ground state of a time-independent Hamiltonian $\hat{H}_0$. We can now add to the system Hamiltonian some external impurity potentials able to create and pin one anyon each. In this way we obtain a new Hamiltonian $\hat{H}(t)$, whose time-dependence is only due to a set of parameters $\eta_\mu(t)$ defining the positions of the external potentials. At this point, it is easy to understand that from the theoretical point of view the braiding and the exchange processes discussed in this Chapter are nothing but the adiabatic change of some Hamiltonian parameters, and that as such they can be studied using the adiabatic theorem.

---

[4]When we say "to create an anyon" we have in mind the anyonic excitations on top of a quantum many-body state which can indeed be created by means of some external potential.

However, we can not limit ourselves to the formulation of the adiabatic theorem as originally proposed by Born and Fock [1928]. In the case of non-Abelian anyons, the Hamiltonian $\hat{H}(t=0)$ will be characterized by a m-fold degenerate ground-state manifold $\mathcal{H}_{E_0}$ indeed, and one needs to take this into account, see for instance in Rigolin and Ortiz [2012] and in Bonderson et al. [2011].

Since in the next Chapters we will make extensive use of the adiabatic theorem for the case of degenerate ground states, we decided to explicitly report it here: Let us assume that at time $t=0$ the system is described by the state $|\Psi(0)\rangle$ which belongs to the m-fold degenerate ground state manifold $\mathcal{H}_{E_0(0)}$, and that $\mathcal{H}_{E_0(0)}$ is spanned by the basis $\{|\psi_\alpha\rangle\}_{\alpha=1,\dots,m}$, such that $\hat{H}(t=0)|\psi_\alpha\rangle = E_0(0)|\psi_\alpha\rangle$ and $\langle\psi_\alpha|\psi_\beta\rangle = \delta_{\alpha\beta}$. Then the adiabatic theorem tells us that if we adiabatically vary in time some Hamiltonian parameters, the time-evolved state $|\Psi(T)\rangle$ will be given by

$$|\Psi(T)\rangle = \mathcal{U}(T)|\Psi(0)\rangle \in \mathcal{H}_{E_0(T)}. \tag{1.12}$$

where the unitary transformation $\mathcal{U}(T)$ is gauge invariant if and only if the adiabatic process describes a closed path in parameter space (namely if $\hat{H}(T) = \hat{H}(0)$) and it is in general the product of three different contributions: (i) The dynamical phase factor

$$\mathcal{U}_{\text{dyn}} = \exp\left[-\frac{i}{\hbar}\int_0^T E_0(t)dt\right], \tag{1.13}$$

in which $E_0(t)$ denotes the energy of the states in the ground-state manifold at time t.
(ii) The geometric contribution

$$\boxed{\mathcal{U}_{\text{B}} = \mathcal{P}\exp\left[i\int_0^T \mathcal{A}(t)dt\right]}, \tag{1.14}$$

known as Berry matrix[5] [Wilczek and Zee, 1984, Rigolin and Ortiz, 2012], in which $\mathcal{P}$ stands for path –or time– ordering and the Berry connection $\mathcal{A}(t)$ has matrix elements

$$
\begin{aligned}
\mathcal{A}_{\alpha\beta}(t) &= i\langle\psi_\alpha(t)|\frac{d}{dt}|\psi_\beta(t)\rangle = \mathcal{A}_{\alpha\beta}^{\vec{\lambda}}\cdot\frac{d\vec{\lambda}(t)}{dt}, \\
\mathcal{A}_{\alpha\beta}^{\vec{\lambda}} &= i\langle\psi_\alpha(\vec{\lambda})|\frac{\partial}{\partial\vec{\lambda}}|\psi_\beta(\vec{\lambda})\rangle,
\end{aligned}
\tag{1.15}
$$

where $\vec{\lambda}(t)$ is the set of time-dependent Hamiltonian parameters which are varied in time.
(iii) A unitary transformation $\mathcal{B}$ taking into account the evolution of the basis states during the adiabatic process and projecting the final state (otherwise expressed in the time-evolved basis) onto the states on the basis at $t=0$. It has matrix elements

$$\boxed{\mathcal{B}_{\alpha\beta} = \langle\psi_\alpha(0)|\psi_\beta(T)\rangle}, \tag{1.16}$$

so that $|\psi_\alpha(T)\rangle = \mathcal{B}|\psi_\alpha(0)\rangle$ [6].

Now that we have shown the different terms entering into the definition of the unitary transformation $\mathcal{U}(T) = \mathcal{U}_{\text{dyn}}\mathcal{U}_{\text{B}}\mathcal{B}$ for a generic adiabatic process, there are few last remarks which must be made before concluding this Chapter.

First of all, when considering the adiabatic braiding (or exchange) of anyonic excitations, the time-dependent Hamiltonian parameters $\vec{\lambda}(t)$ correspond to the positions of the external potentials pinning the anyons at coordinates $\eta_\mu(t)$. Moreover, quantum many-body systems supporting anyons are typically gapped in the bulk, meaning that one can safely apply the adiabatic theorem as long as the time duration of the braiding process T satisfies $T \gg h/\Delta E$, where ΔE is the just mentioned energy gap. In order words, in this kind of systems it is always possible to move the pinning potentials (at finite velocity) and perform braiding (or exchange) operations without closing the gap.

There is another point which is worth highlighting and it concerns the geometric contribution to $\mathcal{U}(T)$: Although it is well known that the adiabatic motion of a quantum state in parameter

---

[5]Note that $\mathcal{U}_{\text{B}}$ represents the matrix generalization of the Berry [1984] phase, which is known to encode (part of) the geometric contribution to time dynamics.
[6]As we will see in Chapters 2 and 7, this term plays a crucial role in determining the statistical properties of anyons.
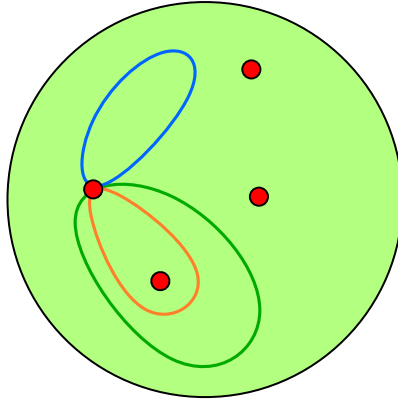
Figure 1.3: Schematic representation of a quantum many-body state (green area) in which the anyons (red circles) are pinned at positions $\eta_\mu(t)$ by means of some external potentials. The blue, orange and green lines represents three different paths which can be followed by the leftmost anyonic excitation. The blue path does not encircle any other anyon and therefore the unitary transformation $\mathcal{U}(T)$ associated with it will not encode any information about the anyonic statistics. On the contrary, the orange and the blue path both encircle another anyon. As a consequence the two different $\mathcal{U}(T)$ describing them will contain the same topological contribution due to the anyon braiding.

space may lead to a geometric contribution to the time dynamics [Berry, 1984], it is important to recall that it is composed of two parts. One of them is non-topological and depends on the specific path followed by the anyons[7] (meaning that it is different for all paths depicted in Fig. 1.3). The other one has topological nature instead, and only depends on whether two anyons have been exchanged or not, namely on the topology of the path. Therefore if we consider the paths reported in Fig. 1.3 this contribution will be absent for the blue path, while it will be present and equal for the orange and the green paths. Anyonic statistics is fully encoded in this latter term, as discussed for instance in Nayak et al. [2008].

Finally, we would like to stress that only the product $\mathcal{U}_B \mathcal{B}$ is a gauge-invariant quantity. On the contrary, if taken singularly, both $\mathcal{U}_B$ and $\mathcal{B}$ depend on the particular choice of the basis states $\{|\psi_\alpha\rangle\}_{\alpha=1,...,m}$. The choice of one basis with respect to another may move part of the statistical properties of the anyons from $\mathcal{U}_B$ to $\mathcal{B}$, and viceversa [see for instance the example reported in Sec. 3.4.1]. As we will see in Chapter 7, one can exploit this fact to link the statistical properties of anyons to experimentally observable quantities.

---

[7]In the following Chapters we will consider the anyonic excitations on top of fractional quantum Hall states and we will show that in this particular case the non-topological geometric contribution to $\mathcal{U}(T)$ can be identified with an Aharonov-Bohm phase [Aharonov and Bohm, 1959].

Chapter 2

The fractional quantum Hall effect in atomic and photonic systems.

$\mathcal{A}$mong the many different wonderful phenomena occurring in condensed-matter physics, the quantum Hall effect (QHE) is for sure one of the most surprising. Despite the myriad of astonishing properties related to it, its observation only required the restriction of an electron gas in a 2D plane under the effect of a strong orthogonal magnetic field. This was exactly what von Klitzing et al. [1980] did, when they observed for the first time the most experimentally visible manifestation of the QHE, i.e. the quantization of the Hall resistivity, which was found to take the form

$$R_{\mathrm{H}} = \left(\frac{h}{e^2} \right) \frac{1}{\nu}.$$

Concerning the value of ν, originally it was measured to be an integer to extraordinary precision so that the phenomenon discovered by von Klitzing et al. [1980] took the name of integer quantum Hall effect (IQHE). After that it was found that ν is not restricted to take integer values, but it can also take some particular rational values. In this case one has the so-called fractional quantum Hall effect (FQHE) which was discovered by Tsui et al. [1982], when they measured the Hall resistivity quantization at $\nu = 1/3$ and $\nu = 2/3$.

Although the study of the IQHE is certainly interesting (it for instance allowed Thouless et al. [1982] to relate the quantization of the Hall conductance to the non-trivial topology of the energy bands for electrons in the quantum Hall regime), it is in the FQHE context where the most remarkable things happen. Indeed in this case Coulomb interactions lead to the formation of a highly correlated quantum state, which has been identified with a new phase of matter called quantum liquid. This kind of phases turned out to be characterized by a peculiar internal order, known as topological order [Wen, 1989], and by many astonishing properties, as for instance the presence of elementary bulk excitations displaying fractional charge and anyonic statistics. In addition to these elementary excitations, a FQH system can also have chiral gapless edge excitations, in which transport occurs only in one direction [Chang, 2003].

As a consequence of this striking behavior, the QHE (and in particular its fractional version) has been a constant source of new ideas, which laid the foundation for many research fields. Important examples include the field of topological insulators [Hasan and Kane, 2010, Qi and Zhang, 2011], topological order [Wen, 2019] and topological quantum computing [Nayak et al., 2008], which have their origins in the QHE.

For years since their discovery, FQH states have been observed only in electronic systems, however nowadays they have bosonic counterparts which can be studied in ultracold atomic and photonic systems. This opportunity, which has constantly increased the interest for the quantum Hall physics, is intimately related to the recent technological advances made in the field of the so-called quantum simulators [Georgescu et al., 2014], and in particular to the possibility given by the so-called artificial gauge fields to simulate the behavior of charged particles experiencing an external magnetic field with neutral objects, such as atoms and photons.

In the following we shall review the basic aspects of the QHE, starting from the quantum mechanical treatment of a charged particle immersed in an orthogonal magnetic field (the so-called Landau quantization) to conclude with a discussion about the most promising platforms for the simulation of the FQHE.

2.1 The Landau quantization

In this section we would like to recall what happens, from the quantum mechanical point of view, to a 2D charged particle in the presence of a strong orthogonal magnetic field. This is known as Landau quantization and represents a fundamental background to understand the quantum Hall effect (both the integer and the fractional one). It consists of the quantization of the particle kinetic energy into so-called Landau levels [Landau and Lifshitz, 2013], which are basically nothing but the spectrum of a 1D harmonic oscillator with oscillator frequency given by the cyclotron frequency $\omega_C = qB/m$, where B is the magnetic field strength while q and m denotes the particle charge and mass, respectively.

In the following, we will consider such a particle to be an electron and we will neglect its spin. We will obtain the LLs in the first part of this section, while the second one will be devoted to the discussion of the degeneracy of such energy levels and of two possible gauge choices for the vector potential: the symmetric gauge and the Landau gauge.

2.1.1 Landau Levels

The Lagrangian describing an electron moving in a magnetic field is

$$\mathcal{L} = \frac{1}{2}m\,\dot{\mathbf{r}}^2 - e\,\dot{\mathbf{r}}\cdot\mathbf{A}, \tag{2.1}$$

where $\mathbf{A}$ is the vector potential associated with the magnetic field $\mathbf{B} = \nabla\times\mathbf{A} = B\,\hat{e}_z$. The knowledge of the system Lagrangian allows one to compute the canonical momentum, which reads:

$$\mathbf{p} = \frac{\partial\mathcal{L}}{\partial\dot{\mathbf{r}}} = m\dot{\mathbf{r}} - e\mathbf{A}. \tag{2.2}$$

From the expression above we can easily see that the canonical momentum is not a gauge-invariant quantity, since the vector potential $\mathbf{A}$ is not[1]. Therefore, in order to describe free electrons in the presence of a magnetic field, we need to replace the canonical momentum $\mathbf{p}$ by its gauge-invariant form $\mathbf{\Pi}$, known as mechanical momentum. For this purpose we use the so-called minimal substitution:

$$\boxed{\mathbf{p}\to\mathbf{\Pi} = \mathbf{p} + e\mathbf{A}}. \tag{2.3}$$

Note that the mechanical momentum obtained in this way is indeed gauge-invariant and that it corresponds to the "usual" physical momentum $m\,\dot{\mathbf{r}}$.

At this point, starting from the Lagrangian in Eq. (2.1), we can use the Legendre transformation to obtain the system Hamiltonian, which reads

$$\boxed{H = \mathbf{p}\cdot\dot{\mathbf{r}} - \mathcal{L} = \frac{1}{2m}(\mathbf{p} + e\mathbf{A})^2}, \tag{2.4}$$

and which can be expressed in terms of the gauge-invariant mechanical momentum $\mathbf{\Pi}$ as

$$H(\mathbf{\Pi}) = \frac{\mathbf{\Pi}^2}{2m}. \tag{2.5}$$

Now we are ready to move to the quantum-mechanical framework by means of the so-called canonical quantization procedure. The first step in this direction is to identify which variables are canonical. In this particular case the canonical variables are given by the electron position in the 2D plane $\mathbf{r} = (x, y)$ and the gauge-dependent canonical momentum $\mathbf{p} = (p_x, p_y)$, which are characterized by the following Poisson brackets:

$$\{r_i, p_j\} = \delta_{ij} \quad\text{and}\quad \{r_i, r_j\} = \{p_i, p_j\} = 0. \tag{2.6}$$

---

[1]Consider for instance a gauge transformation $\mathbf{A}\to\mathbf{A}' = \mathbf{A} + \nabla\lambda$, where λ is an arbitrary differentiable function. Under this gauge transformation the canonical momentum $\mathbf{p}$ transforms as $\mathbf{p}\to\mathbf{p}' = \mathbf{p} - e\nabla\lambda$ meaning that it is a gauge-dependent quantity.

To move from the classical to the quantum description now we simply have to promote the electron position **r** and the canonical momentum **p** to operators and transform their Poisson brackets into canonical commutation relations

$$[\hat{r}_i, \hat{p}_j] = i\hbar\,\delta_{ij} \quad \text{and} \quad [\hat{r}_i, \hat{r}_j] = [\hat{p}_i, \hat{p}_j] = 0. \tag{2.7}$$

These commutation relations imply that the components of the gauge-invariant momentum do not commute and, in particular, that they obey

$$\left[\hat{\Pi}_x, \hat{\Pi}_y\right] = -ie\hbar B = -i\frac{\hbar^2}{l_B^2}, \tag{2.8}$$

where we have introduced the magnetic length

$$\boxed{l_B = \sqrt{\frac{\hbar}{eB}}}. \tag{2.9}$$

It represents the characteristic length scale governing quantum phenomena in presence of a magnetic field and, as we will discuss in Sec. 8.1, plays a central role also in the presence of lattice potentials.

At this point we introduce two new operators, which are linear combinations of $\hat{\Pi}_x$ and $\hat{\Pi}_y$. These are ladder operators, exactly as those defined in the quantum-mechanical treatment of a 1D harmonic oscillator, and have the following form:

$$\begin{aligned}
\hat{a} &= \frac{1}{\sqrt{2e\hbar B}}\left(\hat{\Pi}_x - i\,\hat{\Pi}_y\right) = \frac{l_B}{\sqrt{2}\hbar}\left(\hat{\Pi}_x - i\,\hat{\Pi}_y\right) \\
\hat{a}^\dagger &= \frac{1}{\sqrt{2e\hbar B}}\left(\hat{\Pi}_x + i\,\hat{\Pi}_y\right) = \frac{l_B}{\sqrt{2}\hbar}\left(\hat{\Pi}_x + i\,\hat{\Pi}_y\right),
\end{aligned} \tag{2.10}$$

where the normalization factor has been chosen to have the usual commutation relation between ladder operators, i.e.

$$\left[\hat{a}, \hat{a}^\dagger\right] = 1. \tag{2.11}$$

Expressions in Eq. (2.10) for a and $a^\dagger$ can be inverted to write the two components of **Π** in terms of the ladder operators:

$$\begin{aligned}
\hat{\Pi}_x &= \sqrt{\frac{e\hbar B}{2}}(\hat{a}^\dagger + \hat{a}) = \frac{\hbar}{\sqrt{2}l_B}(\hat{a}^\dagger + \hat{a}) \\
\hat{\Pi}_y &= -i\sqrt{\frac{e\hbar B}{2}}(\hat{a}^\dagger - \hat{a}) = -i\frac{\hbar}{\sqrt{2}l_B}(\hat{a}^\dagger - \hat{a}).
\end{aligned} \tag{2.12}$$

If we now insert the previous expressions in the Hamiltonian (2.4), we can see that it takes the same form as the one of a 1D harmonic oscillator, i.e.

$$\hat{H} = \frac{\hat{\mathbf{\Pi}}^2}{2m} = \frac{1}{2m}\left(\hat{\Pi}_x^2 + \hat{\Pi}_y^2\right) = \hbar\omega_C\left(\hat{a}^\dagger\hat{a} + \frac{1}{2}\right), \tag{2.13}$$

where $\omega_C = eB/m$ is the already mentioned cyclotron frequency.

Of course, the eigenstates of the Hamiltonian in Eq. (2.13) are the same as those of the number operator $\hat{a}^\dagger\hat{a}$, i.e. states $|n\rangle$ such that $\hat{a}^\dagger\hat{a}|n\rangle = n|n\rangle$. The action of the ladder operators on these states is the usual one, namely

$$\hat{a}^\dagger\,|n\rangle = \sqrt{n+1}\,|n+1\rangle \quad \text{and} \quad \hat{a}\,|n\rangle = \sqrt{n}\,|n-1\rangle, \tag{2.14}$$

where the last equation holds only for $n > 0$. By means of the equations above one can construct the Hilbert space of the theory by simply introducing a ground state $|0\rangle$ and acting with $\hat{a}^\dagger$. Any state $|n\rangle$ can indeed be expressed as

$$|n\rangle = \frac{\left(\hat{a}^\dagger\right)^n}{\sqrt{n!}}\,|0\rangle. \tag{2.15}$$

Since the state $|n\rangle$ is an eigenstate of $\hat{a}^\dagger \hat{a}$ with eigenvalue n, its energy will be given by

$$E_n = \hbar \omega_C \left(n + \frac{1}{2} \right),$$ (2.16)

where n is a non-negative integer.

As a consequence, the energy levels of an electron in a background magnetic field, are equally spaced and the energy gap between two of them is given by $\hbar \omega_C$. These energy levels are known as Landau levels (LLs) and, being linear in the cyclotron frequency $\omega_C = eB/m$, they scale linearly with the magnetic field. It is important to notice that this spectrum looks completely different from that of a free particle in the absence of a background magnetic field.

2.1.2   Level degeneracy and gauge choices

We have just seen that the energy of an electron in presence of an orthogonal magnetic field is characterized by a single quantum number n, labelling the different LLs. But it seems there is something missing in our description of the electron. The original Hamiltonian is a function which depends on two pairs of conjugate operators ($\hat{x}$ and $\hat{p}_x$, and $\hat{y}$ and $\hat{p}_y$, to be precise) [see Eq. (2.4)] and therefore we would expect the quantum states to be described by two quantum numbers. However, when we express such a Hamiltonian in terms of the gauge-invariant momentum $\hat{\mathbf{\Pi}}$, or in terms of the ladder operators, it depends only on a single pair of conjugate operators. Be careful, this does not mean that we made a mistake in the evaluation of the energies E_n. On the contrary, the energy levels in Eq. (2.16) are the correct spectrum of the theory but, differently from the harmonic oscillator case, each of them is wildly degenerate. Thus there are many different states with the same quantum number n (and therefore the same energy) and if we want a complete description of them, we need a second pair of conjugate operators which must commute with the Hamiltonian.

To observe the LL degeneracy with the algebraic approach we adopted before, we can introduce yet another kind of "momentum"

$$\hat{\mathbf{\Gamma}} = \hat{\mathbf{p}} - e\mathbf{A},$$ (2.17)

which we will call pseudo-momentum. Note that the pseudo-momentum we have just introduced and the mechanical momentum in Eq. (2.3) only differ by the minus sign. As a result it turns out to be gauge-dependent and therefore it can not represent any physical quantity[2]. The commutator between the pseudo-momentum components is gauge-independent instead, and it is given by

$$[\hat{\Gamma}_x, \hat{\Gamma}_y] = ie\hbar B = i\frac{\hbar^2}{l_B^2}.$$ (2.18)

Concerning the mixed commutators, they read:

$$\begin{aligned}
\left[\hat{\Pi}_x, \hat{\Gamma}_x\right] &= 2ie\hbar \frac{\partial A_x}{\partial x}, \\
\left[\hat{\Pi}_y, \hat{\Gamma}_y\right] &= 2ie\hbar \frac{\partial A_y}{\partial y}, \\
\left[\hat{\Pi}_x, \hat{\Gamma}_y\right] &= \left[\hat{\Pi}_y, \hat{\Gamma}_x\right] = ie\hbar \left(\frac{\partial A_x}{\partial y} + \frac{\partial A_y}{\partial x} \right).
\end{aligned}$$ (2.19)

Expressions in Eq. (2.19) tell us that in general we can not simultaneously diagonalize $\hat{\mathbf{\Gamma}}$ and the Hamiltonian, since they do not commute. Indeed the commutators between $\hat{H}$ and the x and y

---

[2]Even though the pseudo-momentum $\mathbf{\Gamma}$ is a gauge-dependent quantity, one can give a physical interpretation of it within a semi-classical description of the Landau levels degeneracy, as done for instance in Tong [2016].

components of $\hat{\mathbf{\Gamma}}$ are given by:

$$
\begin{aligned}
\left[\hat{H}, \hat{\Gamma}_x\right] = {}& i\frac{e\hbar}{m}\left[\hat{\Pi}_x\left(\frac{\partial A_x}{\partial x}\right) + \left(\frac{\partial A_x}{\partial x}\right)\hat{\Pi}_x\right] + \\
& i\frac{e\hbar}{2m}\left[\hat{\Pi}_y\left(\frac{\partial A_x}{\partial y} + \frac{\partial A_y}{\partial x}\right) + (\frac{\partial A_x}{\partial y} + \frac{\partial A_y}{\partial x})\hat{\Pi}_y\right], \\
\left[\hat{H}, \hat{\Gamma}_y\right] = {}& i\frac{e\hbar}{m}\left[\hat{\Pi}_y\left(\frac{\partial A_y}{\partial y}\right) + \left(\frac{\partial A_y}{\partial y}\right)\hat{\Pi}_y\right] + \\
& i\frac{e\hbar}{2m}\left[\hat{\Pi}_x\left(\frac{\partial A_x}{\partial y} + \frac{\partial A_y}{\partial x}\right) + \left(\frac{\partial A_x}{\partial y} + \frac{\partial A_y}{\partial x}\right)\hat{\Pi}_x\right],
\end{aligned}
\tag{2.20}
$$

which are both different from zero. However, this situation can be fixed though an appropriate gauge choice. Indeed, by choosing the so-called symmetric gauge

$$
\boxed{\mathbf{A} = -\frac{1}{2}\,\mathbf{r} \times \mathbf{B} = \frac{B}{2}(-y, x, 0)}\,,
\tag{2.21}
$$

all mixed commutators in Eq. (2.19) vanish and the components of the pseudo-momentum commute with the Hamiltonian.

The symmetric gauge clearly breaks translational symmetry in both the x and the y direction. However it preserves rotational symmetry with respect to the origin. This indicates that the angular momentum is a good quantum number, as we will see in the following. This particular choice of $\mathbf{A}$ is important for two reasons: It permits to give a semi-classical interpretation to the LLs degeneracy, as discussed for example by Tong [2016], but, most importantly, the wave functions obtained in this gauge represent the key ingredient to describe the fractional quantum Hall effect. Note that the symmetric gauge is only one of the possible choices; a second popular gauge is the so-called Landau gauge, which will be discussed at the end of this section.

Starting from the two mutually conjugate components of the pseudo-momentum we can now define a second pair of raising and lowering operators

$$
\begin{aligned}
\hat{b} &= \frac{1}{\sqrt{2e\hbar B}}(\hat{\Gamma}_x + i\,\hat{\Gamma}_y) = \frac{l_B}{\sqrt{2}\hbar}(\hat{\Gamma}_x + i\,\hat{\Gamma}_y) \\
\hat{b}^\dagger &= \frac{1}{\sqrt{2e\hbar B}}(\hat{\Gamma}_x - i\,\hat{\Gamma}_y) = \frac{l_B}{\sqrt{2}\hbar}(\hat{\Gamma}_x - i\,\hat{\Gamma}_y),
\end{aligned}
\tag{2.22}
$$

satisfying $[\hat{b}, \hat{b}^\dagger] = 1$. In the symmetric gauge these new ladder operators both commute with $\hat{a}$ and $\hat{a}^\dagger$, and, as a consequence, they commute also with the Hamiltonian $\hat{H}$, i.e. $[\hat{b}, \hat{H}] = [\hat{b}^\dagger, \hat{H}] = 0$.

At this point, as we did for the $\hat{a}$ and $\hat{a}^\dagger$ operators, one can introduce the number operator $\hat{b}^\dagger\hat{b}$, whose eigenstates satisfy the eigenvalue equation $\hat{b}^\dagger\hat{b}|m\rangle = m|m\rangle$ (with m a non-negative integer). In this way we obtain a second quantum number m, providing the degeneracy of the different LLs. Furthermore, we can use this second quantum number, together with the previous one, to label a generic quantum state in the Hilbert space of the theory. In particular, we can define such a state as

$$
\boxed{|n, m\rangle = \frac{(\hat{a}^\dagger)^n(\hat{b}^\dagger)^m}{\sqrt{n!m!}}|0, 0\rangle}\,,
\tag{2.23}
$$

where $|0, 0\rangle$ is the ground state of the theory, i.e. a state which is annihilated by both lowering operators: $\hat{a}|0, 0\rangle = \hat{b}|0, 0\rangle = 0$. Finally, for a given state $|n, m\rangle$, the energy can be calculated by applying on it the Hamiltonian in Eq. (2.13). The resulting energies coincide with the Landau levels in Eq. (2.16), which do not depend on the m quantum number.

Before entering the discussion about the specific form of the wave functions describing the states $|n, m\rangle$, we would like to stress some subtle points which we intentionally overlooked in the above reasoning. In particular, one may wonder why, for a given value of n, there must be a state $|n, m = 0\rangle$ such that $\hat{b}|n, 0\rangle = 0$. If the presence of a state with $n = 0$ is ensured by the fact the the energy must be bound from below, this argument can not by applied to the eigenstates $|m\rangle$ of the $\hat{b}^\dagger\hat{b}$ operator since, independently on the value of m, all of them will have the same energy. Therefore, how can we be sure that there are no eigenstates of $\hat{b}^\dagger\hat{b}$ having negative or non-integer eigenvalues? The answer to this completely legitimate question can be found in Cohen-Tannoudji

et al. [2019], where the authors explicitly show that m must be a positive integer, and also that no further quantum number is needed to describe the possible quantum states of a 2D electron experiencing an orthogonal magnetic field.

Lowest Landau level wave functions in the symmetric gauge

Now we want to calculate the electronic wave functions $\varphi_{n,m}(x,y) = \langle x,y|n,m \rangle$ in the symmetric gauge. In particular we focus our attention on the lowest Landau level (LLL) wave functions $\varphi_{0,m}(x,y) \equiv \varphi_m(x,y)$, which are of crucial importance to discuss both the fractional quantum Hall effect and the Jack polynomial formalism presented in Chapter 5.

States in the LLL ($n = 0$) are annihilated by the lowering operator $\hat{a}$, i.e.,

$$\hat{a}|0,m\rangle = 0 \quad \forall m. \tag{2.24}$$

The above condition can be rewritten as a differential equation. In order to do that we can start manipulating the previous expression for $\hat{a}$ [see Eq. (2.10)] in the following way:

$$
\begin{aligned}
\hat{a} &= \frac{l_B}{\sqrt{2}\hbar}(\hat{\Pi}_x - i\,\hat{\Pi}_y) \\
&= \frac{l_B}{\sqrt{2}\hbar}\left[\hat{p}_x - i\hat{p}_y + e\left(A_x - iA_y\right)\right] \\
&= \frac{l_B}{\sqrt{2}\hbar}\left[-i\hbar\left(\frac{\partial}{\partial x} - i\frac{\partial}{\partial y}\right) + \frac{eB}{2}\left(-y - ix\right)\right],
\end{aligned}
\tag{2.25}
$$

in which we have used the definition (2.3) of the mechanical momentum, the explicit form (2.21) of the vector potential in the symmetric gauge and the position representation of the momentum operator $\mathbf{p} = -i\hbar\nabla = -i\hbar(\partial/\partial x, \partial/\partial y)$. To further simplify Eq. (2.25) we adopt the complex coordinates notation by introducing

$$z = x - iy \quad \text{and} \quad \bar{z} = x + iy. \tag{2.26}$$

Note that this definition of the complex coordinates has inverted signs with respect to the usual one. However, this is necessary to have holomorphic LLL wave functions rather than anti-holomorphic ones. We also introduce the associated holomorphic and anti-holomorphic derivatives, which read

$$\partial = \frac{1}{2}\left(\frac{\partial}{\partial x} + i\frac{\partial}{\partial y}\right) \quad \text{and} \quad \bar{\partial} = \frac{1}{2}\left(\frac{\partial}{\partial x} - i\frac{\partial}{\partial y}\right). \tag{2.27}$$

We can now express $\hat{a}$ in terms of these new coordinates as

$$\hat{a} = -i\sqrt{2}\left(l_B\,\bar{\partial} + \frac{z}{4l_B}\right), \tag{2.28}$$

and the same can be done for $\hat{a}^\dagger$, which reads

$$\hat{a}^\dagger = -i\sqrt{2}\left(l_B\,\partial - \frac{\bar{z}}{4l_B}\right). \tag{2.29}$$

This allows us to write the LLL condition described by Eq. (2.24) as the following differential equation

$$\left(l_B\,\bar{\partial} + \frac{z}{4l_B}\right)\varphi_m(z,\bar{z}) = 0, \tag{2.30}$$

which is easily solved by

$$\varphi_m(z,\bar{z}) = f_m(z)\,e^{-|z|^2/4l_B^2}, \tag{2.31}$$

where $f_m(z)$ can be any holomorphic function. This ambiguity in the position representation should not be a big surprise. It simply reflects that there is an additional degree of freedom, which we already know being related to the second quantum number m.

To obtain the explicit expression for the different LLL wave functions we need to write also $\hat{b}$ and $\hat{b}^\dagger$ in the position representation. Indeed, once we know their form as differential operators, we can first evaluate the $m = 0$ wave function by solving $\hat{b}|n = 0, m = 0\rangle = 0$, and then construct

all the others by applying $b^\dagger$. Thus, exactly as we did for $\hat{a}$, we find the position representation of the ladder operators which now depend on the pseudo-momentum $\mathbf{\Gamma}$. These are given by

$$\hat{b} = -i\sqrt{2}\left(l_B\,\partial + \frac{\bar{z}}{4l_B}\right) \quad \text{and} \quad \hat{b}^\dagger = -i\sqrt{2}\left(l_B\,\bar{\partial} - \frac{z}{4l_B}\right). \tag{2.32}$$

The generic solution of

$$\hat{b}\,|n,0\rangle = \left(l_B\,\partial + \frac{\bar{z}}{4l_B}\right)\varphi_{n,0}(z,\bar{z}) = 0 \tag{2.33}$$

is $\varphi_{n,0}(z,\bar{z}) = g_n(\bar{z})\,e^{-|z|^2/4l_B^2}$, in which $g_n(\bar{z})$ is an anti-holomorphic function. However we are interested in $\varphi_{n=0,m=0} \equiv \varphi_0$, which is solution of both Eq. (2.30) and Eq. (2.33). As a consequence, φ_0 can be nothing but the Gaussian term with a prefactor which is simultaneously holomorphic and anti-holomorphic, i.e., a constant fixed by the normalization. Thus we end with

$$\varphi_0(z,\bar{z}) = \frac{1}{\sqrt{2\pi l_B^2}}\,e^{-|z|^2/4l_B^2}. \tag{2.34}$$

Now that we have found $\varphi_0(z,\bar{z})$, we can build up the states with higher values of m by acting with $b^\dagger$. In particular, for a given value of m one has

$$\boxed{\varphi_m(z,\bar{z}) = \frac{1}{\sqrt{2\pi l_B^2 m!}}\left(\frac{z}{\sqrt{2}l_B}\right)^m e^{-|z|^2/4l_B^2}}. \tag{2.35}$$

Note that such a wave function is cylindrically symmetric and peaked on a ring of radius $r \simeq \sqrt{2m}\,l_B$, making the symmetric gauge the natural choice for the description of disk-shaped and ring-shaped samples [see Sec. 6.1].

These LLL-wave functions have also the property of being eigenstates of the z-component of the angular momentum operator. To show this we express the angular momentum operator $\hat{L}_z$ in complex coordinates

$$\hat{L}_z = (\mathbf{r} \times \mathbf{p})_{\hat{z}} = i\hbar\left(x\frac{\partial}{\partial y} - y\frac{\partial}{\partial x}\right) = \hbar\left(z\partial - \bar{z}\bar{\partial}\right). \tag{2.36}$$

and then we apply it to the generic LLL wave function in Eq. (2.35). In this way we obtain

$$\hat{L}_z\,\varphi_m(z,\bar{z}) = \hbar m\,\varphi_m(z,\bar{z}), \tag{2.37}$$

which allows us to identify the second quantum number m as the angular momentum eigenvalue[3].

The Landau gauge

As we have already mentioned, the symmetric gauge in Eq. (2.21) is not the only possible choice for the vector potential $\mathbf{A}$. Another famous gauge is the so-called Landau gauge[4]

$$\boxed{\mathbf{A} = B\,(0,x,0)}. \tag{2.38}$$

This choice of $\mathbf{A}$ clearly breaks both rotational symmetry around the z axis and translational symmetry in the x direction. However, it preservers the translation symmetry in the y direction and this will be shown by the explicit form of the Hamiltonian within this gauge. Indeed, if we insert the above expression for the vector potential in Eq. (2.4) we obtain the Hamiltonian

$$\hat{H} = \frac{1}{2m}\left[\hat{p}_x^2 + (\hat{p}_y + eBx)^2\right], \tag{2.39}$$

---

[3]Remember that the symmetric gauge preserves rotational symmetry and therefore it should not be strange to you that the second quantum number m is related to the angular momentum eigenvalue.

[4]Note that there is not a unique Landau gauge. Another common choice of the vector potential known as Landau gauge is $\mathbf{A} = B(-y,0,0)$. In this case x and y are basically inverted and $\mathbf{A}$ results invariant under translation in the x direction.
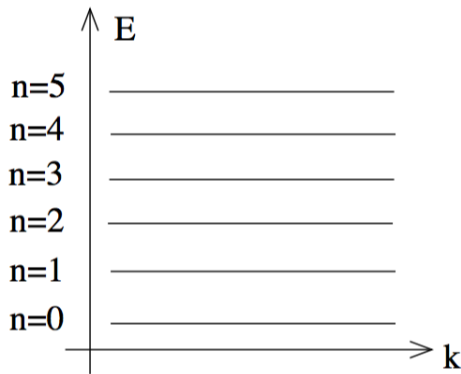
Figure 2.1: Landau Levels as a function of the k quantum number. This picture has been taken from Tong [2016].

which is manifestly invariant for translations along the y axis, as expected. As a consequence, instead of looking for eigenstate of the angular momentum $\hat{L}_z$ as we have done for the symmetric gauge, we can now look for energy eigenstates which are also eigenstate of $\hat{p}_y$.

Since the eigenstates of the y component of the momentum operator are plane-waves in the y direction, we can reasonably assume the following plane-wave ansatz for the Hamiltonian eigenstates:

$$\varphi_k(x, y) = f_k(x)\, e^{iky}, \tag{2.40}$$

where k is related to the eigenvalue of the operator $\hat{p}_y$, in particular

$$\hat{p}_y\, \varphi_k(x, y) = -i\hbar \frac{\partial}{\partial y} \varphi_k(x, y) = \hbar k\, \varphi_k(x, y). \tag{2.41}$$

At this point it is easy to see that, if we apply the Hamiltonian in Eq. (2.39) to a wave function of this kind, the y component of the momentum operator can be replaced by its eigenvalue $\hbar k$,

$$\hat{H}\, \varphi_k(x, y) = \frac{1}{2m} \left[\hat{p}_x^2 + (\hbar k + eBx)^2 \right] \varphi_k(x, y) = \hat{H}_k\, \varphi_k(x, y). \tag{2.42}$$

This Hamiltonian can be recast in a much more familiar form

$$\hat{H}_k = \frac{1}{2m} \left[\hat{p}_x^2 + (\hbar k + eBx)^2 \right] = \frac{\hat{p}_x^2}{2m} + \frac{e^2 B^2}{2m} \left(x + \frac{\hbar}{eB} k \right)^2 = \frac{\hat{p}_x^2}{2m} + \frac{1}{2} m \omega_C^2 \left(x + k l_B^2 \right)^2, \tag{2.43}$$

which is nothing but the Hamiltonian of a 1D harmonic oscillator centered at $x = -k l_B^2$. Note that the frequency of the harmonic oscillator described by $\hat{H}_k$ corresponds to the cyclotron frequency $\omega_C = eB/m$. Before moving on we would like to highlight the fact that we started with a 2D Hamiltonian but now we have a 1D Hamiltonian. However, while in Sec. 2.1.1 we did not know where the second degree of freedom "disappeared", here it is easy to see that the momentum in the y direction has turn into a shift (along x) in the position of the harmonic oscillator.

The eigenvalues of $\hat{H}_k$ are then easy to find: they are indeed given by the LLs in Eq. (2.16), and do not depend on the second quantum number k [see Fig. 2.1]. At the same time, we can also explicitly write down the wave functions describing the Hamiltonian eigenstatess, which read

$$\boxed{\varphi_{n,k}(x, y) \propto e^{iky}\, \mathrm{H}_n(x + k l_B^2)\, e^{(x + k l_B^2)/2 l_B^2}}, \tag{2.44}$$

in which H_n denote the Hermite polynomials. Note that for $n = 0$ these wave functions look like stripes, which extend along y while they have a Gaussian shape in the x direction. Hence, they are completely different from those obtained in the symmetric gauge [see Eq. (2.35)], which are characterized by ring shape.

To conclude we would like to count the total number of degenerate states in each LL and to see in this way how large this degeneracy is. For this purpose, we consider a finite region of the (x, y)-plane. In particular, since we want to use the above results obtained in the Landau gauge,

we pick a rectangle region of size $L_x \times L_y$. Now we have only to count how many states of the form $\varphi_{n,k}(x,y)$ fit inside this rectangle for a given value of n.

On the one hand, having a finite extension along y corresponds to putting the system in an infinite potential well (in the y direction), which implies the quantization of k in units of $2\pi/L_y$. On the other hand, having a finite size L_x does not lead to any quantization of the momentum along x since the Landau gauge in Eq. (2.38) breaks translational symmetry in the x direction. However, wave functions in Eq. (2.44) are exponentially localised around $x = -kl_B^2$ and therefore, since we assumed $0 \le x \le L_x$, we would expect the allowed values of k to range in the interval $-L_x/l_B^2 \le k \le 0$. Then the the number of degenerate states in a given LL can be evaluated as

$$N_\phi = \frac{L_y}{2\pi} \int_{-L_x/l_B^2}^{0} \mathrm{d}k = \frac{A}{2\pi l_B^2} = \frac{eBA}{2\pi\hbar} = \frac{BA}{\Phi_0}, \tag{2.45}$$

where $A = L_x L_y$ is the area of the sample and the magnetic flux quantum $\Phi_0 = 2\pi\hbar/e$. Note that Eq. (2.45) tells us that the LL degeneracy is given by the number of magnetic flux quanta passing through the sample. Although we evaluated the LL degeneracy for the particular case of a rectangular sample, it is important to stress that the same result can be obtained without additional difficulties by considering a disk-shaped sample and the symmetric gauge.

2.1.3 Landau levels and the integer quantum Hall effect

In the following we will say a few words about the integer quantum Hall effect (IQHE), with the aim of providing all the relevant information to understand the Secs. 2.2 and 2.3, treating the fractional quantum Hall effect and the so-called fractional Chern insulators, respectively. All interested readers can find a more detailed analysis of this topic in the notes by Girvin [1999], Goerbig [2009] and Tong [2016].

The IQHE was discovered in 1980 in the pioneering experiments performed by von Klitzing, using samples prepared by Dorda and Pepper [von Klitzing et al., 1980]. It consists in the quantization of the Hall resistance, which is no longer linear in B, as in the classical Hall effect, but shows plateaus at particular values of the magnetic field. At the plateaus the Hall resistance can be expressed in terms of universal constants. In particular, it reads

$$R_{\mathrm{H}} = \left(\frac{h}{e^2}\right)\frac{1}{\nu}, \tag{2.46}$$

where ν is dimensionless. Actually in the values of R_{H} measured by von Klitzing ν was an integer number and for this reason his observations took the name of *integer* quantum Hall effect. A second feature of the IQHE is that each plateau in the Hall resistance is accompanied by a vanishing longitudinal resistance, as shown in Fig. 2.2.

The key ingredient for the understanding of the IQHE is the previously introduced Landau quantization. The IQHE can indeed be explained by neglecting the Coulomb interactions between the electrons. As a consequence the quantum states responsible for the IQHE can be constructed starting from the single-particle states obtained in the previous sections and filling them by taking into account the Pauli exclusion principle.

We have seen that LLs are labelled by an integer and that, even though they are largely degenerate, each of them can house a finite number of electrons if our sample is finite. The fact that both the energy spectrum characterizing electrons in the presence of an orthogonal magnetic field and the Hall resistance[5] can be described in terms of an integer number may lead one to think that this is not a mere coincidence. As done for instance by Tong [2016], one can indeed prove that these two integers are related and, in particular, that the Hall resistance is given by $R_{\mathrm{H}} = h/e^2\nu$ when precisely ν LLs are filled. This implicitly means that an electron must have a vanishing probability of being spontaneously promoted in a higher LL. Such a probability is proportional to $\exp(-\hbar\omega_C/k_{\mathrm{B}}T)$, and it vanishes only if the energy scale set by the temperature $k_{\mathrm{B}}T$ is significantly smaller than $\hbar\omega_C$.

---

[5]Note that for classical systems of size L in D dimensions, the resistance R and the resistivity ρ are related by $R = \rho L^{2-D}$. Therefore in two dimensions ($D = 2$) the resistance does not depend on the size of the sample, and it coincides with the resistivity.
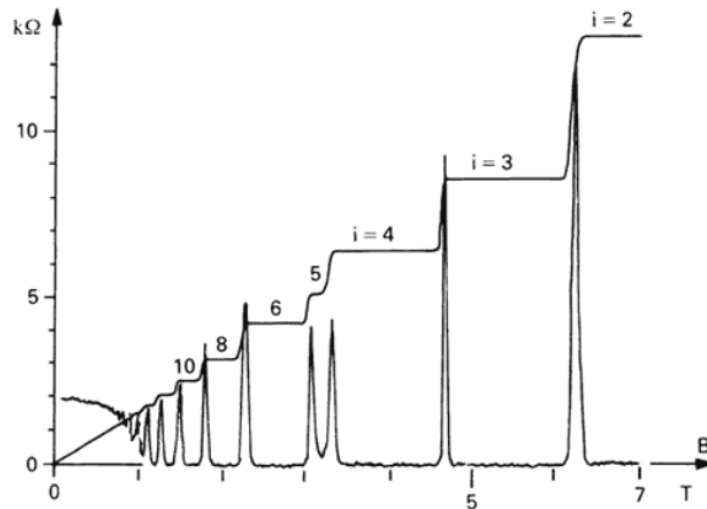
Figure 2.2: The Hall and longitudinal resistances as function of the magnetic field B. The Hall resistance varies stepwise, while the longitudinal resistance has zero value in correspondence of the plateaus. Taken from https://www.nobelprize.org/prizes/physics/1998/press-release/.

Before entering the discussion about the fractional quantum Hall effect there is an important question we would like to address: the quantum Hall phase is considered the first observed topological phase, but where does topology enter in its physics? The answer to this question was provided by Thouless et al. [1982], who took advantage of the Kubo [1957] formula to relate the Hall conductance of a 2DEG, experiencing a uniform magnetic field and a strong periodic potential, to the topological invariant (the first Chern number) associated with the filled bands, i.e.,

$$\boxed{\sigma_{\mathrm{H}} = -\frac{e^2}{\hbar} \sum_{n \in \mathrm{occ}} \mathcal{C}_n}. \tag{2.47}$$

Although we will not prove it here, each LL has Chern number $\mathcal{C}_n = -1$.

The previous expression, known as TKNN formula, allows us to understand both why in the IQHE the conductance is quantized in units of e^2/h and why this quantity is so robust against external perturbations, such as the presence of disorder in the sample. On the one hand, each time we fill a new band the sum in Eq. (2.47) increases by one. On the other hand, being a topological invariant, the Chern number of a given band (or better of a given LL) cannot change unless we close the gap.

To conclude, we would like to comment about the appearance of plateaus in the Hall resistance. Experiments have shown indeed that, for a fixed value of the electron density n, the Hall resistance is given by Eq. (2.46) not only when $B = n\Phi_0/\nu$, i.e., when the electron density is the correct one in order to fill exactly ν LLs, but also if we vary the magnetic field around that value [see Fig. 2.2]. Note that for $B \neq n\Phi_0/\nu$ the higher LL is only partially filled, and therefore if we apply an external electric field in one direction the electrons in such a LL should be able to move, generating a longitudinal current. This, in turn, should give rise to a finite longitudinal resistance and a change in the Hall one. However, this apparent inconsistency between theoretical description and experimental observations of the IQHE can be solved by taking into account the presence of impurities in the sample, as reviewed for instance by Goerbig [2009]. In particular, if the impurities are not too strong, the impurities can be described as a spatial-dependent potential landscape affecting the system Hamiltonian just in a perturbative way. Under this assumption, one can prove that the effect of such a perturbation on the energy spectrum is the broadening of the LLs due to the appearance of some localized states which can be populated (or depleted) without modifying the conduction properties of the system, explaining in this way the observed plateaus in the longitudinal and in the Hall resistance.
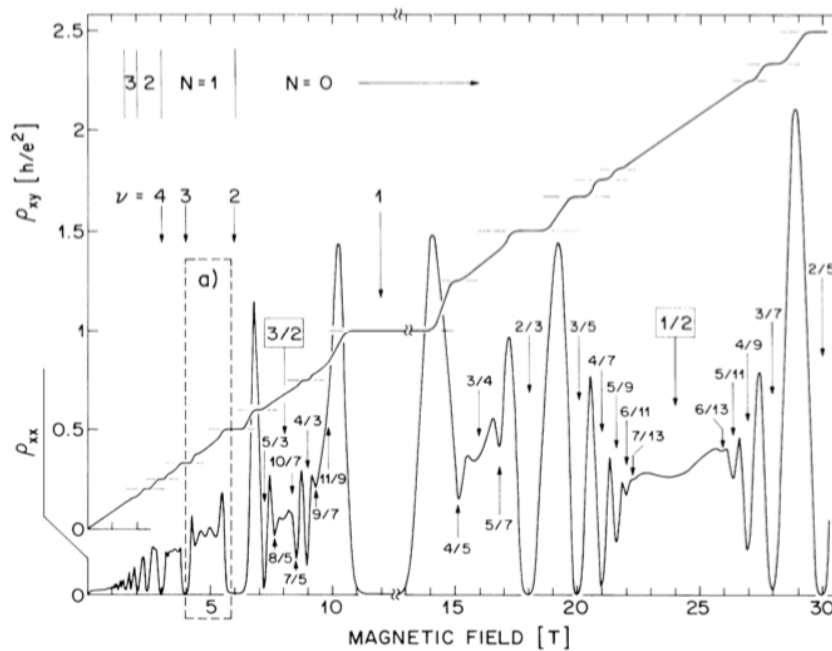
Figure 2.3: The behaviour of Hall and longitudinal resistivities as function of the magnetic field B for the FQHE. On the plateaus the Hall resistance takes the form in Eq. (2.46) but with non integer values of ν in this case. This picture has been taken from Willett et al. [1987].

2.2 The fractional quantum Hall effect

The fractional quantum Hall effect (FQHE) was discovered when, in the Magnetic Lab at MIT, Tsui et al. [1982] put a two-dimensional electron gas (2DEG) under a strong magnetic field at very low temperatures and observed quantized values of the Hall resistance R_H with non-integer values of the filling $\nu = N/N_\phi$ [see Eq. (2.46)]. After its first observation at $\nu = 1/3$ and $\nu = 2/3$, many other FQH states have been discovered both in the LLL, such as those with filling factors $\nu = 1/5, 2/5, 3/7, 4/9, 5/9, 3/5, \ldots$, and in higher LLs, for example those at $\nu = 4/3, 5/3, 7/5, 5/2, 12/5, 13/5, \ldots$. Nowadays there are around 80 quantum Hall plateaus that have been observed.

The FQHE owes its name to the fact that, for all these states, ν is a fractional number (and not an integer number as in the IQHE). From the phenomenological point of view, the two effects are very similar. Both of them are indeed characterized by the presence of plateaus in the Hall resistivity, which are accompanied by vanishing longitudinal resistivity [see Fig. 2.3]. However, whereas in the previous Chapter we could easily understand the IQHE starting from the Landau quantization, the understanding of the FQHE requires a whole new theory. The first step in this direction was done by Laughlin [1983], who showed that the FQHE with $\nu = 1/M$ (where M is an odd integer) is characterized by the presence of strong electronic correlations caused by the Coulomb interactions, which lead to the formation of a strongly correlated state. As we will see in Chapter 3, the state proposed by Laughlin [1983] is not exactly right in the case of electrons, but it captures all the relevant physics. For instance it shows that such a strongly correlated state of electrons is not a crystal as originally expected, but it is a whole new kind of state named quantum liquid.

One of the main properties of these FQH liquids is the incompressibility that, as we will see in Sec. 2.2.2, allowed to exclude the hypothesis that electrons in FQH states organize themselves into crystalline structures. This kind of systems are also characterized by the presence of extremely exotic excitations. On the one hand, they have bulk elementary excitations displaying fractional charge and anyonic statistics [see Chapter 1]. On the other hand, in the presence of external confinements, FQH liquids can also host chiral edge excitations, which from the phenomenological point of view are similar to those of the IQH states, but actually characterized by a much richer physics [see for instance Chapter 6 and the discussion in Sec. 7.3.3].

2.2.1   Fractional quantum Hall liquids and topological order

Before entering the discussion about the crucial role played by interactions in the FQHE, we believe it is worthwhile to spend a few words trying to explain why so many physicists, both theorists and experimentalists, are still involved in this field of research. The reason is that FQH states represent a whole new class of phases of matter, characterized by a new kind of internal order. This new order is known as topological order and it was introduced by Wen [1989] in the context of spin liquids. This kind of internal order is so different from those known before its discovery that it opened up a completely new territory for physical studies [Wen, 2017]. In this section we will follow Wen to give an intuitive description of the topological order characterizing FQH states.

As we know, one of the main properties of matter is the internal order of its constituents (atoms, ions, molecules, ...). In nature there are many different phases of matter, much more than just gas, liquid and solid which everyone knows. In the last century, indeed, scientists discovered many other states of matter such as ferromagnets, superfluids, plasmas and liquid crystals. However, all of them have been found to be distinguished by their internal structures or orders. Let us consider a crystal, for instance: The internal structure of such a state of matter is characterized by a very regular disposition of the atoms, which are therefore strongly correlated (i.e. the motion of an atom is not independent from the one of the others). The internal order plays a crucial role in this case. This fact is pointed out by the possibility of having different crystals starting from the same initial constituents and by changing only their disposition and/or the interactions between them. This scenario completely changes if we start heating the crystal and we continue to increase the temperature until it first melts and then takes the form of a gas. In this latter phase of matter atoms have no more an ordered disposition but they can move freely in all directions. Thus, since its constituents are uncorrelated object, a gas is a disordered state of matter.

Hence the constituents of matter can organize in many ways which lead to many different orders and many different states of matter. As a consequence of this large variety scientists felt the need to develop a general theory to describe all these internal orders and to gain a deeper understanding of the related phases of matter. A crucial step in this direction was realizing that all orders are associated with symmetries (or rather, the breaking of symmetries)[6]. This led to the so-called Landau theory of phase transitions, as discussed for instance in Huang [2019].

Landau's theory is a mean-field theory, in the sense that the system under study is assumed to be adequately described with only macroscopic quantities, which assumes the existence of a continuous transition and is valid only in the vicinity of the critical point (i.e. close to the phase transition). It allows one to understand the behaviour of second-order phase transitions and it is based on the following ideas:

- when a system undergoes a second-order phase transition from a disordered to an ordered phase, one has the breaking (or reduction) of the initial symmetry and therefore one needs to introduce an extra parameter to describe the state of the system. This extra parameter is called order parameter.

- the free energy, whose minima correspond to the equilibrium states of the system, is an analytic function and close to the phase transition it can be expended in powers of the order parameter, which becomes the only relevant thermodynamic quantity in the critical region.

- the free energy obeys the same symmetry of the Hamiltonian and this fixes some constraints on its general form in term of powers of the order parameter.

This theory has been so successful that nowadays it is a cornerstone of condensed-matter physics. It has allowed to understand so many different phenomena that, for a long time, physicists believed that Landau's theory was able to describe all possible orders of matter and all possible second-order phase transitions. However, it was not so.

As we have just said, in 1982 Tsui, Störmer and Gossard discovered the first FQH states and after that many others were found at certain magical filling factors. The existence of different FQH states can easily lead to the hypothesis that each of them could be associated with a specific internal order (or "pattern") which fixes in some way the value of the filling factor to the correct one. We

---

[6]For instance, whereas a gas does not change if we displace it by an arbitrary distance, a crystal remains the same only for specific translations (translations given by an integer number of lattice constants). Therefore the phase transition gas → crystal reduces the continuous translational symmetry of the gas to the discrete translational symmetry of the crystal
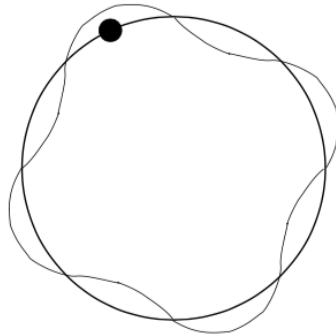
Figure 2.4: A particle, its circular orbit and its quantum wave. Picture taken from Wen.

can also think that breaking these internal "patterns" will cost a finite amount of energy and try to explain in this way to the above-mentioned incompressibility of the FQH states. However, FQH states are liquids and therefore, having in mind the previous comparison between the internal order of a crystal and the one of a gas, a reasonable question arises[7]: How can liquids have any internal order?

The internal orders characterizing FQH liquids are indeed different from any other order of matter previously found in nature. Surprisingly they can not be associated to any symmetries (or the breaking of symmetries) and therefore they can not be described by Landau's theory of phase transitions. Moreover the constituents of a liquid are free to move and so the internal order of a FQH state can not be related to their positions. However, they are not just uncorrelated objects which move randomly in the material, as it happens in classical liquids. On the contrary they have a highly correlated motion and the origin of the internal order in FQH liquids is exactly this. So the main difference between the internal order present in FQH liquids and those previously observed is that while the latter are associated with the static positions of the constituents, the topological order is a sort of "dynamical" order.

Let us try to figure out the correlated motion of electrons in a FQH state. As we know, an electron in presence of an orthogonal magnetic field carries out a circular motion, known as cyclotron motion. Furthermore, due to the wave-particle duality, we can imagine that the orbits characterizing the cyclotron motion are quantized (as they actually are). To be precise these circular orbits must contain an integer number of the electron wavelength[8] [see Figure 2.4]. To understand the collective motion of the electrons, it is convenient to interpret the electron wavelength as a step length. In this picture each electron takes an integer number of steps to carry out its circular motion and the number of steps depends on which Landau level the electron occupies. In particular, if an electron takes n steps to complete its orbit we will say that the electron is in the $(n-1)$-th LL. For the sake of simplicity, we can now consider electrons in the LLL, so that they take a single step to perform their cyclotron motion.

At this point we are ready to see what happens in the presence of many electrons. In fact in FQH states the electrons not only do their own cyclotron motion in the LLL they also move around each other. Also these additional motions are quantized, however the Fermi statistic of electrons imposes a non-trivial constrain: an electron always takes an odd integer number of steps to go around another one. This constraint can be understood in the following way: since electrons are fermions, the exchange of two of them must induce a minus sign to the total wave function. At the same time, exchanging two electrons can be seen as moving one electron half way around the other electron. Therefore, if a complete circle of one electron around the other one takes an odd integer number of steps, the exchange of two electrons will take a half integer number of steps. As a consequence, the quantum wave associated with the electron which is moving around the other one will take a half integer number of wavelengths, at which correspond a minus sign. In this way also the total wave function will pick up a global minus sign, as request by the statistics.

---

[7]Strictly speaking FQH states represent an entirely new phase of matter (as we stated at the beginning), but if we look for a classical analogy, a liquid is the best.

[8]The idea is similar to the de Broglie interpretation of the atomic orbitals quantization in the Bohr model: the atomic orbitals are quantized due to the fact that the quantum wave of the electron must fit along the circumference of the electron orbit.

Finally we have to consider the Pauli exclusion principle and the Coulomb repulsion between the electrons, which force the electrons to stay away from each other as much as possible. These two effects result in the tendency of each electron to take more steps to go around one of the others.

Therefore the collective motion of the electrons in a FQH liquid is highly correlated as a consequence of the following constraints:

- all electrons do their own cyclotron motion in the LLL;

- an electron takes an odd integer number of steps to go around another electron (due to Fermi statistics);

- electrons try to stay away from each other as much as possible (due to Coulomb interaction and the Pauli exclusion principle).

At this point it is important to understand which are the consequences of the quantum nature of electrons. Indeed if one supposes of dealing with classical particles (which will be completely reasonable at high temperatures), only the last constraint would be valid. In this case electrons would repel each other only due to the Coulomb repulsion and they would form a correlated classical liquid. However, FQH states are found at very low temperatures where the quantum nature of the electrons is of crucial importance. Thus in these systems, known also as quantum liquids, the electrons must respect all the above motion constraints. This fact leads to a unique global motion of the electrons, named "dancing pattern" by Wen [2019], which corresponds to the topological order in a FQH state. So, within this intuitive picture of moving electrons, different FQH states are associated with different "dancing patterns". For instance, if we consider the simplest FQH state, i.e. the Laughlin state at filling $\nu = 1/M$, we can imagine that each electron takes M steps to move around another one.

This simplified description of the topological order allows us also to understand the origin of the FQH state incompressibility[9]. An infinitesimal compression of a FQH liquid forces some electrons to reduce the number of steps needed to go around the others. However, this can not be done in a continuous way: Due to the quantum mechanical nature of electrons, the number of steps must be an odd integer. Therefore the allowed distances between the electrons are quantized and this explains why a compression of systems of this kind, even if it is infinitesimal, costs a finite amount of energy. Therefore, we can conclude that the incompressibility characterizing FQH liquids is a quantum effect caused by the presence of the topological order.

Now that the concept of topological order is more clear, one may ask himself how is it possible to measure and characterize the different topological orders. The answer to this question is far from trivial. Indeed physicist had to find completely new ways both to gain information about these internal orders and to mathematically characterize them[10]. A complete answer goes beyond the goals of this work, however we can say that in order to characterize a topological order one studies different properties of the system. Some of them are the degeneracy of the ground state, which depends on the topology of the space [Wen and Niu, 1990], the fractional charge and statistics of the quasiparticle excitations and the structure of the edge excitations [Wen, 1995].

2.2.2   The crucial role played by interactions

As we have discussed, the Coulomb interaction between electrons plays a crucial role in determining the internal order of FQH states. This fact can be seen, for example, from the above characterization of the topological order in terms of "dancing patterns", in which the electrons try to stay away from each other in order to minimize Coulomb repulsion.

To point out the importance of the electron-electron interaction in the FQHE, we can compare the different situations of completely and partially filled LLs: On the one hand, the IQHE can be understood within a single-particle picture which makes use of the Landau quantization, as discussed for instance by Goerbig [2009] and by Tong [2016]. In particular, the Hall resistivity is quantized exactly when ν LLs are completely filled. In this case there is a single non-degenerate (Fermi-liquid-like) ground state and any additional electron is forced, due to Pauli principle, to

---

[9]Note that the description of the topological order in terms of electron "dancing patterns" actually applies only to Abelian FQH states. The topological order associated with non-Abelian FQH states can not be described in this intuitive way.

[10]A classification of topological orders has been proposed in terms of an integer symmetric matrix, usually denoted with K, and an integer charge vector Q. See for instance [Blok and Wen, 1990a,b, Read, 1990, Fröhlich and Zee, 1991, Ezawa and Iwazaki, 1991, Wen and Zee, 1992].

populate the higher LL. As a consequence adding an electron to the system costs a finite amount of energy, equal to LL spacing $\hbar\omega_C$, and therefore the state corresponding to ν completely filled LLs is said to be incompressible, since one can not vary the filling factor (by keeping the number of particles fixed) and pay only an infinitesimal amount of energy. Moreover, in these circumstances the physics of the system is governed by the kinetic energy while interactions can be treated within a perturbative approach. On the other hand, in the case of partially filled LLs the situation is completely different. Suppose that we have $\nu < 1$ so that the partially filled LL is the lowest one. As we have calculated in Sec. 2.1.2, each LL can host a finite but macroscopic number of electrons given by $N_\phi = BA/\Phi_0$ [see Eq. (2.45)]. The number of ways to fill νN_ϕ of these states is given by $\binom{N_\phi}{\nu N_\phi}$, which is an extremely large number. Therefore, if we neglect both the presence of impurities and the interactions between the electrons, the ground state of any partially filled LL would be wildly degenerate[11].

All these different configurations are characterized by the same kinetic energy, given by $\nu N_\phi \hbar\omega_C/2$, which effectively drops out of the problem, since we can neglect the so-called inter-LL excitations, as belonging to high-energies degrees of freedom. There are indeed many unoccupied states in the partially filled LL and so an electronic excitation does not require the occupation of a state in the higher LL. The fact that if we consider only the low-energy degrees of freedom the kinetic energy term plays the role of a constant energy shift leads us to argue that the driving mechanism of the FQHE is one between the presence of impurities in the sample or else the Coulomb repulsion. However, the FQHE only occurs in high-quality samples and meaning that one typically works with the following hierarchy of energy scales:

$$\hbar\omega_C \gtrsim V_{\text{Coulomb}} \gg V_{imp} \tag{2.48}$$

Therefore we can not attribute the FQHE to the presence of impurities and we need to consider seriously Coulomb interactions as its origin. We expect the electron-electron interactions to lift the degeneracy of the Landau level, resulting in a spectrum of states of width given by the Coulomb energy. Actually the experimental observations would be nicely explained if such a spectrum had gaps at the filling factors ν corresponding to the observed Hall plateaus[12]. In this case indeed one could use the same arguments related to the presence of impurities that we mentioned in Sec. 2.1.3, to explain both the observed plateaus in the Hall resistivity ρ_{H} and the vanishing of the longitudinal resistivity ρ_{L}.

Before the observation of the FQHE, people thought that electrons in a partially filled LL behave as classical charged particles which organize themselves into a crystalline structure to minimize their mutual Coulomb repulsion. Such a solid phase is known as Wigner [1934] crystal (WC) and consists of a two-dimensional triangular electron lattice. Even if the WC was found to be the ground state at very low filling factors ($\nu \lesssim 1/7$), it can not explain the FQHE. Let's see why.

As we have said, one of the main features of FQH states is their incompressibility. On the other hand crystals are states which spontaneously break a continuous spatial symmetry (the translational symmetry) and as a consequence their spectra present the gapless long-wavelength excitations known as Goldstone modes. The crystalline Goldstone modes are acoustic phonons and they have linear dispersion relations (their energy linearly tends to zero as the wave vector, or the momentum, does). Thus one can compress such a system infinitesimally and pay only an infinitesimal amount of energy. Crystals are therefore compressible phases of matter and this fact is at odds with incompressibility characterizing FQH states. Note that this also explains why, even if FQH states represent a whole new phase of matter, from a simplistic point of view they should be thought of as a liquid phase of electrons rather than a solid phase.

2.3 Fractional Chern insulators

After the observation of the IQHE, condensed-matter physicists started to inspect under which conditions such a phenomenon manifests itself. In particular, they tried to answer the following questions: First, in electronic samples displaying the QHE the periodic structure of the material

---

[11]Note that this situation is the exact contrary to what one has for a completely filled LL, where there exists only a single non-degenerate ground state.

[12]In this Thesis we will not explore the case of Coulomb interactions in a deeper way, however the presence of gaps in the energy spectra for the correct values of ν has been shown in many works. See for instance the paper by Haldane and Rezayi [1985].

---

has a very modest effect on the properties of the electrons forming the 2DEG[13]. Does the QHE survive also when the lattice potential describing the solid structure affects the electron motion more seriously and one needs to take the split of each LL in energy bands into account? Second, we have seen that the presence of a uniform magnetic field leads to the formation of peculiar single-particle states (the LLs) which can be used to explain the appearance of IQHE, but is a magnetic field really necessary to observe such a phenomenon?

The first question was answered in the seminal paper by Thouless et al. [1982], where the authors studied the QHE in the presence of a strong periodic potential which was known to lead to the complicated energy spectrum named Hofstadter butterfly [Hofstadter, 1976]. As mentioned at the end of Sec. 2.1.3, Thouless, Kohmoto, Nightingale, and den Nijs showed that, even when electrons experience a significant lattice potential, the IQHE manifest itself whenever the chemical potential lies in a band gap; and that in this case the Hall conductance can be related to the Chern number of the filled bands through the TKNN formula in Eq. (2.47).

The answer to the second question arrived few years later when Haldane [1988] proved that a quantized Hall conductance can arise from a completely filled band also in the absence of a net external magnetic field. In particular, he proposed a tight-binding model on the honeycomb lattice in which electrons hop with real-valued nearest-neighbor (NN) amplitudes, as well as with complex-values next-nearest-neighbor (NNN) amplitudes which break time-reversal symmetry. Even though the complex NNN hoppings describe an inhomogeneous magnetic field, it turns out to have zero average proving in this way that a net magnetic field is not necessary to observe the QHE. What one needs is instead the complete filling of a given number of bands with a non-zero Chern number, which can be obtained when the system Hamiltonian contains a term that breaks time-reversal symmetry. These band insulators exhibiting non-vanishing Hall conductance are generally known as Chern insulators.

Thus, few years after the discovery of the IQHE, physicists figured out that the appearance of this phenomenon was only due to the filling of an integer number of Chern bands with independent electrons. They then started to wonder if such a reasoning could be extended to the FQHE. As we have seen, the FQHE occurs when we partially fill a LL. In the absence of defects, LLs are perfectly flat and therefore (when partially filled) they can house an exponentially large number of Slater determinants, among which the incompressible quantum liquid states describing the FQHE are selected by interactions for particular values of the filling factor. Note that with respect to the integer case, now there is an additional but crucial ingredient, besides the partial filling of the band. To realize lattice versions of the FQHE one needs indeed topologically non-trivial bands which at the same time are also flat (or nearly-flat, at least).

The first theoretical investigations in this direction have been done (simultaneously) by Tang et al. [2011], Sun et al. [2011] and Neupert et al. [2011]. In particular, Neupert et al. [2011] showed that in principle to have bands which are perfectly flat, one should consider electrons hopping over arbitrarily large distances. However, at the same time they proved that the hopping amplitudes exponentially decay as a function of the hopping distance, so that one can construct reasonably flat (topologically non-trivial) bands by considering only a small set of hopping terms. The relevant parameter to quantify the flatness of the band (named flatness parameter) is the ratio between the bandwidth and the band gap, which sets a sort of upper bound to the strength of the interactions one can consider[14]. The smaller the flatness parameter, the stronger the effect of interactions. By considering the Haldane model and the so-called chiral-π-flux square lattice model, Neupert et al. [2011] showed that the flatness parameters can be as small as $1/7$. In a similar way Tang et al. [2011] and Sun et al. [2011] inspected the flatness parameters for other models (based on the kagome and checker-board lattices) displaying topological non-trivial bands, by observing even smaller values of it. To conclude their work Neupert et al. [2011], included repulsive NN interactions[15] and studied the ground state properties of the system at fractional filling $\nu = 1/3$. They observed a fractional hall conductance, close to $1/3$, and a three-fold ground-state degeneracy in the presence of periodic boundary conditions; both signatures of the $\nu = 1/3$ FQH state. Similar results have been found few months later by Sheng et al. [2011] for filling fractions $\nu = 1/3$ and $\nu = 1/5$.

Although the observations of Neupert et al. [2011] and Sheng et al. [2011] were compatible with the existence of a fractional many-body state for partial filling of topological bands, they did not

---

[13]The fact that electrons are embedded in a solid-state device can be described by simply modifying their effective mass which therefore can deviate from the one they have in free space.

[14]Note that since in principle the band mixing could destroy the band flatness, interactions can be safely introduced only if their strength does not overcome the band gap.

[15]Note that for spinless fermions one can not have interactions with shorter range.

rule out charge-density-wave states as possible ground states of the system. This possibility was excluded by Regnault and Bernevig [2011] in a later work, where the authors investigated also some properties of the system in the presence of elementary excitations (the previously mentioned quasiholes). In particular, their findings for the entanglement spectrum, for the spectral flow upon flux insertion and for the counting of quasiholes states clearly proved that they were observing the lattice analog of a FQH state, named fractional Chern insulator (FCI) [Parameswaran et al., 2013].

Before moving on, we would like to stress that Sørensen et al. [2005], Palmer and Jaksch [2006] and Hafezi et al. [2007] studied the FQH physics on lattices before Tang et al. [2011], Sun et al. [2011] and Neupert et al. [2011]. However, they considered the bosonic version of the Harper-Hofstadter model in the presence of on-site Hubbard [1963] interaction [see Sec. 8.1], i.e. systems in which particles experience a non-vanishing effective magnetic field.

After these pioneering works, many other groups started to investigate lattice counterparts of the FQHE, by considering models related to the Harper-Hofstadter one, as done for instance by Bhat et al. [2007], Cho et al. [2008] and Kapit and Mueller [2010], but also models in which topologically non-trivial bands appear in the absence of a net external magnetic field, as in Wu et al. [2012] and in Grushin et al. [2014]. In particular, several theoretical studies inspected the adiabatic preparation of different FCI states and the associated phase diagrams [Kapit et al., 2014, Grusdt et al., 2014, Barkeshli et al., 2015, He et al., 2017, Motruk and Pollmann, 2017, Hudomal et al., 2019]. Some works focused on the numerical characterization of these states by inspecting key quantities such as the many-body Chern number, the particle entanglement spectrum, the behavior of the correlation functions and the topological entanglement entropy [Sterdyniak et al., 2012, Gerster et al., 2017, Rosson et al., 2019], while others proposed experimentally applicable schemes to identify these elusive strongly correlated phases of matter [Dong et al., 2018, Repellin and Goldman, 2019]. Finally, growing attention has been given to FCI elementary excitations [Liu et al., 2015, Nielsen et al., 2018, Račiūnas et al., 2018, Umucalılar, 2018, Jaworowski et al., 2019, Manna et al., 2019, Macaluso et al., 2019b], which (similarly to those characterizing the FQHE) display fractional charge and anyonic statistics.

An in depth study of the properties of the QH excitations on top of a $\nu = 1/2$ bosonic FCI is reported in Chapter 8, where we also discuss how these features (i.e., the fractional charge and the anyonic statistics of QHs) can be easily probed through local density-profile measurements.

2.4 Fractional quantum Hall states of atoms and photons

In the previous sections, we often mentioned bosonic versions of FQH and FCI states (or papers studying them). Here we want to show in which conditions and in which kind of systems these exotic phases of matter can appear. They indeed can not be observed in electronic gases in solid-state devices as their fermionic counterparts. Their realization is instead intimately related to the progresses made in the last years in the field of the so-called quantum simulators [Georgescu et al., 2014].

2.4.1 Quantum simulators and artificial gauge fields

The idea of quantum simulators goes back to Feynman [1982] who proposed to solve quantum problems by means of properly designed quantum systems, instead of using intrinsically inefficient classical computers. Thus, roughly speaking, a quantum simulator is a quantum system which mimics a particular quantum model (or Hamiltonian). However it is important to highlight that such an artificial system can have huge advantages compared to the "original" one. It can for instance allow us to study a wider range of Hamiltonian parameters [see e.g. in Sec. 8.1], or provide access to physical observables which could not be inspected otherwise.

Nowadays there are many different platforms which can serve as quantum simulators, e.g. ultracold atomic gases [Bloch et al., 2012], ensembles of trapped ions [Blatt and Roos, 2012], photonic systems [Aspuru-Guzik and Walther, 2012], superconducting circuits [Houck et al., 2012], etc.. At this point you may ask yourself what is the utility of having different platforms to study the same physics. The answer is simple: each system has its own advantages and limitations, and having many of them allows us to tackle different aspects of the same physical problem.

Although the original aim of quantum simulators was to reproduce the physics of already known systems, we would like to stress that sometimes the use of them led to completely new observations. One of the most remarkable examples in this direction is represented by the possibility of using

internal degrees of freedom of the system as synthetic dimensions to engineer effectively higher-dimensional systems, which do not have any other counterpart in nature [Boada et al., 2012, Celi et al., 2014, Ozawa and Price, 2019].

If in general the simulation of a quantum system seems to be a difficult task in and of itself, reproducing the physics of the QHE is even more demanding (especially in its fractional version). As we have learned in this Chapter, at the root of the QHE phenomenology there is a very peculiar structure of the energy spectrum, which organizes itself in topologically non-trivial bands known as LLs. The appearance of such energy bands is however intimately related to the action of an orthogonal magnetic field on electrons, which are known to be charged particles. Thus, a reasonable question arises at this point: How is it possible to reproduce the physics of charged particles affected by an external magnetic field with systems made of neutral objects, such as ultracold atoms and photons? It looks, at first, an unreachable goal. Orbital magnetism is absent for neutral particles indeed, and therefore the simulation of quantum-mechanical magnetic effects seems to be demanding too much. Physicists however circumvented this apparent impossibility through the introduction of the so-called artificial (or synthetic) gauge fields [Dalibard et al., 2011, Goldman et al., 2014, Ozawa et al., 2019].

At present, there are tens of experimental realizations of artificial gauge fields in both ultracold atomic and photonic systems, and the number of theoretical proposal in this direction is even larger [Cooper et al., 2019, Ozawa et al., 2019, Ozawa and Price, 2019]. As a consequence, and given the subject of this Thesis, in the following we will focus our attention mainly on the most promising set-ups for the actual realization of FQH states with quantum simulators.

Ultracold atoms in rapidly rotating traps and optical lattices

These systems consist of dilute gases of neutral atoms which are cooled down to extremely low temperatures by means of sophisticated cooling and trapping techniques. At these temperatures, typically lower than 10^{-6} K, the thermal (or de Broglie) wavelength $\lambda_T = \sqrt{2\pi\hbar/mk_BT}$ of the atoms becomes larger than the mean interatomic distance and quantum effects start to play a crucial role. Although ultracold atoms were initially developed in order to observe quantum fluid phenomena such as Bose-Einstein condensation and superfluidity [Pitaevskii and Stringari, 2016], nowadays they represent one of the most appealing platforms for general quantum simulation.

The reasons why ultracold atomic systems have a central role among quantum simulators are various and generally related to the high level of flexibility and control one typically has on the experimental parameters characterizing these set-ups [Bloch et al., 2008].

First of all, one can use suitable designed laser beams to let the atoms feel different trapping potentials: harmonic potentials, hard-wall (or box) potentials but also periodic optical lattice potentials[16] [Jaksch and Zoller, 2005, Lewenstein et al., 2007]. In particular, the high tunability of the potential parameters can be used to confine the atoms in different shapes and/or in different dimensions, but also to implement a very large variety of lattice models [Morsch and Oberthaler, 2006, Cooper et al., 2019].

A second remarkable property of these systems is the possibility of enhancing interactions between their constituents. In most ultracold atomic set-ups, atoms interact via effective short-range contact interactions[17] and one can tune their strength through the so-called Feshbach resonances [Chin et al., 2010].

The properties of the atomic cloud, such as the momentum distribution of the atoms and their quantum coherence are typically inspected through the time-of-flight technique [Bloch et al., 2008]. This simply consists of switching off all trapping potentials and then imaging the freely expanding gas. Recently, the advent of the so-called quantum gas microscopes, giving access to density distributions of atoms in optical lattices with single-site and single-atom resolution [Bakr et al., 2009, Sherson et al., 2010, McDonald et al., 2019, Subhankar et al., 2019], has made possible the study of these systems also in situ with unprecedented resolution.

As we mentioned above, neutral particles can be used to reproduce the physics of charged particles experiencing an external magnetic field through the implementation of artificial gauge fields. As reviewed by Dalibard et al. [2011] and by Goldman et al. [2014], in ultracold atomic

---

[16]These lattice potentials are generated by making use of laser interference patterns. Indeed, the alternating bright and dark regions are experienced by the atoms as a periodic lattice potential through the so-called optical dipole force [Bloch et al., 2008].

[17]Note that some atomic species can have more "exotic" interaction such as anisotropic dipole-dipole interactions, as reviewed by Lahaye et al. [2009].

set-ups this can be achieved in different ways both for harmonically trapped clouds and for atoms in the presence optical lattices.

An early proposal in this direction has been to rapidly rotate trapped atoms and to take advantage of the analogy between the Coriolis force acting on them in the rotating frame and the Lorentz force affecting charged particles in a magnetic field [Cooper, 2008]:

$$\mathbf{F}_{\text{Coriolis}} = -2m\mathbf{\Omega} \times \mathbf{v} \qquad \mathbf{F}_{\text{Lorentz}} = q\mathbf{v} \times \mathbf{B}, \tag{2.49}$$

where $\mathbf{\Omega} = (0, 0, \Omega)$ is the rotation vector (so that Ω is the rotation frequency). Note that $\mathbf{F}_{\text{Coriolis}}$ and $\mathbf{F}_{\text{Lorentz}}$ coincide if we assume $2m\mathbf{\Omega} = q\mathbf{B}$. In Hamiltonian terms moving to the rotating frame generally implies

$$\hat{H} \to \hat{H}_{\Omega} = \hat{H} - \mathbf{\Omega} \cdot \hat{\mathbf{L}}, \tag{2.50}$$

which for the particular case of a single atom harmonically trapped in 2D reads

$$\hat{H}_{\Omega} = \frac{(\mathbf{p} - m\mathbf{\Omega} \times \mathbf{r})^2}{2m} + \frac{1}{2}m\omega^2\mathbf{r}^2 - \frac{1}{2}m\Omega^2\mathbf{r}^2. \tag{2.51}$$

By looking at the kinetic term in the previous expression one can easily identify the artificial gauge field $q\mathbf{A} = m\mathbf{\Omega} \times \mathbf{r}$. In addition to that, it is important to highlight the presence of the centrifugal term which impose a constraint on the maximum rotation frequency (and in turn on the maximum magnetic field that can be achieved), known as centrifugal limit: $\Omega \leq \omega$. Note that if the rotation frequency Ω exceeds the trapping one (ω), the gas is no longer confined and the atoms fly away.

Later on, physicists exploited the idea of associating a Berry phase with the atomic motion by dressing the atoms with suitably designed optical and magnetic fields [Dum and Olshanii, 1996, Juzeliūnas and Öhberg, 2004, Juzeliūnas et al., 2006, Dalibard et al., 2011]. Although this second approach does not suffer from the previous constraint imposed by the centrifugal limit, it typically has to face spurious thermal effects related to the heating of the atomic cloud by spontaneous emission. Nevertheless, this idea has led first to the nucleation of quantized vortices [Lin et al., 2009] and then to the experimental implementation of the so-called spin-Hall effect [Beeler et al., 2013].

This idea of taking advantage of the atomic internal degrees of freedom to implement artificial gauge fields has been extensively used also for atoms in optical lattices. One of the first theoretical proposals in this direction was made by Jaksch and Zoller [2003]. Their idea was to use a 2D optical lattice trapping two distinct internal states of the atoms in alternating columns so that the hopping in the horizontal direction was only possible with the help of laser beams, which coherently transfer the atoms from one internal state to the other. In this so-called laser-assisted tunnelling scheme, the hopping amplitudes in the lattice Hamiltonian can be controlled by adjusting the laser parameters. This made possible the realization of complex hoppings, corresponding to an artificial magnetic flux piercing the lattice, leading for instance to the experimental implementation of the Harper-Hofstadter model by Aidelsburger et al. [2013] and by Miyake et al. [2013].

This laser-assisted tunneling is not the only way to engineer complex hoppings for ultracold atoms in optical lattice. One can use indeed a complementary protocol, known as Floquet engineering [Bukov et al., 2015], which is based on the temporal modulation of some system parameters. While the fact that ultracold atoms in a shaken optical lattice can be effectively described by a new Hamiltonian with renormalized hopping amplitudes was known since Eckardt et al. [2005, 2009], it took some time to figure out that in order to obtain complex hoppings the lattice must be shaken in a way which breaks time-reversal symmetry, as done for instance in Struck et al. [2012]. This technique has been then employed in the first realization of the Haldane model by Jotzu et al. [2014].

The above discussion proves that in general ultracold atoms represent a very promising set-up to reproduce the FQH Hamiltonian both in continuum and in lattice geometries. The first experimental attempt in this direction was made by Gemelke et al. [2010], who studied small atomic clusters ($1 \leq N \leq 10$) in rapidly rotating micro-traps [see Fig. 2.5 a)]. In this experiment the rotation frequency was very close to the centrifugal limit, and the atoms probably reached the FQH regime. However, the very small sizes of the atomic samples prevented the authors from probing the system with high-enough accuracy to convince the scientific community of the first realization of an atomic Laughlin state. Concerning atoms in optical lattices instead, only recently Tai et al. [2017] started to inspect the interplay of artificial gauge fields and strong interaction. To be precise, they considered the interacting particles in the Harper-Hofstadter model [see Fig. 2.5 b)], and they observed the chiral motion of the two atoms on a two-leg ladder.
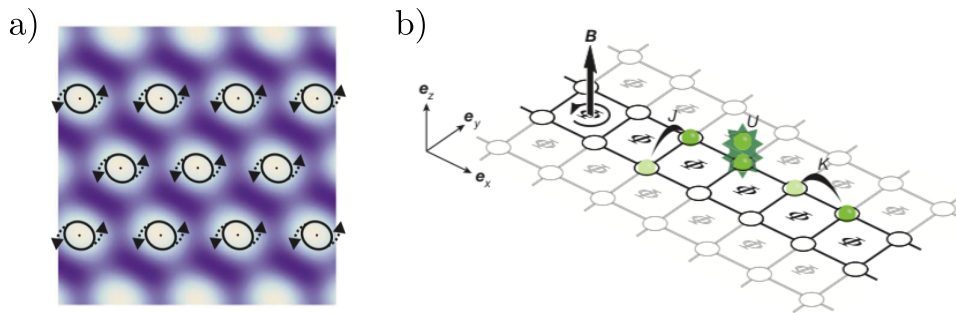
Figure 2.5: a) Rotating minina of an optical lattice potential, leading to rotating microtraps which can be used to let small atomic clusters experience an artificial magnetic field. Picture taken from Gemelke et al. [2010]. b) Two leg ladder pierced by an artificial magnetic flux Φ, which can be obtained by engineering complex hopping between neighboring lattice sites. This picture has been taken from Tai et al. [2017].

Optical systems

Also optical set-ups represent excellent platforms for quantum simulation [Carusotto and Ciuti, 2013, Ozawa et al., 2019]. These systems are in general realized through the manipulation of photons (neutrally-charged non-interacting particles with zero mass), which can occur in many different scenarios, as for instance in free space, waveguides, dielectric material or cavities.

Despite being massless particles in free space, photons can acquire an effective mass when spatially confined inside a cavity. Moreover, the choice of a cavity medium with a sizeable nonlinear optical susceptibility $\chi^{(3)}$ provides the possibility to introduce non-negligible photon-photon interactions. An extensively exploited method to enhance the interactions between photon pairs is the hybridization of photons with long-lived electronic excitations in the cavity medium. Such a hybridization gives rise to photonic quasi-particles called polaritons, which inherit interactions from their medium excitation content, as reviewed by Carusotto and Ciuti [2013]. This strong light-matter coupling regime can be achieved by embedding in the cavity different materials, as semiconductor quantum wells or, as done for instance by Jia et al. [2018], quantum gases of alkali atoms.

Another peculiar property of cavity photons it their intrinsically driven-dissipative evolution. Due to a non-perfect reflectivity of the cavity mirrors, photon-losses are unavoidable in these systems and therefore a non-trivial steady-state configuration can be reached only through a suitable external pumping. Although the presence of dissipation represents an undeniable additional difficulty for the simulation of strongly correlated phases of matter, as reviewed in Lebreuilly and Carusotto [2018] and in Ozawa et al. [2019], it can be also used as a resource: The spectroscopic analysis of the emission spectrum gives indeed a real-time imaging of the photonic wave-function.

Concerning the realization of artificial gauge fields for photons, the first theoretical proposal was made by Haldane and Raghu [2008] and by Raghu and Haldane [2008]. Their idea was to use time-reversal-symmetry-breaking media to build photonic crystals displaying the same chiral edge modes observed for the IQHE. This was experimentally realized by Wang et al. [2009] after few months, giving birth to the constantly expanding field of topological photonics [Ozawa et al., 2019]. After that, many other methods have been proposed to simulate magnetism in photonic set-ups indeed.

Among those suggested for lattice systems, we would like to mention the implementation of Rechtsman et al. [2013], where coupled helical waveguides in the so-called paraxial approximation[18] have been used to reproduce the effect of a temporal modulation of the lattice [see Fig. 2.6 a)], leading to an effective complex hopping between neighboring sites; and the ring-resonator array configuration realized by Hafezi et al. [2013], in which the links (white resonators in Fig. 2.6 b)) between the lattice sites (grey resonators in Fig. 2.6 b)) were built to give a different hopping phase depending on the (clockwise or anti-clockwise) circulation of the light in the rings [see Fig. 2.6 b)].

If we consider artificial gauge fields for photons in continuum geometries, the general idea to try

---

[18]In the paraxial approximation one of the spatial coordinates (typically the one along which photons travel in the waveguide) can be treated as an effetive time. This allowed Rechtsman et al. [2013] to study the time evolution of a 2D lattice system by looking at the spatial evolution of a 3D one.
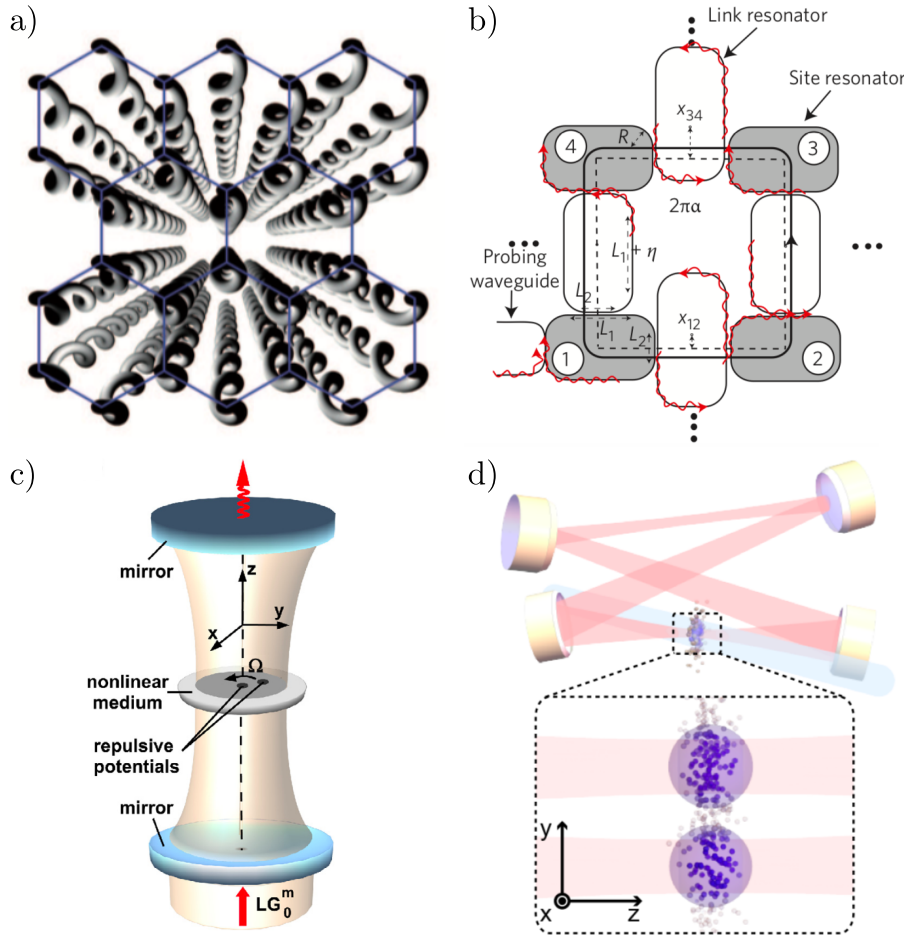
Figure 2.6: a) Pictorial representation of coupled helical waveguides forming a honeycomb lattice in the plane orthogonal to the direction along which the waveguides extend, and breaking "time"-reversal symmetry in that direction. This picture has been taken from Rechtsman et al. [2013]. b) Sketch of the ring resonators used by Hafezi et al. [2013] in the experimental realization of the photonic spin-Hall effect. Picture taken from Hafezi et al. [2013]. c) Possible experimental set-up for an in-cavity simulation of the FQH effect: while the injection of rotating photons by means of a Laguerre-Gauss beam provides the artificial gauge field, the nonlinear medium introduces effective interactions between photon pairs. Picture taken from Umucalılar and Carusotto [2013]. d) Sketch of the twisted cavity initially proposed by Schine et al. [2016] for the realization of photonic Landau levels. While the red beams represent the cavity photons experiencing the artificial gauge field, the blue one denotes the control laser which couples the cavity photons to the Rydberg excitations (purple spheres) of the atomic cloud loaded inside the cavity. The presence of the control laser turns the (otherwise non-interacting) cavity photons into strongly interacting Rydberg polaritons. Picture taken from Clark et al. [2019].

to exploit the previously-discussed relation between rotation and magnetic fields. This was done for the first time by Umucalılar and Carusotto [2013], who proposed to use a Laguerre-Gauss laser beam to inject rotating photons into a cavity with spherical mirrors [see Fig. 2.6 c)]. Note that such a shape of the mirrors provides a harmonic trapping in the plane orthogonal to the cavity axis, so that the photon gas turns out to be exactly in the same conditions of a rotating ultracold atomic cloud. Another way to obtain rotating photons was implemented by Schine et al. [2016], who confined photons in a multimode ring resonator and they employed a non-planar geometry to induce an image rotation on each photon round-trip [see Fig. 2.6 d)]. This idea solved most difficulties of the previous proposals and led first to the experimental observation of photonic Landau levels by Schine et al. [2016] and recently to the claim by Clark et al. [2019] of the first realization of a (two-particle) Laughlin state made of light. In this experiment, a twisted cavity wad used to implement the artificial gauge field, while the photon-photon interactions were mediated
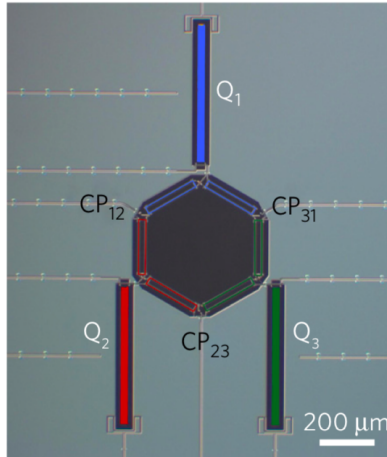
Figure 2.7: Optical image of three superconducting quibits (Q_i) connected by some adjustable couplers (CP_{ij}) to form a triangular closed loop. In this set-up an artificial magnetic flux piercing the triangular plaquette can be engineered by sinusoidally modulating the different couplings in a suitable fashion. This picture has been taken from Roushan et al. [2016].

by collective Rydberg excitations of a Rubidium atomic cloud loaded inside the cavity [Jia et al., 2018].

Arrays of superconducting qubits

To conclude this Chapter, there is a last experimental set-up we would like to mention as promising platform for the simulation of FCI states: superconducting-qubit arrays [Makhlin et al., 2001, Devoret and Martinis, 2004, Clarke and Wilhelm, 2008, Gu et al., 2017]. Even though at the beginning superconducting qubits have been thought as building blocks for quantum computers (here we cannot fail to mention the recent work by Arute et al. [2019], where they claimed the achievement of quantum supremacy), they have been used to simulate a wide range of quantum mechanical phenomena, e.g. the appearance of a localized phase in the presence of disorder Roushan et al. [2017] and the Mott insulator-superfluid transition [Ma et al., 2019].

The lithography-based fabrication of these systems gives access to a wide range of lattice geometries, both in 1D and in 2D. However, since the different qubits are connected through physical links, they are typically used to engineer Hamiltonians having only nearest-neighbor coupling. On the other hand, it is possible to tune many other parameters such as the on-site chemical potentials, the hopping rates between neighboring sites and the strength of Hubbard-like (i.e. density-density) interactions. Along these lines it is important to stress two points: The first one concerns the hopping amplitudes, which can be made complex through a suitable sinusoidal modulation of the couplings between the qubits, as discussed by Fang et al. [2012]. The second one relates to the on site interactions, which are set by the nonlinearity of the qubits and which can be tuned, by playing with the parameters of the Josephson junctions, to even reach the hard-core bosons regime.

The interplay between strong interactions and artificial gauge fields has been experimentally tested by Roushan et al. [2016], in the limit case of three qubits forming a triangular plaquette [see Fig. 2.7]. They observed the presence of chiral currents (as similarly done later by Tai et al. [2017] in the ultracold atomic context) and their dependence on the orientation of the artificial magnetic field, providing an undeniable proof that superconducting-qubit-based set-ups can be used to engineer bosonic FCI states.

In this last section we have seen that there are many different experimental platforms which aim to implement bosonic FQH and FCI states. At the same time, it is important to remark that each of them has its own advantages and limitations and that, for this reason, at the moment it is difficult to say which one is the most suitable for the observation of these exotic phases of matter. As a consequence, in this Thesis we will consider very general models which can describe many different set-ups.

Chapter 3

The Laughlin state.

As a consequence of the discussions in Chapter 2, to describe the FQHE one needs to find a state which does not break any continuous spatial symmetry and which has an energy gap. To find such a state one could think to use brute force. In principle, one can indeed consider the Hilbert space formed by all the degenerate (Fermi-liquid-like) ground states of a partially filled LL, evaluate all the matrix elements associated with the Coulomb potential and construct the interacting Hamiltonian matrix. After that, one can diagonalize such a matrix and obtain in this way all the Hamiltonian eigenstates, including the ground state we are looking for. Well, forget about it! As we have seen in Sec. 2.1.2 in the non-interacting case there exists a macroscopic number of degenerate ground states of a partially filled LL. This would imply the diagonalization of a macroscopically large Hamiltonian matrix, which is extremely hard, even numerically (especially in the 80's, when people discovered the FQHE). Therefore we have to give up all the perturbative approaches starting from the Fermi liquid. The only hope we may have to describe the FQHE is then a well-educated guess of the ground state. Such a guess fortunately arrived in 1983 when Laughlin [1983] proposed the so-called incompressible quantum liquid which describes the FQHE physics at filling factors $\nu = 1/M$ (where M was an odd integer) and for which he earned the Nobel prize in 1998.

In the following we review the main properties of the such Laughlin state, including those of its edge and QH excitations. All concepts we are going to introduce will be of crucial importance to understand what will be discussed in the next Chapters.

3.1 Laughlin's ansatz wave function

In order to present (we cannot speak of a real derivation) the Laughlin wave function it is convenient to start by considering two interacting particles in the LLL. We assume an arbitrary central potential between them, i.e.

$$V(\mathbf{r}_1, \mathbf{r}_2) = V(|\mathbf{r}_1 - \mathbf{r}_2|). \tag{3.1}$$

As we know, in the presence of a central potential working with eigenstates of the angular momentum always turns out to be a good choice. Moreover, in Sec. 2.1.2 we have seen that, if we want to talk about angular momentum in LLs, the appropriate gauge is the symmetric gauge. Within this particular gauge the single-particle wave functions in the LLL are described by an analytic function times a Gaussian factor. To be precise they take the form[1]:

$$\varphi_m(z, \bar{z}) \sim z^m \, e^{-|z|^2/4l_B^2}, \tag{3.2}$$

---

[1]We neglect the numerical pre-factors since they only take into account for the normalization of the wave functions, which is not important here.

where z is the particle coordinate in the complex plain while the integer m can take any value in $[0, \ldots, N_\phi - 1]$ [2]. As we know they describe states which are localised on a ring of radius $r = \sqrt{2m}\, l_B$, and they are also eigenstates of $\hat{L}_z$, with angular momentum quantum number equal to m. The fact that such wave functions are eigenstates of the angular momentum allows us to write down the eigenfunctions for any central potential $V = V(|\mathbf{r}_1 - \mathbf{r}_2|)$. Indeed, as long as we neglect Landau level mixing (which is completely reasonable if $\hbar\omega_C \gg V$), the two-particle wave functions for any central potential must have the form:

$$\Psi = (z_1 + z_2)^W (z_1 - z_2)^M e^{-(|z_1|^2 + |z_2|^2)/4l_B^2}. \tag{3.3}$$

From the above expression it is easy to see that the quantum number M (times $\hbar$) plays the role of the relative angular momentum between the two particles, while W is the quantum number associated with the total angular momentum of the pair.

Before moving on, let us comment on the importance of neglecting the mixing between different LLs: As we have already discussed in Sec. 2.1.2, any LLL single-particle wave functions must be an analytic function times a Gaussian term. A similar constraint applies to the many-particles wave functions defined in the LLL, which must have the form:

$$\Psi(z_1, \ldots, z_N) = f(z_1, \ldots, z_N)\, e^{-\sum_{i=1}^{N} |z_i|^2/4l_B^2}, \tag{3.4}$$

where $f(z_1, \ldots, z_N)$ is an analytic function in the particle coordinates. In the above two-particle problem this constraint allows us to find all the possible eigenfunctions in the presence of any central potential without solving the Schrödinger equation[3].

Laughlin's proposal for the ground-state wave function of the $\nu = 1/M$ FQH states is a straightforward N-particle generalization of the two-particle wave function reported in Eq. (3.3). To be precise, it is given by

$$\boxed{\Psi_{\rm L}(z) = \prod_{i<j} (z_i - z_j)^M\, e^{-\sum_{i=1}^{N} |z_i|^2/4l_B^2}}. \tag{3.5}$$

Due to the fermionic nature of electrons such a wave function must be anti-symmetric, meaning that it must take an overall minus sign under the exchange of any two particles $z_i \leftrightarrow z_j$. This clearly imposes an additional constraint on the values M, which must be an odd integer. Similarly, when M is an even integer, the wave function in Eq. (3.5) describes a bosonic quantum Hall state [see Sec. 2.4]. Moreover, it should be noted that such a wave function only depends on the the relative coordinates between the particle pairs, and not on the center of mass. Note also that the polynomial pre-factor has a zero of order M whenever two particles approach each other, while the Gaussian factor decreases quickly whenever the particles get too far from the origin. As a consequence, the Laughlin wave function is peaked on configurations that balance these two effect, leading to its characteristic flat density in the bulk region [see Fig. 3.1].

At this point we want to show that the Laughlin wave function describes a state with the desired filling factor. For this purpose look at what $\Psi_{\rm L}(z)$ can tell about an arbitrary electron, for instance the one with coordinate z_1. In the polynomial pre-factor of the Laughlin wave function there are $N-1$ factors like $(z_1 - z_j)^M$, one for each of the remaining $N-1$ electrons labelled by j,

$$\prod_{i<j} (z_i - z_j)^M \sim \prod_{j=2}^{N} (z_1 - z_j)^M. \tag{3.6}$$

Therefore the highest power of z_1 entering in $\Psi_{\rm L}(z)$ is $M(N-1)$ and, as a consequence, also the maximum angular momentum of the first electron is $M(N-1)$. Now, we can recall that an electron in the LLL having angular momentum $M(N-1)$ is described by the following single-particle wave function:

$$\varphi_{M(N-1)}(z, \bar{z}) \sim z^{M(N-1)} e^{-|z|^2/4l_B^2}, \tag{3.7}$$

and therefore such an electron will be localized on a ring of radius $r = \sqrt{2M(N-1)}\, l_B$. Thus, if we replace $N-1$ with N (which corresponds to assume $N \gg 1$), $r \approx \sqrt{2MN}\, l_B$ and we can

---

[2] We recall that m labels the different states in a given Landau level, and that the number of these states is fixed by the number N_ϕ of magnetic fluxes passing through the sample.

[3] Note that this is not the case if we consider $N > 2$ particles. In a many-particles problem indeed the analyticity of $f(z_1, \ldots, z_N)$ is not enough to determine the Hamiltonian eigenstates.
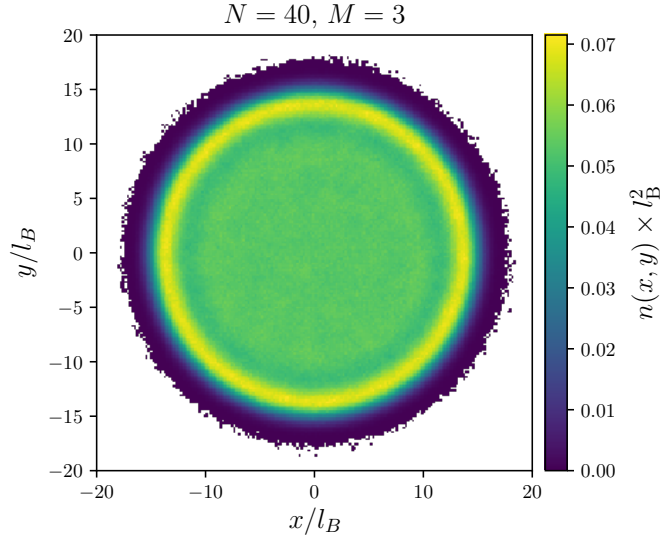
Figure 3.1: 2D density profile of the $N = 40$ $M = 3$ (fermionic) Laughlin state. Note that the bulk region of the Laughlin droplet is characterized by a flat density.

estimate the area of the FQH droplet as $A \approx 2\pi M N l_B^2$. Finally, as shown by Eq. (2.45), the total number of states in the LLL is given by $N_\phi = A/2\pi l_B^2$, which in this case reads

$$N_\phi = \frac{A}{2\pi l_B^2} \approx \frac{2\pi M N l_B^2}{2\pi l_B^2} = MN. \tag{3.8}$$

This gives us directly the expected filling factor

$$\boxed{\nu = \frac{N}{N_\phi} = \frac{1}{M}}. \tag{3.9}$$

The Laughlin wave function is therefore a good candidate to describe the FQH states observed at filling factors $\nu = 1, 1/3, 1/5, \ldots$, where we remember that the odd value of the denominators is required by the fermionic nature of the electrons.

Laughlin's wave function at $\nu = 1$

On the one hand, according to the above discussion, the Laughlin state with $M = 1$ should give the correct description of the completely filled LLL. On the other hand, from Sec. 2.1.3, we know that the case of $\nu = 1$ can be described within a non-interacting picture, where there exists a single (Fermi-liquid-like) ground state. Therefore, $M = 1$ provides a first check for the correctness of the Laughlin ansatz in Eq. (3.5).

As usual, in the case of non-interacting particles the many-particle ground state wave function can be obtained starting from the single-particle wave functions. In particular, since electrons are fermions, in order to build the many-particle ground state we have to fill the single-particle states $\psi_i(x)$, with $i = 1, \ldots, N$, by taking into account the Pauli exclusion principle. Finally, we need to anti-symmetrise over all electrons. Fortunately, there is an easy way to obtain such an anti-symmetric wave function; it can be done through the so-called Slater determinant:

$$\Psi(x) = \det \begin{bmatrix} \psi_1(x_1) & \psi_1(x_2) & \cdots & \psi_1(x_N) \\ \psi_2(x_1) & \psi_2(x_2) & \cdots & \psi_2(x_N) \\ \vdots & & & \vdots \\ \psi_N(x_1) & \psi_N(x_2) & \cdots & \psi_N(x_N) \end{bmatrix}. \tag{3.10}$$

Now we can apply this to the case of electrons in the LLL, where the single-particle wave functions are those in Eq. (2.35), i.e.

$$\varphi_i(z, \bar{z}) = z^{i-1} e^{-|z|^2/4l_B^2} \qquad \text{with again} \qquad i = 1, \ldots N. \tag{3.11}$$

The resulting Slater determinant gives a wave function of the form (3.4), where the analytic prefactor $f(\{z_i\})$ is given by the so-called Vandermonde determinant,

$$f(z) = \det \begin{bmatrix} z_1^0 & z_2^0 & \cdots & z_N^0 \\ z_1 & z_2 & \cdots & z_N \\ \vdots & & & \vdots \\ z_1^{N-1} & z_2^{N-1} & \cdots & z_N^{N-1} \end{bmatrix} = \prod_{i<j}(z_i - z_j). \tag{3.12}$$

Thus, by substituting the above result in Eq. (3.4), we obtain:

$$\Psi(z) = \prod_{i<j}(z_i - z_j)\, e^{-\sum_{i=1}^{N}|z_i|^2/4l_B^2}, \tag{3.13}$$

which is indeed nothing but the Laughlin wave function in Eq. (3.5) with $M = 1$.

Laughlin's wave functions vs true ground states

As shown by Laughlin [1983], if we limit ourselves to a small number of electrons, the Laughlin wave function has a greater than 99% overlap with the system ground state in the presence of Coulomb repulsions, as well as for other repulsive potentials. This incredibly high numerical overlap with the exact ground state is often considered as a clear proof of the correctness of the Laughlin ansatz. However, even if this result is astonishing in and of itself, we should take it with a grain of salt. We can indeed numerically obtain the ground state only for few tens of particles (even less in the case of bosons) and, although the overlap is very high for these small N systems, it is likely to be essentially zero if we consider 10^{11} particles or so. Thus, as highlighted by Tong [2016], we should consider the Laughlin wave function as a state different from the true ground state of the electronic FQH system observed in the laboratory. We should rather think of it as a state which lies in the same "universality class" as the true ground state, namely as a state which has many of the properties of the true ground state as for instance the same elementary excitations and the same topological order.

Therefore the Laughlin wave function does not represent the true ground state for electrons interacting through the Coulomb repulsion. The scenario is instead completely different for bosonic particles interacting through contact interactions [see Sec. 2.4]. In this case the $M = 2$ Laughlin state is the exact ground state of the system indeed, as shown for instance by Wilkin and Gunn [2000] in the atomic context.

In the FQH context, the interaction term of the Hamiltonian is often treated by bringing into play the so-called Haldane [1983] pseudopotentials [4], which allows us to write

$$\hat{H}_{\text{int}} = \sum_{m=0}^{\infty} \sum_{i<j} v_m\, \hat{\mathcal{P}}_m(ij), \tag{3.14}$$

where the operator $\hat{\mathcal{P}}_m(ij)$ projects the wave function onto the state in which the i-th and j-th particles have relative angular momentum equal to m. This formalism allows us to build up toy Hamiltonians having the Laughlin state at filling $\nu = 1/M$ as their ground state [5]. For instance, if we consider Haldane pseudopotentials given by

$$v_m = \begin{cases} 1 & \text{if} \quad m < M \\ 0 & \text{if} \quad m \geq M \end{cases}, \tag{3.15}$$

we pay a finite energy cost whenever two particles have angular momentum lower than M. Therefore, the wave function for the ground state of the Hamiltonian described by the previous pseudopotentials must include a factor $(z_i - z_j)^M$ for each pair of particles. This ensures that there are no particle pairs with relative angular momentum lower than M, avoiding in this way any energy cost associated with the v_m in Eq. (3.15).

As we will see in Sec. 3.3, starting from the Laughlin state one can construct many other states having vanishing energy contributions from the interaction Hamiltonian described by Eq. (3.15). However, it is possible to prove that one can select the Laughlin state as the unique ground state of the systems by adding to the toy Hamiltonian an external potential. We will explicitly show this fact in Sec. 3.3, for the particular case of a harmonic confinement.

---

[4] A more detailed treatment of this topic can be found for instance in Yoshioka [2002] and in Tong [2016].
[5] Note that for the just-mentioned case contact interactions, all Haldane pseudopotentials vanish expect v_0, explaining why in that particular case the Laughlin state has been found to be the exact ground state of the system.

3.2 Laughlin's plasma analogy

In what follows we will present the so-called Laughlin's plasma analogy. It consists of the identification of the modulus square of the Laughlin wave function with the Boltzmann factor $e^{-\beta U}$ of a classical system of 2D charged particles. While this analogy was proposed by Laughlin [1983] himself to give a physical interpretation to his wave function and to the properties of its elementary excitations, it also represents a very powerful numerical tool [see Appendix E].

To point out this analogy, suppose that we want to compute the average density of a FQH droplet described by the Laughlin wave function. What we have to do is compute the expectation value of the density operator, which is usually expressed as

$$n(z) = \sum_{i=1}^{N} \delta^{(2)}(z - z_i), \tag{3.16}$$

where $\delta^2(x)$ denotes the two-dimensional delta functions. Such an expectation value therefore reads

$$\langle \Psi_{\mathrm{L}} | n(z) | \Psi_{\mathrm{L}} \rangle = \frac{\int \prod_{i=1}^{N} d^2 z_i \, n(z) \, P[z_i]}{\int \prod_{i=1}^{N} d^2 z_i \, P[z_i]}, \tag{3.17}$$

where $P[z_i]$ is the un-normalised probability density associated with the Laughlin wave function, i.e.

$$P[z_i] = \prod_{i<j} \frac{|z_i - z_j|^{2M}}{l_B^{2M}} e^{-\sum_{i=1}^{N} |z_i|^2 / 2l_B^2}. \tag{3.18}$$

At this point we can notice that the expectation value in Eq. (3.17) has the same form of what we call average density in classical statistical mechanics, if we interpret its denominator as the canonical partition function

$$Z = \int \prod_{i=1}^{N} d^2 z_i \, P[z_i]. \tag{3.19}$$

On the other hand, we know that in the canonical ensemble the probability distribution $P[z_i]$ looks like a Boltzmann distribution function, namely

$$P[z_i] = e^{-\beta U(z_i)}. \tag{3.20}$$

By using the expression in Eq. (3.18) for the probability distribution, we can rewrite the previous equation as

$$\beta U(z_i) = -2M \sum_{i<j} \log\left(\frac{|z_i - z_j|}{l_B}\right) + \frac{1}{2} \sum_{i=1}^{N} \frac{|z_i|^2}{l_B^2}. \tag{3.21}$$

Now, to explicitly show the plasma analogy, we have to choose a particular value of β, that is

$$\beta = \frac{2}{M}. \tag{3.22}$$

Before proceeding with the derivation of the potential $U(z_i)$ describing a 2D plasma of classical particles, we would like to spend a few words on β. In the statistical mechanics framework β is interpreted as the inverse of temperature, or rather as the inverse of energy, i.e. $\beta = 1/k_B T$. However, in the present case we can not link $\beta = 2/M$ to any physical temperature, least of all to the temperature at which the quantum Hall state is observed. Indeed, it is important to stress that we are dealing with an auxiliary, or fake, "temperature". This can be immediately understood for instance by noting that in Eq. (3.22) β is dimensionless. To compensate this fact also the potential $U(z_i)$ is dimensionless and for the previous choice of β it reads

$$\boxed{U(z_i) = -M^2 \sum_{i<j} \log\left(\frac{|z_i - z_j|}{l_B}\right) + \frac{M}{4} \sum_{i=1}^{N} \frac{|z_i|^2}{l_B^2}.} \tag{3.23}$$

To conclude we have only to show that what we just wrote is exactly the potential energy for a plasma of 2D charged particles, where each particle has electric charge $Q = -M$.

Let us focus our attention on the first term of $U(z_i)$: It is easy to see that it describes interactions between the charged particles forming the plasma. In particular, each term of the sum represents the Coulomb potential between two particles of charge $Q = -M$ when both the particles and the electric field lines lie in a 2D plane. This can be shown with the help of Poisson's equation in two dimensions for the electrostatic potential generated by a point-like charge Q, namely

$$- \nabla^2 V = 2\pi Q\, \delta^{(2)}(\mathbf{r}), \tag{3.24}$$

which implies

$$V = -Q \log\left(\frac{r}{l_B}\right). \tag{3.25}$$

Finally, once we know the electrostatic potential V, we can easily obtain the potential energy as $U = QV$, which indeed corresponds to the first term in Eq. (3.23).

Consider now the second term in Eq. (3.23): It describes the interactions of the charged plasma particles with a neutralising background of positive charge. Let us assume that such a constant background has charge density ρ_0. If this is the case, the corresponding electrostatic potential must obey $-\nabla^2 V = 2\pi\rho_0$. On the other hand, by looking at the second term in Eq. (3.23), we can identify such an electrostatic potential with $-|z|^2/4l_B^2$. In this way we end with:

$$- \nabla^2 V = \nabla^2\left(\frac{|z|^2}{4l_B^2}\right) = \frac{1}{l_B^2} = 2\pi\rho_0, \tag{3.26}$$

which tells us that each particle of charge $-M$ feels a background charge density

$$\rho_0 = \frac{1}{2\pi l_B^2} = n_\phi, \tag{3.27}$$

where n_ϕ is the flux density.

Now that we have justified the Laughlin plasma analogy, we would like to see if it tells us something new about the Laughlin wave function. In order to minimise the energy, the plasma needs to neutralize the background charge density, i.e. the charge density of the plasma particles must compensate the one of the positive background. This translates into the following condition for the particle density n:

$$Mn = \rho_0. \tag{3.28}$$

which implies:

$$\boxed{n = \frac{1}{2\pi l_B^2 M} = \frac{n_\phi}{M}}. \tag{3.29}$$

This is the expected (bulk) density of a state with filling factor $\nu = 1/M$ [6]. However, as it is pointed out by Tong [2016], the above arguments tells us something more. By looking at the form of the Laughlin wave function [see Eq. (3.5)], one could think that the origin plays some special role. Note for instance that in the Laughlin wave function for each particle there is a Gaussian term which tends to zero if such a particle is very far from the origin. But this is misleading. The plasma analogy indeed tells us that FQH states are characterized by average particle densities which are constant [see for instance Fig. 3.1]. The fact that the density of a FQH state does not depend on the spatial coordinates, as long as we remain in the bulk region of the system, will be of crucial importance in Sec. 7.2.3.

3.3   Edge excitations of the Laughlin state

As we have already mentioned a few times, the edges of quantum Hall systems display an astonishing behavior. They represent indeed the paradigmatic example of a chiral quantum liquid, i.e. a 1D system in which the transport occurs only in one direction [7] [Wen, 1989, Chang et al., 1996, Chang, 2003]. Moreover, the dynamical properties of these excitations provide a direct way to

---

[6] This can be immediately understood by recalling the definition of the filling factor $\nu = N/N_\phi = n/n_\phi$, from which we can directly obtain $n = n_\phi/M$ when $\nu = 1/M$.

[7] The chirality of the FQH edge is due to the presence of an orthogonal magnetic field which breaks time-reversal symmetry. Note that this feature can be also understood at the semi-classical level, in terms of the so-called skipping orbits [Tong, 2016].
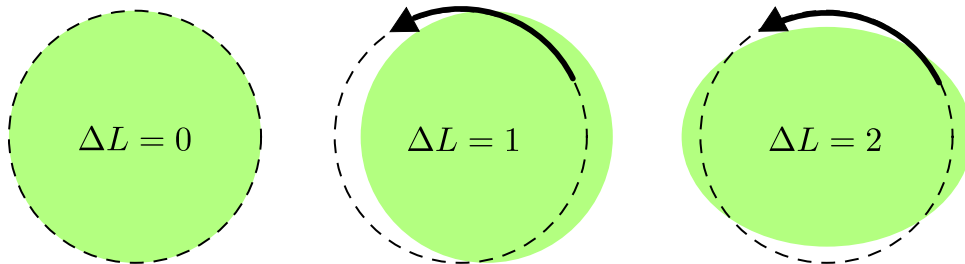
Figure 3.2: Sketch of the first few edge excitations of the Laughlin state ($\Delta L = 0$). While the state with $\Delta L = 1$ describes the center of mass motion of the Laughlin state, the one with $\Delta L = 2$ can be interpreted as a quadrupole mode. However, in general all states with $\Delta L \geq 2$ should be thought of as ripples propagating around the circumference of the droplet.

measure the topological order characterizing the different FQH states. For this reason the dynamics of the FQH edge modes has been the subject of intense investigation since the landmark papers of Wen [1990a,b, 1991a,b, 1992, 1995], where it has been shown that the low-energy dynamics of the edge modes in the thermodynamic limit ($N \to \infty$) is given by the so-called chiral Luttinger liquid (χLL). To be precise, it was found that these modes are described by a linear χLL, meaning that they have a dispersion relation which is linear in the wave vector k, i.e. $\omega(k) = vk$.

Although for generic FQH systems one recovers the χLL behavior of the edges only in the limit of low energies and large system sizes, in the case of harmonically-confined contact-interacting particles (in the FQH regime) the edge dispersion has been found to be linear independently on the system size and at all energies. Note that these conditions are exactly those typically considered for ultracold atoms in rotating traps [Cooper, 2008], for which the χLL behavior of the edge has been proved by Cazalilla [2003] and Cazalilla et al. [2005].

What happens if we move away from this special case has been studied in Fern et al. [2018], where the authors also proposed an effective theory able to reproduce the observed non-linear dispersion of the FQH edge in the presence of anharmonic confinements and/or short(but finite)-range interactions.

Despite being an extremely interesting topic, in the following we will not enter into the details of the χLL description proposed by Wen [1990a,b, 1991a,b, 1992, 1995] nor of the effective theory discussed in Fern et al. [2018]. We will limit ourselves to treat the edge modes of a $\nu = 1/M$ Laughlin state from a microscopic perspective, instead. In particular, we will focus our attention on the wave functions describing such a kind of excitations, by showing that they can be used to easily explain both the chirality of the FQH edges and the linear dispersion observed for harmonically-trapped atomic systems.

Edge-state wave functions

Let us consider a FQH at filling factor $\nu = 1/m$ in presence of a (radially symmetric) confining potential. The basic idea is that the ground state forms an incompressible disk and the low-energy excitations of this state are area-preserving shape deformations of the disk [see examples in Fig. 3.2]. But let us now figure out the wave functions associated with these excitations.

For this purpose, we can consider the toy Hamiltonian described by the Haldane pseudopotentials in Eq. (3.15). As we have already explained, any wave function including a factor $(z_i - z_j)^M$ ensures that there are no particle pairs with relative angular momentum lower than M and, as a consequence, zero energy contributions from the pseudopotentials v_m. At the same time, if we restrict ourselves to many-body states in the LLL, this implies the following form for the ground-state wave function

$$\Psi(z) = S(z) \prod_{i<j}(z_i - z_j)^M \, e^{-\sum_{i=1}^{N} |z_i|^2/4l_B^2}, \tag{3.30}$$

where $S(z)$ is any symmetric polynomial in the particle coordinates. Note that the symmetry constraint on $S(z)$ is needed to have a global wave function which displays the correct statistical properties, which we know to be fixed by the parity of M. Moreover, if the system Hamiltonian is rotationally invariant, as it is in the case of isotropic interactions and radially symmetric confinements, $S(z)$ must be also homogeneous.

At this point it is easy to see that the Laughlin wave function, for which $S(z) = 1$, is the lowest-angular-momentum state among those described by Eq. (3.30) and it is therefore the most compact state. As a consequence, we can select the Laughlin state as the unique ground state of the system by adding an external confining potential. One possible choice for the confining potential (strongly motivated by the discussions in Sec. (2.4)) could be the harmonic one, i.e.

$$\hat{H}_{\mathrm{conf}}(z) = v \sum_i |z_i|^2 \sim v \hat{L}_z, \tag{3.31}$$

where L_z is the angular momentum operator. In presence of this potential the Laughlin state is clearly the ground state and its energy reads

$$E_{\mathrm{L}} = v L_{\mathrm{L}} = v \frac{MN(N-1)}{2}, \tag{3.32}$$

where $L_{\mathrm{L}} = MN(N-1)/2$ is the total angular momentum of the Laughlin state (in units of $\hbar$).

We have just seen that the Laughlin state is the ground state of the Hamiltonian $\hat{H} = \hat{H}_{\mathrm{int}} + H_{\mathrm{conf}}$, but what about the other states described by wave functions of the form (3.30)? If we consider the following basis of symmetric polynomials

$$S_l(z) = \sum_i z_i^l, \tag{3.33}$$

the most general (symmetric and homogeneous) polynomial pre-factor $S(z)$ can be written as a linear combination of terms products of the form

$$\prod_{l=1}^{\infty} S_l(z)^{d_l}, \tag{3.34}$$

with the constraint that all of them must have the same degree

$$\Delta L = \sum_{l=0}^{\infty} l \, d_l. \tag{3.35}$$

As a consequence, the angular momentum of any state described by Eq. (3.30) will be of the form

$$L = L_{\mathrm{L}} + \Delta L. \tag{3.36}$$

Now that we know the angular momentum L of the most general edge state, it is straightforward to obtain its energy in the presence of a harmonic confinement, which reads

$$E = vL = E_{\mathrm{L}} + v\Delta L. \tag{3.37}$$

To conclude we would like to say a few more words about states with $S(z) \neq 1$. First of all, actually not all these states describe edge modes. For instance, the state obtained by multiplying the Laughlin wave function by $S_1(z) = \sum_i z_i$, having $\Delta L = 1$, does not describe a deformation of the FQH droplet boundary. It represents a small translation of the droplet centre of mass instead, which leaves the shape of the boundary unchanged [see Fig. 3.2]. Another particular class of states are those with $S(z) = \prod_i z_i^n$ which, as we will see in the next section, describe states presenting n QH excitations located in the origin. Secondly, since both l and d_l entering in Eq. (3.34) must be higher than zero, otherwise the resulting wave function would not respect the analyticity condition and the corresponding state would not be in the LLL, all these states describe excitations which can only increase the total angular momentum of the system and, as such, can be thought of as chiral excitations.

Finally, as we can see from Eq. (3.37), edge states characterized by the same additional angular momentum ΔL are degenerate in the presence of a harmonic confinement. Moreover it is possible to prove that the number of degenerate states corresponds to the number of partitions of ΔL, namely the number of ways in which one can write ΔL as a sum of positive integers [see Chapter 5].

Before entering the discussion about the bulk excitations of the Laughlin state, we would like to stress that the degeneracy of states with the same total angular momentum is a peculiar feature of harmonically confined FQH systems. As shown for instance by Cooper and Simon [2015], this picture breaks down as soon as one adds a quartic term to the harmonic potential. What happens to the edge-modes dispersion in the presence of confinements even steeper than the quartic one, will be the subject of Chapter 6.

3.4   Bulk excitations of the Laughlin state

After having inspected the properties of the Laughlin wave function and having briefly discussed the edge excitations on top of the FQH droplet that such a wave function describes, now we turn our attention to its bulk excitations.

In these systems there exist two different kinds of bulk excitations: On the one hand, there are charged elementary excitations, which are distinguished into quasiholes and quasiparticles, displaying fractional charge and anyonic statistics. They are one of the main subjects of this Thesis.

On the other hand, there are neutral collective excitations describing the case in which both the density and the charge of the FQH liquid ripple in a wave-like behavior over large distances. These collective excitations are similar to phonons in superfluids, with the difference that these modes are gapped for any value of the momentum $\hbar k$ (and so their energy does not go to zero when the momentum does). The dispersion relation of these neutral excitations has a minimum (called magneto-roton minimum in analogy with the roton minimum present in the superfluid dispersions) at some finite wave vector k which, as shown by Girvin et al. [1986], indicates the desire of the system to form a crystalline structure (a Wigner crystal) at small fillings ($\nu < 1/7$). Nowadays there is a strong interest in the neutral collective modes of FQH systems, especially after Haldane [2011] has interpreted the magneto-roton mode as an internal geometrical degree of freedom (or metric) whose quantum fluctuations represent the FQH analog of gravitons [Golkar et al., 2016, Liou et al., 2019]. However, in the following we will not study these excitations in detail, but we will rather concentrate on the FQH charged elementary excitations and on their exotic properties.

3.4.1   Quasihole excitations

The wave function describing a QH excitation at position η is

$$\Psi_{\mathrm{QH}}(\eta; z) = \prod_{i=1}^{N}(z_i - \eta)\, \Psi_{\mathrm{L}}(z) = \prod_{i=1}^{N}(z_i - \eta) \prod_{i<j}(z_i - z_j)^M\, e^{-\sum_{i=1}^{N}|z_i|^2/4l_B^2}. \tag{3.38}$$

From the above expression it is easy to see that the particle density now vanishes at η. In other words, the pre-factor $\prod_{i=1}^{N}(z_i - \eta)$ represents a density depletion in the quantum fluid.

Once identified such a pre-factor with the presence of a QH at position η, writing the wave function for the state presenting n QHs at positions η_μ, with $\mu = 1, \dots, n$, is straightforward:

$$\boxed{\Psi_{n\mathrm{QH}}(\eta; z) = \prod_{\mu=1}^{n}\prod_{i=1}^{N}(z_i - \eta_\mu) \prod_{i<j}(z_i - z_j)^M\, e^{-\sum_{i=1}^{N}|z_i|^2/4l_B^2}}. \tag{3.39}$$

At this point we can see some properties of the QH wave function in Eq. (3.38): First of all we can notice that it is a zero-energy eigenstate of the interacting Hamiltonian described by the Haldane pseudopotentials in Eq. (3.15) [8].

It is also possible to show that multiplying the Laughlin state by $\prod_{i=1}^{N}(z_i - \eta)$ corresponds to introducing an additional magnetic flux quantum to the system. For this purpose we can expand the wave function describing the state with a QH in the center of the droplet, i.e. at $\eta = 0$. In this way we obtain

$$\Psi_{\mathrm{QH}}(\eta = 0; z) = \sum_{\{m_i\}} A_{m_1,\dots,m_N}\, z_1^{m_1+1} \dots z_N^{m_N+1}\, e^{-\sum_{i=1}^{N}|z_i|^2/4l_B^2}, \tag{3.40}$$

where each exponent is increased by one ($m_i \to m_i + 1$) with respect to the expansion of Ψ_{L}. Therefore we can give the following interpretation to what happens when we create a QH excitation: each particle forming the FQH state jumps from the single-particle state with angular momentum m to the state with angular momentum increased by one, leaving behind an empty state at $m = 0$. Since this involves all particles in the FQH state, the net result is an increase of the sample size by the surface occupied by one flux quantum ($2\pi l_B^2$), while the total number of particles is kept constant. Therefore the creation of a QH implies the introduction of one additional magnetic flux quantum $N_\phi \to N_\phi + 1$, which lowers the filling factor by a tiny amount.

---

[8]Note that, if we only consider the interacting Hamiltonian, the symmetric polynomial pre-factor $S(z)$ does not need to be homogeneous.

Quasihole's fractional charge

As we have mentioned at the beginning of this Chapter, one of the main properties of FQH liquids is that they can host emergent elementary excitations characterized by fractional charge. However, we have not yet shown its value. To compute the QH charge let us consider the filling factor as fixed. In this case, since the presence of a QH in the system implies the insertion of an additional flux quantum, we need to add some negative charge to compensate it. From the relation in Eq. (3.8) we can see that the extra flux ΔN_ϕ and the compensating extra charge ΔN are related by

$$\Delta N_\phi = M \Delta N \qquad \Longleftrightarrow \qquad \Delta N = \frac{\Delta N_\phi}{M}. \tag{3.41}$$

Thus, in order to compensate the presence of a single extra quantum flux ($\Delta N_\phi = 1$), we need to add the M-th fraction of one of the particles forming the FQH state. Therefore, since we defined the electron charge as $-e$, the charge deficit caused by the QH excitation in the electronic case results

$$\boxed{e^\star = \frac{e}{M}}. \tag{3.42}$$

The same result for the QH charge can be obtained through the Laughlin plasma analogy. The additional factor $\prod_{i=1}^{N}(z_i - \eta)$ in the QH wave function (3.38) yields an additional term in the potential energy of the 2D one-component plasma, which in the case of n QHs reads

$$U(z_i, \eta_\mu) = -M^2 \sum_{i<j} \log\left(\frac{|z_i - z_j|}{l_B}\right) + \frac{M}{4}\sum_{i=1}^{N}\frac{|z_i|^2}{l_B^2} - M\sum_{i,\mu}\log\left(\frac{|z_i - \eta_\mu|}{l_B}\right). \tag{3.43}$$

This additional term describes the interaction of the plasma particles with impurities with unitary charge located at positions η_μ. The plasma particles are expected to screen these impurities in order to maintain charge neutrality[9]. Thus, since each plasma particle has charge $Q = -M$, one needs only $1/M$ plasma particles to screen an impurity of unitary charge. However, we know that each particle of the plasma corresponds to a single electron in the original FQH liquid and therefore we end with the same charge fractionalization obtained before.

The existence of fractional charges is certainly surprising, but it could be also confusing. According to the charge-quantization principle the charge of any object in nature must be an integer multiple of the elementary charge e, thus one may think that here we are violating one of the fundamental laws of physics. Of course, we are not. Indeed, if you isolate the FQH liquid and measure the total charge you will always find an integer multiple of the electron charge. Nevertheless, if one creates a hole by removing one electron from the system, it can split into M QHs. On top of that, these elementary excitations behaves as independent particles. They can indeed independently respond to external probes such as confining potentials or applied electric fields. Therefore the fractional charge of such elementary excitations should not be interpreted as a mere mathematical concept but rather as an actual physical quantity. This was experimentally demonstrated for the first time for QPs [see Sec. 3.4.2] in the shot-noise experiment by de Picciotto et al. [1997], where they directly measured the charge $e^\star = -e/3$ of the carriers in edge of the $\nu = 1/3$ FQH state.

Quasihole's anyonic statistics

As first realized by Halperin [1984], the QH excitations of the Laughlin state not only have fractional charge, but they also display anyonic statistical properties. To be more precise, Laughlin QHs are Abelian anyons and for a given set of their coordinates $(\eta_1, \ldots, \eta_n)$ there is a single (non-degenerate) ground state, indeed.

To point out the statistical phase of Laughlin QHs we will follow the procedure used by Arovas et al. [1984], who studied the effect of adiabatically exchanging two of them. As we discussed in Chapter 1, the unitary operator $\mathcal{U}$ describing this kind of processes is composed of two parts: the Berry matrix $\mathcal{U}_B$ and what we called basis-change matrix $\mathcal{B}$. Note that since we are dealing with a non-degenerate ground state, both these matrices are actually scalars in this case (phase factors to be precise).

---

[9]Note that screening is a phenomenon in which mobile charges rearrange themselves to compensate for the introduction of a charged impurity. Therefore to use this argument, we have to ensure that the plasma lies in the liquid phase. As discussed in Tong [2016], this is the case for $M \lesssim 70$, while the plasma is in the solid phase otherwise.

To compute $\mathcal{U}_B$ and $\mathcal{B}$ associated with the adiabatic exchange of QHs we consider a renormalized QH wave function, i.e.

$$\Psi_{n\mathrm{QH}}(\eta;z) = \prod_{\mu=1}^{n}\prod_{i=1}^{N}(z_i - \eta_\mu)\prod_{i<j}(z_i - z_j)^M e^{-\sum_{i=1}^{N}|z_i|^2/4l_B^2} \times \prod_{\mu<\nu}^{n}(\eta_\mu - \eta_\nu)^{\frac{1}{M}} e^{-\sum_{\mu=1}^{n}|\eta_\mu|^2/4Ml_B^2}.$$
(3.44)

Note that this wave function is exactly the one in Eq. (3.39) times a term which depends on the QH coordinates, but not on the particle ones, meaning that it can be considered as a normalization factor. However, this normalization factor introduces two extra terms in the potential of the 2D one-component plasma associated with $|\Psi_{n\mathrm{QH}}(\eta;z)|^2$, which reads

$$U(z_i,\eta_\mu) = -M^2\sum_{i<j}\log\left(\frac{|z_i - z_j|}{l_B}\right) + \frac{M}{4}\sum_{i=1}^{N}\frac{|z_i|^2}{l_B^2} - M\sum_{i,\mu}\log\left(\frac{|z_i - \eta_\mu|}{l_B}\right)$$
$$- \sum_{\mu<\nu}\log\left(\frac{|\eta_\mu - \eta_\nu|}{l_B}\right) + \sum_{\mu=1}^{n}\frac{|\eta_\mu|^2}{l_B^2}\ .$$
(3.45)

The new terms in $U(z_i,\eta_\mu)$ can be easily interpreted as the Coulomb interaction between the different impurities, describing the QHs, and between the impurities and the constant background charge, respectively.

Now we would like evaluate the holomorphic and the anti-holomorphic Berry connections

$$\mathcal{A}^{\eta_\mu} = i\int\prod_{k=1}^{N}d^2z_k\,\frac{\bar{\Psi}}{\sqrt{Z}}\frac{\partial}{\partial\eta_\mu}\left(\frac{\Psi}{\sqrt{Z}}\right),$$
(3.46)

$$\mathcal{A}^{\bar{\eta}_\mu} = i\int\prod_{k=1}^{N}d^2z_k\,\frac{\bar{\Psi}}{\sqrt{Z}}\frac{\partial}{\partial\bar{\eta}_\mu}\left(\frac{\Psi}{\sqrt{Z}}\right),$$
(3.47)

where Ψ must be interpreted as the n-QH wave functions in Eq. (3.44) (and $\bar{\Psi}$ as its complex conjugate), and where we introduced

$$Z = \int\prod_{k=1}^{N}d^2z_k\,|\Psi_{n\mathrm{QH}}(\eta;z)|^2 = \int\prod_{k=1}^{N}d^2z_k\,e^{-\beta U(z_k,\eta_\mu)}$$
(3.48)

to have properly normalized wave functions[10]. The Berry connections in Eqs. (3.46) and (3.47) are difficult to compute exactly, however the study of the behavior of the plasma described by $U(z_i,\eta_\mu)$ can give us extremely useful insights in this direction.

First of all, we recall that Z can be interpreted as the partition function of the plasma, and as such can be expressed in terms of the free energy F, i.e. $Z = \exp\{-\beta F\}$. At this point one can use the result by Caillol et al. [1982], who showed that as long as $M \lesssim 70$ the 2D one-component plasma is in the screening phase. In this phase the plasma particles rearrange themselves around the impurities describing the QHs so that their presence is effectively hidden at distances much larger than the so-called Debye screening length. This implies that for all values of M which are relevant in the FQH context, the free energy of the plasma is independent on the impurity positions, at least up to exponentially small corrections. In particular, as shown by Laughlin [1987],

$$Z = e^{-\beta F} = C + O\left(e^{-|\eta_\mu - \eta_\nu|/\xi}\right),$$
(3.49)

where both C and ξ are constant which do not depend on the QH coordinates η_μ.

Now we are ready to compute $\mathcal{A}^{\eta_\mu}$ and $\mathcal{A}^{\bar{\eta}_\mu}$. As a first step we can rewrite the holomorphic Berry connections as

$$\mathcal{A}^{\eta_\mu} = i\frac{\partial}{\partial\eta_\mu}\left(\frac{1}{Z}\int\prod_{k=1}^{N}d^2z_k\,|\Psi|^2\right) - i\int\prod_{k=1}^{N}d^2z_k\,\frac{\partial}{\partial\eta_\mu}\left(\frac{\bar{\Psi}}{\sqrt{Z}}\right)\frac{\Psi}{\sqrt{Z}}.$$
(3.50)

---

[10]In the original paper by Arovas et al. [1984], the authors did not consider normalized wave functions. The fact that the normalization constant might play an important role in the calculation of the Berry connection was pointed out by Stone [1992].

Then we can note that the former term in the previous expression trivially vanishes, while in the latter the derivative with respect to η_μ only acts on the Gaussian term $\exp\{-\sum_\mu |\eta_\mu|^2/4Ml_B^2\}$ of the wave function $\Psi_{nQH}(\eta; n)$. Similarly the derivative with respect to $\bar{\eta}_\mu$ entering in Eq. (3.47) only acts on the same Gaussian term. Thus, the holomorphic and the anti-holomorphic Berry connection read

$$\mathcal{A}^{\eta_\mu} = i\frac{\bar{\eta}_\mu}{4Ml_B^2} + O\left(e^{-|\eta_\mu - \eta_\nu|/\xi}\right) \qquad \text{and} \qquad \mathcal{A}^{\bar{\eta}_\mu} = -i\frac{\eta_\mu}{4Ml_B^2} + O\left(e^{-|\eta_\mu - \eta_\nu|/\xi}\right), \qquad (3.51)$$

respectively.

At this point, the evaluation of the Berry matrix acquired by the n-QH wave function when we adiabatically exchange two of them becomes straightforward. In particular, it results

$$\begin{aligned}
\mathcal{U}_{\mathrm{B}} &= \mathcal{P}\exp\left[i\int_0^T \mathcal{A}(t)dt\right] \\
&= \exp\left[-\frac{1}{4Ml_B^2}\int_0^T dt \sum_{\mu=1}^n \left(\bar{\eta}_\mu \frac{d\eta_\mu}{dt} - \eta_\mu \frac{d\bar{\eta}_\mu}{dt}\right)\right] + O\left(e^{-|\eta_\mu - \eta_\nu|/\xi}\right) \\
&= \exp\left(i\frac{e}{M}\frac{BA}{\hbar}\right) + O\left(e^{-|\eta_\mu - \eta_\nu|/\xi}\right),
\end{aligned} \qquad (3.52)$$

where A denotes the area encircled by the QHs in the adiabatic exchange process. This dependency on A clearly identify the Berry phase $\varphi_{\mathrm{B}} = -i\log(\mathcal{U}_{\mathrm{B}})$ as a non-topological quantity, meaning that it cannot be the QH statistical phase we are looking for. However, it can be interpreted as the Aharonov and Bohm [1959] phase associated with the QH motion. Laughlin QHs are indeed charged objects and therefore moving them in the presence of the orthogonal magnetic field B will let the many-body wave function acquire an Aharonov-Bohm phase $\varphi_{\mathrm{AB}} = e^\star\Phi/\hbar$. Note that the comparison between the definition of φ_{AB} and the result in Eq. (3.52) provides an alternative and equivalent way to calculate the QH fractional charge.

Now, to complete the calculation, we have to compute $\mathcal{B} = \langle\Psi(0)|\Psi(T)\rangle$. In the present case it is easy to see that $|\Psi(T)\rangle$ differs from $|\Psi(0)\rangle$ by a phase factor $\exp[i\pi/M]$, coming from the exchange of the coordinates of two QHs in the wave function (3.44). This allows us to identify the QH statistical phase

$$\boxed{\varphi_{\mathrm{st}} = \frac{\pi}{M}}. \qquad (3.53)$$

Note that for the completely filled LLL ($M = 1$) the QHs are fermions ($\varphi_{\mathrm{st}} = \pi$), as one would expect (they are actual holes in this case), while for FQH states described by the Laughlin state they are anyons.

Before discussing the QP excitations of the Laughlin state there is a last remark we would like to make. We would like to stress that the above results for $\mathcal{U}_{\mathrm{B}}$ and $\mathcal{B}$ strongly depends on the particular form of the wave function $\Psi_{nQH}(\eta; z)$. Indeed, it is possible to prove that by substituting $\prod_{\mu<\nu}(\eta_\mu - \eta_\nu)^{1/M}$ with $\prod_{\mu<\nu}|\eta_\mu - \eta_\nu|^{1/M}$ in (3.44) one obtains a trivial $\mathcal{B}$ (equal to the identity), while the Berry phase φ_{B} corresponds to the sum of the Aharonov-Bohm and the statistical phases. This is due to the fact only the product of $\mathcal{U}_{\mathrm{B}}$ and $\mathcal{B}$ is a gauge-independent quantity. We will come back to this point in Chapter 7, where the gauge dependency of $\mathcal{U}_{\mathrm{B}}$ and $\mathcal{B}$ will play a crucial role.

3.4.2 Quasiparticle excitations

Up to now we have focused our attention only on the elementary excitations known as QHs, i.e. those obtained by introducing additional flux quanta (one for each QH excitation) to the system. However, the Laughlin state can host another kind of elementary excitations: the so-called QPs. Contrary to QHs, QPs are associated with the lowering of the number of magnetic flux quantum passing through the system. They also carry fractional charge, which however in this case has the same sign of the charge of particles forming the Laughlin state, i.e. (in the case of electrons)

$$e^\star = -\frac{e}{M}. \qquad (3.54)$$

Despite being as interesting as QHs are (also QPs have anyonic statistics indeed), QP excitations have been only marginally studied, as compared to QHs. This is consequence of the fact that the

wave functions describing states hosting QP excitations are harder to write down with respect to those for QHs. To understand this difficulty, note that we want to increase the electron density inside the FQH fluid and therefore we have to decrease the relative angular momentum of some electron pairs. As we have seen, one can easily increase the angular momentum of the FQH system by multiplying $\Psi_L(z)$ by a symmetric polynomial in the particle coordinates. In particular, for the case of a QH at $\eta = 0$, such a polynomial pre-factor has been found to be $\prod_i z_i$. However, to describe a QP excitation we cannot divide by $\prod_i z_i$ as the resulting wave function would be badly singular. One may think to reduce the angular momentum of the Laughlin state (which we recall to be given by the degree of the $\prod_{i<j}(z_i - z_j)^M$ polynomial) by simply multiplying $\Psi_L(z)$ by $\prod_i \bar{z}_i$, but this would lead to a wave function with unwanted components in higher LLs [11]. To heal the QP wave function obtained in this way, one can projects it into the LLL, i.e.

$$\Psi_{QP}(\bar{\eta}, z) = \hat{\mathcal{P}}_{LLL} \prod_{i=1}^{N} (\bar{z}_i - \bar{\eta}) \, \Psi_L(z). \tag{3.55}$$

There are several ways to project such a wave function into the LLL level. One of the most common consists of replacing the non-analytic variables $\bar{z}_i$ by the derivative respect to z_i. In this way one reduces the degree of the polynomial pre-factor entering in the Laughlin wave function, by means of differentiation. This leads to the following candidate as quasi-particle wave function

$$\Psi_{QP}(\bar{\eta}, z) = \left[\prod_{i=1}^{N} \left(2\frac{\partial}{\partial z_i} - \bar{\eta} \right) \prod_{i<j} (z_i - z_j)^M \right] e^{-\sum_{i=1}^{N} |z_i|^2 / 4l_B^2}. \tag{3.56}$$

The QP wave function in Eq. (3.56) involves derivatives and this fact makes it much harder to handle with respect to the QH one. Note for instance that the square modulus $|\Psi_{QP}(\bar{\eta}, z)|^2$ can not be expressed as the Boltzmann factor of any 2D plasma of classical particles. Moreover, while one can easily build up toy Hamiltonians having the QH state described by the wave function in Eq. (3.38) as an eigenstate, doing the same for the QP wave function seems to be far from trivial.

Finally, if one considers toy Hamiltonians similar to the one used in Sec. 3.3, all states obtained by decreasing the angular momentum of the Laughlin state will have a finite energy contribution coming from the interaction term. This means that in general states presenting QP excitations will be separated by an energy gap (called many-body gap or Laughlin gap) from the Laughlin state and its QH and edge excitations.

---

[11]Note that such a wave function would not satisfy the analyticity conditions of the LLL.

Chapter 4

The Moore-Read state.

The Moore-Read (or Pfaffian) state was proposed by Moore and Read [1991], and it represent a second paradigmatic wave function for the fractional quantum Hall effect. However, it is important to stress that this state is qualitatively different from the Laughlin one. It is, indeed, a non-Abelian fractional quantum Hall state, whose elementary excitations (quasiholes and quasiparticles) obey non-Abelian statistics and whose edge excitations include a fermionic branch, in addition to the usual bosonic one which is present also for the Laughlin state.

Although the physics of the Moore-Read edge modes is surely an interesting topic [Wen, 1995, Milovanović and Read, 1996, Wan et al., 2006], in the following we will focus our attention only on the Moore-Read state and its quasihole excitations. These elementary excitations represent the simplest example of non-Abelian anyons and they will be one of the main subjects of the analysis reported in Chapter 7.

4.1 The Pfaffian state

In order to explain the FQH state observed at filling $\nu = 5/2$, Moore and Read [1991] introduced the celebrated Pfaffian state. Such a state is described by the wave function

$$\Psi_{\mathrm{MR}}(z) = \mathrm{Pf}\left(\frac{1}{z_i - z_j}\right) \prod_{i<j} (z_i - z_j)^M \ e^{-\sum_i |z_i|^2 / 4l_B^2}, \tag{4.1}$$

where $\mathrm{Pf}(W)$ denotes the Pfaffian of the $N \times N$ anti-symmetric matrix W, such that $|\mathrm{Pf}(W)| = \sqrt{|\det(W)|}$. For instance, if we consider $N = 4$, the explicit form of the Pfaffian appearing in the Moore-Read wave function reads

$$\mathrm{Pf}\left(\frac{1}{z_i - z_j}\right) = \frac{1}{z_1 - z_2}\frac{1}{z_3 - z_4} - \frac{1}{z_1 - z_3}\frac{1}{z_2 - z_4} + \frac{1}{z_1 - z_4}\frac{1}{z_2 - z_3}. \tag{4.2}$$

At this point we would like to stress that the wave function (4.1) describes only states with an even number of particles N. The Pfaffian indeed vanishes for N odd, since the determinant of an anti-symmetric matrix is null for odd values of N. However, a generalization for odd N exists and it can be obtained by modifying in a suitable way the matrix W entering in the Pfaffian [Baraban, 2010]. In particular, if N is odd W is a $(N + 1) \times (N + 1)$ matrix[1] with matrix elements

$$W_{ij} = \begin{cases} 0 & i = j \\ \frac{1}{z_i - z_j} & i, j < N + 1 \\ 1 & i = N + 1, j \leq N \\ -1 & j = N + 1, i \leq N . \end{cases} \tag{4.3}$$

---

[1] Note that $N + 1$ is even when N is odd, as required to have a non-vanishing Pfaffian.

Note that in this way the Pfaffian appearing in Eq. (4.1) is replaced by a sum over N Pfaffians, where each Pfaffian depends only on $N-1$ particle coordinates.

As discussed for instance in Nayak et al. [2008] and in Tong [2016], for even (odd) values of the positive integer M, the above wave function represents a fermionic (bosonic) FQH state at filling $\nu = 1/M$, which belongs to the LLL. Note that, due to the presence of the Pfaffian factor (which is anti-symmetric), the relation between the parity of M and the global symmetry of the wave function is the opposite of the one of the Laughlin state. The wave function in Eq. (4.1) is indeed globally anti-symmetric (symmetric) when M is even (odd).

The Moore-Read is the exact ground state for 2D particles, in the presence of a magnetic (or synthetic) field and of a specific three-body repulsion [Greiter et al., 1991]. For instance, for the bosonic $M = 1$ wave function in Eq. (4.1) does not vanish when two particles coincide, but it vanishes when three particles are on top of each other. As a consequence, by following the same reasoning done for the Laughlin state, the $M = 1$ Moore-Read state will be the zero-energy ground state of the three-body Hamiltonian

$$H_{3B} = A \sum_{i<j<k} \delta^{(2)}(z_i - z_j)\,\delta^{(2)}(z_i - z_k), \tag{4.4}$$

independently on the interaction strength A. Similar toy Hamiltonians can be constructed for the other values of M, as discussed for example discussions by Greiter et al. [1992] and by Rezayi and Haldane [2000].

For the particular case of $M = 2$, the state described by Eq. (4.1) is also believed to be in the same universality class of the FQH state observed at filling $\nu = 5/2$ [Greiter et al., 1992, Morf, 1998, Rezayi and Haldane, 2000]. Note that the Moore-Read state with $M = 2$ is only one among the possible candidates to describe the FQH state observed at filling $\nu = 5/2$ [Ma and Feldman, 2019a]. Other possibilities include its particle-hole conjugate, named anti-Pfaffian state [Lee et al., 2007, Levin et al., 2007], the so-called particle-hole Pfaffian (PH-Pfaffian) introduced by Son [2015], and the possibility of having a state microscopically composed of domains made of Pfaffian and anti-Pfaffian states [Mross et al., 2018, Wang et al., 2018b]. Although a recent experiment by Banerjee et al. [2018] seems to rule out the two major candidates for the description of the $\nu = 5/2$ FQH state (i.e., the Pfaffian and the anti-Pfaffian states), the interpretation of the results of such an experiment is still matter of an intense debate [Simon, 2018a, Feldman, 2018, Simon, 2018b, Ma and Feldman, 2019b,a, Simon et al., 2019].

While the fermionic ($M = 2$) version of the wave function in Eq. (4.1) is mainly relevant in the context of 2DEGs in the FQH regime, its bosonic ($M = 1$) counterpart might occur for instance when neutral atoms are placed in rapidly rotating traps [Wilkin and Gunn, 2000, Cooper et al., 2001, Rezayi et al., 2005].

Another interesting feature of the Moore-Read wave function is that it represents the quantum Hall analog of a $p_x + ip_y$ superconductor, where vortices hosting non-Abelian anyons, known as Majorana zero modes, can exist [Read and Green, 2000, Ivanov, 2001]. The relation between these two states can be explained through the introduction of new effective degrees of freedom: the composite fermions (CFs) proposed by Jain [2007]. However, this goes far beyond the aim of this Thesis and therefore we invite the interested reader to look at the paper by Read and Green [2000] or at the review by Tong [2016].

4.2 Moore-Read's quasiholes: Abelian vs non-Abelian

The $M = 2$ fermionic Moore-Read state can host QH excitations which charge $e/4$, in addition to those with charge $e/2$ which are present also in the $M = 2$ bosonic Laughlin state. These excitations, not only have different charges, but they behave in a complete different way from the statistical point of view: $e/4$ QHs are believed to be non-Abelian anyons [Moore and Read, 1991, Nayak and Wilczek, 1996, Nayak et al., 2008], while $e/2$ QHs are believed to behave as Abelian anyons, exactly as those of the Laughlin state. To be precise, the $e/4$ QHs have been predicted to be Ising anyons, with an additional Abelian contribution to their braiding phase, and as such they can fuse in two different ways [see Sec.1.2]. Furthermore, for a given set of coordinates $(\eta_1, \ldots, \eta_{2n})$ of $2n$ such QHs, there is a 2^{n-1}-fold degenerate set of ground states Nayak and Wilczek [1996].

Another peculiarity of $e/4$ QHs is that they can be created only in pairs if one works on a closed manifold (e.g., on the sphere or on the torus). A single QHs with charge $e/4$ can be created

in MR states lying on open manifolds (e.g., on a disk), instead, but this induces a strong change in the edge properties of the cloud [Wen, 1995, Milovanović and Read, 1996, Wan et al., 2006, 2008].

All the above arguments can be extended to the bosonic case ($M = 1$), where Abelian and non-Abelian QHs have different "charges" with respect to their counterparts in the fermionic case[2]. To be precise the Abelian QHs correspond to the depletion of an entire particle, while the non-Abelian ones to the depletion of half of a particle. However, for the sake of simplicity, we will continue to denote them as $e/4$ and $e/2$ QHs, to distinguish the two kinds of excitations. Nevertheless all the general expressions such as wave functions, statistical phases and so on, will be written as functions of the M parameter.

4.2.1 Two Moore-Read quasiholes

Similarly to what happens for the Laughlin state, the wave function for the Moore-Read state hosting n QHs with charge $e/2$ at positions $\eta_1, \ldots, \eta_n$ can be easily constructed by multiplying the one in Eq. (4.1) by a global prefactor. In particular

$$
\begin{aligned}
\Psi_{n\mathrm{QH}}^{e/2}(\eta; z) &= \prod_{\mu=1}^{n} \prod_{i=1}^{N} (\eta_\mu - z_i) \, \Psi_{\mathrm{MR}}(z) \\
&= \prod_{\mu=1}^{n} \prod_{i=1}^{N} (\eta_\mu - z_i) \left[\mathrm{Pf}\left(\frac{1}{z_i - z_j}\right) \prod_{i<j} (z_i - z_j)^M \, e^{-\sum_i |z_i|^2/4l_B^2} \right],
\end{aligned}
\tag{4.5}
$$

which for $n = 2$ QHs reduces to

$$
\begin{aligned}
\Psi_{2\mathrm{QH}}^{e/2}(\eta; z) &= \prod_{i=1}^{N} (\eta_1 - z_i) \prod_{i=1}^{N} (\eta_2 - z_i) \, \Psi_{\mathrm{MR}}(z) \\
&= \prod_{i=1}^{N} (\eta_1 - z_i)(\eta_2 - z_i) \left[\mathrm{Pf}\left(\frac{1}{z_i - z_j}\right) \prod_{i<j} (z_i - z_j)^M \, e^{-\sum_i |z_i|^2/4l_B^2} \right].
\end{aligned}
\tag{4.6}
$$

From the above expressions it is easy to see that the overall prefactor, taking into account for the presence of the Abelian QHs, implies a vanishing particle density in correspondence with the QH positions η_μ.

Regarding the wave function describing the states with two $e/4$ quasiholes at positions η_1, η_2, it can not be obtained by simply multiplying the one for the Moore-Read state by an overall prefactor and we have to a change the Pfaffian factor, instead. To be precise such a wave function reads

$$
\boxed{\Psi_{2\mathrm{QH}}^{e/4}(\eta; z) = \mathrm{Pf}\left(\frac{(\eta_1 - z_i)(\eta_2 - z_j) + (i \leftrightarrow j)}{z_i - z_j}\right) \prod_{i<j} (z_i - z_j)^M \, e^{-\sum_i |z_i|^2/4l_B^2}.}
\tag{4.7}
$$

Similarly to the Moore-Read wave function in Eq. (4.1), also the above wave function can be generalized in order to describe states with an odd number of particles, as discussed in Baraban [2010]. As we will see in the following, the parity P_N of the particle number is a crucial quantity in the case of two non-Abelian QHs, as it strongly affects the QH statistical properties. Therefore, we explicitly report here the general expression for the wave function describing the Moore-Read state with two $e/4$ QHs:

$$
\boxed{\Psi_{2\mathrm{QH}}^{e/4}(\eta; z) = \mathrm{Pf}(W) \prod_{i<j} (z_i - z_j)^M \, e^{-\sum_i |z_i|^2/4l_B^2},}
\tag{4.8}
$$

where the form of the anti-symmetric matrix W depends on the parity P_N of the particle number. If $P_N = 0$ (N even), W is a $N \times N$ matrix with

$$
W_{ij} = \begin{cases} 0 & i = j \\ \frac{(\eta_1 - z_i)(\eta_2 - z_j) + (i \leftrightarrow j)}{z_i - z_j} & i \neq j, \end{cases}
\tag{4.9}
$$

---

[2]We would like to recall that bosonic fractional quantum Hall states are typically made of neutral constituent. Thus in this context with quasihole "charge" we indicate the amount of density depleted by the such an excitation.

while if $P_N = 1$ (N odd), W is a $(N+1) \times (N+1)$ matrix with

$$
W_{ij} = \begin{cases} 0 & i = j \\ \frac{(\eta_1 - z_i)(\eta_2 - z_j) + (i \leftrightarrow j)}{z_i - z_j} & i, j < N + 1 \\ 1 & i = N+1, j \le N \\ -1 & j = N+1, i \le N . \end{cases} \tag{4.10}
$$

4.2.2 Are states with two non-Abelian quasiholes interesting?

As we mentioned above, in the presence of $2n$ $e/4$ QHs, there is 2^{n-1}-fold degenerate set of ground states. Therefore, one may think that the case of $2n = 2$ non-Abelian QHs is trivial and not interesting, since the non-Abelian properties of such excitations manifest themselves when the ground state is degenerate, i.e., for $n \ge 2$. However, this is not totally true. It has been shown indeed that for a Moore-Read state with two non-Abelian QHs, the effect of the QH braiding (or exchange) depends on the parity of the particle number N [Bonderson et al., 2011, Baraban et al., 2009]. This is due to the fact that for even values of N, all the particles in the Moore-Read state are paired, and the QHs are expected to be in the $\mathbb{1}$ fusion channel. For N odd instead, one of the particles cannot pair, and so it exists as an excitation which is shared between the two QHs, which will be in the ψ fusion channel. As a consequence the braiding phase for two non-Abelian Moore-Read QHs depends on the parity P_N:

$$
\boxed{\frac{\varphi_{\mathrm{br}}}{2\pi} = \frac{1}{4M} - \frac{1}{8} + \frac{P_N}{2}} . \tag{4.11}
$$

The dependence of φ_{br} on P_N is thus an indirect signature on the non-Abelian nature of the $e/4$ QHs. The above discussion clearly explains why systems with just two non-Abelian QHs, and so with a non-degenerate ground state, are interesting. However, the importance of studying simple configurations with two anyons goes beyond the possibility to identify multiple fusion channels.

As discussed in Nayak et al. [2008] and in Baraban et al. [2009], in order for topological schemes for quantum computation to be scalable (i.e., to be applicable also to large scale quantum computation), three conditions must be satisfied:

(i) The energy splitting between the states belonging to the ground-state manifold must converge to zero at least as fast as e^{-R/ξ_E}, where R is the minimum distance between anyons.

(ii) As anyons are moved apart from each other, the unitary transformation $\mathcal{U}$ that results from adiabatic braiding of the anyons must converge to its asymptotic limit at least as fast as $e^{-R/\xi_{\mathcal{U}}}$.

(iii) One must be able to measure the topological quantum number associated with a group of anyons.

Two non-Abelian QHs are thus enough to check condition (ii). By looking at the behavior of the QH braiding phase, as a function of the spatial separation between the QHs, one can indeed inspect its convergence properties and also estimate the typical decay length $\xi_{\mathcal{U}}$, as done by Baraban et al. [2009].

The study of the braiding properties of two non-Abelian QHs can be also employed to identify the topological order characterizing the state hosting the anyons. For instance, it could be used to distinguish the Moore-Read and the anti-Pfaffian state, whose QHs have different Abelian contributions to the braiding phase as discussed in Lee et al. [2007] and in Levin et al. [2007].

In this section we have presented several reasons why one should look at states hosting just two non-Abelian QHs. Among them there is the possibility of detecting the existence of multiple fusion channels for QH excitations of the Moore-Read state. This is exactly what we will do in Sec. 7.3.2, where we will prove that the non-Abelian nature of these excitations can be probed through simple density-profile measurements.

4.2.3 Four non-Abelian quasiholes

Similarly to what has been done for the wave function in Eq. (4.7), one can construct (from conformal field theory arguments) the wave function for an arbitrary number of non-Abelian QHs [Moore and Read, 1991, Nayak and Wilczek, 1996].

For the particular case of four QHs, the wave function is given by

$$\Psi_{(ab)(cd)}(\eta; z) = \mathrm{Pf}\left(\frac{(\eta_a - z_i)(\eta_b - z_i)(\eta_c - z_j)(\eta_d - z_j) + (i \leftrightarrow j)}{z_i - z_j}\right) \prod_{i<j}(z_i - z_j)^M e^{-\sum_i |z_i|^2/4l_B^2}$$
(4.12)

Note that there are three different possibilities in which we can choose the couples (ab) and (cd) out of $1, 2, 3$ and 4 to obtain a different $\Psi_{(ab)(cd)}$. This means that the wave functions $\Psi_{(13)(24)}$, $\Psi_{(14)(23)}$ and $\Psi_{(12)(34)}$ are all equally valid. Nevertheless, in Nayak and Wilczek [1996] and in Read and Rezayi [1999] it has been proved that only two of them are linearly independent, recovering in this way the predicted 2^{n-1}-fold degeneracy of the ground states.

Although the states $\Psi_{(13)(24)}$ and $\Psi_{(14)(23)}$ form a basis of the two-dimensional ground state-manifold for a given set QH coordinates $(\eta_1, \eta_2, \eta_3, \eta_4)$, they are not orthogonal. Among the different orthonormal states one can construct, those which are usually found in literature are

$$\Psi_0(\eta; z) = \prod_{\mu<\nu}^{4} \eta_{\mu\nu}^{\frac{1}{4M}-\frac{1}{8}} \frac{(\eta_{13}\,\eta_{24})^{1/4}}{\sqrt{1+\sqrt{1-x}}} \left[\Psi_{(13)(24)}(\eta; z) + \sqrt{1-x}\,\Psi_{(14)(23)}(\eta; z)\right] e^{-\frac{1}{8M}\sum_{\mu=1}^{4}|\eta_\mu|^2},$$
(4.13)

$$\Psi_1(\eta; z) = \prod_{\mu<\nu}^{4} \eta_{\mu\nu}^{\frac{1}{4M}-\frac{1}{8}} \frac{(\eta_{13}\,\eta_{24})^{1/4}}{\sqrt{1-\sqrt{1-x}}} \left[\Psi_{(13)(24)}(\eta; z) - \sqrt{1-x}\,\Psi_{(14)(23)}(\eta; z)\right] e^{-\frac{1}{8M}\sum_{\mu=1}^{4}|\eta_\mu|^2},$$
(4.14)

where

$$\eta_{\mu\nu} = \eta_\mu - \eta_\nu \qquad \text{and} \qquad x = \frac{\eta_{12}\,\eta_{34}}{\eta_{13}\,\eta_{24}} = \frac{(\eta_1 - \eta_2)(\eta_3 - \eta_4)}{(\eta_1 - \eta_3)(\eta_2 - \eta_4)}.$$
(4.15)

States Ψ_0 and Ψ_1 are such that they transform into one another upon braiding η_2 and η_3, as explicitly demonstrated in Baraban [2010]. Furthermore, in the states Ψ_0 and Ψ_1, the QHs at η_1 and η_2 (and of course also those at η_3 and η_4) are in the $\mathbb{1}$ and ψ fusion channels, respectively [Bonderson et al., 2011, Baraban, 2010].

The effect of exchanging two QHs on the wave functions Ψ_0 and Ψ_1 has been explicitly computed in Bonderson et al. [2011]. Although, from a conceptual point of view the calculation done by Bonderson et al. [2011] is the same done by Arovas et al. [1984] for the Laughlin QHs [see Sec. 3.4], the more complex structure of the wave functions Ψ_0 and Ψ_1 and the presence of a degenerate ground-state manifold have made it much more demanding[3]. Nevertheless, Bonderson and co-authors have shown that the geometrical contribution coming from the Berry matrix $\mathcal{U}_B$ is simply the (non-topological) Aharonov-Bohm contribution due to the QH motion, while the statical properties of the QHs are fully encoded in analytic continuation matrices $\tilde{\mathcal{B}}_{\alpha\beta} = \langle\psi_\alpha(\eta_\mu(0))|\psi_\beta(\eta_\mu(T))\rangle$. If we denote with $\eta_a \rightleftarrows \eta_b$ the counterclockwise exchange of QHs at positions η_a and η_b, its effect on the the wave functions Ψ_0 and Ψ_1 defined in Eqs. (4.13) and (4.14) is

$$\eta_1 \rightleftarrows \eta_2 \quad \text{or} \quad \eta_3 \rightleftarrows \eta_4 : \quad \begin{aligned} \Psi_0 &\mapsto e^{i\pi(\frac{1}{4M}-\frac{1}{8})}\Psi_0 \\ \Psi_1 &\mapsto e^{i\pi(\frac{1}{4M}-\frac{1}{8})}i\,\Psi_1, \end{aligned}$$
(4.16)

$$\eta_2 \rightleftarrows \eta_3 \quad \text{or} \quad \eta_1 \rightleftarrows \eta_4 : \quad \begin{aligned} \Psi_0 &\mapsto e^{i\pi(\frac{1}{4M}+\frac{1}{8})}\frac{\Psi_0 - i\Psi_1}{\sqrt{2}} \\ \Psi_1 &\mapsto e^{i\pi(\frac{1}{4M}+\frac{1}{8})}\frac{-i\Psi_0 + \Psi_1}{\sqrt{2}}, \end{aligned}$$
(4.17)

$$\eta_1 \rightleftarrows \eta_3 \quad \text{or} \quad \eta_2 \rightleftarrows \eta_4 : \quad \begin{aligned} \Psi_0 &\mapsto e^{i\pi(\frac{1}{4M}+\frac{1}{8})}\frac{\Psi_0 + \Psi_1}{\sqrt{2}} \\ \Psi_1 &\mapsto e^{i\pi(\frac{1}{4M}+\frac{1}{8})}\frac{-\Psi_0 + \Psi_1}{\sqrt{2}}, \end{aligned}$$
(4.18)

---

[3]Suffice is to say that such a calculation has required the mapping of the Pfaffians terms entering in the overlap $\langle\Psi_\alpha|\Psi_\beta\rangle$ onto the Boltman factor of a two-component plasma with exotic interactions.

implying the following adiabatic continuation matrices

$$
\tilde{\mathcal{B}}^{(1 \rightleftarrows 2)} = \tilde{\mathcal{B}}^{(3 \rightleftarrows 4)} = e^{i\pi(\frac{1}{4M} - \frac{1}{8})} \begin{bmatrix} 1 & 0 \\ 0 & i \end{bmatrix},
$$

$$
\tilde{\mathcal{B}}^{(2 \rightleftarrows 3)} = \tilde{\mathcal{B}}^{(1 \rightleftarrows 4)} = \frac{e^{i\pi(\frac{1}{4M} + \frac{1}{8})}}{\sqrt{2}} \begin{bmatrix} 1 & -i \\ -i & 1 \end{bmatrix}, \tag{4.19}
$$

$$
\tilde{\mathcal{B}}^{(1 \rightleftarrows 3)} = \tilde{\mathcal{B}}^{(2 \rightleftarrows 4)} = \frac{e^{i\pi(\frac{1}{4M} + \frac{1}{8})}}{\sqrt{2}} \begin{bmatrix} 1 & -1 \\ 1 & 1 \end{bmatrix}.
$$

Before moving on, we would like to stress that these results strongly depend on the specific choice of the basis states spanning the ground-state manifold during the adiabatic process. Along this line, in Sec. 7.1 we will show that, by means of a suitable basis choice, one can move the Abelian part of the QH anyonic statistics to the Berry matrix and even link it to observable quantities.

To conclude, we comment about the possibility of building suitable wave functions for states presenting $2n$ QHs [Tong, 2016]. To do that one has first to divide the QHs into two groups, let say $(\eta_1, \ldots, \eta_n)$ and $(\eta_{n+1}, \ldots, \eta_{2n})$. Then the wave function will have the same form as that in Eq. (4.12), but with a different Pfaffian, i.e.

$$
\mathrm{Pf} \left(\frac{(\eta_1 - z_i)(\eta_2 - z_i) \ldots (\eta_n - z_i)(\eta_{n+1} - z_j)(\eta_{n+2} - z_j) \ldots (\eta_{2n} - z_j) + (i \leftrightarrow j)}{z_i - z_j} \right). \tag{4.20}
$$

Of course this wave function again depends of our particular choice for the splitting of the QHs into the two groups. The number of different ways in which one can split $2n$ QHs into two group of n each is given by

$$
\frac{1}{2} \frac{2n!}{n!n!}. \tag{4.21}
$$

However, as it happened for the case of four QHs, not all the different wave functions we can construct are linearly independent. The number of the linearly independent ones it has been proved to be [Nayak and Wilczek, 1996]

$$
2^{n-1}, \tag{4.22}
$$

as we mentioned at the beginning of this section.

Chapter 5

Jack polynomial formalism.

$\mathcal{A}$s we have seen in the previous Chapters, many of the exotic properties characterizing the fractional quantum Hall effect can be understood by means of suitably constructed ansatz wave functions. Among these wave functions, those describing states in the lowest Landau level are particularly simple to write down due to the analyticity constraint discussed in Chapter 2. However, despite their explicit availability, they still remain very difficult to handle, especially because of the intractability of their polynomial term.

At this point we would like to emphasize the ironic situation characterizing the fractional quantum Hall effect: While in most quantum many-body problems one can not even dream to find an approximated expression for the wave function of the system ground-state, in the fractional quantum Hall context one can do that and the obtained wave functions can even be exact in some situations [see for instance the discussion in Sec. 3.1]. However, they are so strongly-correlated that one can not use them to calculate correlation functions or many other interesting observables.

This peculiar (and frustrating) problem pushed physicists to look closely at the polynomials entering in the fractional quantum Hall wave functions, and led to the development of the so-called Jack polynomials formalism [Bernevig and Haldane, 2008a,b,c, Bernevig and Regnault, 2009, Thomale et al., 2011]. The introduction of Jack polynomials in the fractional quantum Hall context has been a real breakthrough, especially from the numerical point of view. They indeed allow one to efficiently express most of the fractional quantum Hall ansatz wave functions in the so-called occupation number basis, i.e. as linear combinations of states obtained by filling the different lowest Landau level single-particle wave functions, making them much more easy to treat.

Here we shall review the main features of Jack polynomials and especially those that will be used in Chapter 6 to interpret the energy spectra of $\nu = 1/2$ bosonic FQH droplets experiencing particular external potentials, confining them in disk-shaped and ring-shaped geometries.

Part of the Jack polynomial formalism which we present in the following to describe the edge excitations of a Laughlin droplet has been published in Macaluso and Carusotto [2017] and in Macaluso and Carusotto [2018]. The other results reported in these works will be the subject of Chapter 6, instead.

5.1 Jack polynomials and fractional quantum Hall states

In general, Jack polynomials (or simply Jacks) J_λ^α are homogeneous symmetric polynomials identified by a rational parameter α, called Jack parameter, and by a root partition λ. Here, by partition we mean a non-growing sequence of positive integers, $\lambda = [\lambda_1, \lambda_2, \ldots]$, so that the sum of the integers in the sequence corresponds to the number that gets partitioned. The degree of the Jack is given by this number, indicated by $|\lambda|$. Furthermore, Jacks have been found to exhibit clustering properties [Bernevig and Haldane, 2008a] and also to correspond to some of the polynomial

solution of the so-called Laplace-Beltrami operator [Stanley, 1989]:

$$H_{\mathrm{LB}}^{\alpha} = \sum_i (z_i \partial_i)^2 + \frac{1}{\alpha} \sum_{i<j} \frac{z_i + z_j}{z_i - z_j} (z_i \partial_i - z_j \partial_j), \tag{5.1}$$

where we introduced $\partial_i \equiv \partial/\partial z_i$.

Partitions of length P can be biunivocally associated to symmetrized monomials in $N \geq P$ variables in the following way: the partition $[\lambda_1, \lambda_2, \lambda_3, \ldots, \lambda_P]$ corresponds to the monomial $\mathrm{Sym}(z_1^{\lambda_1} z_2^{\lambda_2} z_3^{\lambda_3} \ldots z_P^{\lambda_P})$ where all other variables $z_{P+1} \ldots z_N$ appear with degree 0. For example, the partition $[4, 2, 2, 1]$ corresponds to the symmetrized monomial $\mathcal{M}_{[4,2,2,1]} \equiv \mathrm{Sym}(z_1^4 z_2^2 z_3^2 z_4^1)$. In this perspective, Jacks have a peculiar expansion in terms of symmetrized monomials $\mathcal{M}_\mu$'s:

$$\boxed{J_\lambda^\alpha = \mathcal{M}_\lambda + \sum_{\mu \succ \lambda} c_{\lambda\mu}(\alpha) \, \mathcal{M}_\mu}, \tag{5.2}$$

where μ runs over all partitions that can be obtained from the root partition λ through all possible sequences of squeezing operations, as explained in Bernevig and Haldane [2008a,b]. Under such an operation, one starts from a parent partition $[\ldots, \lambda_i, \ldots, \lambda_j, \ldots]$ to generate another one (called descendant) given by $[\ldots, \lambda_i - \delta m, \ldots, \lambda_j + \delta m, \ldots]$, with $\lambda_i - \delta m \geq \lambda_j + \delta m$. The corresponding coefficients $c_{\lambda\mu}(\alpha)$ instead can be computed by means of a recursive construction algorithm [Dumitriu et al., 2007, Thomale et al., 2011].

Jack polynomials with negative α appear in the theory of the quantum Hall effect. In this context the admissible root configurations are given by some of the so-called (k, r) admissible root configurations. The (k, r) admissibility condition means that there can not be more than k particles into r consecutive orbitals. In particular the bosonic Read-Rezayi k series of states has been proven to be given by single Jacks of parameter $\alpha = -(k+1)/(r-1)$ and suitable root partition, as discussed in Bernevig and Haldane [2008a,b]. Note that, among these bosonic FQH states there are both the $\nu = 1/2$ Laughlin state, for which $(k = 1, r = 2)$ and $\alpha = -2$, and the $\nu = 1$ Moore-Read state, for which $(k = 2, r = 2)$ and $\alpha = -3$. For these two particular examples the root partitions are given by $\Omega = [2N - 2, 2N - 4, \ldots, 2]$ and $\Lambda = [N - 2, N - 2, N - 4, N - 4, \ldots, 2, 2]$, respectively, and the corresponding root configurations are $\mathcal{M}_\Omega \equiv |1\,0\,1\,0 \ldots 1\,0\,1\rangle$ and $\mathcal{M}_\Lambda \equiv |2\,0\,2\,0 \ldots 2\,0\,2\rangle$. This is easy to prove for the Laughlin state (with a small number of particles): one has only to expand $\prod_{i<j}(z_i - z_j)^2$ and check that the obtained expansion is exactly the one in Eq. (5.2) with root partition Ω, as explicitly done by He et al. [2015] for instance. Thus, from the knowledge of the Jack parameter α and of the root configuration $\mathcal{M}_\lambda$, one can construct the associated FQH state by simply applying the proper squeezing operations and the recursive formula for the coefficients.

To better understand this relation between Jacks and LLL wave functions, it is useful to establish a link between a partition and a distribution of particles among the different LLL orbitals. By neglecting the ubiquitous Gaussian factor and the normalization constant, each LLL single-particle wave function of angular momentum m corresponds to a monomial z^m [see Eq. (2.35)]. So, any bosonic many-particle state $|n_0, n_1, n_2, \ldots\rangle$, obtained by occupying each LLL wave function of angular momentum m with a well-defined number n_m particles, can be described as a symmetrized monomial $\mathcal{M}_\lambda$, where $\lambda \equiv [\lambda_1, \lambda_2, \ldots]$ is a sequence of positive integers (i.e., a partition) which indicates the LLL wave functions occupied by the different particles in descending order. For example, states of $N \geq 4$ particles having one particle in the $m = 4$ orbital, two in the $m = 2$ orbital, one in the $m = 1$ orbital and the remaining in the $m = 0$ orbital can be written as $|N - 4, 1, 2, 0, 1\rangle = \mathrm{Sym}(z_1^4 z_2^2 z_3^2 z_4^1) \equiv \mathcal{M}_{[4,2,2,1]}$.

As a consequence of this connection between monomials and many-body states obtained by filling the different LLL wave functions, all rotationally symmetric states of the form

$$|\psi\rangle = \sum_i c_i \, |n_0, n_1, n_2, \ldots\rangle_i, \tag{5.3}$$

correspond to homogeneous symmetric polynomials in the particle coordinates of degree given by the eigenvalue of the angular momentum operator

$$L = \sum_m m \, \bar{n}_m, \tag{5.4}$$

with $\bar{n}_m = \langle \psi | \hat{a}_m^\dagger \hat{a}_m | \psi \rangle$.

At this point it is worth mentioning that a similar formalism exists also for fermionic fractional quantum Hall states, where each single particle wave function can host at most one particle ($n_m = 0, 1$) and the total many-body wave function must be globally anti-symmetric [Thomale et al., 2011]. For instance, the $\nu = 1/3$ fermionic Laughlin state has Jack parameter $\alpha = -2$ and root configuration $|1\,0\,0\,1\,0\,0\ldots 1\,0\,0\,1\rangle$, while the fermionic $\nu = 1/2$ Moore-Read state has $\alpha = -3$ and root configuration $|1\,1\,0\,0\,1\,1\,0\,0\ldots 1\,1\,0\,0\,1\,1\rangle$.

5.2 Jack polynomials for the excitations of the Laughlin state

We have already seen that Jack polynomials provide an efficient way to construct the Laughlin state. In the following we show that they can be also used to describe some of the excitations of such a state, and in particular those with wave functions of the form

$$\psi(z) = S(z)\,\Psi_{\mathrm{L}}(z), \tag{5.5}$$

where $\Psi_{\mathrm{L}}(z)$ is the $\nu = 1/2$ bosonic Laughlin wave function [1] and $S(z)$ is again a generic homogeneous symmetric polynomial in the particle coordinates, whose degree gives the additional angular momentum $\Delta L = L - L_{\mathrm{L}}$, with respect to the one of the Laughlin state $L_{\mathrm{L}} = N(N-1)$. As we have seen in Sec. 3.3, since $S(z)$ is a homogeneous symmetric polynomial, also the wave functions in Eq. (5.5) with $S(z) \neq 1$ represent eigenstates of the angular momentum operator with eigenvalue L.

For low additional angular momenta ($\Delta L \ll N$) the wave functions in Eq. (5.5) describe area-preserving shape deformations of the FQH liquid [Cazalilla, 2003, Cazalilla et al., 2005], which we will call outer-edge excitations (OEEs). Another particular class of states whose wave functions can be written in this form are the QH excitations[2]. While a Laughlin state hosting κ QHs at generic positions $(\eta_1, \ldots, \eta_\kappa)$ can be described by the wave function in Eq. (3.39), in the following we will restrict our attention to the cylindrically symmetric case where all QHs are located at the center of the FQH droplet, i.e. $\eta_1 = \cdots = \eta_\kappa = 0$:

$$\Psi_{\kappa \mathrm{QH}}(\eta = 0; z) = \prod_i z_i^\kappa\,\Psi_{\mathrm{L}}(z). \tag{5.6}$$

Finally, in the case of ring shaped FQH droplets one can have excitations living both on the inner and on the outer edge of the system. As we will see, also state presenting excitations of this kind can be described by wave functions of the form of Eq. (5.5) and, as a consequence, in terms of Jacks.

5.2.1 Jack polynomials for the edge excitations

In general, an excited stated described by Eq. (5.5) can not be expressed as a single Jack polynomial J_λ^α with Jack parameter α and root partition λ, but can be written as a linear combination of a finite set of them [Lee et al., 2014]. In particular, any excited state with angular momentum $L = L_{\mathrm{L}} + \Delta L$ can be written as a linear combination of Jacks having Jack parameter $\alpha = -2$ and root partition λ, obtained by adding[3] to the root partition of the Laughlin state $\Omega = [2N - 2, 2N - 4, \ldots, 2]$ a generic partition $\gamma = [\gamma_1, \gamma_2, \ldots]$, called edge partition (EP), of the additional angular momentum ΔL, namely

$$\boxed{\lambda = \Omega + \gamma}, \tag{5.7}$$

with $|\gamma| = \sum_i \gamma_i = \Delta L$ [see Fig. 5.1, left]. For reasons that will be clear in the following, we also assume that the length of the allowed EPs can not exceed the number of particles N in the system.

With this prescription for the admissible λ, it is easy to check that the associated Jack polynomials J_λ^α have total degree equal to $|\lambda| = |\Omega| + |\gamma| = L_{\mathrm{L}} + \Delta L = L$, and therefore any linear combination of them will be a wave function of total angular momentum $L = L_{\mathrm{L}} + \Delta L$, as required.

---

[1]Note that the analysis we report in this Chapter is focused on the excitations of the $\nu = 1/2$ Laughlin state. However, it can be generalized to other filling factors.

[2]Note that states presenting quasiparticle excitations can not be written as in Eq. (5.5).

[3]The sum of two partitions $\lambda = [\lambda_1, \ldots, \lambda_l]$ and $[\mu_1, \ldots, \mu_m]$ with $l \geq m$ is defined as a partition of length l whose elements are $\lambda + \mu = [\lambda_1 + \mu_1, \ldots, \lambda_m + \mu_m, \lambda_{m+1}, \ldots, \lambda_l]$. Generalization to $l < m$ cases is straightforward by requiring the commutativity of the partitions sum operation.
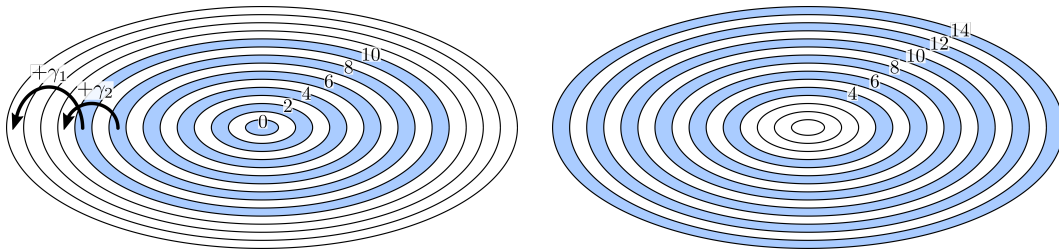

Figure 5.1: Left: Pictorial representation of the root configuration for the $N = 6$ Laughlin state, i.e. $\mathcal{M}_{[10,8,6,4,2]} = |1\,0\,1\,0\,1\,0\,1\,0\,1\,0\,1\rangle$, where the $m = 0, 2, 4, 6, 8, 10$ orbitals are occupied by one particle (light-blue circles) while all the other are empty (white circles). Arrows show instead how to obtain the configuration corresponding to $\lambda = \Omega + \gamma = [10, 8, 6, 4, 2] + [4, 3]$, by moving the particles occupying the outermost orbitals. Right: Pictorial representation of the root configuration for the $\kappa = 4$ quasihole state, i.e. $\mathcal{M}_{[14,12,10,8,6,4]} = |0\,0\,0\,0\,1\,0\,1\,0\,1\,0\,1\,0\,1\,0\,1\rangle$, where the $m = 4, 6, 8, 10, 12, 14$ orbitals are occupied by one particle while the four inner orbitals ($m = 0, 1, 2, 3$) are empty. Note that the root partition for the 4-QH state can be expressed as $\lambda = \Omega + \sigma^4 = [10, 8, 6, 4, 2] + [4, 4, 4, 4, 4, 4]$.

Furthermore, this choice for the possible EPs γ is in agreement with the edge-state degeneracy predicted by the chiral Luttinger liquid theory proposed by Wen [1992] [see Sec. 3.3].

In terms of configurations, the addition of an EP γ to the Laughlin root partition Ω then corresponds to moving particles in the outermost occupied orbitals to even higher m orbitals. In particular, given a generic EP $\gamma = [\gamma_1, \gamma_2, \dots]$, the configuration corresponding to $\lambda = \Omega + \gamma$ is the one in which the particle occupying the outermost occupied orbital of the Laughlin root configuration, say, the m_1 orbital, is promoted to the $m_1 + \gamma_1$ orbital, the particle occupying the second outermost occupied orbital m_2 is promoted to the $m_2 + \gamma_2$ orbital, and so on [see Fig. 5.1, left]. This interpretation gives a transparent physical explanation of the restriction that needs to be imposed on the length of the EP γ: No more than N different particles can in fact be moved in an N-particle system.

While Jacks are labeled by their root partition λ, it is important to stress that they do not coincide with the corresponding configuration. They contain contributions also from all the other configurations that can be obtained from the root one by means of the aforementioned squeezing operations [Bernevig and Haldane, 2008a,b]. In this respect, the work by Lee et al. [2014] pointed out an interesting relation between the Hilbert spaces spanned by the configurations contributing to different Jacks J_λ^α, known as squeezed Hilbert spaces $\mathcal{H}_{sq}(\lambda)$. They observed that the dominance order $\lambda \succeq \mu$ [4] between two root partitions λ and μ of the same integer number $L = L_L + \Delta L$ implies the relation

$$\boxed{\mathcal{H}_{sq}(\lambda) \subseteq \mathcal{H}_{sq}(\mu)} \tag{5.8}$$

between the squeezed Hilbert spaces associated with the two different partitions.

As a consequence, since for any value of the additional angular momentum ΔL the partition $\lambda_{\Delta L} = \Omega + [\Delta L]$ dominates all the other admissible root partitions obtained as $\Omega + \gamma$ with $|\gamma| = \Delta L$ [Lee et al., 2014], all possible excited states in Eq. (5.5), with additional angular momentum ΔL, exist in the squeezed Hilbert space $\mathcal{H}_{sq}(\lambda_{\Delta L})$. Note that the root configuration associated with $\lambda_{\Delta L}$ can be obtained from the Laughlin one by promoting the particle in the outermost occupied orbital m to the $m + \Delta L$ orbital.

Initially the interest in Jack polynomials in the context of FQH edge states was mainly motivated by this last result, which has been used for instance in Lee et al. [2014] and in Jiang and Hu [2016] as a tool for numerical calculations.

Later on, we observed in Macaluso and Carusotto [2017] and in Macaluso and Carusotto [2018] (together with Fern and Simon [2017]) that the low energy eigenstates (that is, the ones below the Laughlin gap) of disk-shaped and ring-shaped $\nu = 1/r$ Abelian FQH liquids confined by hard-wall potentials can be fully interpreted in terms of the Jacks and the EPs presented in this section. This analysis will the subject of Chapter 6.

---

[4]Given two partitions λ and μ, we say that μ is dominated by λ or, symbolically, that $\mu \succeq \lambda$ if $\sum_{i=1}^{j} \lambda_i \geq \sum_{i=1}^{j} \mu_i$ for every j.

5.2.2   Jack polynomials for the quasiholes excitations

We have just presented the general formalism for the description of FQH wave functions like those in Eq. (5.5) in terms of Jacks. Even though all ingredients to extend that formalism to excitations existing on both edges of a ring-shaped FQH liquid are implicitly present there, the consequences of dealing with such a shape are worth illustrating in more detail. In addition to the presence of two different edges with opposite chiralities, a ring-shaped FQH liquid has in general a macroscopic hole in the center of its density profile[5]. In the FQH context, the central region of vanishing density can be interpreted as a certain number of QHs sitting in the hole. Therefore, the starting point for the extension of the Jack polynomial formalism to the inner-edge excitations (IEEs) of a ring-shaped system cannot be the Laughlin state, but must be a κ-QH state, where all κ QHs are located at in the origin.

Such a state is described by a wave function of the form (5.5) [see Eq. 5.6] and it has an angular momentum $L_{\kappa\text{QH}} = L_{\text{L}} + \kappa N$. As a consequence, it will belong to the $\mathcal{H}_{\text{sq}}(\lambda_{\Delta L = \kappa N})$ squeezed Hilbert space. While in general a κ-QH wave function corresponds to a linear combination of Jacks, the wave function for the particular case in which all κ QHs are placed at the origin can be written as a single Jack of root configuration $|0^{\kappa}\,1\,0\,1\ldots1\,0\,1\rangle$ [Bernevig and Haldane, 2008c], where 0^{κ} denotes the κ empty orbitals from $m = 0$ to $m = \kappa - 1$.

This state can be obtained from the Laughlin state by promoting each particle from the m orbital to the $m + \kappa$ one. Correspondingly, its root partition can be written as

$$\boxed{\lambda = \Omega + \sigma^{\kappa}}\,, \tag{5.9}$$

where the κ-QH partition $\sigma^{\kappa} = [\kappa, \kappa, \ldots, \kappa]$ repeats the integer κ for N times. In this partition, the additional angular momentum $\Delta L = \kappa N$ is equally distributed among the N particles.

5.2.3   Jack polynomials for the inner-edge excitations

Excitations of the different edges of a ring-shaped FQH droplet have opposite chiralities. Therefore, since exciting the outer edge implies an increase of the total angular momentum, excitations of the inner edge will lead to a decrease of it. As a consequence, only states with total angular momenta $L > L_{\text{L}}$ can sustain excitations of this kind, which is in accord with the previous statement that the ground state of a ring-shaped FQH liquid will be reasonably given by QH wave functions like (5.6) having total angular momentum $L_{\kappa\text{QH}} = L_{\text{L}} + \kappa N > L_{\text{L}}$.

At this point we can easily extend the Jack polynomial formalism to κ-QH states presenting IEEs. These states will be characterized by total angular momenta of the form $L = L_{\kappa\text{QH}} - \Delta I$, where ΔI is the angular momentum associated with the IEE, in analogy with the discussion in Sec. 5.2.1 for the excitations of the outer edge. Therefore, one can think that the wave function describing a κ-QH state with an IEE of momentum ΔI can be obtained as a linear combination of Jacks having as the Jack parameter $\alpha = -2$ and as root partitions all those obtained by subtracting[6] from the root partition of the κ-QH state $\Omega + \sigma^{\kappa}$ any partition $\rho = [\rho_1, \rho_2, \ldots]$, which we will call inner-edge partition (IEP), of the IEE angular momentum ΔI, namely,

$$\boxed{\lambda = \Omega + \sigma^{\kappa} - \rho}\,. \tag{5.10}$$

In terms of configurations, this corresponds to an inward shift of the particles occupying the lowest m orbitals of the κ-QH state root configuration $|0^{\kappa}\,1\,0\,1\ldots1\,0\,1\rangle$. In addition to the constraint already mentioned for the γ EPs, whose maximum length is fixed by the number of particles N, the IEPs must satisfy the extra condition that the maximum value of their elements ρ_i is fixed by the number of QHs in the state hosting the IEE, i.e.,

$$\rho_1 \leq \kappa. \tag{5.11}$$

Note that, since partitions are defined as ordered sequences of positive integers, the constraint (5.11) actually imposes that $\rho_i \leq n$ for all i.

This constraint can be easily understood by looking at the root configuration of the κ-QH state, having the lowest κ orbitals empty [see Fig. 5.1, right]. Since the LLL wave functions in Eq. (2.35)

---

[5]In this context with the term "hole" we mean the physical hole present in the system and not an elementary excitation of this latter.

[6]The subtraction of two partitions $\lambda = [\lambda_1, \ldots, \lambda_l]$ and $[\mu_1, \ldots, \mu_m]$ with $l \geq m$ and $\lambda_l \geq \mu_1$ is defined as a partition of length l whose elements are $\lambda - \mu = [\lambda_1, \ldots, \lambda_{l-m}, \lambda_{l-m+1} - \mu_m, \ldots, \lambda_l - \mu_1]$.

---

are labeled by non-negative integers m, the lowest occupied orbital is the one with $m = \kappa$ and therefore by moving inwards a particle occupying such an orbital can reduce the total angular momentum at most by κ. These limitations on the IEPs ρ imply that, for a given value of ΔI, the number of IEEs of a ring-shaped FQH liquid depends on the dimension of the internal hole. To be precise, for an κ-QH state the number of different possible IEEs with angular momentum ΔI is the one predicted by the edge theory of single-branch chiral bosons only for $\Delta I \leq \kappa$.

Finally, the dominance relations between the root partitions in Eq. (5.10), for fixed values of κ and ΔI, can be obtained from those of the IEPs ρ. In particular, given two IEPs ρ and ρ' of ΔI such that $\rho \succeq \rho'$, the partitions $\lambda = \Omega + \sigma^\kappa - \rho$ and $\lambda' = \Omega + \sigma^\kappa - \rho'$ are related by $\lambda \succeq \lambda'$ and therefore $\mathcal{H}_{\mathrm{sq}}(\lambda) \subseteq \mathcal{H}_{\mathrm{sq}}(\lambda')$. Thus, for a fixed value of κ, all IEEs of momentum ΔI belong to $\mathcal{H}_{\mathrm{sq}}(\lambda_{-\Delta I})$, where $\lambda_{-\Delta I} = \Omega + \sigma^\kappa - [\Delta I]$.

5.2.4 Orthogonal and non-orthogonal Jacks

Before entering the discussion on how one can distinguish Jack polynomials describing states with excitations of different edges, there is a last point we have to clarify. It concerns the orthogonality properties of Jacks with root partitions $\lambda = \Omega + \gamma$.

Lee et al. [2014] have shown that Jacks with the EPs γ as their root partitions and Jacks with root partitions of the form $\lambda = \Omega + \gamma$ are related by

$$J^\alpha_{\Omega + \gamma} = J^\beta_\gamma \, J^\alpha_\Omega, \tag{5.12}$$

where, for the Laughlin state at filling $\nu = 1/r$, $\alpha = -2/(r-1)$, $\beta = 2/(r+1)$. Note that for $\nu = 1/2$ we have $\beta = 2/3$. This is consequence of the fact that the polynomial prefactor $S(z)$ entering in Eq. (5.5) can be expanded in terms of the Jacks of parameter $\beta = 2/3$ and partitions γ of the degree ΔL of $S(z)$.

Even though choosing $\beta = 2/3$ has the advantage of allowing us to express wave functions of the form $J^{2/3}_\gamma \Psi_{\mathrm{L}}(z)$ in terms of a single Jack polynomial $J^{-2}_{\Omega + \gamma} = J^{2/3}_\gamma \, J^{-2}_\Omega$, it has also a drawback: for different EPs γ the wave functions obtained in this way are not orthogonal.

This potential problem can be overcome by considering a different set of Jacks J^β_γ for the expansion of the prefactors $S(z)$ and in particular those with $\beta = \nu$, where we recall $\nu = 1/r$ to be the filling factor. As discussed for instance in Fern and Simon [2017], the Jacks J^ν_γ are orthogonal in the thermodynamic limit, i.e.

$$\langle J^\nu_\gamma | J^\nu_\mu \rangle = j_\mu(\nu) \, \delta_{\gamma,\mu} \quad \text{for} \quad N \to \infty \tag{5.13}$$

under the Laughlin scalar product

$$\langle \phi | \chi \rangle \equiv \int_{\mathbb{C}^N} \mathrm{d}z \, [\phi(z)]^* \chi(z) \, |\Psi_{\mathrm{L}}(z)|^2. \tag{5.14}$$

As a consequence, the wave functions associated with these Jacks, i.e. those of the form $J^\nu_\gamma \Psi_{\mathrm{L}}(z)$, will be also orthogonal in the limit $N \to \infty$. While the use of these Jacks J^ν_γ with parameter ν has the great advantage of leading to many-body wave functions which are orthogonal in the thermodynamic limit, its drawback is that these wave functions in general can not be written as single Jacks, as it instead happens for those with parameter $\beta = 2/(r+1)$ [see Eq. (5.12)].

In Chapter 6 we will make use of both kind of wave functions to interpret the result of our numerical exact diagonalization calculations. In particular we will show that, despite being non-orthogonal, Jack polynomials of the form $J^\alpha_{\Omega + \gamma}$ are extremely close to the eigenstates of the Hamiltonians describing ring-shaped and disk-shaped FQH liquids in the presence of hard-wall confinements.

5.3 How to distinguish excitations on different edges

To explicitly show that linear combinations of Jacks with Jack parameter $\alpha = -2$ and root partition λ defined in Eq. (5.10) describe the IEEs of an κ-QH state, in Macaluso and Carusotto [2018] we inspect the density profiles characterizing these Jacks. As an example, Fig. 5.2 a) reports the density profiles of the two admissible Jacks for $N = 6$, $\kappa = 3$, and $\Delta I = 2$, i.e. $J^{-2}_{[13,11,9,7,4,2]}$ and $J^{-2}_{[13,11,9,7,5,1]}$. While at large distances their density profiles are almost indistinguishable from the
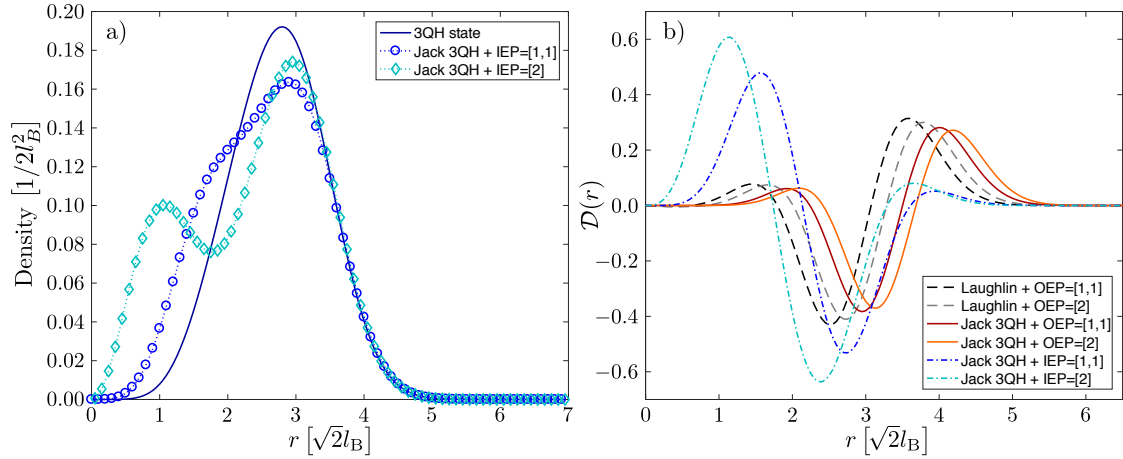
Figure 5.2: a) Radial density profile of a 3-QH state (blue solid line) and of Jacks with root partitions $\lambda = \Omega + \kappa^3 - [1,1] = [13,11,9,7,4,2]$ (blue circles) and $\lambda = \Omega + \kappa^3 - [2] = [13,11,9,7,5,1]$ (light-blue diamonds) for a system of $N = 6$ particles. All density profiles are characterized by the same shape on the outer edge, while they are characterized by very different shapes on the inner edge, as expected for states presenting inner-edge excitations. b) Rescaled density difference $\mathcal{D}(r)$ for different Jack polynomials, compared to the $(\kappa = 3)$-QH state. The comparison of the $\lambda = \Omega + \rho$ (black and grey dashed lines) and the $\lambda = \Omega + \kappa^3 + \rho$ (red and orange solid lines) cases allows us to identify the latter ones with a outer-edge excitation of the 3-QH state: The density differences $\mathcal{D}(r)$ only differ by a global shift, reflecting the presence of three empty orbitals in the 3-QH state, and by a weak attenuation of the peaks, which is a consequence of the slightly different length of the edges. At the same time, since the behavior of the $\mathcal{D}(r)$ associated with Jack polynomials of partitions $\lambda = \Omega + \kappa^3 - \rho$ (blue and light-blue dash-dotted lines) are similar to those characterizing the outer-edge excitations of the 3-QH state, with the difference that the peaks occurs in proximity to the inner edge of the 3-QH state, we can conclude that Jacks with $\lambda = \Omega + \kappa^3 - \rho$ well describe the inner-edge excitations of the 3-QH state. Also in this case the difference in the peaks heights can be attributed to a difference in the length of the edges. Adapted from Macaluso and Carusotto [2018].

one of the 3-QH state, at shorter distances they behave in a completely different way, as one would expect for states presenting IEEs. Note that similar results can be obtained for different sets of the physical parameters N, κ, and ΔI.

To further reinforce our proof in terms of density profiles, we compared Jacks obtained by either adding or subtracting the same partition ρ to a given κ-QH partition σ^κ. As Jacks with root partitions of the form $\lambda = \Omega + \rho$ can be associated with the OEEs of the Laughlin state [Lee et al., 2014, Fern and Simon, 2017, Macaluso and Carusotto, 2017], those with $\lambda = \Omega + \sigma^\kappa + \rho$ will reasonably describe the same excitation, but on the outer edge of the κ-QH state. By pushing this reasoning even further, if Jacks with root partitions like that in Eq. (5.10) actually describe κ-QH states with IEEs, one can expect that by subtracting the same partition ρ from the κ-QH root, one should induce a similar deformation but now located on the inner edge of the state with κ QHs.

To check this guess, we compared the density differences obtained by subtracting the radial density profile of the state with κ QHs from those characterizing Jacks with root partitions $\lambda = \Omega + \sigma^\kappa \pm \rho$. To better visualize the density variations induced on the edges, we focused on the related quantity $\mathcal{D}(r)$ defined as the just mentioned density difference multiplied by $2\pi r$, i.e.,

$$\mathcal{D}(r) \equiv 2\pi r \left[n_{\Omega + \sigma^\kappa \pm \rho}(r) - n_{\Omega + \sigma^\kappa}(r) \right], \tag{5.15}$$

where r denotes the radial distance from the center of the system and $n_{\Omega + \sigma^\kappa \pm \rho}(r)$ and $n_{\Omega + \sigma^\kappa}(r)$ denote the radial density profiles of $J^{-2}_{\Omega + \kappa^n \pm \rho}$ and $J^{-2}_{\Omega + \kappa^n}$, respectively.

The main results of our calculations are summarized in Fig. 5.2, where we plot the density profiles of the states described by different Jacks. As we can see in Fig. 5.2 b), the density differences obtained by considering the n-QH state and the $J^{-2}_{\Omega + \kappa^n + \rho}$ Jacks show the same behavior, modulo a translation which simply reflects the presence of n empty orbitals in the n-QH state, of those
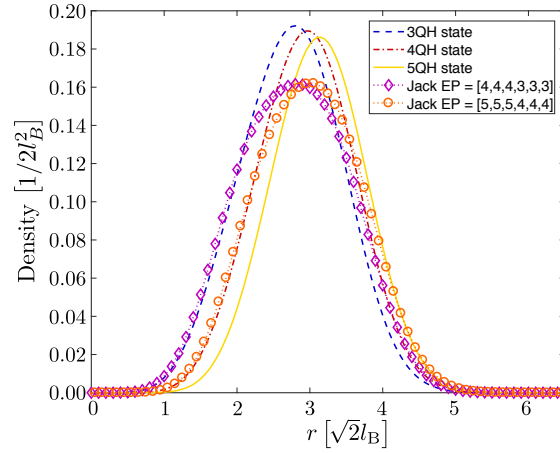
Figure 5.3: Radial density profile for the 3-QH state (blue dashed line), the 4-QH state (red dash-dotted lined) and the 5-QH state (yellow solid line) and for the Jacks with root partitions $\lambda = \Omega + [4, 4, 4, 3, 3, 3]$ (purple diamonds) and $\lambda = \Omega + [5, 5, 5, 4, 4, 4]$ (orange circles). While at small distances the density profile of the former (latter) Jack polynomial follows the one of the 3-QH state (4-QH state), at large distances it is very similar to the behavior of the 4-QH state (5-QH state) density profile. Adapted from Macaluso and Carusotto [2018].

characterizing the OEEs of the Laughlin state. This confirms the expectation that Jacks with root partitions $\lambda = \Omega + \kappa^n + \rho$ can indeed be associated with OEEs of the n-QH state.

Even more interestingly, Jacks with $\lambda = \Omega + \kappa^n \pm \rho$ describe similar density deformations taking place on the different edges. This confirms our identification of Jacks $J_{\Omega+\kappa^n-\rho}^{-2}$ with the IEEs of the n-QH state. As a further check, we have verified that the imbalance between the peaks in the rescaled density differences $\mathcal{D}(r)$ for excitations of the inner and the outer edge is a consequence of the shorter length of the inner edge and decreases when the ring dimensions (that is, n and $\mathcal{N}$) are consistently increased.

As a final remark we would like to discuss the competition between states presenting a different number of QHs and excitations on different edges. To be more precise, one might wonder which is the correct interpretation of a Jack polynomial with root partition

$$\lambda = \Omega + \gamma = \Omega + [\kappa, \ldots, \kappa, \kappa - \rho, \ldots, \kappa - \rho], \tag{5.16}$$

where γ has N elements, half of which are equal to κ while the remaining are given by $\kappa - \rho$. This partition can indeed be expressed in the two equivalent ways

$$\lambda = \Omega + \sigma^{\kappa-\rho} + [\rho, \ldots, \rho] \tag{5.17}$$

or

$$\lambda = \Omega + \sigma^{\kappa} - [\rho, \ldots, \rho], \tag{5.18}$$

where the length of $[\rho, \ldots, \rho]$ is given by $N/2$. The first form suggests that we are dealing with an $(\kappa - \rho)$-QH state presenting an OEE, while the second form rather indicates an κ-QH states with an IEE. Since the radial density profile of a state of this kind resembles that of the $(\kappa - \rho)$-QH at short distances and that of the κ-QH state at large distances [see Fig. 5.3], the two descriptions seem to be equivalent.

To conclude, we can say that for a given value of ΔI the above description of QH states with IEEs in terms of Jacks correctly applies if $\Delta I \ll N/2$. On the other hand, for IEPs ρ having both weight $|\rho|$ and length of the order of $N/2$ the identification of the associated Jacks $J_{\Omega+\kappa^n-\rho}^{-2}$ with states presenting IEEs is in general much less accurate.

Part II

Discussion of the original results

Chapter 6

Laughlin's edge excitations in the presence of hard-wall confinements.

$\mathbb{T}$he previous Chapter has been devoted to the introduction of the Jack polynomial formalism. As we have already widely discussed in there, Jack polynomials represent an extremely useful tool for the analysis of the edge modes of a fractional quantum Hall droplet as they allows one to easily construct the Hilbert space containing all excitations (below the many-body gap) of the Laughlin state for a given additional angular momentum.

However, in the following we will use exact diagonalization calculations [see Appendix A] to show that the importance of Jacks in the fractional quantum Hall context goes far beyond this, if one considers particular confinements of the Laughlin droplet. In the presence of hard-wall potentials it is indeed possible to fully classify the low-energy excitations of the system in terms of Jacks.

The analysis of fractional quantum Hall droplets experiencing hard-wall confinements pursued in this Chapter is surely of theoretical interest. The edge modes of fractional quantum Hall liquids affected by potentials of this kind show for instance unexpected (but evident) deviations from the standard chiral Luttinger theory proposed by Wen [1990a]. However, the framework in which we envision a major impact of our study is the experimental one, and in particular that of driven-dissipative photonic systems [Schine et al., 2016, Clark et al., 2019]: On the one hand, Umucalılar and Carusotto [2017] have already theoretically proved that the single hard-wall configuration discussed in Macaluso and Carusotto [2017] [see Sec. 6.2] can be used to create a $\nu = 1/2$ bosonic Laughlin state of light in the presence of frequency-dependent incoherent pumping. On the other hand, we show that more complicated potential configurations [see Sec. 6.4] could be used in photonic set-ups to stabilize fractional quantum Hall liquids with an arbitrary number of quasiholes in the origin. As we will see in Chapter 7, states presenting a single quasihole and two quasiholes on top of each other are exactly what one needs to probe the anyonic statistics of such excitations by means of static density-profile measurements.

The main results of the present Chapter are published in Macaluso and Carusotto [2017] and Macaluso and Carusotto [2018].

6.1 FQH droplets with hard-wall potentials

Atomic and photonic systems generally offer a wider flexibility in the generation, manipulation, and diagnostics of quantum states than electronic solid-state devices. Thus one can expect more precise control of the external potential confining the FQH droplet and, as a consequence, of the properties of the edge modes. In this sense, after years of theoretical studies mainly focused on harmonically confined FQH droplets [Cooper and Wilkin, 1999, Wilkin and Gunn, 2000, Cooper et al., 2001, Regnault and Jolicoeur, 2003, Cazalilla, 2003, Cazalilla et al., 2005], the recent realization of flat-bottomed traps for ultracold atoms by Gaunt et al. [2013] and the flexibility in designing optical

cavities [Schine et al., 2016, Clark et al., 2019] and arrays of them [Roushan et al., 2016] have motivated researchers to investigate the effects of hard-wall (HW) confinements on the spectral properties of FQH droplets [Fern and Simon, 2017, Macaluso and Carusotto, 2017, Umucalılar and Carusotto, 2017, Macaluso and Carusotto, 2018].

As we will see in the following, external potentials of this kind induce significant deviations from the standard chiral Luttinger liquid theory proposed by Wen [1990a]. On top of that, in the presence of HW potentials, an extremely accurate one-to-one correspondence between the eigenstates of the FQH cloud and certain trial wave functions expressed in terms of Jack polynomials has been found, as discussed in Fern and Simon [2017], in Macaluso and Carusotto [2017] and in Macaluso and Carusotto [2018].

We model the FQH liquid in the presence of HW potentials as a 2D system of N interacting bosons described by a Hamiltonian of the form $\hat{H} = \hat{H}_0 + \hat{H}_{\text{int}} + \hat{H}_{\text{conf}}$, where

$$\hat{H}_0 = \sum_{i=1}^{N} \frac{(\mathbf{p}_i + \mathbf{A})^2}{2M} \tag{6.1}$$

is the kinetic energy term in the presence of an orthogonal (synthetic) magnetic field $\mathbf{B} = \nabla \times \mathbf{A} = B \, \hat{e}_z$,

$$\hat{H}_{\text{int}} = g_{\text{int}} \sum_{i<j} \delta^{(2)}(\mathbf{r}_i - \mathbf{r}_j) \tag{6.2}$$

describes contact interactions of strength g_{int}, and

$$\hat{H}_{\text{conf}} = \sum_{i=1}^{N} \left[V_{\text{in}} \, \theta(R_{\text{in}} - |\mathbf{r}_i|) + V_{\text{ext}} \, \theta(|\mathbf{r}_i| - R_{\text{ext}}) \right], \tag{6.3}$$

accounts for the spatial confinement of the FQH droplet within the ring-shaped region delimited by a pair of concentric, cylindrically symmetric, repulsive HW potentials. The inner HW radially extends from $r = 0$ to $r = R_{\text{in}}$ and has a height V_{in}, the outer one instead extends from $r = R_{\text{ext}}$ to infinity with a height V_{ext}. In the previous expression $\theta(x)$ denotes the Heaviside step function, while the potential heights $V_{\text{in/ext}}$ and extensions $R_{\text{in/ext}}$ can be set at will.

Note that the confinement Hamiltonian in Eq. (6.3) can describe three different system configurations, depending on the values of the parameters V_{in} and V_{ext}: for $V_{\text{in}} = 0$ and $V_{\text{ext}} \neq 0$ we have a disk-shaped FQH droplet, for $V_{\text{in}} \neq 0$ and $V_{\text{ext}} = 0$ we obtain a system in a homogeneous potential landscape pierced by a HW potential, while for $V_{\text{in}}, V_{\text{ext}} \neq 0$ the FQH liquid is spatially confined in a ring-shaped region. This three different geometries of the system will be discussed in Sec. 6.2, Sec. 6.3 and Sec. 6.4, respectively.

To take advantage of the cylindrical rotational symmetry of the confining Hamiltonian H_{conf}, we choose to consider the symmetric gauge for the vector potential, i.e. $\mathbf{A} = B(-y/2, x/2, 0)$. As we have seen in Sec. 2.1, for this particular gauge the LLL single-particle wave functions can be labeled by the angular momentum quantum number m and have the simple form

$$\varphi_m(r, \phi) = \frac{1}{\sqrt{2\pi l_B^2 m!}} \, e^{im\phi} \left(\frac{r}{\sqrt{2}l_B} \right)^m e^{-r^2/4l_B^2}. \tag{6.4}$$

Note that, since the total angular momentum operator $\hat{L}_z$ commutes with the Hamiltonian, i.e. $[\hat{H}, \hat{L}_z] = 0$, all many-body eigenstates have a well-defined total angular momentum (which we will express in units of $\hbar$).

Moreover, as long as we restrict to the low-energy physics of the system and assume that the cyclotron energy $\hbar\omega_C = \hbar B/m$ is much larger than all other energy scales of the problem, typically set by the potential energies $V_{\text{in/ext}}$ and the characteristic interaction energy $V_0 = g_{\text{int}}/2l_B^2$, we are legitimated to make to so-called LLL approximation. Within this approximation, the system dynamics is restricted to the LLL and the Hamiltonian can be rewritten in a second quantized fashion in terms of the ladder operators $\hat{a}_m$ and $\hat{a}_m^\dagger$, which respectively create and annihilate particles in the LLL state of angular momentum m:

$$\hat{H}_0 = \varepsilon_0 \sum_m \hat{a}_m^\dagger \hat{a}_m, \tag{6.5}$$
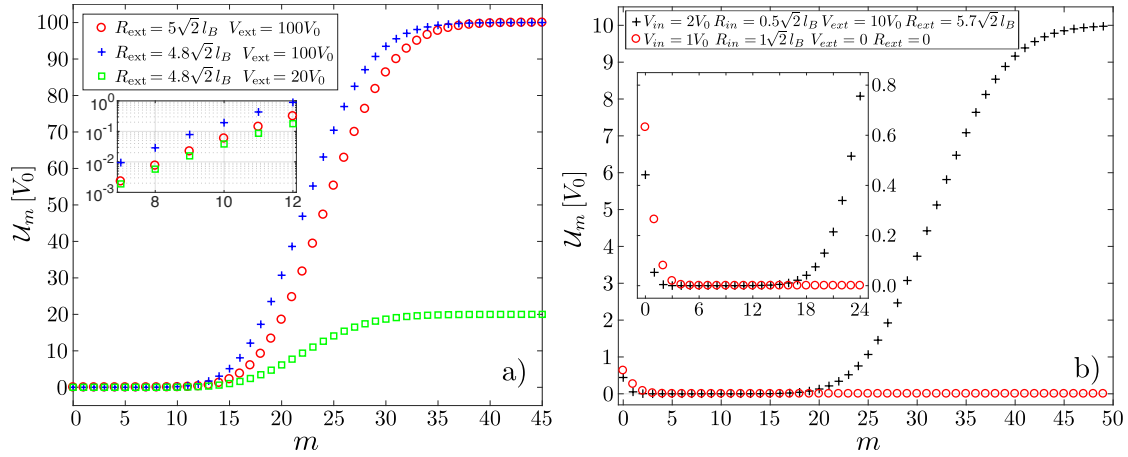
Figure 6.1: Typical behavior of the $\mathcal{U}_m$ potentials as a function of the single-particle angular momentum m for different sets of confining parameters. a) Three different sets of potential parameters which corresponds to FQH liquids in disk-shaped geometries ($V_{\text{in}} = 0$). b) $\mathcal{U}_m$ potentials for confining parameters describing FQH liquids in ring (black pluses) and pierced (red circles) geometries. Insets provide a magnified view of the main panel. As expected, the extremely steep condition discussed in the text is not fulfilled for the experimentally realistic potential parameters considered here. Adapted from Macaluso and Carusotto [2017] and Macaluso and Carusotto [2018]

$$\hat{H}_{\text{int}} = \frac{g_{\text{int}}}{2l_B^2} \sum_{\alpha\beta\gamma\rho} \frac{\Gamma(\alpha + \beta + 1)}{\pi\sqrt{\alpha!\beta!\gamma!\rho!}} \frac{\delta_{\alpha+\beta,\gamma+\rho}}{2^{(\alpha+\beta+2)}} \hat{a}_\alpha^\dagger \hat{a}_\beta^\dagger \hat{a}_\gamma \hat{a}_\rho, \tag{6.6}$$

$$\hat{H}_{\text{conf}} = \sum_m \mathcal{U}_m \, \hat{a}_m^\dagger \hat{a}_m = \sum_m \left[\frac{V_{\text{in}}}{m!} \gamma_\downarrow \left(m+1, \frac{R_{\text{in}}^2}{2l_B^2} \right) + \frac{V_{\text{ext}}}{m!} \gamma_\uparrow \left(m+1, \frac{R_{\text{ext}}^2}{2l_B^2} \right) \right] \hat{a}_m^\dagger \hat{a}_m, \tag{6.7}$$

where $\varepsilon_0 = \hbar\omega_C/2$ is the kinetic energy of a single particle in the LLL, $\Gamma(t)$ is the Euler gamma function

$$\Gamma(t) \equiv \int_0^\infty x^{t-1} e^{-x} dx, \tag{6.8}$$

and $\gamma_{\downarrow,\uparrow}(t, R)$ are the so-called lower and upper incomplete gamma functions

$$\gamma_\downarrow(t, R) \equiv \int_0^R x^{t-1} e^{-x} dx, \tag{6.9}$$

$$\gamma_\uparrow(t, R) \equiv \int_R^\infty x^{t-1} e^{-x} dx. \tag{6.10}$$

Note that since we are neglecting excitation to higher Landau levels, all N-particle states will have the same kinetic energy $N\varepsilon_0$, which effectively drops out of the problem. As a consequence, we neglect the kinetic term and we focus on the Hamiltonian $\hat{\tilde{H}} = \hat{H} - \hat{H}_0 = \hat{H}_{\text{int}} + \hat{H}_{\text{conf}}$.

From Eq. (6.7), we can immediately see that, if one restricts the description of the system to the LLL, all information on the confinement potential is encoded in the potential energies $\mathcal{U}_m = \langle \varphi_m | \hat{H}_{\text{conf}} | \varphi_m \rangle$ of the different states with angular momentum m. Their typical behavior, as a function of m, is reported in Fig. 6.1 for few different sets of potential parameters $R_{\text{in(ext)}}$ and $V_{\text{in(ext)}}$, corresponding to realistic disk, pierced and ring geometries. In the former case, V_{in} is set to zero and only the outer HW confinement is present, meaning that the Laughlin droplet is confined within a disk-shaped region of space. In the second case, only the inner repulsive HW potential of strength V_{in} is applied to the atoms and creates a central hole in the FQH liquid but no outer confinement is applied ($V_{\text{ext}} = 0$), so the liquid can extend outwards to arbitrary distances. In the latter case, both the inner V_{in} and the outer V_{ext} confinements are present, and therefore the Laughlin puddle is confined within a finite ring-shaped region.

In their recent work, Fern and Simon [2017] considered a single HW potential ($V_{\text{in}} = 0$) and assumed the extremely steep limit condition

$$\mathcal{U}_{m-1} \ll \mathcal{U}_m \ll \mathcal{U}_{m+1}, \tag{6.11}$$

for the confining potentials $\mathcal{U}_m$. However, in Macaluso and Carusotto [2017] we showed that this condition is hard to satisfy with experimentally realistic potentials.

For $V_{\text{in}} = 0$ and sufficiently large values of R_{ext}, we can in fact approximate

$$\mathcal{U}_m \simeq \frac{V_{ext}}{m!} \left(\frac{R_{\text{ext}}^2}{2l_B^2} \right)^m \exp \left(-\frac{R_{\text{ext}}^2}{2l_B^2} \right), \tag{6.12}$$

so that having a large ratio

$$\frac{\mathcal{U}_m}{\mathcal{U}_{m-1}} \simeq \frac{R_{\text{ext}}^2}{2ml_B^2} \tag{6.13}$$

requires a wide disk radius $R_{\text{ext}} \gg \sqrt{2m}\, l_B$, much larger than the FQH droplet we intend to study.

Due to the exponential factor in Eq. (6.12), simultaneously having an overall appreciable potential $\mathcal{U}_m$ and a very steep m-dependence [see Eq. 6.13] requires a very large potential strength V_{ext}: physically, this comes from the fact that the HW potential only acts on the far tail of the LLL wave function. However, having a very far, but strong HW potential makes the system extremely sensitive to weak variations of the HW parameters. For instance, if we consider a small variation ΔR_{ext}, this induces a relative variation of the confinement potential $\Delta \mathcal{U}_m / \mathcal{U}_m$ which can be estimated to be a large number

$$\left| \frac{\Delta R_{\text{ext}}}{R_{\text{ext}}} \left[2m - \frac{R_{\text{ext}}^2}{2l_B^2} \right] \right| \simeq \frac{R_{\text{ext}}}{l_B} \frac{\Delta R_{\text{ext}}}{l_B}. \tag{6.14}$$

These arguments on the difficulty of satisfying the condition assumed by Fern and Simon [2017] further motivate our numerical calculations including a realistic form of the confinement potential.

A similar analysis can be done for the inner HW potential, for which the extremely steep condition in Eq. (6.11) reads $\mathcal{U}_{m-1} \gg \mathcal{U}_m \gg \mathcal{U}_{m+1}$. However, also in this case the ratio $\mathcal{U}_m / \mathcal{U}_{m+1}$ of realistic potentials does not exceed values of the order 5 even at small values of m where, for the values of R_{in} considered here, it is largest [see Fig. 6.1]. As a result, not only in the disk geometry, but also in the pierced (ring) geometry the confinement energy does not come from a single (two) $\mathcal{U}_m$ potential(s), but may receive significant contributions from several m orbitals.

6.2   Disk-shaped geometries: a single hard-wall confinement

After having discussed the microscopic models describing bosonic FQH liquids in the presence of HW potentials, we are going to present and discuss our ED numerical results for the low-energy part of the many-body spectra characterizing disk-shaped Laughlin puddles for different values of the HW potential parameters V_{ext} and R_{ext}. Different regimes can be distinguished depending on the value of these parameters: in particular we identify a weak confinement regime, which will be discussed in Sec. 6.2.1, and a strong confinement regime, which will be considered in Sec. 6.2.2 instead. In both cases we restrict to the $R_{\text{ext}} \gtrsim R_{cl}$ case, where $R_{\text{cl}} \simeq \sqrt{N/\nu}\,\sqrt{2}l_B$ represents the semiclassical radius of a N-particle Laughlin droplet with filling factor ν. While this assumption guarantees that the $\mathcal{U}_m$ components of $\hat{H}_{\text{conf}}$ grow as a function of m, it can describe a wider set of potentials than just the extremely steep HW limit discussed in Fern and Simon [2017].

6.2.1   Weak confinement regime

As we will see, the weak confinement regime is characterized by a weak mixing of the Laughlin state and its edge and QH excitations with states above the many-body gap, e.g. quasiparticle (QP) excitations. In this regime, as shown in Fig. 6.2, the ground state of the system is non-degenerate and is extremely close to the $\nu = 1/2$ Laughlin state. At the same time, the HW potential pushes the low-lying excited states to higher energies and removes the degeneracy between edge excitations with the same additional angular momentum ΔL. In particular, for a given ΔL, the number of states with energies lying below the many-body gap depends on the parameters V_{ext} and R_{ext}: More we increase the potential strength (or we reduce the potential radius) more edge excitations end up having energies lying above the many-body gap. As a consequence, only for the lowest values of ΔL one can resolve all edge excitations [see Fig. 6.2 a)-c)].

As a first step of our analysis, we will present a classification of the many-body states into branches and sub-branches and we will highlight its relation to the edge partitions (EPs) of the
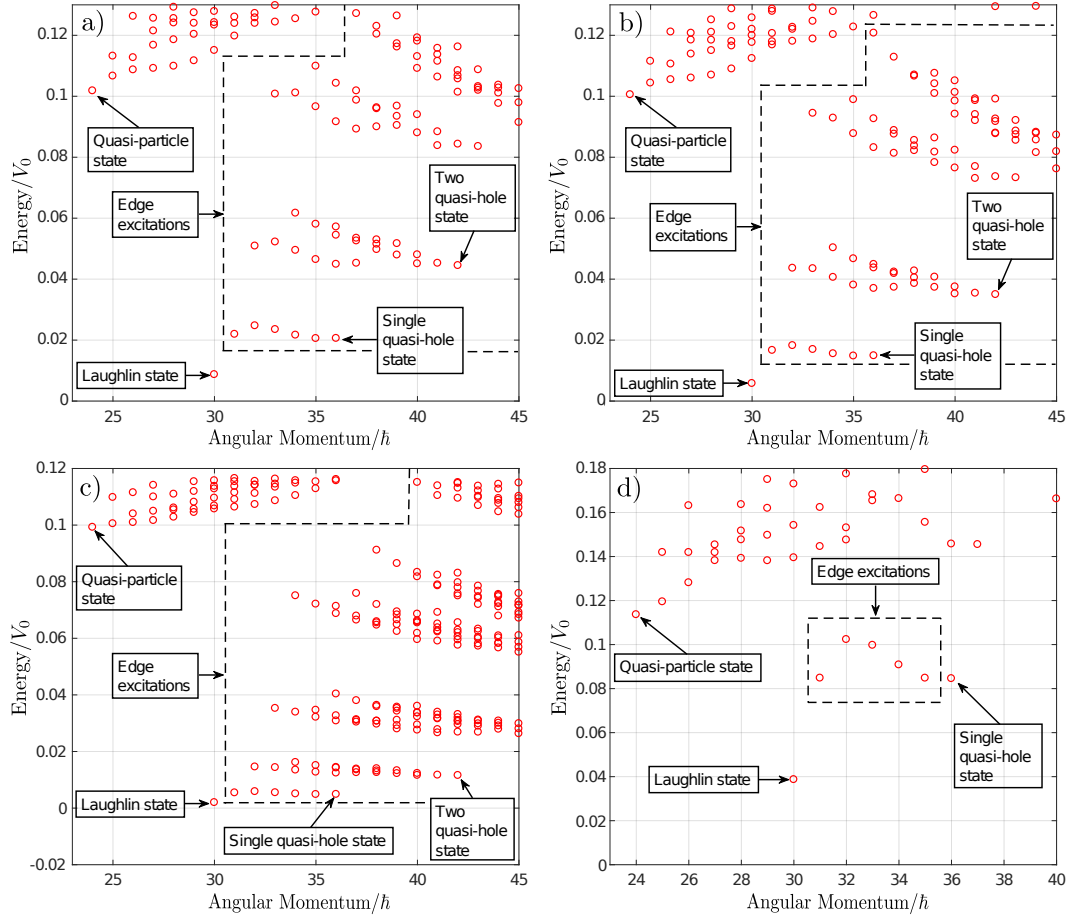
Figure 6.2: Many-body spectra for $N = 6$ particle systems in the weak confinement regime, experiencing different hard-wall potentials. While the chiral Luttinger liquid theory well captures the number of energy branches and sub-branches for each value of ΔL, the characteristic linear relation between energy and angular momentum breaks down for all choices of V_{ext} and R_{ext}. Panels a) and b) correspond to a hard-wall confinement with $V_{ext}/V_0 = 20$ and $R_{ext}/\sqrt{2}\,l_B = 4.95$ and with $V_{ext}/V_0 = 100$ and $R_{ext}/\sqrt{2}\,l_B = 5.25$, respectively. In both cases the ground state is given by the Laughlin state and for a given value of ΔL different non-degenerate edge excitations can be resolved below the many-body gap. In these spectra also the two different sub-branches of the second energy branch can be easily resolved. Panel c) corresponds to an even weaker hard-wall confinement with $V_{ext}/V_0 = 30$ and $R_{ext}/\sqrt{2}\,l_B = 5.25$. In this case all low-lying excited states up to $L = 34$ have energies below the many-body gap, so that the first four energy branches are visible. Panel d) corresponds to a stronger hard-wall confinement with $V_{ext}/V_0 = 100$ and $R_{ext}/\sqrt{2}\,l_B = 4.95$ for which the ground state and first excited one are given by the Laughlin state and the single-QH state, respectively. Here, for a given value of $\Delta L < N$ there is just one non-degenerate branch of excited states below the many-body gap. Taken from Macaluso and Carusotto [2017].

corresponding Jack polynomials: the excellent overlap with the analytic trial wave function is remarkably associated to significant deviations from the chiral Luttinger liquid theory of the edge, as visible in both the degeneracy of states and in their ordering within a given sub-branch. After that we will focus on the ordering of the different sub-branches: discrepancies from the extremely steep limit considered by Fern and Simon [2017] are pointed out and a unexpected energy-crossing between states sharing the same total angular momentum highlighted for varying V_{ext} and R_{ext} parameters. Then, we shall discuss how the dispersion of states within a given subbranch can be controlled via the HW parameters. As a striking example, we shall present a confinement regime in which the single-QH state is the first excited state. Finally, the compressibility of the FQH liquid and of its QH and QP excitations is characterized in terms of the dependence of the eigenstate energies on the confinement potential strength.

Classification of eigenstates in terms of Jacks

The overall organization of the excited state can be understood from Fig. 6.2 c), where the confinement is weakest: by looking at the full spectrum, instead of focusing on a specific value of ΔL, we can see that the excited states organize themselves in a sort of energy branches: The k-th branch starts from an angular momentum $L = L_L + k$ and ends with a state presenting k QHs at $\eta = 0$. In between, it splits into k sub-branches.

Even though such a spectral structure could seem quite complicated, it can be fully explained in terms of Jacks. In particular, in the weak confinement regime, the edge excitations turn out to be well described by the wave functions of the form

$$\boxed{\phi_\gamma(z) = J_\gamma^{1/2}\, \Psi_L(z)}, \tag{6.15}$$

and the k-th energy branch contains all states whose wave functions can be obtained by multiplying $\Psi_L(z)$ by Jacks with partitions of the form

$$\gamma = [\gamma_1, \gamma_2, \gamma_3, \dots] = [k, \gamma_2, \gamma_3, \dots]. \tag{6.16}$$

As a first point, simple angular momentum arguments based on the observed extension of the different branches support this statement. Since a Jack with partition $\lambda = \Omega + \gamma$ has angular momentum $L = L_L + |\gamma|$, the lowest ΔL compatible with Eq. (6.16) is the one associated with $\gamma = [k]$, i.e. $\Delta L = k$. At the same time partitions are ordered sequences of positive integers and therefore they must satisfy

$$\gamma_1 \geq \gamma_2 \geq \cdots \geq \gamma_N. \tag{6.17}$$

This implies that the maximum additional angular momentum that can be obtained by considering EPs with $\gamma_1 = k$ is $\Delta L = Nk$ and that it comes from the partition $[k, \dots, k]$ corresponding to the k-QH state.

With this picture in mind, the monotonically growing behavior (as a function of k) of the energy of the different bands is easily understood as the main contribution to the confinement energy is given by the outermost occupied orbital. For the k-th branch, it corresponds the LLL wave function of angular momentum $\Omega_1 + k$, namely the one associated to the particle that was moved by k orbitals in the outward direction from the outermost occupied orbital of the Laughlin root configuration [see Sec. 5.2.1].

Along the same lines, energy order of sub-branches within a given branch can be related to the value of the second element γ_2 of the partition. In particular the j-th sub-branch of the k-th energy branch is formed by states whose trial wave functions can be constructed from Jacks having partitions

$$\gamma = [\gamma_1, \gamma_2, \gamma_3, \dots] = [k, j, \gamma_3, \dots], \tag{6.18}$$

with the exception of the 1-st sub-branch in which there is also the Jack with partition $\gamma = [k]$ having $\gamma_1 = k$ and no γ_2. This interpretation of the different sub-branches, together with the constraint in Eq. (6.17), is further supported by the fact that the number of states in a given sub-branch depends only on the sub-branch index j (and on the number of particles N, which fixes the maximum number of partition elements γ_i), but not on the branch index k. Subtle features related to this ordering of levels will be highlighted in more detail in the following and compared to the results of Fern and Simon [2017] for the extremely steep HW limit.

The just presented description of the energy branches is numerically validated in Fig. 6.3, where we successfully compare the density profiles predicted by the trial wave functions in Eq. (5.12) to those numerically obtained via ED. The hardly visible deviations can be attribute to the mixing with QP excitations induced by the confinement, as well as to the non-orthogonality of wave functions associated with different EPs of the same additional angular momentum ΔL. Note that the calculation of the density profiles shown in this picture is made significantly simpler by the expression of the edge state wave function in terms of single Jacks via (5.12).

In some panels, we have added the corresponding density profiles calculated using the trial wave function (6.15) (in others, the curves for the two kinds of Jacks are indistinguishable on the scale of the figure). The agreement with the numerical results is once again excellent. As these trial wave functions are orthogonal in the thermodynamic limit, we expect that the remaining deviations will disappear if one considers $N \to \infty$ and vanishingly HW potential $R_{\text{ext}} \to \infty$ (or $V_{\text{ext}} \to 0$).

A further corroboration of our interpretation is given by the overlaps between the numerical eigenstates and the Jacks trial wave functions: As shown in Table 6.1, overlaps are very good with
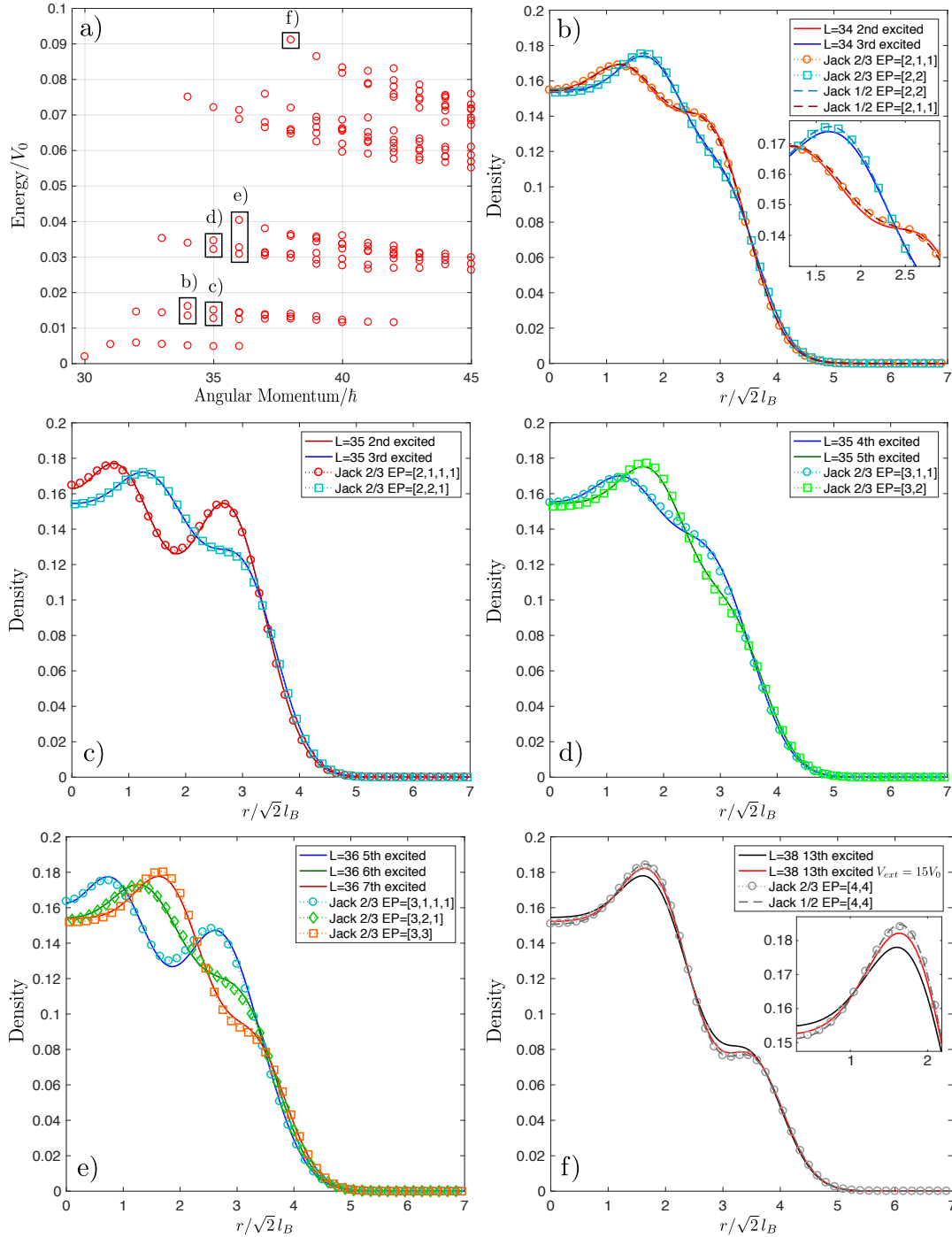
Figure 6.3: a) Energy spectrum of a $N = 6$ particle system experiencing an hard-wall potential of parameters $V_{ext}/V_0 = 30$ and $R_{ext}/\sqrt{2}\,l_B = 5.25$ showing the energies lying below the many-body gap and for states with angular momenta $L \leq 45$. b)-f) Comparison between the density profiles of some of the eigenstates depicted in a) and the associated trial wave functions constructed starting from Jacks of parameter $\nu = 1/2$ (dashed lines) and/or $\beta = 2/3$ (dotted lines with markers). As we can see, the eigenstate description in terms of Jacks is so good that discrepancies in the density profiles are hardly visible in most cases. To show how deviations of the numerical eigenstates from the Jacks trial wave functions can be further reduced by considering weaker confinements, panel f) reports also the density profile (red solid line) for a smaller value of the potential strength, i.e. $V_{ext}/V_0 = 15$. Insets in b) and f) show that, on these scales, differences between trial wave functions associated to the same edge partition but a different Jack parameter are not visible. Adapted from Macaluso and Carusotto [2017].

EP	$\langle J_\gamma^\beta \Psi_L | \Psi \rangle$	$\langle J_\gamma^\nu \Psi_L | \Psi \rangle$	$\langle J_\gamma^\beta \Psi_L | J_\gamma^\nu \Psi_L \rangle$
$\gamma = [1,1,1,1]$	0.9991	0.9991	1.0000
	0.9994	0.9994	
$\gamma = [2,1,1]$	0.9783	0.9936	0.9878
	0.9798	0.9953	
$\gamma = [2,2]$	0.9896	0.9902	0.9908
	0.9914	0.9922	
$\gamma = [4,4]$	0.9473	0.9501	0.9452
	0.9669	0.9733	

Table 6.1: Overlaps of the numerical ED eigenstates $|\Psi\rangle$ with the corresponding trial wave functions in Eqs. (5.12) and (6.15) for a system of $N = 6$ particles. Values in black refer to a HW confinement of parameters $R_{\text{ext}}/\sqrt{2}\, l_B = 5.25$ and $V_{\text{ext}}/V_0 = 30$, while those in red to the $R_{\text{ext}}/\sqrt{2}\, l_B = 5.25$ and $V_{\text{ext}}/V_0 = 15$ case.

Jacks in Eq. (5.12) and they get even closer to 1 when we consider ansatz wave functions of the form (6.15) [1] and/or a weaker confinement.

Order of sub-branches

We have just presented a general criterion for the energetic ordering of the different branches and of the different sub-branches within a given branch. As clearly visible in Fig. 6.3 a), sub-branches associated with higher values of the second EP element γ_2 have increasing energies. For instance among the two $L = 34$ eigenstates in the second energy branch [see Fig. 6.3 b)], the one in the $\gamma_2 = 1$ sub-branch has a lower energy with respect to the one in the $\gamma_2 = 2$ sub-branch.

Although this behavior persists for all considered values of the HW parameters, it is important to notice that this result is in contrast to what was found by Fern and Simon [2017] in the extremely steep limit case, where sub-branches associated with increasing values of γ_2 are characterized by decreasing energies.

This discrepancy can be easily understood by noting that the energy shifts in the extremely steep HW limit only depend on the highest m occupation number, while, as we have seen, this is no longer true for more realistic confining potentials. To be precise, the observed ordering of the sub-branches in the two cases is explained by the fact that larger values of γ_2 correspond to slightly lower occupations of the highest m orbital but also much higher occupations of the second highest one [see example in Fig. 6.5 h)].

This behavior of the energies characterizing sub-branches belonging to the same energy branch, together with the observation that the eigenstates are the same in different confining regimes, suggests that in the transition between the two regimes the eigenstates in the different sub-branches cross in energy without mixing. While such a crossing would be obviously protected by rotational symmetry for eigenstates with different angular momenta, it is quite unexpected for same L_z eigenstates which would typically mix in a non-trivial and potential-dependent way.

However, according to our calculations, this is not the case and wave function of the form (6.15) remain precise eigenstates of the Hamiltonian for all considered confinement potentials. To further support this statement, we have studied the value of the matrix elements of the $\hat{a}_m^\dagger \hat{a}_m$ operators contributing to the confinement energy $\langle \hat{H}_{\text{conf}} \rangle$. As reported in Fig. 6.4, in the Jack basis the off-diagonal matrix elements of $\hat{a}_m^\dagger \hat{a}_m$, turn out to be much smaller in magnitude than the diagonal ones and, even more remarkably, have a clear oscillating dependence on m.

As a consequence, they easily average to very small values when realistic potentials $\mathcal{U}_m$ are considered. For instance, for the potential parameters we used in Fig.6.3(a), the rescaled expectation value,

$$\frac{\langle \phi_\gamma | \hat{H}_{\text{conf}} | \phi_\mu \rangle}{\sqrt{\langle \phi_\gamma | \hat{H}_{\text{conf}} | \phi_\gamma \rangle \langle \phi_\mu | \hat{H}_{\text{conf}} | \phi_\mu \rangle}}, \tag{6.19}$$

takes respectively the (very small) values 0.0033, 0.0202 and 0.0119 for the wave functions ϕ_γ and ϕ_μ considered in the three panels of Fig. 6.4.

---

[1] Note that Jacks with EPs as those in Eq. (6.16) with $k = 1$ correspond to single monomials $\mathcal{M}_\gamma$'s independently on the Jack parameter and therefore for the $k = 1$ energy branch wave functions (6.15) and (5.12) coincide.
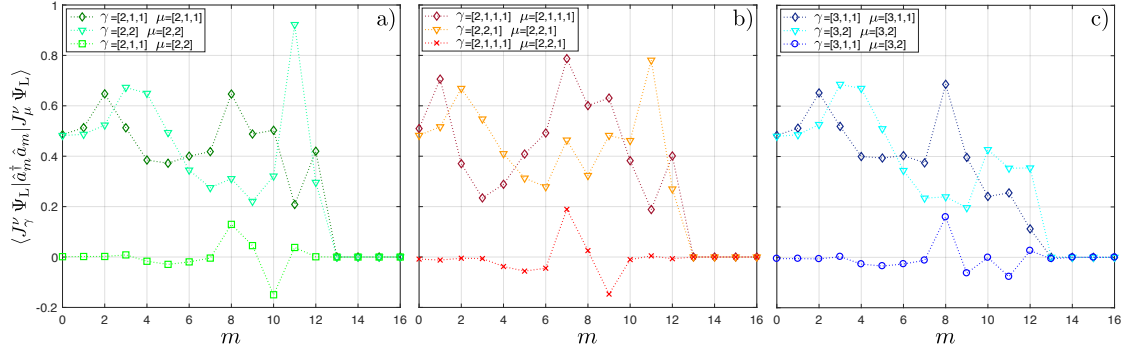

Figure 6.4: Matrix elements of the operators $\hat{a}_m^\dagger \hat{a}_m$ evaluated on the trial wave functions in Eq. (6.15), which describe states having the same angular momentum eigenvalue and belonging to the same energy branch but to different sub-branches. In particular: panel a) shows results for Jacks with edge partitions $[2, 1, 1]$ and $[2, 2]$, panel b) concerns Jacks with edge partitions $[2, 1, 1, 1]$ and $[2, 2, 1]$ and finally panel c) reports $\hat{a}_m^\dagger \hat{a}_m$ matrix elements evaluated by considering Jacks with edge partitions $[3, 1, 1]$ and $[3, 2]$. In all cases the off-diagonal matrix elements in the Jack basis are much smaller than the diagonal ones and they are also characterized by an oscillating dependence on m. Both these features lead to very small values once averaged on the different m's and provide an explanation for the unexpected energy crossing with no mixing that take place when passing from our realistic potential regime to the extremely steep limit studied in Fern and Simon [2017]. Adapted from Macaluso and Carusotto [2017].

Fine structure of the spectrum

We have seen that Jack polynomials provide a hierarchical classification of the Hamiltonian eigenstates in terms of the first entries of the EPs γ. While this criterion allows one to order in energy of the different branches and sub-branches, it does not offer much insight on the physical mechanisms which are responsible for the relative energy of states within a given branch or sub-branch. Note that, as the derivative of the energy dispersion with respect to angular momentum determines the angular speed of a perturbation propagating along the edge of the disk-shaped cloud, an experimental study of the surface dynamics and its collective modes may provide a valuable insight on the nature of the edge excitations and on its deviation from standard chiral Luttinger liquid theory [Wen, 1990a, 1992].

A complete physical interpretation of the observed energy spectra is a very complicate task, thus in the following we mainly focus our attention on the possibility of having the state with a single QH at $\eta = 0$, i.e.

$$\Psi_{1QH}(\eta = 0; z) = \prod_i z_i \, \Psi_L(z), \tag{6.20}$$

as the first excited state above the Laughlin ground state. The interest of this particular feature is motivated by its marked deviation from the chiral Luttinger liquid theory for the edge states (which predicts a monotonical increase of the eigenenergies as a function of the additional angular momentum ΔL) as well as from the potential utility of a massive population of states with QHs, in view of studies of the anyonic properties of these excitations. In Fig.6.2 d), we report a set of confinement parameters for which this is indeed the case.

This peculiar energetic behavior of the lowest energy excited states in the weak confinement regime can be explained by looking at the expectation value of occupation numbers $\bar{n}_m = \langle \Psi | \hat{a}_m^\dagger \hat{a}_m | \Psi \rangle$ taken on the trial wave functions corresponding to the states forming the $k = 1$ energy branch. In the presence of stronger confinements one should take into account the reorganization of the states within the manifold of non-interacting states, as well as the possible mixing with QP states above the many-body gap. However, this a simple analysis, based on the study of occupation number expectation values, is expected to be accurate at a linear response level in the weak confinement regime.

The distribution of particles among the different LLL wave functions is shown in panel a)-g) of Fig. 6.5 for the states forming the $k = 1$ energy branch. As we consider increasing values of ΔL, the broad central peak of occupation visible around $m \simeq N = 6$ for the $\Delta L = 0$ Laughlin state slowly moves towards lower m's and becomes less pronounced. At the same time, another
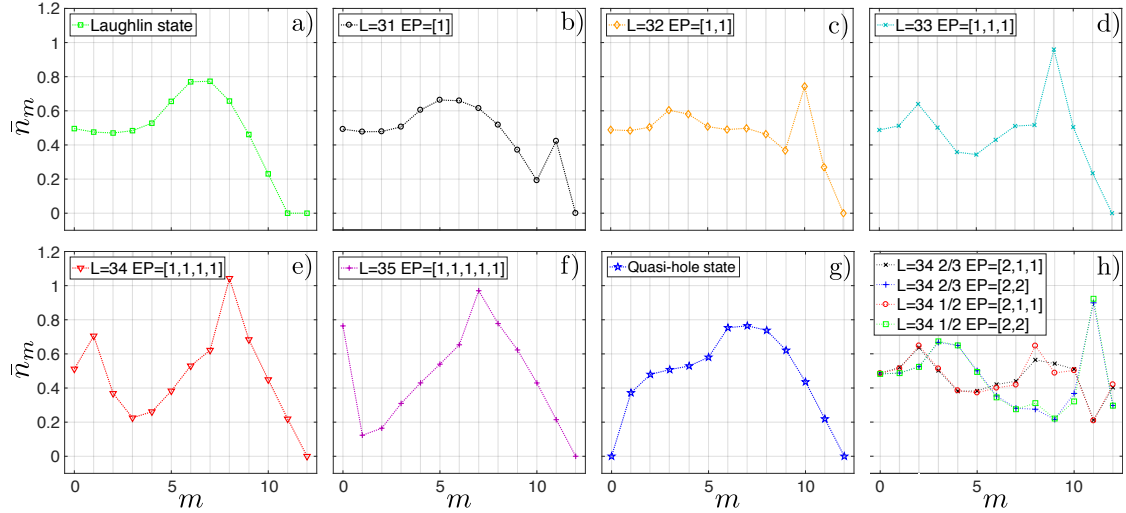
Figure 6.5: a)-g) Average occupation numbers $\bar{n}_m = \langle\Psi|\hat{a}_m^\dagger\hat{a}_m|\Psi\rangle$ of single-particle LLL orbitals calculated on Jack trial wave functions for states in the $k = 1$ energy branch. The different shapes of $\bar{n}_m$ shown in panels a)-g) for the different states within the lowest $k = 1$ energy branch can be used to explain their energetic ordering. h) Comparison between the $\bar{n}_m$ of states within the $k = 2$ energy branch described by Jack trial wave functions with different Jack parameters ($\beta = 2/3$ vs $\nu = 1/2$): the differences are minor and the global behavior of $\bar{n}_m$ as function of m has been found to be mostly determined by the EP. In particular, trial wave functions with EP's $[2, 2]$ and $[2, 1, 1]$ are characterized by very different values of $\bar{n}_m$ for $m = 11, 12$. This, together with the fact that the potential energy is dominated by the highest-m $\mathcal{U}_m$, explains the different ordering of sub-branches found in our calculations compared to the extremely steep limit of Fern and Simon [2017]. Adapted from Macaluso and Carusotto [2017]

peak in the $\bar{n}_m$ appears at the high-m values and moves towards lower m while becoming more pronounced, until it transforms into a central peak in the single-QH state. Interestingly, the values of the different $\bar{n}_m$ for this latter state are quite similar to those characterizing the Laughlin state, just shifted by one unit of m. Note that, although for growing values of ΔL the features of the m-distribution shift towards small m's, the overall center of mass of the distribution grows, as expected.

From these curves, we can observe that the occupation number values for the highest m's, i.e. $\bar{n}_9$, $\bar{n}_{10}$ and $\bar{n}_{11}$, are very similar for the single-QH state and for the neighboring state with $L = 35$ and described by the Jack with EP $\gamma = [1, 1, 1, 1, 1]$. Actually those $\bar{n}_m$ are slightly smaller for this latter state. This explains why, for large enough values of R_{ext}, the energy shift due to the HW confinement is extremely similar for these two states and, in particular, why the edge state with $L = 35$ is (by a small difference) the first excited state. For very large values of R_{ext} indeed all contributions to $\langle\hat{H}_{\text{conf}}\rangle$ coming from the occupation of the lower m orbitals can be neglected and the occupation number expectation values of the highest m orbital fully determine the confining energy, as widely discussed in Fern and Simon [2017].

Nevertheless, it is also possible to obtain spectra in which the single-QH state is the first excited one, as shown in Fig. 6.2 d). This happens when, for fixed values of V_{ext}, we slightly reduce the HW radius R_{ext} and can be attributed to the fact that the $\gamma = [1, 1, 1, 1, 1]$ Jack polynomial has higher $\bar{n}_{m=8,9}$ values than the single-QH state. As a consequence, for lower values of R_{ext} the energy contribution given by these orbitals may overcome the one relative to orbitals with higher m's, so that the shift in energy caused by the HW confinement on the $L = 35$ edge state may be bigger than that on the single-QH state. Fig. 6.5 shows also that for $m < 7$ the single-QH state has occupation number expectation values which are higher than those of the $\gamma = [1, 1, 1, 1, 1]$ Jack polynomial. Thus, in light of what we have just said, we expect that for even smaller values of R_{ext} the single-QH state will cease to be the first excited one in favor of edge states with lower angular momentum.

This behavior is summarized in the left panel of Fig. 6.6, where we report the R_{ext}-dependence of the energies characterizing the Laughlin state and of its QH and edge excitations. For a fixed
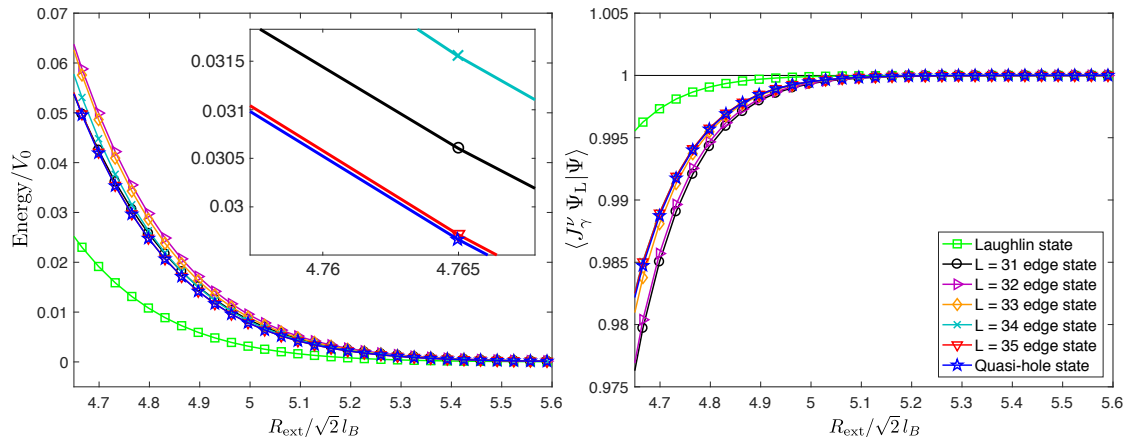
Figure 6.6: Left panel: energetic behavior of the Laughlin state and its single-QH and edge excitations, as function of the potential radius R_{ext}, for fixed values of the potential strength ($V_{ext}/V_0 = 10$) and of the particle number ($N = 6$). As displayed in the inset, it is possible to find an interval of R_{ext} values in which the single-QH state is the first excited one. Right panel: overlaps between the states obtained via exact diagonalization and the Jack trial wave functions describing states in the 1st energy branch. The overlap between the lowest energy eigenstate with $L = 36$ and the single-QH wave function is of the order of 1 for large values of R_{ext}, as expected. However, it is important to notice that it remains very high also for smaller values of R_{ext}, for which the $L = 36$ state is the first excited one. Adapted from Macaluso and Carusotto [2017].

value of V_{ext} there exists in fact a finite range of R_{ext} values in which the single-QH state is indeed the first excited one. At the same time, we stress that, even though for these HW parameters the energies of the Hamiltonian eigenstates are not negligible with respect to the Laughlin gap ($0.1\,V_0$), the overlaps between the states obtained with ED and the $\gamma = [1, \dots]$ Jack polynomials remain extremely high [see Fig. 6.6, right panel], meaning that the first excited state is indeed the single-QH one.

Also the energetic behavior of the other edge states, i.e. those with $32 < L < 35$, can be explained in terms of the occupation numbers reported in Fig. 6.5. We can note indeed that Jack polynomials, describing states in the $k = 1$ energy branch with increasing values of ΔL, are characterized by $\bar{n}_m$ which show peaks at lower m's. Therefore, since for sufficiently large R_{ext} the dominant contribution to $\langle H_{\text{conf}} \rangle$ comes from the large m terms (for which the $\mathcal{U}_m$ potentials have larger values), it is completely reasonable that states with higher ΔL have lower energies. At this point we would like to stress that the decrease of energy as a function of ΔL means that wavepackets made of states forming such an energy branch propagate backwards with respect to the cyclotron orbits, which is in contrast with the usual chiral Luttinger liquid description of the edge modes of a FQH state.

Although this explanation is in complete agreement with our findings for $L \geq 32$, it seems to be in contrast with the energy of the $L = 31$ Hamiltonian eigenstate, which corresponds to the global dipole-like motion of the cloud. The Jack associated with this state has EP $\gamma = [1]$ and it has the highest occupation of the $m = 11$ LLL single-particle wave function. However, this Jack has the peculiarity of having all the other high m occupation numbers lower than those characterizing both the single-QH state and the $\gamma = [1, 1, 1, 1, 1]$ Jack. This explains why the energy of the $L = 31$ state is very close to those of the $L = 35$ and of the single-QH states.

Starting from these intriguing numerical results, a future work could be trying to better understand the physical origin of the deviations from the chiral Luttinger liquid theory (as partially done by Fern et al. [2018]), so to highlight new interesting edge physics, which may include non-linear effects in the edge dynamics that were anticipated by Bettelheim et al. [2006] and might be responsible for the mixing of different modes of the Luttinger liquid.

(In)compressibility of the states

Before entering the discussion on the effects of stronger HW potentials, we would like to complete our analysis of the weak confinement regime with a short study of the response of the Laughlin state and its low-lying excitations to an increase of the HW potential strength V_{ext}. We consider
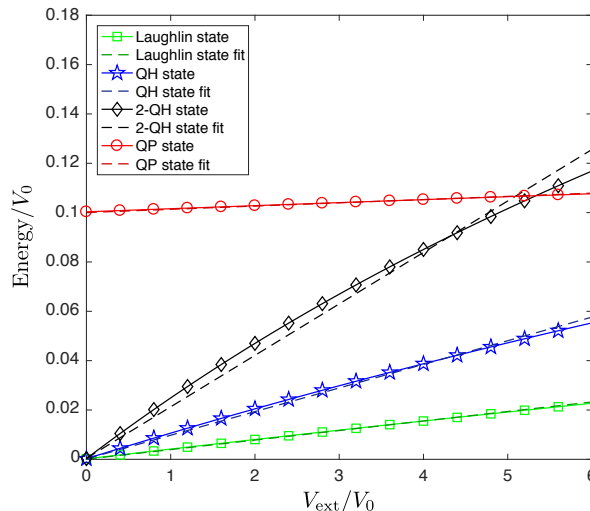
Figure 6.7: Energies of the Laughlin state and its QH and QP excitations (solid lines with markers), as function of the hard-wall potential strength V_{ext}, and the associated linear fits (dashed lines): The more accurate the fit, the weaker the compressibility of the state. As expected, the system compressibility increases when quasihole excitations are inserted in the fluid, while it is not affected by the presence of quasiparticle excitations. For all values of V_{ext}, fixed values of R_{ext} and N have been considered (in particular, $R_{ext}/\sqrt{2}\,l_B = 4.65$ and $N = 5$). Adapted from Macaluso and Carusotto [2017].

this as a way probe the compressibility of these states, which, being one of the most celebrated properties of FQH liquids, could be of great interest, especially in view of future experimental studies.

As reported in Fig. 6.7, the exact diagonailzation energies of the Laughlin state and of the single-QP state[2] grow almost linearly in the external potential strength, confirming the predicted incompressible behavior. On the other hand, the energies of states hosting QHs grow less than linearly, as a function of V_{ext}, which witness the ability of these states to rearrange themselves in response to the confinement. We interpret this behavior as a manifestation of their finite compressibility. As expected, the larger the number of QHs, the stronger this compressibility. Note that a similar compressible behavior is also found for edge excitations (not shown in the figure).

While these results have been found for relatively weak confinement potentials that are not able to generate extra QP excitations in the fluid, in the next section we will see how a strong compression of the cloud is able to distort the density profile of the FQH puddle in quite unexpected ways.

6.2.2   Strong confinement regime

As we have seen, in the weak confinement regime all the physics takes place within the non-interacting state manifold, meaning that it involves only states below the many-body (or Laughlin) gap. In the following we turn our attention to the strong confinement regime instead, where significant mixing with states above the many-body gap can occur and the density distribution characterizing the FQH puddle is spatially compressed in considerable way. Note that the study of this case exhausts the analysis of the physics characterizing a FQH liquid confined by a HW potential.

With no loss of generality, we now consider HW potential strengths V_{ext} of the same order as before, but much smaller radii R_{ext}[3]. For such values of HW strength, the strong confinement condition can be reached as soon as $R_{ext} \gtrsim R_{cl}$.

---

[2]Note that here we name single-QP state the lowest energy state with angular momentum $L = L_L - N$. Such a state lies above the many-body gap and it is characterized by a bump in the density [see upper-left panel in Fig. 6.8] corresponding to about half of a particle.

[3]Note that similar results can be obtained by keeping R_{ext} constant and by increasing the potential strength V_{ext}.
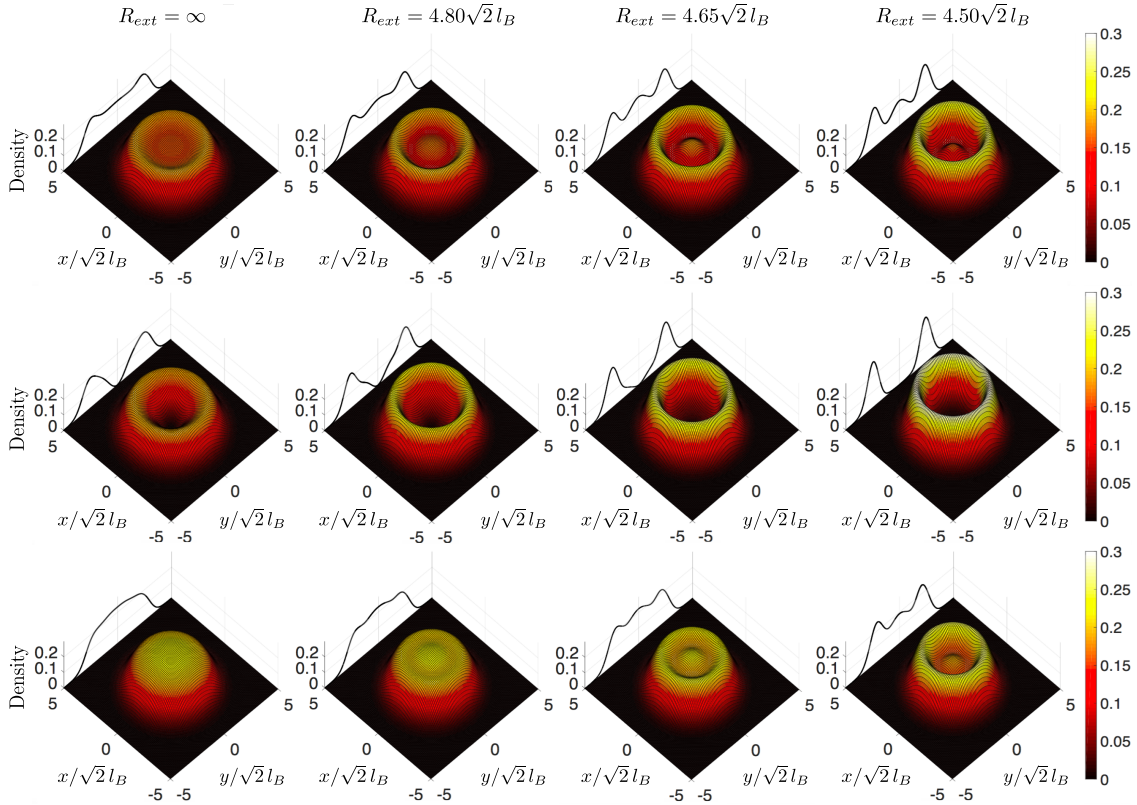

Figure 6.8: Behavior of the density profiles characterizing the Laughlin state (first row), the single-QH state (second row) and the single-QP state (third row), as function of the hard-wall radius R_{ext}, for given potential strength $V_{ext}/V_0 = 100$ and particle number $N = 6$. As we can see, more we reduce the potential radius R_{ext} (from left to right), more the densities of the Laughlin state and its excitations decrease at the center. Densities normalization have been chosen by imposing that spatial integral (over the whole 2D plane) of the density profile has to be equal to the total number of particles N. Taken from Macaluso and Carusotto [2017].

For sufficiently strong potentials, the lowest part of the spectrum is formed by many-body states having total angular momenta lower than the one of the $\nu = 1/2$ Laughlin state, i.e. lower than $L_{\text{L}} = N(N-1)$. Even though for no (or weak) confinement all Hamiltonian eigenstates with $L < L_{\text{L}}$ have energies which lie above the Laughlin gap, the effect of the confining potential is in fact much smaller on these states than on the spatially more extended states of the Laughlin type (i.e. described by wave functions of the form (5.5)). Therefore, in the presence of sufficiently strong confinements, one can have the swap of their relative order in energy.

Although this peculiar energetic ordering of the Hamiltonian eigenstates can be considered as physically expectable, it is accompanied by a surprising behavior of the density profiles, that we report in Fig. 6.8 for the Laughlin state and its QH and QP excitations: the more we squeeze the system (by reducing R_{ext}), the more the the density at the center of the droplet decreases. This apparently counterintuitive behavior can be explained by taking into account the total angular momentum conservation imposed by the rotational invariance of the Hamiltonian.

As discussed in Sec. 5.1, many-body states defined in the LLL (and so the eigenstates of the Hamiltonians under study) can be expressed as a linear combination of elements of the occupation number basis sharing the same angular momentum [see Eq. (5.3)]. Therefore, a large occupation of high m orbitals must be compensated by a large occupation of the low m orbitals as well. As the confining potential mostly affects the high-m orbitals, the minimization of the confinement energy leads to a reorganization of the Hamiltonian eigenstates in favor of those configurations which have a reduced occupation of high-m orbitals and, consequently, of low-m orbitals as well. Finally, since the density at the center of the droplet is determined by the occupation low-m states, the mechanical compression of the FQH puddle from outside leads to a clear depletion of the central region as well, as displayed by the $r \approx 0$ region of the right-most panels of Fig. 6.8.
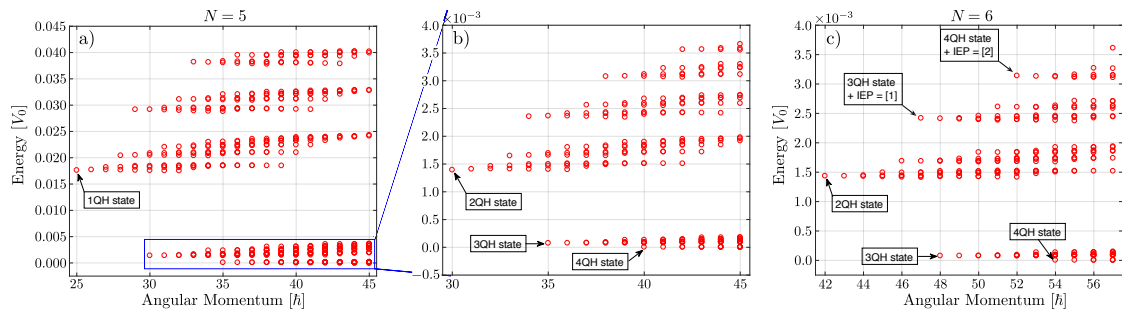
Figure 6.9: Many-body spectra for $N = 5$ (a) and b)) and for $N = 6$ (c)) particle systems experiencing a piercing potential of parameters $V_{in}/V_0 = 2$ and $R_{in}/\sqrt{2}\,l_B = 0.5$. THese spectra clearly show an energetic behavior characterized by the presence of branches and subbranches. By comparing a) and b), a recursive structure taking place at different energy scales can also be appreciated. On the other hand, the comparison between a) and c) proves that the structure of the spectra does not depend much on the number of particles, as expected from the arguments based on the eigenstate description in terms of Jack polynomials. Adapted from Macaluso and Carusotto [2018].

6.3 Pierced geometries: a hard-wall potential piercing the system

In the previous section we have studied the physics characterizing FQH droplets confined in a disk-shaped region by a single HW potential of strength $V_{ext} \neq 0$. Here we consider the opposite case where the confinement potential in Eq. (6.3) has $V_{ext} = 0$ and consists of a single inner repulsive HW of strength V_{in} which spatially extends to the region described by $r < R_{in}$. As we will see, FQH liquids in these so-called pierced geometries, are characterized by many-body spectra showing massively (quasi-)degenerate ground-state manifolds accompanied by recursive structures of energy branches and subbranches.

As done in Sec. 6.2 for disk-shaped geometries, in the following we propose a description of the observed spectral properties in terms of Jacks, which is then quantitatively validated in terms of the overlaps between the states obtained via ED and the proposed Jack trial wave functions. Then, we show how to identifying different Jacks with specific excitations of the FQH cloud, to give a physical interpretation of the numerically obtained spectra in terms of QH and edge excitations. Finally, we conclude the section with an accurate study of the inner-edge excitations, for which we have found an unexpected relation between their density profiles and the value of the angular momentum ΔI characterizing them.

6.3.1 Jack description of the energy spectra

As it happens in the case of disk-shaped geometries, also FQH liquids in pierced geometries have energy spectra showing a recursive structure of energy branches, which in turn organize themselves in different subbranches [e.g. in Fig. 6.9]. While the subbranch structure is qualitatively the same for all branches, its characteristic energy scale strongly depends on the specific branch we are looking at. Moreover, for large enough angular momenta ($L \geq L_{GSM}$), we can observe a (quasi-)degenerate ground-state manifold (GSM) made of a huge number of states and starting at an angular momentum value L_{GSM} (which depends on the potential parameters V_{in} and R_{in}).

In analogy to what we have done in Sec. 6.2, we can attempt a description of the many-body spectra, again obtained by diagonalizing the system Hamiltonian [see Appendix A], in terms of Jack polynomials also for the case of pierced geometries. The one-to-one correspondence between Jack polynomial wave functions and the Hamiltonian eigenstates found via ED is numerically proved in Table 6.2, reporting the overlaps between some eigenstates of the system and the corresponding Jacks. While Jack polynomials with EPs of the form $\gamma = \sigma^\kappa + [1, \ldots, 1]$ have overlaps which can be considered equal to 1, small discrepancies are present in the other cases. Despite being of the order of only few percents, these deviations can be almost completely attributed to the non-orthogonality of the Jacks with parameter $\beta = 2/3$ and partitions $\Omega + \gamma$, as already discussed in Sec. 6.2.1 [see for instance Table 6.1], where (almost) orthogonal wave functions of the form

EP	Eigenstate index	(κ, ρ_1)	$\langle J_{\Omega+\gamma}^{-2}|\Psi\rangle$
$\gamma = [2,2,2,2,2,2]$	1st $L = 42$	$(2,0)$	0.9999
$\gamma = [7,2,2,2,2,2]$	1st $L = 47$	$(2,0)$	0.9886
$\gamma = [6,3,2,2,2,2]$	2nd $L = 47$	$(2,0)$	0.9710
$\gamma = [5,4,2,2,2,2]$	3rd $L = 47$	$(2,0)$	0.9584
$\gamma = [5,3,3,2,2,2]$	4th $L = 47$	$(2,0)$	0.9712
$\gamma = [4,4,3,2,2,2]$	5th $L = 47$	$(2,0)$	0.9733
$\gamma = [4,3,3,3,2,2]$	6th $L = 47$	$(2,0)$	0.9795
$\gamma = [3,3,3,3,3,2]$	7th $L = 47$	$(2,1)$	0.9999

Table 6.2: Overlaps of several many-body eigenstates $|\Psi\rangle$, calculated through exact diagonalization of the Hamiltonian, with the corresponding Jack polynomials, for a system of $N = 6$ particles subject to a piercing potential of parameters $V_{\text{in}} = 2V_0$ and $R_{\text{in}} = 0.5\sqrt{2}l_B$. While the Jacks considered are labeled by their EPs, the corresponding ED eigenstates are identified by a couple of integers (κ, ρ_1), corresponding to the branch and subbranch indices, but also through the total angular momentum eigenvalue plus an ordinal number indicating the eigenstate position along the energy axis. For instance, the state denoted by 1st $L = 42$ corresponds to the lowest energy state with angular momentum $L = 42$, that belongs to the $\rho_1 = 0$ subbranch of the $\kappa = 2$ branch.

$J_\gamma^{1/2}J_\Omega^{-2}$ have been found to give better results. Note that, for the particular case of Jacks with EPs given by $\gamma = \sigma^\kappa + [1, \dots, 1]$, the wave functions $J_{\Omega+\gamma}^{-2}$ and $J_\gamma^\nu J_\Omega^{-2}$ coincide, explaining why the calculated overlaps are much higher in these cases.

This analysis of the energy spectra in terms of Jacks allows us to identify the lowest angular momentum states of each energy branch as a Jack polynomial with EP $\sigma^\kappa = [\kappa, \kappa, \dots, \kappa]$, namely as a κ-QH state, while the other states of the branch can be associated with Jacks having EPs of the form $\gamma = [\gamma_1, \gamma_2, \dots, \gamma_{N-1}, \gamma_N = \kappa]$ [4]. Therefore, any branch of the energy spectrum can be univocally labeled with the value of γ_N characterizing the states forming it.

Similarly, the value of the $(N-1)$-th element γ_{N-1} of the EP γ, or actually the value of $\rho_1 = \gamma_{N-1} - \gamma_N$, can be used to label the different subbranches. In particular, the lowest energy subbranch of the κ-th branch, namely the one with the κ-QH state as lowest L state, is made of all edge excitations described by Jacks with $\gamma_{N-1} = \kappa$ which means $\rho_1 = 0$; the next energy subbranch (the first excited one) contains all edge excitations with $\gamma_{N-1} = (\kappa + 1)$, i.e. $\rho_1 = 1$; and so on for the higher values of γ_{N-1}. Of course, further spectral structures can be observed inside the different subbranches; for them an analogous reasoning in terms of the values of γ_{N-2} can be put forward.

After the above discussion, it is straightforward to associate the particular energy scale characterizing a given energy branch to the value of $\mathcal{U}_m$ for the innermost occupied orbital, namely the one with $m = \gamma_N = \kappa$. In particular, the fact that the values $\mathcal{U}_m$ rapidly decrease with m [see the example in Fig. 6.1] explains the very different energy scales observed for consecutive branches.

Moreover, we would like to stress that states described by Jacks which only differ for the value of γ_1 have energies which are almost indistinguishable, at least as long as the system contains a large enough number of particles. On the one hand, this explains why the physics of the system is not affected by what happens to the outer edge. On the other hand, it suggests that if N is sufficiently large the energetic behavior of the FQH liquid in the pierced geometry is almost completely independent of the particle number, as one can see by comparing the many-body spectra in panels b) and c) of Fig. 6.9. At the same time, we have found that the GSMs characterizing FQH liquids in this geometry are formed by all states presenting at least κ_{GSM} QHs and their edge excitations having $\gamma_N \geq \kappa_{\text{GSM}}$[5].

Even though the fact that a single repulsive HW potential cannot select a non-degenerate ground state (with a well-defined number of QHs) might seem obvious, it highlights the crucial role played by the external trapping in the selection of the number of QH excitations in the system ground state. A detailed study of this physics will be the subject of Sec. 6.4 and of Appendix B.

---

[4]Since γ must be a partition, the condition $\gamma_N = \kappa$ implies $\gamma_i \geq \kappa$ for all $i = 1, \dots, N-1$.

[5]Note that this allows us to express the minimum angular momentum of a state in the GSM as $L_{\text{GSM}} = L_{\text{L}} + \kappa_{\text{GSM}} N$.
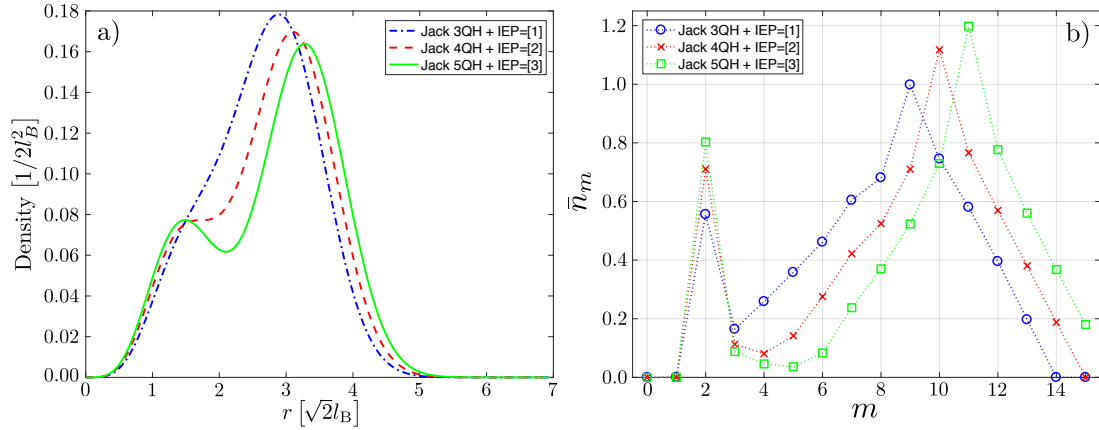
Figure 6.10: a) Radial density profiles and b) occupation number expectation values associated with the 3-QH state with the $\rho = [1]$ IEE, the 4-QH state with the $\rho = [2]$ IEE, and the 5-QH state with the $\rho = [3]$ IEE. Even though for all these states the lowest m occupied orbital is the $m = 2$ one, its occupation is different for the considered states. The 5-QH state with the $\rho = [3]$ IEE is for instance the state characterized by the highest occupation of the $m = 2$ orbital. In terms of densities, this is reflected in the higher density of the 5-QH state with the $\rho = [3]$ IEE in the inner region $r < 1.5\sqrt{2}l_B$. Adapted from Macaluso and Carusotto [2018].

6.3.2   A closer look at the excitation of the inner edge

Actually more information about the physics of the IEEs can be extracted from the previous observations. As we have discussed in Sec. 5.2.3, Jacks with EPs $\gamma = [\gamma_1, \gamma_2, \ldots, \gamma_{N-1}, \kappa]$ can also describe states which correspond to IEEs of QH states containing more than κ QHs. To be more precise, since the j-th subbranch of the κ-th branch is formed by all states with EPs of the form $\gamma = [\gamma_1, \gamma_2, \ldots, \gamma_{N-2}, (\kappa + j), \kappa]$, the lowest angular momentum state in this subbranch will be the one with EP $\gamma = [(\kappa + j), \ldots, (\kappa + j), \kappa]$. At the same time, we can rewrite such a partition as $\sigma^{(\kappa+j)} - \rho = [(\kappa+j), \ldots, (\kappa+j), (\kappa+j)] - [j]$, which corresponds to the EP associated with the $(\kappa + j)$-QH state sustaining the IEE described by $\rho = [j]$ [see Eq. (5.10)]. Therefore we can conclude that the j-th subbranch is composed of such a state and all its OEEs satisfying the conditions $\gamma_{N-1} = \kappa + j$ and $\gamma_N = \kappa$. Note that this observation explains why we choose $\rho_1 \equiv \gamma_{N-1} - \gamma_N$ as a label for the different subbranches.

According to our interpretation of the energy spectra and of the states forming the different branches, the $\rho = [j]$ IEE of the $(\kappa+j)$-QH state (having $\gamma = [\kappa+j, \ldots, \kappa+j, \kappa]$) and the $\rho = [j-1]$ IEE of the $(\kappa+j-1)$-QH state (having $\gamma = [\kappa+j-1, \ldots, \kappa+j-1, \kappa]$) belong to the same energy branch, as both of them have EPs with $\gamma_N = \kappa$. At the same time, the former state will be part of a higher energy subbranch, since the $(N-1)$-th element of its EP is larger than the one of the latter state ($\kappa + j > \kappa + j - 1$). As a consequence, since the energy of the different states below the many-body gap is determined by the overlap with the inner repulsive potential, this suggests that the $\rho = [j]$ IEE of the $(\kappa+j)$-QH state explores the inner regions more substantially than the $\rho = [j-1]$ IEE of the $(\kappa+j-1)$-QH state, which is a quite unexpected fact.

To be more clear, let us consider for instance the $\rho = [2]$ IEE of the 4-QH state and the $\rho = [1]$ IEE of the 3-QH state of an $N = 6$ particle system [see panel c) of Fig. 6.9 and Fig. 6.10]: The former state has root configuration $|0\,0\,1\,\underline{0}\,0\,0\,1\,0\,1\,0\,1\,0\,1\rangle$, while for the latter it is given by $|0\,0\,1\,0\,0\,1\,0\,1\,0\,1\,0\,1\,0\rangle$. In both cases the innermost occupied orbital is the one with $m = 2$. However, in the first root configuration all other particles (i.e. those occupying the outermost orbitals) are shifted by one angular momentum unit with respect to those in the second configuration, as highlighted by the presence of an additional empty orbital [see the underlined zero in the above formula]. Therefore, one could think that the 4-QH state with the $\rho = [2]$ IEE would be less affected by the HW potential with respect to the 3-QH state with the $\rho = [1]$ IEE. Quite unexpectedly, Fig. 6.10 actually shows that is not the case.

On the one hand, Fig. 6.10 a) shows that states belonging to higher energy subbranches are characterized by higher values of the density in the inner region, in agreement with our guess that the $\rho = [j]$ IEE of the $(\kappa + j)$-QH state explores more internal regions as compared with the $\rho = [j - 1]$ IEE of the state with $\kappa + j - 1$ QHs. On the other hand, Fig. 6.10 b) reports the

occupation number expectation values $\bar{n}_m$, taken on the Jack polynomials describing the lowest angular momentum states of different subbranches: The lowest-m occupied orbital is the same for all states within a given energy branch since they are characterized by the same value of γN; however, the mean occupation of such an orbital increases (as the energy does), as a function of ρ_1.

Note that, even if the pierced geometry studied here will hardly be of experimental relevance, it has proven that the Jack polynomial formalism we developed in Sec. 5.2.3 for FQH liquids in two-edge geometries provides a very accurate description of the Hamiltonian eigenstates. At the same time, the analysis done in this section has demonstrated that our identification of some particular Jacks with states characterized by the presence of IEEs is completely meaningful and physically relevant. A clear example in this sense is represented by the unexpected relation we have found between IEEs with different ρ and the radial density profiles characterizing them.

6.4   Ring-shaped geometries: two hard-wall potentials

In the preceding sections we studied the effect of a single repulsive HW potential on a bosonic FQH liquid at filling $\nu = 1/2$. While in Sec. 6.2 such a potential has been used to confine the FQH droplet within a disk-shaped region of space, in Sec. 6.3 it has been used to create a hole in the system density and to study the behavior of the excitations of this inner edge. We now investigate the physics of a FQH droplet experiencing two concentric HW potentials confining the system within a ring-shaped region.

The first part of the section is devoted to the discussion of the system ground state. In this context we propose a simple yet efficient method to predict the number of QHs in the ground state by looking at the confining potential shape in the angular momentum basis. Then we study the presence (or absence, depending on the potential parameters) of any regular structure in the energy spectra and the possibility of describing them again in terms of Jack polynomials. Finally we conclude with a brief analysis of the interplay between edge e QH excitations. As we will see, neither the energies nor the density profiles of the edge excitations seem to carry straightforward signatures of the anyonic statistics characterizing QH excitations.

6.4.1   The system ground state

The energy spectra reported in Fig. 6.11 [see panel b) and c)] clearly show that FQH liquids experiencing a confining potential with $V_{\text{in}}, V_{\text{ext}} \neq 0$ have very complicated energy spectra, in which, however, one can easily recognize a non-degenerate ground state. Moreover, independently of the particular values of the potential parameters, the non-generate ground state of the system has been found to have an excellent overlap with an κ-QH state. What depends on the form of the external potential is the number κ of QHs, instead. This fact can be easily explained by looking at the behavior of the potentials $\mathcal{U}_m$ when V_{in} and V_{ext} are both different zero [see the example in Fig. 6.11 a)], and by recalling the form of the root configuration characterizing the κ-QH state, that is $|0^\kappa\, 1\, 0\, 1 \ldots 1\, 0\, 1\rangle$. Root configurations of this kind are indeed the densest in angular momentum space, in the sense that the sequence of 1's and 0's does not contain any additional empty orbital[6]. On the contrary, in the presence of an excitation of one of the edges we would have extra 0's in the root configurations and consequent extra energy contributions coming from higher-valued $\mathcal{U}_m$. As a consequence, both inner and outer EEs of a given κ-QH state will have a higher energy. Therefore, the system ground state must be the κ-QH state which minimizes the energy contributions coming from the different $\mathcal{U}_m$.

The above reasoning not only explains why FQH liquids in ring-shaped geometries always have a ground state which corresponds to a κ-QH state, but it also allows us to predict the number κ of QHs in the ground state simply from the knowledge of the $\mathcal{U}_m$ values. To prove this statement we numerically investigate the dependence of the number of QHs in the ground state on the potential parameters [see Fig. 6.12]. As we already stressed in the previous section, the value of κ depends not only on the parameters of the inner HW potential, but also on those of the external confinement. Therefore, in order to study the dependence of κ on the inner HW radius R_{in}, by keeping V_{in} fixed,

---

[6]We recall that the alternation of empty and occupied orbitals (which manifest itself in the sequence $\ldots 1\, 0\, 1\, 0 \ldots$) is required by the (k, r) admissibility condition discussed in Chapter 5. What makes the root configurations of QH states the densest in angular momentum space is the fact that they do not have more than one 0 between two consecutive 1's.
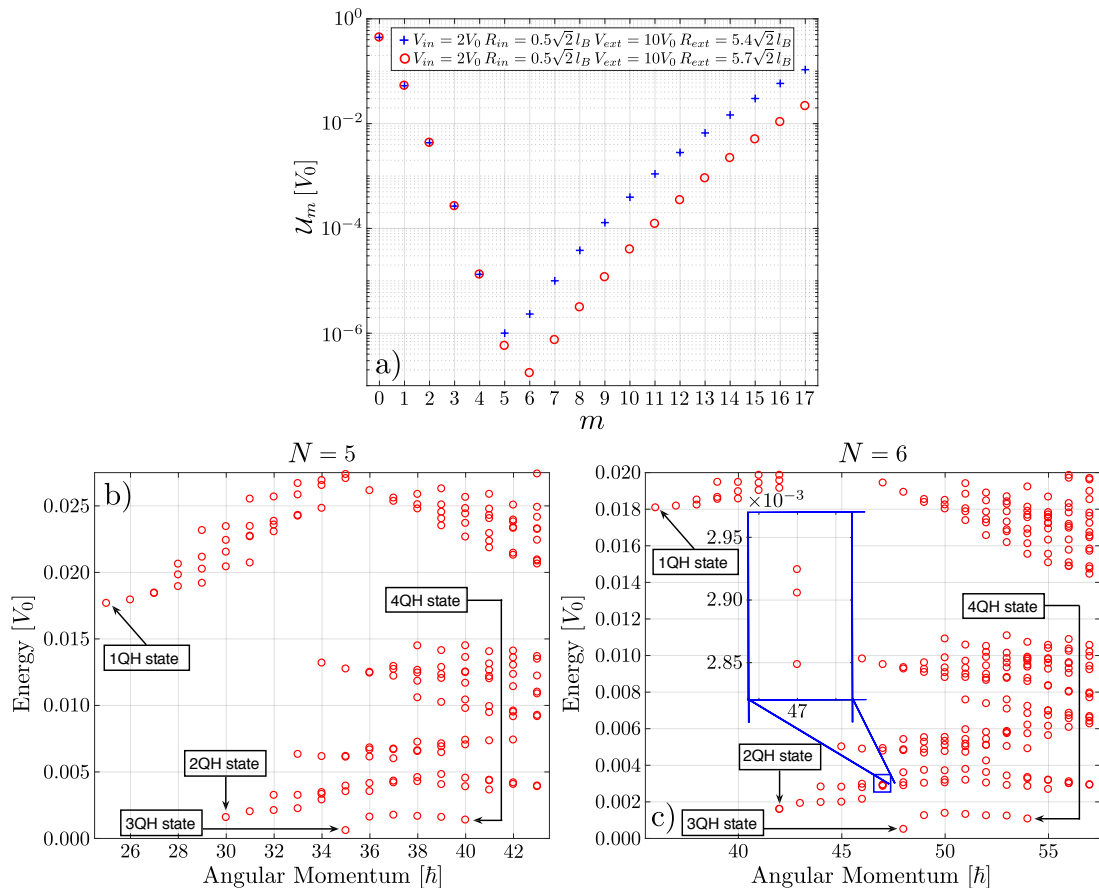
Figure 6.11: a) Values of the $\mathcal{U}_m$ potentials for hard-walls of parameters $V_{\mathrm{in}} = 2V_0$, $R_{\mathrm{in}} = 0.5\sqrt{2}l_B$, $V_{\mathrm{ext}} = 10V_0$ and $R_{\mathrm{ext}} = 5.4\sqrt{2}l_B$ (blue pluses) or $R_{\mathrm{ext}} = 5.7\sqrt{2}l_B$ (red circles). b) Many-body energy spectrum of an $N = 5$ particle system subject to the potential illustrated with blue pluses in a). The ground state is non-degenerate and corresponds to the 3-QH state, while it is hard to point out any energetic structure in the excited states. c) Energy spectrum of an $N = 6$ particle system subject to the potential illustrated by red circles in a). The similarity to the one in b) is a consequence of the similarity of the $\mathcal{U}_m$ in the two cases. In particular, for large m the U_m potentials have a very similar shape except for an outward shift by two orbitals. As a consequence, the energy shifts due to the outermost and innermost occupied orbitals are roughly the same for Jacks with the same EP, but describing $N = 5$ and $N = 6$ particle states. The inset shows the three (almost degenerate) lowest-energy states in the $L = 47$ angular momentum sector. Adapted from Macaluso and Carusotto [2018].

we adopt a constant surface condition to guarantee the balance between the inner and the outer potentials. The introduction of this condition is motivated by the FQH liquid incompressibility and consists in considering only values of R_{in} and R_{ext} which satisfy

$$\mathcal{A} = \pi \left(R_{\mathrm{ext}}^2 - R_{\mathrm{in}}^2 \right), \tag{6.21}$$

where $\mathcal{A}$ is chosen to be the surface delimited by a single HW potential which confines the FQH cloud in the weak-confinement regime [see Sec. 6.2.1]. Notice that choice for $\mathcal{A}$ ensures that for $R_{\mathrm{in}} = 0$ the system ground state is given by the Laughlin state.

Within this condition, the behavior of the energies for different QH state, as a functions of R_{in}, is reported in Fig. 6.12. On the one hand, in Fig. 6.12 b) we show that states having an increasing number of QHs become energetically favorable as the inner HW potential gets wider. On the other hand, in Fig. 6.12 c) we prove that for the values of R_{in} in which a given state has the lowest energy, its overlap with the corresponding κ-QH wave functions is higher than 95%. The deviations from perfect overlap can be attributed to mixing (induced by the confinement) with states lying above the many-body gap.

Finally, Fig. 6.12 a) reports (in logarithmic scale) the potentials $\mathcal{U}_m$ for two particular values
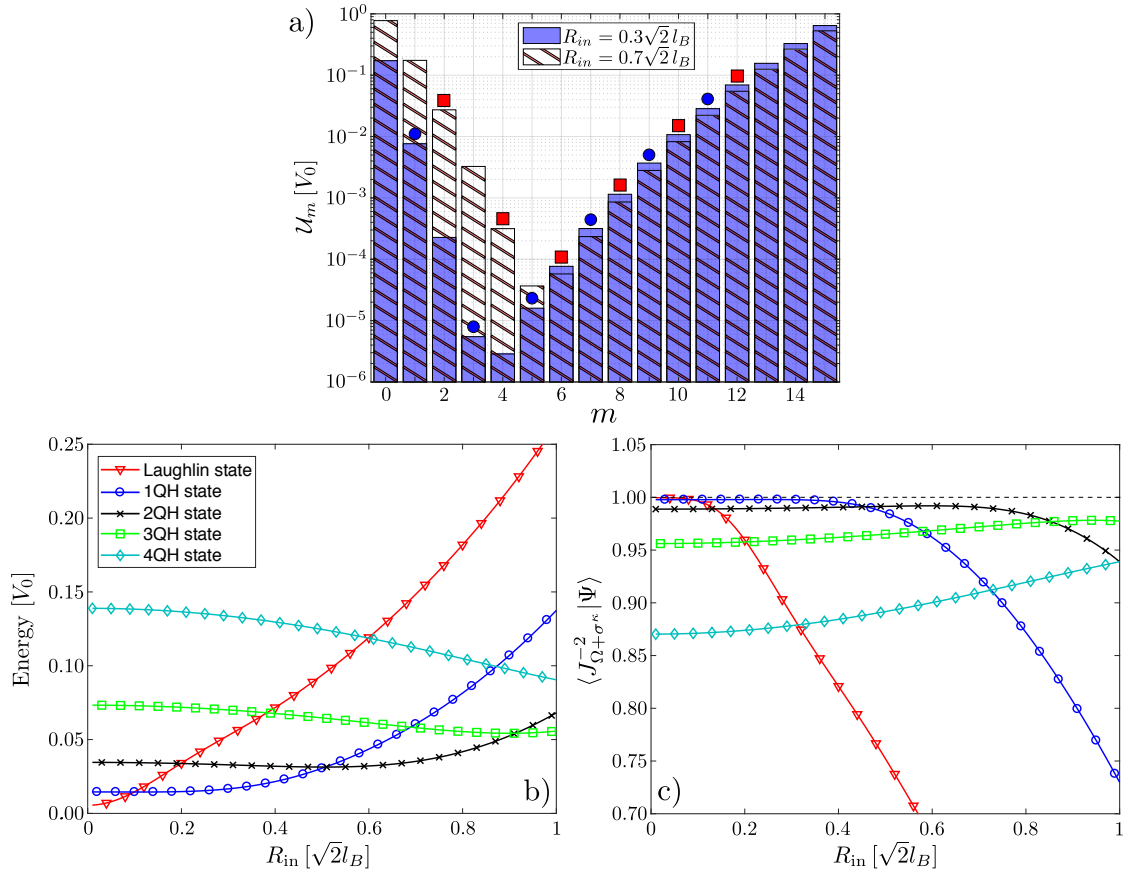
Figure 6.12: a) m-dependence of the $\mathcal{U}_m$ values for $R_{\rm in}/\sqrt{2}\,l_B = 0.3$ (blue bars) or $R_{\rm in}/\sqrt{2}\,l_B = 0.7$ (bars with red stripes). Blue circles and red squares represents the root configuration of the 1-QH and 2-QH states, respectively. b) Energy of the different κ-QH states, as a function of inner hard-wall radius $R_{\rm in}$. As expected, by increasing $R_{\rm in}$, states containing a higher number κ of QHs become energetically favorable. Moreover, by comparing a) and b), we can see that the lowest energy QH state is the one whose root configuration minimizes the energy contribution coming from the different $\mathcal{U}_m$ potentials. c) Overlaps between states obtained with exact diagonalization ($|\Psi\rangle$) and Jacks describing the associated QH states, which show that for any value of $R_{\rm in}$ the lowest energy states is extremely well described by a κ-QH state. In all panels we considered $V_{\rm in} = 2V_0$, $V_{\rm ext} = 100V_0$ and $R_{\rm in}, R_{\rm ext}$ satisfying Eq. (6.21) with $\mathcal{A} = \pi(5.25\sqrt{2}\,l_B)^2$. Adapted from Macaluso and Carusotto [2018].

of $R_{\rm in}$, fixed $V_{\rm in}$ and $V_{\rm ext}$[7], and illustrates how one can predict the number of QHs in the system ground state for a given external potential. For this purpose, let us consider the specific case of $R_{\rm in}/\sqrt{2}\,l_B = 0.7$: Red squares represents particles in the many-body state associated with the root configuration of the $N = 6$ 2-QH state, that is $|n_0\,n_1\,\ldots\rangle = |0\,0\,1\,0\,1\,0\,1\,0\,1\,0\,1\,0\,1\rangle$. Among the root configurations for the different κ-QH states, the previous one minimizes the energy contribution coming from the $\mathcal{U}_m$ potentials, in agreement with the fact that the 2-QH state has the lowest energy for $R_{\rm in}/\sqrt{2}\,l_B = 0.7$ [see Fig. 6.12 b)]. The 1-QH and 3-QH states would in fact require the occupation of the $m = 1$ and $m = 13$ LLL wave functions, respectively, which are both characterized by much-higher values of the $\mathcal{U}_m$ potential.

This method not only allows us to predict the system ground state without diagonalizing the Hamiltonian (which is remarkable just by itself), but it can be also used as a tool to push forward numerical calculations. The above observations, together with the properties characterizing the squeezed Hilbert spaces [see Sec. 5.2.1], indeed allow us to efficiently construct the most suitable Hilbert space for the diagonalization procedure, depending on the potential parameters. A detailed discussion of this last point can be found in Appendix A.

---

[7]We recall that for a given value $R_{\rm in}$, the value of $R_{\rm ext}$ is fixed by the constant surface condition described by Eq. 6.21.

EP	Eigenstate index	$\langle J_{\Omega+\gamma}^{-2}|\Psi\rangle$
$\gamma = [3,3,3,3,3,2]$	1st $L = 47$	0.9954
$\gamma = [4,3,3,3,2,2]$	2nd $L = 47$	0.9813
$\gamma = [4,4,3,2,2,2]$	3rd $L = 47$	0.9926
$\gamma = [4,4,3,3,3,3]$	1st $L = 50$	0.9961
$\gamma = [4,4,4,4,2,2]$	2nd $L = 50$	0.9915
$\gamma = [5,3,3,3,3,3]$	3rd $L = 50$	0.9978
$\gamma = [4,4,4,3,3,2]$	4th $L = 50$	0.9792
$\gamma = [4,4,4,3,3,3]$	1st $L = 51$	0.9970
$\gamma = [5,4,3,3,3,3]$	2nd $L = 51$	0.9865
$\gamma = [4,4,4,4,3,2]$	3rd $L = 51$	0.9811
$\gamma = [6,3,3,3,3,3]$	9th $L = 51$	0.9933

Table 6.3: Overlaps between several Hamiltonian eigenstates $|\Psi\rangle$ and the corresponding Jack polynomials, for a $N = 6$ particle system experiencing two hard-wall potentials of parameters $V_{in}/V_0 = 2$ and $R_{in}/\sqrt{2}\,l_B = 0.5$ and $V_{ext}/V_0 = 10$ and $R_{ext}/\sqrt{2}\,l_B = 5.7$. As in Table **??**, the Jacks considered are labeled by their EPs γ, while the corresponding Hamiltonian eigenstates are identified through their total angular momentum eigenvalue plus an ordinal number indicating the eigenstate position along the energy axis.

6.4.2 Energy branches and Jack description

As compared to the disk-shaped and the pierced geometries discussed in Secs. 6.2 and 6.3, respectively, for FQH liquids in ring-shaped geometries is in general more difficult to identify a regular structure in the energy spectra [see examples in Fig. 6.11]. Nonetheless, as shown in Table 6.3, the one-to-one correspondence between Hamiltonian eigenstates, obtained via ED, and Jack polynomials is perfectly preserved.

However, it is important to stress that this difficulty in observing a clear spectral structure is not intrinsic of the ring-shaped geometry, but rather comes from the small system sizes we are dealing with. Considering systems made of few particles limits in fact the possible extension of the inner piercing potential and, unless special care is taken, typically results in very asymmetric values of the $\mathcal{U}_m$ potentials with respect to their minimum. As a result, states which present excitations of the same kind but on different edge (i.e., IEEs and OEEs with EPs of the form $\gamma = \sigma^\kappa \pm \rho$) typically turn out to be characterized by very different energies. Note that this partially explains the complicate and nested structure of the energy spectra reported in Fig. 6.11.

As a concrete example of this complexity we focus now our attention on the three almost degenerate eigenstates of the $L = 47$ angular momentum sector [see the inset in Fig. 6.11 c)]. Overlaps in Table 6.3 clearly show that the lowest energy state with $L = 47$ corresponds to the $\rho = [1]$ IEE of the 3-QH state, while the second and the third excited states carry excitations of both edges and they have EPs $\gamma = [4,3,3,3,2,2]$ and $\gamma = [4,4,3,2,2,2]$, respectively. On the one hand, these to states differ from the excited one in the presence of an excitation also on the outer edge, which implies a non-vanishing occupation of the $m = 14$ single-particle orbital. On the other hand, they also have a slightly lower occupation of the $m = 2$ orbital. However, for the potential parameters we are considering $\mathcal{U}_{14} < \mathcal{U}_2$ [see Fig. 6.11(a)] and this results into comparable energies for all three states, even if one of them only presents excitation on a single edge.

In spite of the general complexity of the spectra characterizing ring-shaped geometries, a manifest organization of the energies in branches can be recovered if one fine tunes the potential parameters. In particular, one can obtain potential configurations in which excited stares described by EPs of the form $\gamma = \sigma^\kappa \pm [1,\dots]$ (where the $\pm$ sign denotes excitations of the outer and the inner edge, respectively) are almost equally affected by the external confinement. In our case this regime can be obtained by choosing HW potentials such that $\mathcal{U}_2$ and $\mathcal{U}_{14}$ have comparable values.

As an example we show in Fig. 6.13 the many-body spectrum of an $N = 6$ particle system affected by suitably designed external potentials of parameters $V_{in}/V_0 = 20$, $R_{in}/\sqrt{2}\,l_B = 0.5$, $V_{ext}/V_0 = 7$ and $R_{ext}/\sqrt{2}\,l_B = 5.5$. As we can see the ground state for these confining parameters is given by the 3-QH state, in agreement with the previously introduced criterion. On top of that, the lowest-energy excitations are symmetrically organized in two different energy branches, where the lower one extends from the 2-QH state to the 4-QH one and includes all states having excitations with ρ of the form $[1,\dots]$ on one (and only one) of the two edges of the 3-QH state.
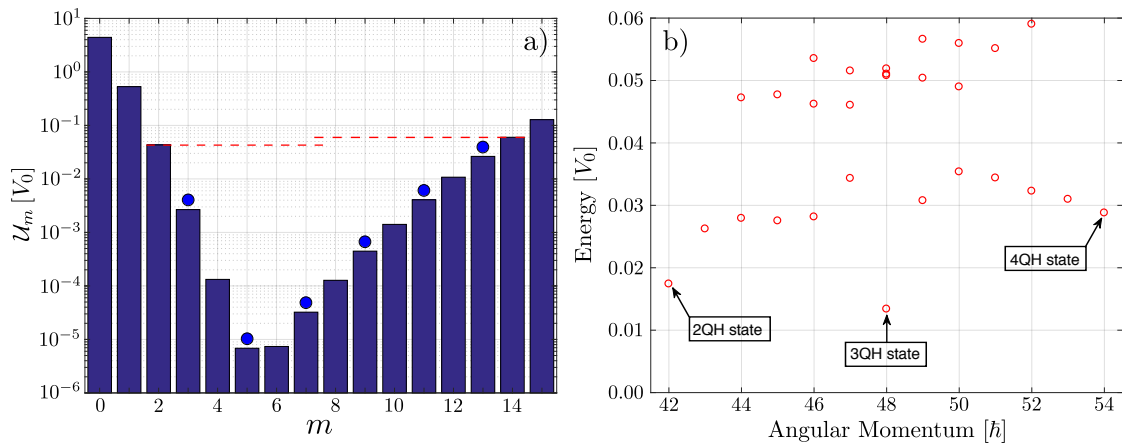
Figure 6.13: a) Plot of the $\mathcal{U}_m$ values for a confinement potential of parameters $V_{in}/V_0 = 20$, $R_{in}/\sqrt{2}\,l_B = 0.5$, $V_{ext}/V_0 = 75$ and $R_{ext}/\sqrt{2}\,l_B = 5.5$. b) Associated $N = 6$ particles spectrum. Blue circles in a) represent the occupied orbitals in the root configuration of the 3-QH state. By recalling that root configurations for the inner-edge excitations (outer-edge excitations) are obtained by moving inward (outward) particles occupying the innermost (outermost) single-particle orbitals, this representation of the ground state root configuration pictorially explains which orbitals are associated with a given inner or outer edge excitation. Since the $\mathcal{U}_2$ and $\mathcal{U}_{14}$ values are comparable [see red dashed lines in a)], the Hamiltonian eigenstates in the spectrum (or at least those with $\bar{n}_i = \langle \Psi | \hat{a}_i^\dagger \hat{a}_i | \Psi \rangle = 0 \; \forall i < 2$ or $i > 14$) are organized in an almost symmetric way. Eigenstates of the lowest branch between the 2-QH and the 3-QH state correspond to Jacks with edge partitions of the form $\gamma = [3, \ldots, 2]$ and are characterized by a non-vanishing occupation of the $m = 2$ orbital, while those between the 3-QH and the 4-QH state have non-vanishing occupation of the $m = 14$ orbital and are well described by Jacks with $\gamma = [4, \ldots, 3]$. Finally, states in the upper branches can be associated with Jacks of edge partitions like $\gamma = [4, \ldots, 2]$ and, as such, describe states presenting both inner-edge and outer-edge edge excitations. Adapted from Macaluso and Carusotto [2018].

The upper branch in formed instead by states presenting excitations of this kind on both edges.

Note that, since IEEs with $\gamma = \sigma^3 - [1, \ldots]$ and OEEs with $\gamma = \sigma^3 + [1, \ldots]$ have non-vanishing occupations of the $m = 2$ and the $m = 14$ orbitals, respectively, the condition $\mathcal{U}_2 \simeq \mathcal{U}_{14}$ implies similar energy shift independently on which edge is actually excited.

6.4.3 Interplay between quasihole and edge excitations

In the following we briefly comment on how the general theory of FQH liquids in ring-shaped geometries presented in this section can be used to address intriguing physical questions such as whether the edge mode properties are affected in any manner by the number of QHs around which these excitations are moving and, in particular, whether one can probe the anyonic statistics of QHs by inspecting the energy spectra or the density profiles associated with such excitations. Although for the moment the answer to these questions is negative, this does not diminish the importance and the utility of the formalism we have developed. As we will see in the next Chapter, the stabilization of states presenting a single QH or two QHs on top of each other represents indeed a crucial step towards the measurement of the anyonic nature of such excitations in ultracold atomic and photonic experiments.

To address these questions, we consider different ring geometries, each of them characterized by a ground state with a different number of QHs. Furthermore, to guarantee that the considered configurations only differ in the number of QHs pinned at the origin, we focus our attention on ad hoc potentials artificially built in terms of $\mathcal{U}_m$. In particular, starting from the $\mathcal{U}_m$ potentials describing the HWs of parameters $V_{in}/V_0 = 2$, $R_{in}/\sqrt{2}\,l_B = 0.5$, $V_{ext}/V_0 = 10$, and $R_{ext}/\sqrt{2}\,l_B = 5.7$, which we denote by $\mathcal{U}_m^{(0)}$, we construct the other sets of potentials $\mathcal{U}_m^{(i)}$ such that $\mathcal{U}_{m+i}^{(i)} = \mathcal{U}_m^{(0)}$ and $\mathcal{U}_q^{(i)} \simeq \mathcal{U}_0^{(0)}$ for $0 \leq q < m$. As we can see from the panels on the left column of Fig. 6.14, this simply represents a global shift of the $\mathcal{U}_m$ towards higher-m values accompanied by the introduction of some arbitrary potentials for the lowest values of m. Note that, since all eigenstates of present
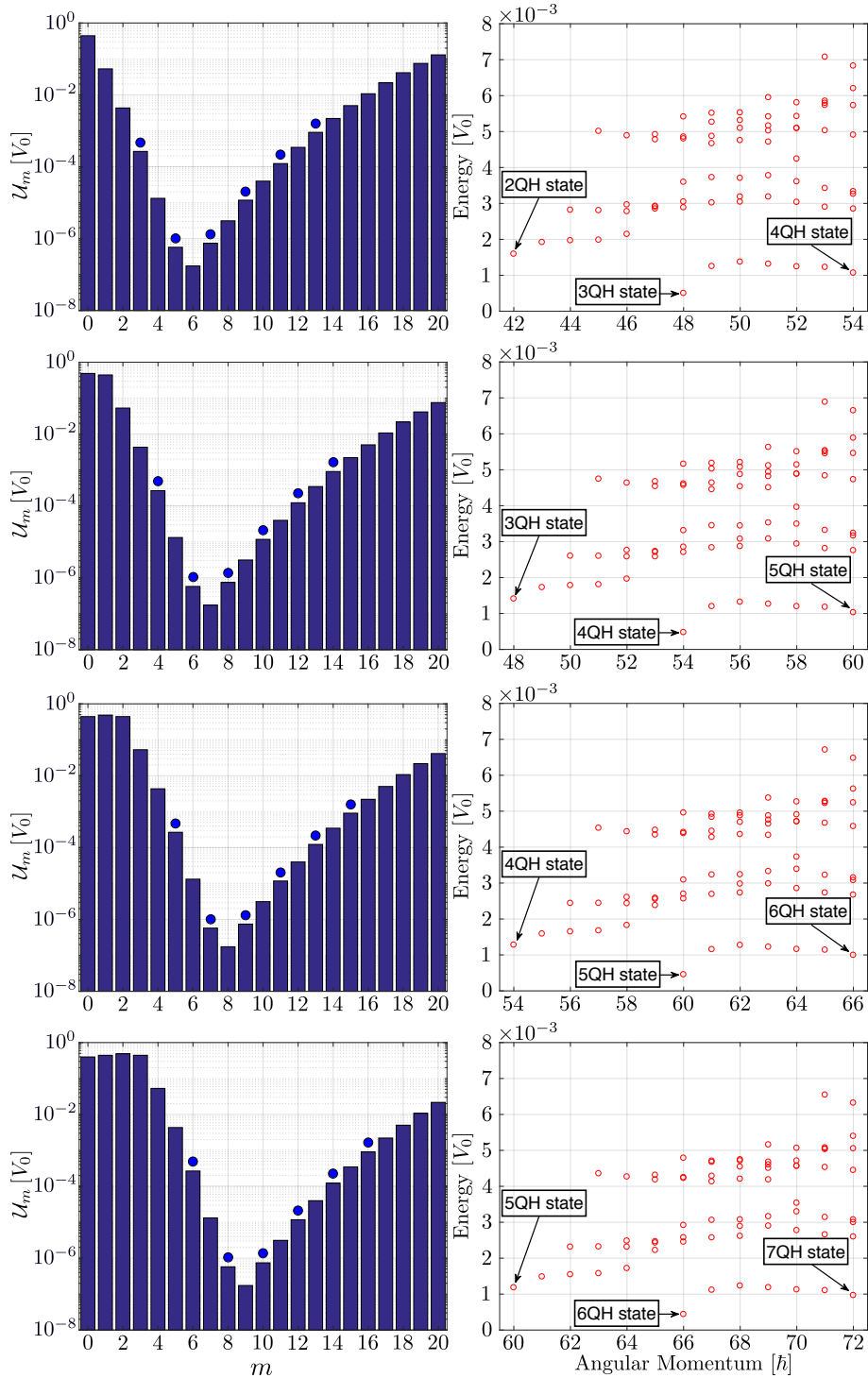
Figure 6.14: Left column: the upper plot shows the $\mathcal{U}_m$ potentials associated with the confining parameters $V_{\mathrm{in}} = 2V_0$, $R_{\mathrm{in}} = 0.5\sqrt{2}l_B$, $V_{\mathrm{ext}} = 10V_0$, and $R_{ext} = 5.7\sqrt{2}l_B$, while the three lower plots display mock $\mathcal{U}_m$ potentials obtained by shifting the previous ones by one, two and three orbitals, respectively. In each panel, blue circles indicate the occupied orbitals in the root configurations of Jacks describing the κ-QH ground state. Right column: energy spectra characterizing $N = 6$ FQH droplets experiencing a confining Hamiltonian with $\mathcal{U}_m$ potentials in the left panels. Energy spectra are almost same for all considered cases and no periodic behavior can be observed as a function of the number of QHs in the ground state. The slow decrease of the excited-state energies, as a function of the number of QHs pinned in the origin, can be imputed to the bigger length of the ring-shaped system edges. Adapted from Macaluso and Carusotto [2018].
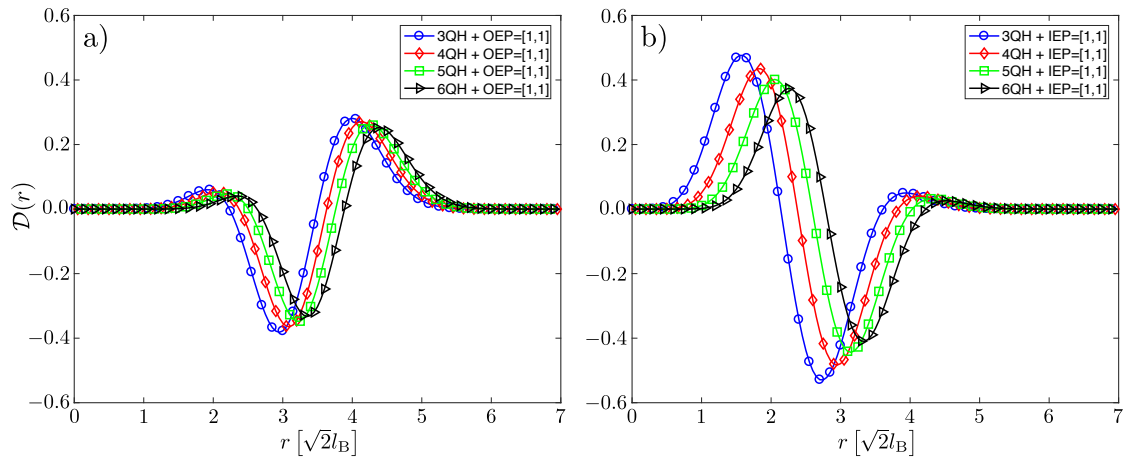
Figure 6.15: a) Rescaled density differences $\mathcal{D}(r)$ associated with the same OEE lying on the edges of QH states containing a different number of QHs. b) The same as a), but for the IEEs. To be precise, the OEE (IEE) with OEP (IEP) of the form $[1, 1]$ has been considered. As it is clearly visible in both panels, having additional QHs in the origin simply results in a outward translation of the curve describing $\mathcal{D}(r)$, which reflects the presence of additional empty orbitals, and in an attenuation of the oscillations characterizing $\mathcal{D}(r)$, which is the consequence of having a longer edge. Adapted from Macaluso and Carusotto [2018].

interest have vanishing occupation of the lowest-m orbitals, actually one can arbitrary choose the values of the lower-m potentials $\mathcal{U}_m$.

As we discussed in Chapter 3, QH excitations of a $\nu = 1/2$ bosonic FQH liquid are anyons with statistical phase $\varphi_{\mathrm{br}}/\pi = 1/2$, also called semions. Therefore, if the spectra and/or the density profiles characterizing the edge excitations of the droplet were in any way affected by the QH anyonic statistics, one should observe a periodicity in the edge excitation properties depending on the number of anyons pinned in the origin. Unfortunately our calculations show that this is not the case. No periodic behavior as a function of the number of QHs at the center of the droplet can be observed in the energy spectra [see right column of Fig. 6.14] or in the density profiles of the edge state [see Fig. 6.15]. On this basis, neither of these quantities seems to be suitable to point out the fractional statistics of QHs. An alternative approach in this direction will be discussed in Chapter 7.

Nevertheless, some interesting features can be still observed in the energy spectra reported in Fig. 6.14. We can note for example that by increasing the number of QHs in the ground state the energies of the edge excitations slightly decrease. In particular, two states associated with Jack polynomials having EPs $\gamma = \sigma^\kappa + \rho$ and $\eta = \sigma^{\kappa+i} + \rho$ end up having different energies even if the $\mathcal{U}_m$ values are properly set. We attribute this behavior to the different length of the edges sustaining the excitation describe by ρ. The rescaled density differences $\mathcal{D}(r)$ show indeed that if such an excitation in create on a longer edge, it induces a smaller density deformation[8]. This provides a reasonable interpretation of why this excitation turns out to be less affected by the confinement when it is created on top of a state presenting a larger number of QHs.

6.5   Conclusions and remarks

In this Chapter we have employed exact diagonalization calculations to study the effect of cylindrically symmetric hard-wall potentials on a bosonic $\nu = 1/2$ fractional quantum Hall droplet.

We have found that, already in the presence of a single hard-wall potential confining the system in a disk-shaped region, the edge excitations show a much richer behavior with respect to those of harmonically confined systems. In particular, we have observed that the hard-wall potential removes the degeneracy between states with the same total angular momentum, giving rise to intricate energy spectra which strongly deviate from the standard predictions of Wen's chiral Luttinger liquid theory. We have then shown that the observed organization of the many-body spectra into energy branches and sub-branches can be fully interpreted in term of Jack polynomials, and

---

[8]Actually the density deformation can be thought to be globally the same but distributed on a longer region.

that there exist a very precise one-to-one correspondence between the Jack ansatz wave functions and the numerically obtained Hamiltonian eigenstates.

After that, we have considered more complicated ring-shaped geometries obtained with two concentric hard-wall potentials. Fractional quantum Hall droplets experiencing this kind of external potentials are characterized by the presence of two different edges, and this has been found to lead to even more complicated energy spectra. Nevertheless, we have shown that still the system eigenstates can be understood in terms of Jacks polynomials, which display excellent overlaps with the exact diagonalization eigenstates and offer a convenient way to classify them. Along this line, it is important to recall a particular feature of the observed spectra, namely that they always have a non-degenerate ground state presenting several quasiholes at the center of the droplet.

From the theoretical point of view, the most exiting outlook of this study is its extension to more complicated fractional quantum Hall states such as the Moore-Read and the Read-Rezayi ones. Although the Jack polynomial formalism has already been extended to the edge excitations of these states by [Jiang and Hu, 2016], at the moment there is no information about the behavior of these edge modes in the presence of a hard-wall confinement. An important question in this direction is whether one can use hard-wall potentials to distinguish the fermionic edge modes, whose presence characterizes the non-Abelian fractional quantum Hall states, from the standard bosonic ones, which we have studied in this Chapter for the Laughlin state.

Finally, we would like to stress that Umucalılar and Carusotto [2017] have proposed an incoherent pumping scheme to stabilize a $\nu = 1/2$ bosonic Laughlin state of light in the presence of the single hard-wall configuration discussed in this Chapter. Their work, together with our analysis of the energy spectra characterizing ring-shaped fractional quantum Hall droplets, suggests that concentric hard-wall potentials could be used in the driven-dissipative photonic context to optimize the stabilization of fractional quantum Hall fluids with an arbitrary number of quasiholes in the origin. As we will see in the next Chapter, states presenting a single quasihole and two quasiholes on top of each other are all one needs to evaluate the anyonic statistics of such excitations through simple density-profile measurements. This makes the content of this Chapter particularly interesting in view of the next-generation experiments with Rydberg polaritons in twisted cavities.

Chapter 7

Anyon detection via angular-momentum and density-profile measurements.

$\mathbb{D}$espite the huge interest in the observation of anyons, mainly in view of their possible application as building blocks to construct topologically protected quantum computers, their existence still lacks a conclusively experimental demonstration. While in solid-state devices quantum Hall interferometry has been the best explored proposal for the detection of anyons [de C. Chamon et al., 1997, Das Sarma et al., 2005, Stern and Halperin, 2006, Bonderson et al., 2006a,b, Chung and Stone, 2006, Campagnano et al., 2012], in ultracold atomic and photonic set-ups also different approaches have been proposed[1]. Among them we recall the idea by Cooper and Simon [2015], then extended to the photonic case by Umucalılar and Carusotto [2017], to demonstrate Haldane's exclusion statistics of quasiholes through spectroscopic measurements, and the proposal by Zhang et al. [2014] to inspect the statistical properties of anyons by looking at the relative angular momentum of two impurities immersed in a fractional quantum Hall bath, then generalized in Zhang et al. [2015] to the case of non-Abelian anyons.

In the previous Chapter, we investigated the edge excitations of trapped fractional quantum Hall clouds, but we could not identify an unambiguous signature of the anyonic statistics in the behavior of the edge excitations on top of Laughlin states presenting a different number quasiholes excitations. In the following we show how the quasihole anyonic statistics can be detected by means of simple density-profile measurements taken on the states presenting a single quasihole and two quasiholes on top of each other. On top of that, our proposal does not rely on any form of interference measurement and, as such, it should be readily applicable in ultracold atomic and photonic set-ups [Gemelke et al., 2010, Clark et al., 2019].

The main results presented in this Chapter are published in Umucalılar et al. [2018] and in Macaluso et al. [2019a].

7.1 Rigid rotations of the anyons

7.1.1 Time-evolution in the co-rotating frame

Our starting point is a two-dimensional (2D) systems made of N particles (bosons or fermions) hosting some anyonic excitations. As usual, the system Hamiltonian $\hat{H}_1$ is a function of particle and position momenta, as well as of time. Thus, by introducing the usual complex coordinate notation $z_j = x_j + iy_j$ for the position of the j-th particle, we can write $\hat{H}_1 = \hat{H}_1(\partial_{z_j}, \partial_{\bar{z}_j}, z_j, \bar{z}_j; t)$. We further assume that the time-dependence of $\hat{H}_1$ is only due to a set of parameters $\eta_\mu(t)$ defining the

---

[1]Note that Nakamura et al. [2019] have recently observed Aharonov-Bohm interference oscillations in the fractional quantum Hall regime. Although in order to measure the anyonic statistics of quasihole/quasiparticle excitations one must be able to add (in a controlled way) such excitations inside the interference path, it seems that the experimental observation of anyons in solid-state devices is only a matter of time [Simon, 2019].
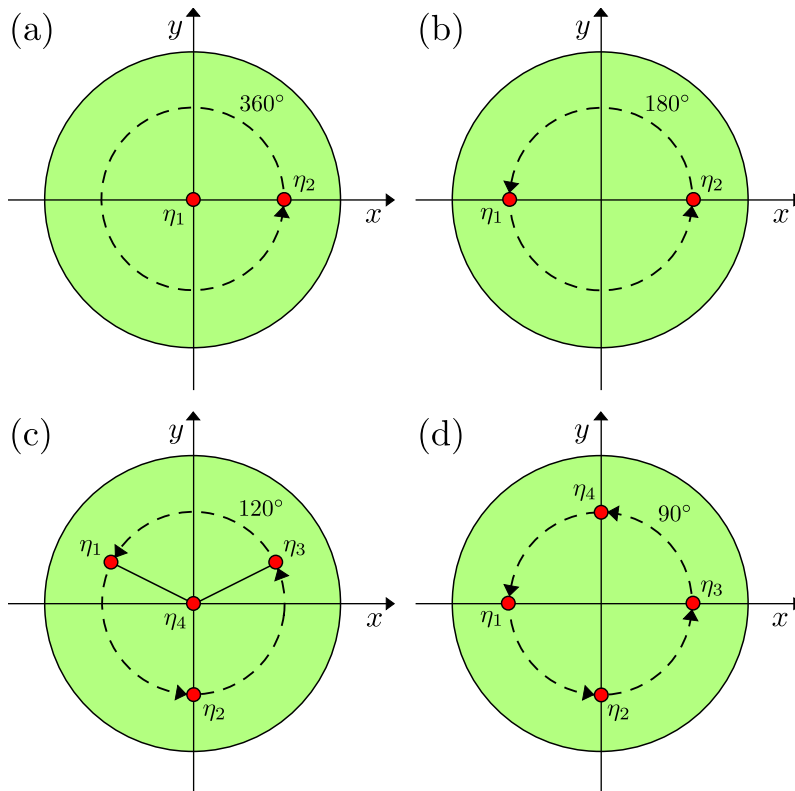
Figure 7.1: Rigid rotations of two anyons [panels (a) and (b)] or four anyons [panels (c) and (d)]. Rotation angles are such that the set of anyonic coordinates (red dots) remains the same after the rigid rotation has been performed.

position of some external impurity potentials $V_{\text{ext}}(z, \eta_\mu(t))$. These local potentials usually couple with the particle density and are responsible for the creation and the pinning of the anyons at positions $\eta_\mu(t)$, as for instance in Paredes et al. [2001], Umucalılar et al. [2018], Macaluso and Carusotto [2018], Wan et al. [2006], Wan et al. [2008] and Prodan and Haldane [2009].

As discussed in Chapter 1, the details of the path adiabatically followed by the anyons in the braiding (exchange) process does not affect their braiding (statistical) phase. Thus, one option is to braid (exchange) the anyons through the rigid rotation of the pinning-potential coordinates [see examples reported in Fig. 7.1]. For a given time t, these transformations are defined as

$$\eta_\mu(t) = \eta_\mu(0)e^{i\theta(t)}, \qquad \theta(t) = \frac{t}{T}\theta_f, \qquad (7.1)$$

where θ_f is the final rotation angle and T is the time duration of the adiabatic process.

Considering rigid rotations has the great advantage that one can study the problem in the reference frame R_2 co-rotating with the anyons, rather then in the laboratory reference frame R_1. At this point we assume that the external potentials $V_{\text{ext}}(z, \eta_\mu(t))$ are only functions of the distance $|z - \eta_\mu(t)|$ between particles and anyons, and that the remaining terms in $\hat{H}_1$ are rotationally invariant. Note that the Hamiltonians describing FQH systems typically satisfy these constraints [see for instance Eqs. (6.5), (6.6) and (6.7)]. Under these assumptions, the generator of the time evolution in R_2 for the time interval $[0, T]$, reads [Pitaevskii and Stringari, 2016]:

$$\hat{H}_2(\partial_{z_j}, \partial_{\bar{z}_j}, z_j, \bar{z}_j; t) = \hat{H}_1(\partial_{z_j}, \partial_{\bar{z}_j}, z_j, \bar{z}_j; t = 0) - \frac{\theta_f}{T}\hat{L}_z, \qquad (7.2)$$

which is explicitly time-independent. On the right-hand side we recognize the initial Hamiltonian in the laboratory reference frame R_1 and a second term, proportional to the angular-momentum operator $\hat{L}_z$, taking into account the effect of rotation. Being interested in an adiabatic process, we consider the limit of $T \to \infty$. As a consequence, the rotation term becomes a small contribution and, as such, can be treated perturbatively.

As we know, in the general case of non-Abelian anyons the Hamiltonian $\hat{H}_1(t = 0)$ is characterized by a m-fold degenerate ground-state manifold $\mathcal{H}_{E_0}$, spanned by the basis $\{|\psi_\alpha\rangle\}_{\alpha=1,\dots,m}$, such

that $\hat{H}_1(t=0)\,|\psi_\alpha\rangle = E_0\,|\psi_\alpha\rangle$ and $\langle\psi_\alpha|\psi_\beta\rangle = \delta_{\alpha\beta}$. Therefore, to study the time-evolution of the system in R_2, we consider an initial state $|\Psi_0\rangle \in \mathcal{H}_{E_0}$ and we apply time-dependent perturbation theory, by considering the rotation term in Eq. (7.2) as a static perturbation that is turned on in the time interval $t \in [0,T]$. The probability that the system at time t has made a transition between $|\Psi_0\rangle$ and a generic state $|\psi_\beta\rangle$ reads [Picasso, 2016]:

$$P_{\Psi_0 \to \beta} = \frac{\theta_f^2}{\hbar^2 T^2}|\,\langle\psi_\beta|\,\hat{L}_z\,|\Psi_0\rangle\,|^2\,\Gamma\left(\frac{E_\beta - E_0}{\hbar}, t\right), \qquad \Gamma(\omega, t) = \frac{\sin^2(\omega t/2)}{(\omega/2)^2}. \tag{7.3}$$

For $T \to \infty$ and finite t/T, this transition probability is non-zero only for states $|\beta\rangle$ with energy E_0. This implies that also the time-evolved state $|\Psi_2(t)\rangle$ belongs to the ground-state manifold $\mathcal{H}_{E_0}$, and that it can be decomposed on the basis $\{|\psi_\alpha\rangle\}_{\alpha=1,\dots,m}$ as

$$|\Psi_2(t)\rangle = e^{-iE_0 t/\hbar} \sum_{\alpha=1}^{m} \gamma_\alpha(t)\,|\psi_\alpha\rangle \qquad \text{with} \qquad \gamma_\alpha(0) = \langle\psi_\alpha|\Psi_0\rangle. \tag{7.4}$$

Note that we could have assume the previous expression for $|\Psi_2(t)\rangle$ by invoking the adiabatic theorem [Born and Fock, 1928, Rigolin and Ortiz, 2012], which ensures that the time-evolution of the system is restricted to $\mathcal{H}_{E_0}$, as long as the dynamics is slow enough. By applying the Schrödinger equation to $|\Psi_2(t)\rangle$, we recover the time-evolution equation of the γ_α coefficients:

$$i\hbar \frac{\mathrm{d}\gamma_\alpha(t)}{\mathrm{d}t} = -\frac{\theta_f}{T} \sum_{\beta=1}^{m} \mathcal{L}_{\alpha\beta}\,\gamma_\beta(t), \tag{7.5}$$

where $\mathcal{L}_{\alpha\beta} = \langle\psi_\alpha|\hat{L}_z|\psi_\beta\rangle$ are the angular-momentum matrix elements between the basis states spanning $\mathcal{H}_{E_0}$. The previous equation is solved by

$$\gamma_\alpha(t) = \sum_{\beta=1}^{m} \left[e^{i\theta_f \mathcal{L} t/(\hbar T)}\right]_{\alpha,\beta} \gamma_\beta(0), \tag{7.6}$$

meaning that, the state describing the system in the co-rotating reference frame R_2 at time $t = T$ will be

$$|\Psi_2(T)\rangle = e^{-i\hat{H}_2 T/\hbar}\,|\Psi_0\rangle = e^{-iE_0 T/\hbar}\,e^{i\theta_f \mathcal{L}/\hbar}\,|\Psi_0\rangle, \tag{7.7}$$

in terms of the matrix exponential $\exp[i\theta_f \mathcal{L}/\hbar]$.

To find the state $|\Psi_1(T)\rangle$ in the laboratory frame, we need to rotate $|\Psi_2(T)\rangle$ by an angle θ_f:

$$\boxed{|\Psi_1(T)\rangle = e^{-i\theta_f \hat{L}_z/\hbar}\,|\Psi_2(T)\rangle = e^{-iE_0 T/\hbar}\,e^{-i\theta_f \hat{L}_z/\hbar}\,e^{i\theta_f \mathcal{L}/\hbar}\,|\Psi_0\rangle} . \tag{7.8}$$

Note that the state in Eq. (7.8) is the exact result for an adiabatic braiding process performed through a rigid rotation of all anyons by an angle θ_f. In the previous expression we recognize a dynamical phase proportional to T, that is completely irrelevant to the discussion of anyonic statistics and therefore neglected from now on. The remaining geometric contribution is the product of two unitary matrices: $\mathcal{B}$, with matrix elements $\mathcal{B}_{\alpha\beta} = \langle\psi_\alpha|\,e^{-i\theta_f \hat{L}_z/\hbar}\,|\psi_\beta\rangle$, and $\mathcal{U}_\mathrm{B} \equiv e^{i\theta_f \mathcal{L}/\hbar}$, which can be prove to be the Berry matrix of the adiabatic process under study, once one makes a suitable choice of the basis states for each angle $\theta(t)$ [see Sec. 7.1.2].

To guarantee that the ground-state manifold is $\mathcal{H}_{E_0}$ at both initial and final times [see Sec. 1.4], the rotation angle θ_f must be such that $\hat{H}_1(t)$ is the same at $t = 0$ and T. Depending on the anyon positions, this constraint can be satisfied even for rotation angles which are not multiple of 2π [see Fig. 7.1 (b)-(d)]. When $\theta_f = 2\pi k$, with k integer, $\mathcal{B}$ is trivially the identity matrix. In this case, $\mathcal{U}_\mathrm{B}$ encodes the full geometrical contribution to the time evolution, made up of both topological and non-topological parts. We stress that $\mathcal{U}_\mathrm{B}$ only depends on measurable properties of the ground-state manifold at the initial time, namely the angular-momentum matrix elements. Therefore no actual time evolution is needed to measure it, which constitutes an undeniable experimental (and theoretical) advantage. For $\theta_f \neq 2\pi k$ instead, the basis-change matrix $\mathcal{B}$ is not proportional to the identity, in general, and it can also have non-vanishing off-diagonal matrix elements. From the experimental point of view this is not the optimal situation, since one cannot easily measure the entries of $\mathcal{B}$. However, the case of $\theta_f \neq 2\pi k$ can be extremely useful in the theoretical context, where –in contrast with experimental studies– nothing precludes the extraction of $\mathcal{B}$. In particular, by computing $\mathcal{U}_\mathrm{B}$ and $\mathcal{B}$ for these rotations, one can demonstrate that the unitary transformation $\mathcal{U}(T)$ has non-vanishing off-diagonal matrix elements, without performing any kind of time evolution [see Sec. 7.4].
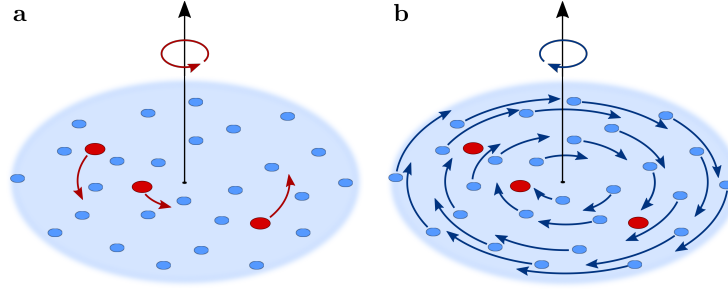
Figure 7.2: Schematic pictures of the rigid rotation of the anyons (a) and of the particles (b). Taken from the supplemental material of Macaluso et al. [2019a].

7.1.2 The adiabatic theorem for rigid rotations of the anyons

In the following we show how the expression in Eq. (7.8) can be alternatively obtained through the straightforward application of the adiabatic theorem in a suitable gauge –i.e., for an appropriate choice of the basis states $\{|\psi_\alpha(t)\rangle\}$. This will make clear why we denoted with $\mathcal{U}_\mathrm{B}$ and $\mathcal{B}$ the geometric contributions entering in Eq. (7.8).

As we have widely discussed in Chapter 1, when considering the adiabatic braiding (or exchange) of anyons, the Hamiltonian parameters varied in time can be identified with the positions of the external potentials pinning the anyons at coordinates $\eta_\mu(t)$. For the special case of rigid rotations of the anyons, where $\eta_\mu(t) = \eta_\mu(0)e^{i\theta(t)}$ [Fig. 7.2 (a)], the only relevant parameter is actually the rotation angle $\theta(t)$ [see Eq. (7.1)].

We further assume that

$$\hat{H}(z_j, t) = \hat{\mathcal{R}}^\dagger_{-\theta(t)}\,\hat{H}(z_j, 0)\,\hat{\mathcal{R}}_{-\theta(t)} = \hat{H}(z_j e^{-i\theta(t)}, 0) \tag{7.9}$$

at any time t, where we introduced the particle-rotation operator

$$\hat{\mathcal{R}}_{\theta(t)} = e^{-i\theta(t)\hat{L}_z/\hbar}. \tag{7.10}$$

Note that Eq. (7.9) is generally satisfied by FQH Hamiltonians with potential terms which only depends on the distance $|z_j - \eta_\mu(t)|$ of the particles from the anyonic coordinates, as those considered in the previous section.

For Hamiltonians satisfying Eq. (7.9), the non-dynamical contributions to unitary transformation $\mathcal{U}(T)$ [see Sec. 1.4], associated with the rigid rotation of the anyons, can be rewritten in a simpler fashion. We define the basis states at time t starting from those of the initial basis and by rotating all the particles [Fig. 7.2 (b)], i.e.

$$|\psi_\alpha(t)\rangle = \hat{\mathcal{R}}_{\theta(t)}|\psi_\alpha(0)\rangle. \tag{7.11}$$

This particle-rotation (PR) basis differs from the one obtained by following the time evolution of the anyon coordinates, i.e. by substituting $\eta_\mu(0)$ with $\eta_\mu(t)$ in the basis states at initial time, as done for instance by Bonderson et al. [2011]. With this second approach one would obtain what we named anyon-rotation (AR) basis

$$|\tilde{\psi}_\alpha(t)\rangle = \mathcal{S}_{\theta(t)}|\tilde{\psi}_\alpha(0)\rangle, \tag{7.12}$$

where $\mathcal{S}_{\theta(t)}$ is the anyon-rotation transformation mapping a generic wave function $\Psi(\eta_\mu; z_j)$ into $\Psi(\eta_\mu e^{i\theta(t)}; z_j)$. Although in general $|\psi_\alpha(t)\rangle \neq |\tilde{\psi}_\alpha(t)\rangle$, Eq. (7.9) ensures that both basis span the same subspace $\mathcal{H}_{E_0(t)}$ at any time t.

Working with the PR basis, allows us to express the Berry connection (1.15) in terms of the angular momentum $\hat{L}_z$,

$$\mathcal{A}^\theta_{\alpha\beta} = \frac{1}{\hbar}\langle\psi_\alpha(\theta)|\hat{L}_z|\psi_\beta(\theta)\rangle = \frac{1}{\hbar}\langle\psi_\alpha(0)|\hat{\mathcal{R}}^\dagger_{\theta(t)}\hat{L}_z\hat{\mathcal{R}}_{\theta(t)}|\psi_\beta(0)\rangle = \frac{1}{\hbar}\langle\psi_\alpha(0)|\hat{L}_z|\psi_\beta(0)\rangle, \tag{7.13}$$

where $\theta \in [0, \theta_f]$, and where we used the fact that $\hat{L}_z$ and $\hat{\mathcal{R}}_{\theta(t)}$ commute. As a consequence the Berry matrix reads

$$\boxed{\mathcal{U}_\mathrm{B} = e^{i\theta_f \mathcal{L}/\hbar}}, \tag{7.14}$$

in which, as in the previous section, the matrix elements of $\mathcal{L}$ are evaluated on the states of the basis at initial time, i.e. $\mathcal{L}_{\alpha\beta} = \langle \psi_\alpha(0)|\hat{L}_z|\psi_\beta(0)\rangle$.

Note that the integration appearing in Eq. (1.14) only gives an overall constant prefactor θ_f in this case. Therefore, by working in the PR basis, one can obtain the Berry matrix $\mathcal{U}_B$ through the measurement of the $\hat{L}_z$ matrix elements at $\theta = 0$, i.e. without performing any actual rotation.

Concerning the basis-change matrix $\mathcal{B}$ instead, in the PR basis it has matrix elements

$$\boxed{\mathcal{B}_{\alpha\beta} = \langle \psi_\alpha(0)|\psi_\beta(T)\rangle = \langle \psi_\alpha(0)|\hat{\mathcal{R}}_{\theta_f}|\psi_\beta(0)\rangle = \langle \psi_\alpha(0)|e^{-i\theta_f \hat{L}_z/\hbar}|\psi_\beta(0)\rangle}, \qquad (7.15)$$

which are the same $\mathcal{B}_{\alpha\beta}$'s introduced in the previous section. With the present derivation of the quantities $\mathcal{U}_B$ and $\mathcal{B}$ we can however give an alternative justification of the constraint $\mathcal{B}(2\pi k) = \mathbb{1}$, with $\mathbb{1}$ the identity operator. It comes from the fact that the basis states at different rotation angles are obtained by acting only on the particle coordinates and that any admissible wave function must be single-valued with respect to them. As a consequence, when considering $2\pi k$-rotations in the PR basis, all geometrical contributions to $\mathcal{U}(T)$ –including those coming from the anyonic braiding statistics– must be in the Berry matrix $\mathcal{U}_B$. On the contrary, wave functions can be in general multi-valued in the anyon coordinates η_μ [Nayak et al., 2008]. Therefore, if one chooses the AR basis, the unitary transformation $\mathcal{U}(T)$ can in principle take non-trivial contributions from basis-change matrix $\tilde{\mathcal{B}}$ also in the case of $2\pi k$-rotations. Note that in the AR basis, the basis-change matrix has matrix elements

$$\tilde{\mathcal{B}}_{\alpha\beta} = \langle \tilde{\psi}_\alpha(0)|\tilde{\psi}_\beta(T)\rangle = \langle \tilde{\psi}_\alpha(0)|\mathcal{S}_{\theta_f}|\tilde{\psi}_\beta(0)\rangle = \langle \psi_\alpha(0)|\mathcal{S}_{\theta_f}|\psi_\beta(0)\rangle, \qquad (7.16)$$

which in prinicple can be different from those of $\mathcal{B}$.

Before moving on, we would like to stress that the fact that both $\mathcal{U}_B$ and $\mathcal{B}$ depend on our basis (or gauge) choice does not represent a problem. When considered separately, there are not gauge invariant quantities indeed. Only their product must be basis (or gauge) independent. We will further discuss this point in Sec. 7.4.

7.2 Quasihole braiding phase from static measurements

We have just related the geometric contribution associated with an adiabatic process in which the anyons are rigidly rotated (and eventually braided or exchanged) to the matrix elements of the angular-momentum and particle-rotation operators, taken on the basis states spanning the ground state manifold at initial time. Now we want to apply these general results to the particular case of two anyons, for which the ground state is typically non-degenerate. To be precise, we will consider QH excitations hosted by FQH states in the LLL and in particular by the Laughlin and the Moore-Read states [see Secs. 3.4 and 4.2], to which the results of the present section similarly apply.

7.2.1 Braiding phase from angular-momentum measurements

As previously discussed, if we consider a 2π rotation of the QHs, $\mathcal{B}$ merely becomes the identity matrix. Therefore, for the non-degenerate (Laughlin or Moore-Read) state with two QHs, the unitary transformation $\mathcal{U}(T)$ associated with this process reduces to the phase factor $\mathcal{U}_B = e^{i\varphi_B}$, in which $\varphi_B = 2\pi\mathcal{L}/\hbar$ is the so-called Berry phase. Note that, for non-degenerate ground states, $\mathcal{L}$ coincides with the expectation value of the angular-momentum operator over the initial state, i.e. $\langle \hat{L}_z \rangle$.

In addition to the topological contribution we are interested in, the Berry phase φ_B has also a non-topological contribution, which can be interpreted as an Aharonov-Bohm (AB) phase [Aharonov and Bohm, 1959]. A detailed analysis of this AB phase can be found in Appendix C. Although this phase factor encodes information on the QH fractional charge, we have to get rid of it to extract the QH braiding phase φ_{br}. As discussed in details in Appendix C, this can be done by considering the difference between the Berry phases, here expressed in terms of angular-momentum expectation values, for two particular states:

$$\boxed{\frac{\varphi_{br}}{2\pi} = \frac{1}{\hbar}\left[\langle \hat{L}_z \rangle_{|\eta_1|=|\eta_2|} - \langle \hat{L}_z \rangle_{\eta_1=\eta_2} \right]}. \qquad (7.17)$$
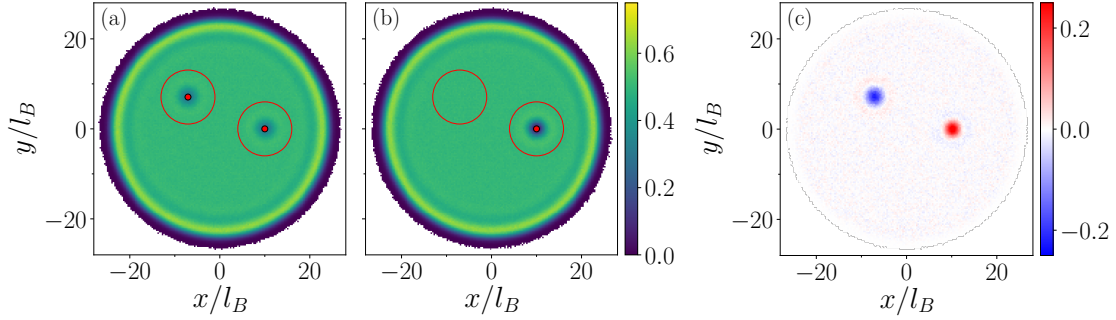
Figure 7.3: (a) 2D density profile of the $N = 150$ $M = 2$ Moore-Read state with quasiholes at positions $\eta_1 = 10\,l_{\mathrm{B}}$ and $\eta_2 = 10e^{i3\pi/2}\,l_{\mathrm{B}}$ (red dots). (b) 2D density profile of the $N = 150$ $M = 2$ Moore-Read state with quasiholes at positions $\eta_1 = \eta_2 = 10\,l_{\mathrm{B}}$. Red circles give a pictorial representation of the regions A_1 and A_2 where the 2D densities depicted in (a) and (b) are different. (c) Difference between the density profiles reported in panels (a) and (b). Panels (a) and (b) have been taken from Macaluso et al. [2019a].

The expectation value $\langle \hat{L}_z \rangle_{|\eta_1|=|\eta_2|}$ is taken on a state with QHs sufficiently far from each other and from the system boundary, at positions η_1 and η_2 satisfying $|\eta_1| = |\eta_2|$ [see Fig. 7.3(a)]. On the other hand, $\langle \hat{L}_z \rangle_{\eta_1=\eta_2}$ is measured on the state with the two QHs on top of each other at $\eta_1 = \eta_2$ [see Fig. 7.3, (b)]. Note that in this latter case a 2π rotation of the QHs cannot induce any exchange/braiding between them since they are on top of each other. This ensures that the Berry phase associated with this process coincides with the aforementioned non-topological Aharonov-Bohm contribution.

7.2.2 Braiding phase from global density-profile measurements

The mean angular momentum of a state defined in the LLL is directly related to its spatial extension and, in particular, to its mean square radius [Ho and Mueller, 2002, Umucalılar et al., 2018]:

$$\frac{\langle \hat{L}_z \rangle}{\hbar} = N \left[\frac{\langle r^2 \rangle}{2l_B^2} - 1 \right]. \tag{7.18}$$

This strongly simplifies Eq. 7.17 which can be rewritten as

$$\boxed{\frac{\varphi_{\mathrm{br}}}{2\pi} = \frac{N}{2l_B^2} \left[\langle r^2 \rangle_{|\eta_1|=|\eta_2|} - \langle r^2 \rangle_{\eta_1=\eta_2} \right].} \tag{7.19}$$

From the experimental point of view, relating the QH braiding phase to density dependent quantities –such as the mean square radius $\langle r^2 \rangle$– represents an undeniable advantage, especially for ultracold atomic and photonic systems. In these set-ups indeed, the mean angular momentum of the system is typically a difficult quantity to probe, while one can easily perform density-profile measurements.

Furthermore, as long as the LLL approximation is valid, the interactions effects during the time-of-flight (TOF) expansion of the system can be neglected [Read and Cooper, 2003]. This implies that the expansion of the FQH droplet is self-similar and that the density profile of the system inside the trap can be reconstructed from the one measured after TOF. As a consequence, the mean angular momentum of a state in the LLL can be alternatively determined by just measuring $\langle r^2 \rangle$ after a TOF expansion of duration t, after the pinning and trapping potentials and the synthetic fields are suddenly turned off [Read and Cooper, 2003]:

$$\frac{\langle \hat{L}_z \rangle}{\hbar} = N \left[\frac{\langle r^2 \rangle}{2l_B^2} - 1 \right] = N \left[\left(\frac{m\sqrt{2}l_{\mathrm{B}}}{\hbar t^2} \right) \langle r^2 \rangle_{\mathrm{TOF}} - 1 \right]. \tag{7.20}$$

Note that for FQH states of photons in twisted cavities [Schine et al., 2016, Clark et al., 2019], the far-field intensity profile of the light emission represents the optical analog of TOF imaging of ultracold atomic clouds, making Eqs. (7.19) and (7.20) applicable also in the photonic context.

7.2.3 Braiding phase from local density-profile measurements

Although the protocol suggested in Eq. (7.19) is already close to the current experimental capabilities, it requires the ability to pin QHs with very high precision and the knowledge of the exact particle number. Moreover, φ_{br} is difficult to compute for large systems, since it is a $\mathcal{O}(1)$ number obtained as the difference between two $\mathcal{O}(N^2)$ quantities. However, Eq. (7.19) can be recast in a form which does not depend neither on N nor on the precise QH positions, as we show in the following[2].

A hallmark of FQH states is their incompressibility, which manifests itself through a flat density in the system bulk [Tong, 2016]. Due to the this feature, the densities of the anyon configurations under study only differ in the regions A_1 and A_2 surrounding the QHs [see red circles in Fig. 7.3 (a) and (b), and the difference between the two density profiles shown in Fig. 7.3 (c)]. Therefore, the integrals in Eq. (7.19) can be rewritten as:

$$
\begin{aligned}
\frac{\varphi_{\mathrm{br}}}{2\pi} &= \frac{N}{2l_B^2} \left[\langle r^2 \rangle_{|\eta_1|=|\eta_2|} - \langle r^2 \rangle_{\eta_1=\eta_2} \right] \\
&= \frac{N}{2l_B^2} \frac{1}{N} \int_{\mathbb{R}^2} r^2 \left[n_{|\eta_1|=|\eta_2|}(\vec{r}) - n_{\eta_1=\eta_2}(\vec{r}) \right] d\vec{r} \\
&= \frac{1}{2l_B^2} \int_{A_1,A_2} r^2 \left[n_{|\eta_1|=|\eta_2|}(\vec{r}) - n_{\eta_1=\eta_2}(\vec{r}) \right] d\vec{r},
\end{aligned}
\tag{7.21}
$$

where in the last equivalence we used exaclty the fact that the densities $n_{|\eta_1|=|\eta_2|}(\vec{r})$ and $n_{\eta_1=\eta_2}(\vec{r})$ are equal over the whole 2D plane, except for the regions A_1 and A_2. In these regions, the densities in Eq. (7.21) can be expressed as

$$
\begin{aligned}
n_{|\eta_1|=|\eta_2|}(\vec{r}) &= n_{\mathrm{b}} - d_{1\mathrm{QH}}(\vec{r} - \eta_j) \quad &\forall \vec{r} \in A_j,\, j = 1,2 \\
n_{\eta_1=\eta_2}(\vec{r}) &= n_{\mathrm{b}} - d_{2\mathrm{QH}}(\vec{r} - \eta_1) \quad &\forall \vec{r} \in A_1, \\
n_{\eta_1=\eta_2}(\vec{r}) &= n_{\mathrm{b}} \quad &\forall \vec{r} \in A_2,
\end{aligned}
\tag{7.22}
$$

where $n_{\mathrm{b}} = 1/2\pi M l_B^2$ is the bulk density, and $d_{1\mathrm{QH}}(\vec{r})$ and $d_{2\mathrm{QH}}(\vec{r})$ represent the density depletions induced by a single QH or by two QHs on top of each other, respectively [see examples in Figs. 7.6 and 7.7]. This allows us to write the braiding phase as

$$
\boxed{\frac{\varphi_{\mathrm{br}}}{2\pi} = \frac{1}{2l_B^2} \int d\vec{\rho}\, \rho^2 \left[d_{2\mathrm{QH}}(\vec{\rho}) - 2 d_{1\mathrm{QH}}(\vec{\rho}) \right]},
\tag{7.23}
$$

in which $\vec{\rho} = \vec{r} - \eta_j$ denotes the distance from the QH center. To ensure the equivalence between Eqs. (7.19) and (7.23), the integration region for the previous integral must be large enough to guarantee an appropriate damping of the density oscillations induced by the QHs [see for example Fig. 7.6 (a)]. At the same time, for finite systems a cutoff $\rho < R_{\max}$ is needed to avoid spurious contributions coming from the presence of the other QHs (if present) or from the density deformations generated at the boundary of the FQH cloud.

With respect to protocol suggested by Eq. (7.19) for the measurement of the QH braiding phase, the one described by Eq. (7.23) has a lot of benefits: First, it only depends on the local density perturbations induced by the QHs in the system bulk, rather than on the global shape of the FQH cloud. This strongly simplifies the measurement of the braiding phase, which is for instance independent on the position of the QHs and on the number of the particles. On top of that, this also makes the experimental procedure suggested by Eq. (7.23) robust against finite-temperatures effects, which typically excite the edge modes of the system [see Chapter 6]. Note that the presence of edge excitations would modify the mean angular momentum –and the mean square radius– of the FQH cloud instead. Finally, in principle Eq. (7.23) does not require states with two spatially separated QHs to be applied[3], making it particularly appealing for experiments with a mesoscopic number of particles. In this case indeed one can hardly have anyons which are simultaneously far from each other and from the system boundary.

---

[2] A more detailed derivation can be found in Appendix D.

[3] Note that the possibility of just considering anyons pinned at the center of the FQH cloud represents a great advantage for ultracold atom experiments aiming at reaching the FQH regime with rotating microtraps, as done by Gemelke et al. [2010].
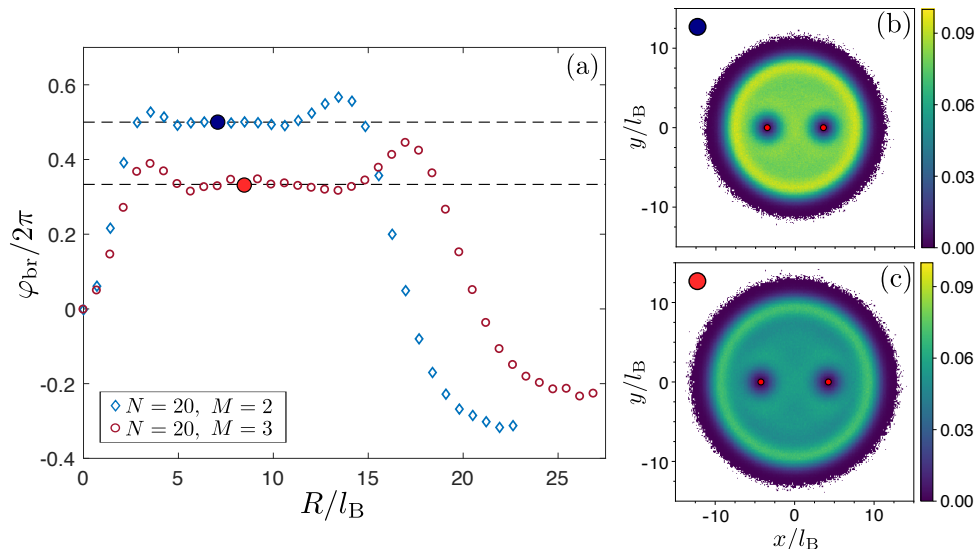

Figure 7.4: (a) Quasihole braiding phase for the bosonic $M = 2$ (blue diamonds) and the fermionic $M = 3$ (red circles) Laughlin state, as a function of the distance R between the quasiholes. Error bars due to Monte Carlo statistical uncertainties are smaller than the marker sizes. (b) Density profile for the $M = 2$ bosonic Laughlin state with quasiholes located along the x axis at $\eta_1 = -\eta_2 = 2.5\sqrt{2}\, l_{\mathrm{B}}$. (c) Density profile for the $M = 3$ fermionic Laughlin state with quasiholes located along the x axis at $\eta_1 = -\eta_2 = 3\sqrt{2}\, l_{\mathrm{B}}$. Adapted from Umucalılar et al. [2018].

Before moving on, we would like to stress that the depletions $d_{1\mathrm{QH}}(\vec{r})$ and $d_{2\mathrm{QH}}(\vec{r})$ have been widely studied in the past both for continuum geometries and for lattice systems. However, before the work by Macaluso et al. [2019a] the analysis of the QH density depletions was mainly done to estimate the charge and the typical size of the QHs, e.g. in Wu et al. [2014], Liu et al. [2015] and Jaworowski et al. [2019].

7.3   Results of the numerical simulations

In this section we provide numerical validation of the expressions in Eqs. (7.19) and (7.23), linking the QH braiding phase to the mean square radius of FQH states presenting QHs in some specific positions and to the density depletions created by the QHs in the bulk density, respectively. To this purpose we consider the QH excitations of both the Laughlin and the Moore-Read state. These two states, not only represent paradigmatic examples of FQH states support Abelian and non-Abelian anyons, but their QH excitations are also described by relatively simple analytical wave functions [see Eqs. 3.39 and 4.7].

Note that dealing with ansatz wave functions, instead of solving the full quantum many-body problem, typically allows one to study system with larger particle numbers (of the order of hundreds), which would be otherwise intractable. This is especially true in the present case, where we only need to compute density-related quantities, which can be easily obtained through the Monte Carlo sampling of the squared modulus of the ansatz wave functions [see Appendix E].

7.3.1   Braiding phase of Laughlin's quasiholes

As a first step we apply Eq. (7.19) to the case of two QHs in the Laughlin state, for both the bosonic $\nu = 1/2$ and the fermionic $\nu = 1/3$. To be precise, we consider $N = 20$ particle systems and, in order to maximize the QH distance, we choose the particular QH configuration in which the anyons are located at diametrically opposite positions [see Fig. 7.4 (b) and (c)]. In other words we choose the QH coordinates $\eta_1 = -\eta_2 = \vec{R}/2$, which obviously satisfy $|\eta_1| = |\eta_2|$. We would like to stress that our choice of studying systems with moderate number particles is motivated by the desire of being as close as possible to realistic near-future experiments, which will hardly realize bigger FQH droplets.

The behavior of the QH braiding phase φ_{br}, as a function of distance R between the QHs, is
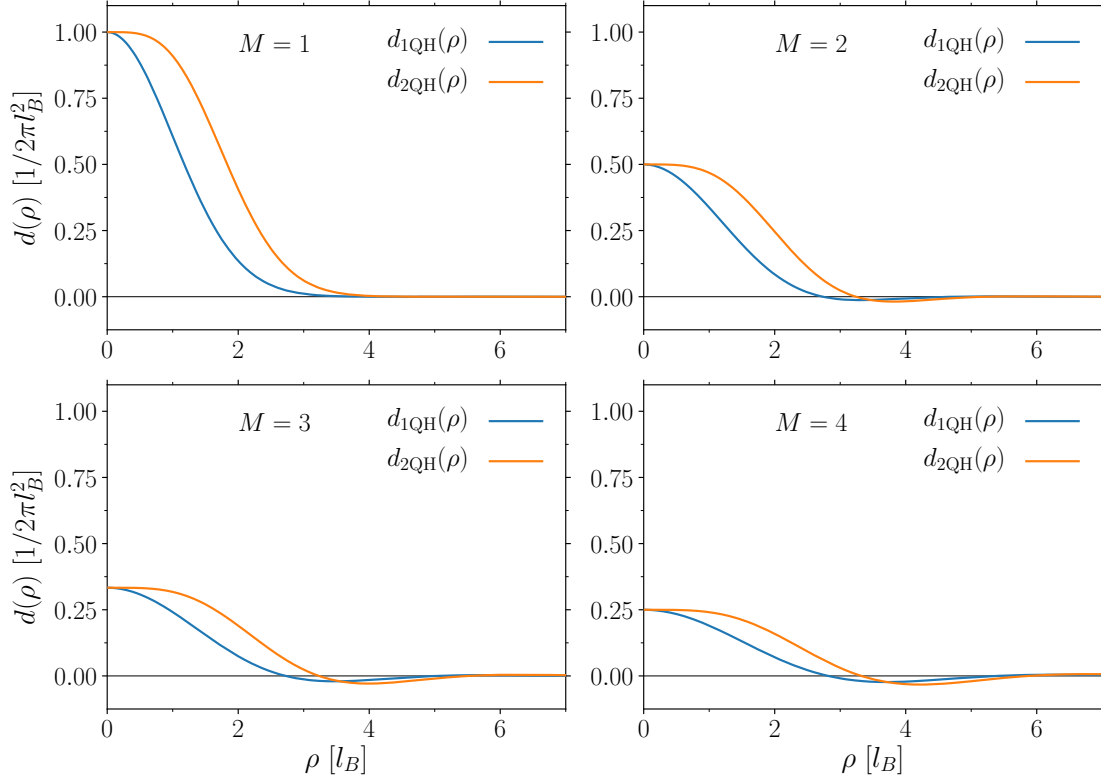
Figure 7.5: Radial profile of the density depletions caused by a single quasihole at $\eta_1 = 0$ (blue line) and two quasiholes on top of each other at $\eta_1 = \eta_2 = 0$ (orange line), for Laughlin states at different filling $\nu = 1/M$. For all values of M we considered $N = 120$ particles.

reported in Fig. 7.4 (a). A clear plateau in the braiding phase, matching the theoretically predicted value $\varphi_{\mathrm{br}}/2\pi = \nu$, can be observed for intermediate values of R. In this interval of distances the QHs are indeed sufficiently far apart form each other and from the system boundary [see Fig. 7.4 (b) and (c)]. Strongly deviations from the expected value of φ_{br} are visible at very small and very large values of the distance between the QHs, instead. However this behavior is completely reasonable: On the one hand, for small value of R the QHs start to overlap and therefore, since they stop to be independent objects, there are no reasons why their braiding phase should be the correct one. Actually one could not even define the braiding phase for objects which are not spatially separated. On the other hand, for large values of R one first observes spurious effects cause by the density peak close to the system boundary [see the enhancement of $\varphi_{\mathrm{br}}(R)$ after the plateau], and then one starts to consider objects which are located outside the system bulk and which are therefore completely different from the Laughlin QHs.

We now validate Eq. (7.23) by considering the QHs of the Laughlin state at different fillings: $\nu = 1, 1/2, 1/3$ and $1/4$. In this case we focus on systems having $N = 120$ particles to study the behavior of φ_{br} as a function of the integration cutoff $R_{\max}$. As discussed in Sec. 7.2.3, Eq. (7.23) does not depend on the specific position of the QHs, as long as they are located in the bulk of the system. Therefore, to fully exploit the extension of the FQH cloud, we decide to consider states presenting either a single QH or two overlapping ones in the center of the cloud. The QH density depletions $d_{1\mathrm{QH}}(\rho)$ and $d_{2\mathrm{QH}}(\rho)$ extracted from these states, are reported in Fig. 7.5, for the different values of the filling $\nu = 1/M$. It is interesting to notice that, for increasing values of M, the typical size of the QHs increases, even thought their charge –given by q/M– decreases. Furthermore, the density deformations created by the QH excitations of Laughlin states at lower fillings –i.e., larger M values– are characterized by enhanced oscillations, which damp on a larger length scale [see for instance Fig. 7.6 (a)].

From panel (b) of Fig. 7.6, we can see that $\varphi_{\mathrm{br}}(R_{\max})$ seems to converge to its expected value (i.e., $2\pi\nu = 2\pi/M$), for all considered fillings. At the same time, the convergence of $\varphi_{\mathrm{br}}(R_{\max})$ to its theoretically-predicted value is clearly filling-dependent. In particular, lower is the filling, larger must be the integration region needed to observe the convergence of the QH braiding phase. This,
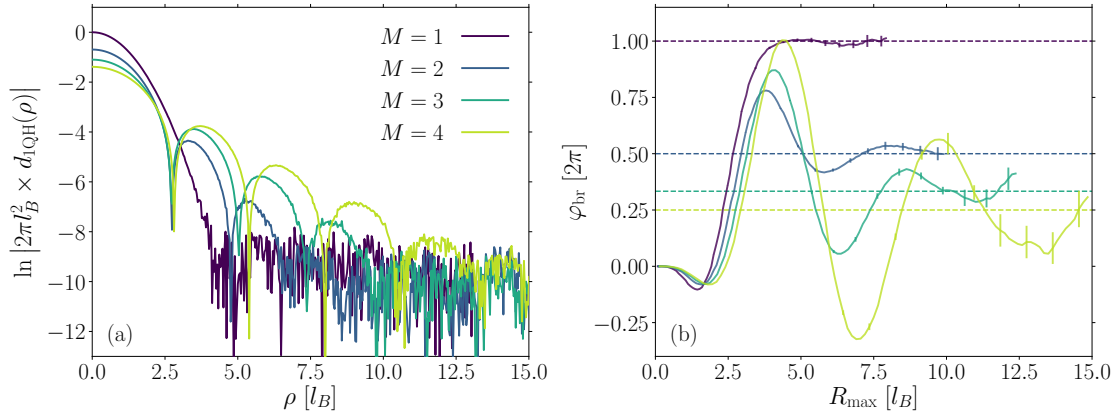
Figure 7.6: (a) Density oscillations (in log scale) characterizing the density depletion of a single Laughlin quasihole [see Fig. 7.5] for the different values of the filling $\nu = 1/M$. (b) Quasihole braiding phase (solid lines) evaluated with equation (7.23) as a function of the cutoff radius $R_{\max}$ for the different values of M. Dashed lines denote the predictions for $\varphi_{\mathrm{br}} = 2\pi/M$.

however, simply reflects the different oscillatory behavior characterizing the QH density depletions at different fillings.

Note that although for a fixed number of particles the spatial extension of the Laughlin state scales proportionally to $\sqrt{M}$, this only partially compensate for the fact that for larger M's the convergence of $\varphi_{\mathrm{br}}(R_{\max})$ occurs at larger distances. If M is large indeed, not only the oscillations in the QH density depletions are more pronounced, they also occur at larger values of ρ. Since in Eq. (7.23) the density depletions $d_{1\mathrm{QH}}(\rho)$ and $d_{2\mathrm{QH}}(\rho)$ are multiplied by a ρ^2 factor, the effect of these oscillations on $\varphi_{\mathrm{br}}(R_{\max})$ is stronger when M is large, making the convergence of the braiding phase more difficult at small fillings.

7.3.2 Fusion channel of two Moore-Read quasiholes

As we reviewed in Sec. 4.2.2, the fusion channel of two non-Abelian Moore-Read QHs depends on the parity $P_N = 0, 1$ of the particle number N. In particular, we recall that the braiding of two such QHs induces a phase φ_{br} that depends on P_N:

$$\frac{\varphi_{\mathrm{br}}}{2\pi} = \frac{1}{4M} - \frac{1}{8} + \frac{P_N}{2}, \tag{7.24}$$

and that this represents a direct indication that Moore-Read QHs obey non-Abelian statistics.

Here, by applying the results of Secs. 7.2.2 and 7.2.3, we show that Eqs. (7.19) and (7.23) can be also used to probe the non-Abelian nature of the Moore-Read QHs. As done for the Laughlin QH states, also in this case we evaluate the mean square radii and the QH density depletions through the Monte Carlo sampling of the squared modulus of ansatz wave functions. To be precise, we consider the wave function in Eq. (4.8) for both parities $P_N = 0$ and $P_N = 1$.

The numerical results obtained through Eq. (7.19) are reported in Table 7.1 for both $M = 2$ (fermions at filling $\nu = 1/2$) and $M = 1$ (bosons at filling $\nu = 1$) and for the different parities

M	P_N	$\varphi_{\mathrm{br}}^{\mathrm{MC}}\ [2\pi]$	$\varphi_{\mathrm{br}}\ [2\pi]$
1 (bosons)	0	0.13 ± 0.04	0.125
	1	0.59 ± 0.04	0.625
2 (fermions)	0	0.05 ± 0.06	0
	1	0.49 ± 0.07	0.5

Table 7.1: Quasihole braiding phase $\varphi_{\mathrm{br}}^{\mathrm{MC}}$ obtained numerically via equation (7.19) (third column, with the Monte Carlo statistical uncertainty) and its prediction φ_{br} in equation (7.24) (fourth column), for $M = 1, 2$ and for different parities P_N of the particle number $N = 150$ and $N = 149$. For the $|\eta_1| = |\eta_2|$ term in equation (7.19), we set $\eta_1 = -\eta_2$, which is the optimal configuration for a finite-size system. For $M = 1$ ($M = 2$) case, $|\eta_1|/l_B$ is equal to 6.5 (7.5).
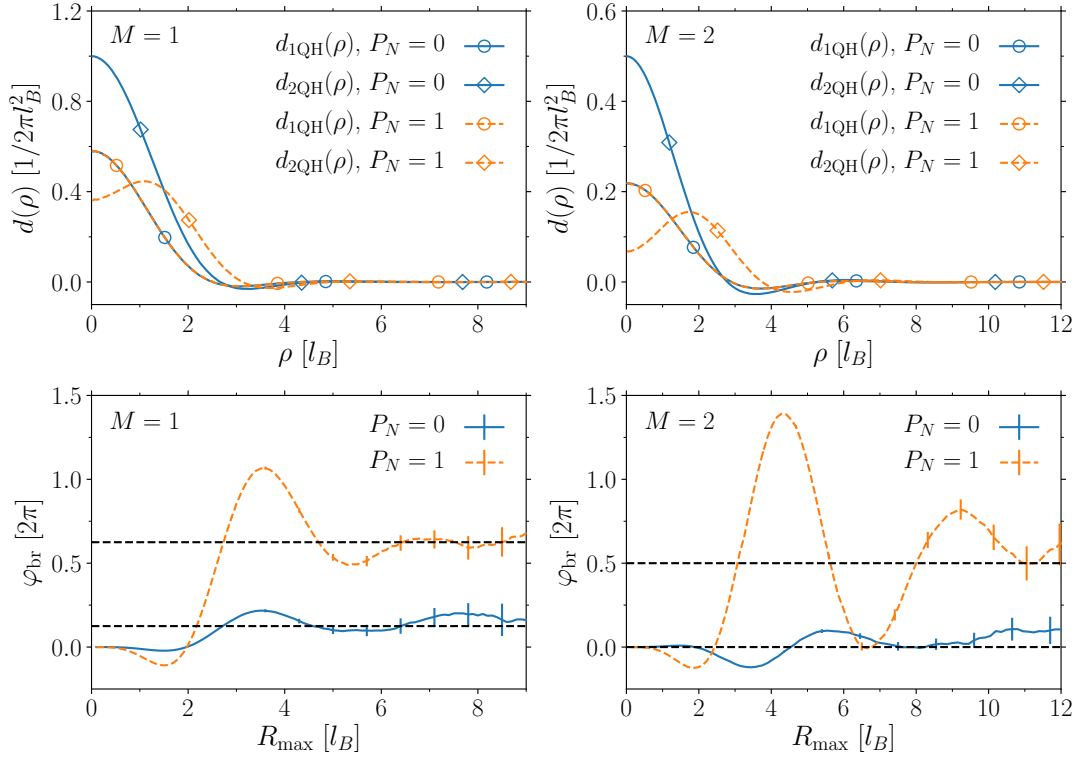

Figure 7.7: Upper left: Radial profile of the density depletions caused by a single quasihole at $\eta_1 = 0$ (circles) and two quasiholes on top of each other at $\eta_1 = \eta_2 = 0$ (diamonds), for even (blue solid lines) and odd (orange dashed lines) parity of N, at filling $\nu = 1/M = 1$. We consider $N = 200$ or $N = 199$. Lower left: Quasihole braiding phase evaluated with equation (7.23) as a function of the cutoff radius R_max, for both $P_N = 0$ (blue solid line) and $P_N = 1$ (orange dashed line) in the $M = 1$ bosonic case. Black dashed lines denote the predictions for φ_br [see equation (4.11)]. Upper right and lower right: Same as upper left and lower left, but for the $M = 2$ fermionic case. Adapted from Macaluso et al. [2019a].

$P_N = 0, 1$ of the particle number. For all considered cases the QH braiding phase is in full agreement with the predicted value, within the statistical uncertainties of the Monte Carlo method.

The behavior of the braiding phase, evaluated by means of Eq. (7.23), is shown in Fig. 7.7 as a function of the cutoff R_max. Also in this case we consider the different parities P_N, for both $M = 1$ and $M = 2$. As expected, φ_br approaches the theoretically predicted value in Eq. (7.24) (up to small deviations due to finite-size effects) for all considered values of M and P_N. This, together with the results in Table 7.1, proves that one can use Eqs. (7.19) and (7.23), not only to measure the braiding phase of Abelian QHs, but also to probe the existence of multiple fusion channels for the Moore-Read QHs, which we recall to be an indirect signature of their non-Abelian nature.

Moreover, it is interesting to note that, for a given value of M, the shape of $d_{1\mathrm{QH}}(\rho)$ does not depend on P_N, meaning that all the information on the fusion channels is encoded in $d_{2\mathrm{QH}}(\rho)$, which is completely different for even and odd values of N [see top panels in Fig. 7.7]. We stress that, although this dependence on P_N was already pointed out in Prodan and Haldane [2009] and in Baraban [2010], the key result of our study is that the depletion profiles also contain quantitative information on the braiding phase.

7.3.3 Probing Moore-Read fusion channels in realistic experiments

We have just numerically proved that the non-Abelian nature of the Moore-Read QHs can be experimentally probed through simple density-profile measurements. However, while $d_{1\mathrm{QH}}(\rho)$ can be indifferently measured in the ground state with either a single QH or two well-separated ones, as discussed in Wan et al. [2006, 2008], the characterization of two overlapping QHs involves more subtleties: First, for $P_N = 1$ the state in Eq. (4.8) with overlapping QHs may not be the ground state in the presence of a given external potential. For instance, having two QHs close to each other
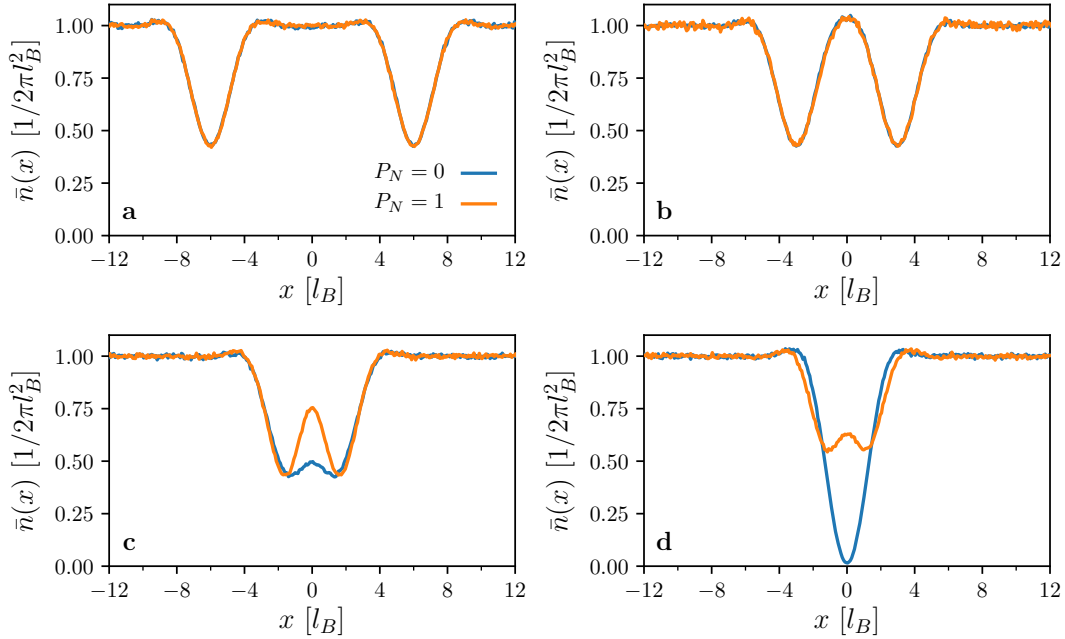
Figure 7.8: **a-d**, Mean particle density $\bar{n}(x)$ along a cut connecting two $M = 1$ Moore-Read quasiholes located at $\eta_{1,2} = \pm R$, with $R/l_B = 6, 3, 1.5$ and 0 for **a**, **b**, **c** and **d** respectively. For each value of R, the blue (orange) solid line indicates the $P_N = 0$ ($P_N = 1$) case. To obtain $\bar{n}(x)$, we average the density profile over a stripe with $|y| < 0.64\,l_B$. Taken from Macaluso et al. [2019a].

might cost more energy than just exciting a low-energy fermionic excitation at the boundary [Wen, 1995, Milovanović and Read, 1996, Wan et al., 2006]. Furthermore, the presence of these fermionic edge modes may modify the relation between the QHs fusion channel and the particle number parity P_N [Wan et al., 2008].

We thus propose to proceed as follows for the measurement of $d_{2QH}(\rho)$: Two QHs are created far from each other and from the system boundary, by cooling the system in the presence of pinning potentials. The two QHs are then slowly brought closer and fused [see Fig. 7.8]. According to the general theory of topological quantum computation [Kitaev, 2003, Nayak et al., 2008], the fusion channel cannot change during this process, so the system is adiabatically transported into the (possibly metastable) desired state, where the depletion profile $d_{2QH}(\rho)$ is measured.

Now the question is whether or not one can create two spatially separated Moore-Read QHs in both fusion channels and, in particular, in the ψ one. To answer this question one should perform numerical experiments starting from a model Hamiltonian and a cooling mechanism, but we leave this study for a future work. What we do in the following instead, is trying to give strong arguments in favor of the fact that in an actual experiments the QH fusion channel is randomly chosen at each repetition. As discussed in Wan et al. [2006, 2008], in the presence of fermionic edge excitations the one-to-one correspondence between the parity of N and the fusion channel of the two Moore-Read QHs breaks down. To be precise, the fusion channel chosen by the QHs will be fixed by the parity of $(N - F)$, where F is the number of fermionic edge excitations. At the same time, one can reasonably argue that the energy of the state with $F = 0$ and the one with $F = 1$, both hosting two well separated QHs, will be very similar (the energy difference between these two states will probably depend on both the distance between the QHs and the particular properties of the confining potential under study). Therefore, since in the cooling process the system does not necessarily reach the ground state (especially when there are almost-degenerate ground states), it is reasonable to expect that in an actual experiment the Moore-Read QHs will randomly select one of the two different fusion channels. Note that, even though at each repetition the QH fusion channel will be randomly selected, the non-Abelian statistics of the QHs will be still visible in the bi-peaked probability for φ_{br}.

As a final remark, we would like to discuss how one could alternatively apply our proposal to measure the braiding phase in the different fusion channels by considering states with four QHs. Although in this case we can restrict to the more familiar case of N even, the application of our

protocol would require both the two degenerate 4-QH states Ψ_0 and Ψ_1 [see Eqs. (4.13) and (4.14)], where, as shown for instance in Bonderson et al. [2011], the QHs at η_1 and η_2 are in the $\mathbb{1}$ and in the ψ fusion channel, respectively. The density profiles resulting from the fusion of these QHs in the states Ψ_0 and Ψ_1 should be exactly the blue and orange lines in Fig. 7.8 (d). Strong indication of this fact can be found in Baraban [2010], where the value of the density at η_1 is studied as a function of the distance between the two QHs.

7.4 Rotations of four quasiholes: non-Abelian contributions to the braiding matrix

In the following we consider the effect of rigid rotations on Moore-Read states with four QHs, where, for a given choice of the QH coordinates, two different ground states appear and the QHs show their actual non-Abelian behavior [see Sec. 4.2]. The main result of this Section is that the non-Abelian (i.e., non-diagonal) terms of the QH braiding matrices enter in the basis-change matrix $\mathcal{B}$, also if we work with the PR basis. Although we prove this only for the specific case of four Moore-Read quasiholes, we have the feeling that this observation reflects the topological protection of the different ground states and the fact that one can mix them only by means of QH braiding or exchange operations. At the same time, this observation also proves that, in the case of four Moore-Read QHs, only rigid rotations of the anyons by angles $\theta_f \neq 2\pi k$ –with k integer– can mix the different ground states. We recall that the study of rotations of this kind is mainly important in the context of theoretical studies, where, from the knowledge of the initial ground states, one can compute both $\mathcal{U}_{\mathrm{B}}$ and $\mathcal{B}$ for any rigid rotation of the anyons.

We start by looking at what happens to the Pfaffian in Eq. (4.12), when one rotates the particle coordinates by a generic angle θ. We consider, in particular, the term

$$Q(\eta_a, \eta_b, \eta_c, \eta_d; z_k, z_j) \equiv \frac{(\eta_a - z_k)(\eta_b - z_k)(\eta_c - z_j)(\eta_d - z_j) + (\eta_a - z_j)(\eta_b - z_j)(\eta_c - z_k)(\eta_d - z_k)}{z_k - z_j},$$
(7.25)

which changes as

$$Q(\eta_a, \eta_b, \eta_c, \eta_d; z_k e^{-i\theta}, z_j e^{-i\theta}) = e^{-i3\theta} Q(\eta_a e^{i\theta}, \eta_b e^{i\theta}, \eta_c e^{i\theta}, \eta_d e^{i\theta}; z_k, z_j)$$
(7.26)

when particle coordinates are rotated by an angle θ.

In the explicit form of the Pfaffian appearing in the wave functions $\Psi_{(ab)(cd)}(\eta; z)$ we have a sum (with alternating signs) of terms given by the product of $N/2$ factors like (7.25). Therefore, the effect of particle rotations on such wave functions is the following:

$$\begin{aligned} \hat{\mathcal{R}}_\theta \, \Psi_{(ab)(cd)}(\eta; z) &= \Psi_{(ab)(cd)}(\eta; z e^{-i\theta}) \\ &= e^{-i\frac{3N}{2}\theta} \, e^{-i\left[\frac{MN(N-1)}{2}\right]\theta} \, \Psi_{(ab)(cd)}(\eta e^{i\theta}; z) \\ &= e^{-i\frac{3N}{2}\theta} \, e^{-i\left[\frac{MN(N-1)}{2}\right]\theta} \, \mathcal{S}_\theta \, \Psi_{(ab)(cd)}(\eta; z), \end{aligned}$$
(7.27)

where the second term on the right-hand side comes from the Laughlin-like part of the wave functions $\Psi_{(ab)(cd)}(\eta; z)$. We recall that $\hat{\mathcal{R}}_\theta$ and $\mathcal{S}_\theta$ are the transformations mapping a generic wave function $\Psi(\eta; z)$ into $\Psi(\eta; z e^{-i\theta})$ and $\Psi(\eta e^{i\theta}; z)$, respectively.

Finally, by noting that the factor $x = (\eta_1 - \eta_2)(\eta_3 - \eta_4)/(\eta_1 - \eta_3)(\eta_2 - \eta_4)$, entering in the definitions of the wave functions $\Psi_{0,1}(\eta; z)$, is invariant under rotation of the QH coordinates, we can write:

$$\begin{aligned} \hat{\mathcal{R}}_\theta \, \Psi_{0,1}(\eta; z) &= \Psi_{0,1}(\eta; z e^{-i\theta}) \\ &= e^{-i\left[6\left(\frac{1}{4M} - \frac{1}{8}\right) + \frac{1}{2}\right]\theta} \, e^{-i\frac{3N}{2}\theta} \, e^{-i\left[\frac{MN(N-1)}{2}\right]\theta} \, \Psi_{0,1}(\eta e^{i\theta}; z) \\ &= e^{-i\,\Sigma(N,M)\,\theta} \, \mathcal{S}_\theta \, \Psi_{0,1}(\eta; z), \end{aligned}$$
(7.28)

where

$$\Sigma(N,M) \equiv \left[6\left(\frac{1}{4M} - \frac{1}{8}\right) + \frac{1}{2}\right] + \frac{3N}{2} + \left[\frac{MN(N-1)}{2}\right].$$
(7.29)

The first term on the right-hand side of the previous expression represents the Abelian part of the topological contribution to $\mathcal{U}(T)$. Note that it compensates the one coming from the η-depending

normalization pre-factor in the wave functions $\Psi_{0,1}(\eta; z)$ when we apply $\mathcal{S}_\theta$ on them [see Eqs. (4.13) and (4.14)], in agreement with the fact that in the PR basis such a term is contained in $\mathcal{U}_{\mathrm{B}}$. At the same time, the second and third terms represent the mean angular momentum $\langle \hat{L}_z \rangle_{0,0,0,0}$ of the 4QH state with all QHs in the origin and they cancel the same term entering – with the opposite sign– in $\mathcal{U}_{\mathrm{B}}$ [cf. Eq. (C.8)]. As a consequence, the remaining non-topological contribution to the product $\mathcal{U}_{\mathrm{B}}\mathcal{B}$ is the Aharonov-Bohm phase due to the QH rotation.

Eq. (7.28) allows us to express the matrix $\mathcal{B}$ –written in the PR basis– in terms of the one written in the AR basis $\tilde{\mathcal{B}}$:

$$\begin{aligned}
\mathcal{B}_{\alpha\beta}(\theta_f) &= \langle \Psi_\alpha(\eta; z) | \hat{\mathcal{R}}_{\theta_f} | \Psi_\beta(\eta; z) \rangle \\
&= e^{-i\,\Sigma(N,M)\theta_f} \langle \Psi_\alpha(\eta; z) | \mathcal{S}_{\theta_f} | \Psi_\beta(\eta; z) \rangle \\
&= e^{-i\,\Sigma(N,M)\theta_f}\, \tilde{\mathcal{B}}_{\alpha\beta}(\theta_f),
\end{aligned} \tag{7.30}$$

where the matrix elements of $\tilde{\mathcal{B}}$ are given by $\tilde{\mathcal{B}}_{\alpha\beta} = \langle \psi_\alpha(0) | \mathcal{S}_{\theta_f} | \psi_\beta(0) \rangle$.

To conclude, we recall that since the unitary transformation $\mathcal{U}(T)$ does not depend on the basis choice, the non-Abelian contributions to it –coming only from the QH exchanges– must be the same if we consider $\mathcal{U}_{\mathrm{B}}\mathcal{B}$ or $\tilde{\mathcal{U}}_{\mathrm{B}}\tilde{\mathcal{B}}$. At the same time, as we have widely discussed in Sec. 4.2.3, Bonderson et al. [2011] have proved that all topological contribution to $\mathcal{U}(T)$ –both the Abelian and the non-Abelian ones– is encoded in $\tilde{\mathcal{B}}$, while $\tilde{\mathcal{U}}_{\mathrm{B}}$ corresponds to the Aharonov-Bohm phase due to the QH motion. Therefore, as $\mathcal{B}$ and $\tilde{\mathcal{B}}$ only differ for a diagonal (i.e. Abelian) term [see Eq. (7.30)], we can conclude that all non-Abelian contributions to $\mathcal{U}(T)$ lie in the basis-change matrix $\mathcal{B}$ also if we work in the PR basis.

7.5 Conclusions and remarks

In this Chapter we have presented a scheme to assess the statistical properties of anyonic excitations which does not rely on any kind of interference. By considering rigid rotations of the anyons, we have obtained a mathematical link between their statistics and the matrix elements of the angular-momentum and rotation operators, evaluated on the states forming the ground state manifold for a given set of the anyonic coordinates. Then we have shown that this relation further simplifies for states in the lowest Landau level and, in particular, that in this case anyonic statistics is encoded in the density profile of the system. Note that, if having access to the statistics of the anyons without performing any interference scheme is already remarkable in itself, relating such a long-sought quantity to density-profile measurements represents an incomparable step forward since it makes our proposal readily applicable to state-of-the-art experiments with ultracold atoms and photons.

To validate our theoretical findings we have considered the two paradigmatic examples: the quasiholes of the Laughlin state and those of the Moore-Read state. We stress that choosing the Moore-Read quasiholes allowed us to show that our proposal can be also used to identify the different fusion channels, which we recall to be a clear signature of the non-Abelian nature of the anyons. At the same time it is important to highlight that the study of the two-anyon case opens several other perspectives beyond the identification of the Moore-Read fusion channels. For example, our method can be employed to distinguish the Moore-Read and the anti-Pfaffian states, whose quasiholes are characterized by different Abelian contributions to the braiding phase, but also to evaluate key properties in topological quantum computation.

We also believe that our findings can be a useful tool for theoretical studies of states supporting anyons of unknown type. Indeed, when one can compute the matrix elements of the angular-momentum and rotation operators in the ground-state manifold, our scheme gives access to all contributions (also to the non-diagonal ones which encode the non-Abelian part of the anyonic statistics) to the time-evolution operator, for any rigid rotation of the anyons, and thus provides invaluable information on their non-Abelian braiding properties.

Given the impressive experimental advances on atomic and photonic systems in lattice geometries quoted in Sec. 2.4, a remaining exciting question is whether the link between the anyonic statistics and the density-profile of the fractional quantum Hall system goes beyond the continuum geometries considered so far. We will answer this question in the next Chapter, where we will focus our attention on the quasihole excitations of a bosonic fractional Chern insulator.

Chapter 8

Charge and statistics of lattice quasiholes.

In this Chapter we numerically investigate the properties of the quasihole excitations above the bosonic fractional Chern insulator state at filling $\nu = 1/2$, in the specific case of the Harper-Hofstadter Hamiltonian with hard-core interactions. For this purpose we make use of a Tree Tensor Network technique, which allows us to study systems with up to $N = 18$ particles on a 16×16 lattice with open boundary conditions and experiencing an additional harmonic confinement. Note that this sophisticated numerical technique allows us to find the ground state of the Hamiltonian and therefore, contrary to the results in Chapter 7, the ones obtained with the Tree Tensor Network method do not rely on any particular ansatz wave function.

As a first step, we study the quantization of the quasihole charge at fractional values and its robustness against the shape and strength of the impurity potentials used to create and localize such excitations [see Sec. 8.3]. Then in Sec. 8.4, we numerically characterize quasihole anyonic statistics by applying a discretized version of the relation derived in Chapter 7 and connecting the quasihole braiding phase to the depletions they create in the system density profile.

As we will see, our results give a direct proof that the anyonic statics of quasiholes can be experimentally probed through local density measurements also in the case of fractional Chern insulators, extending the applicability of our proposal to state-of-the-art experiments with ultra-cold atoms in optical lattices [Aidelsburger et al., 2014, Tai et al., 2017] and superconducting qubits [Roushan et al., 2016, Owens et al., 2018].

The main results of this Chapter are published in Macaluso et al. [2019b].

8.1 The interacting Harper-Hofstadter model

The Harper-Hofstadter (HH) model has been introduced by Harper [1955] and Hofstadter [1976] to describe the physics of a charged particle hopping on a square lattice under the effect of an orthogonal magnetic field. With respect to the problem in continuum space, the presence of lattice introduces in additional length scale: the lattice spacing a. While in solid state system a is in general much smaller than the other length scale (the magnetic length l_B), meaning that we basically recover the physics of continuum space Landau levels; in experiments with ultracold atoms and photons one can also explore the opposite regime where a is comparable with l_B, or even larger to it [Cooper et al., 2019, Ozawa et al., 2019]. The interplay between these two different length scales leads to an extremely reach energy spectrum, nowadays known as Hofstadter [1976] butterfly [see Fig. 8.1, left].

In the presence of on-site interactions and local energy offsets, the system Hamiltonian reads

$$H = -t \sum_{\langle i,j \rangle} e^{i\theta_{ij}} \hat{a}_i^\dagger \hat{a}_j + \frac{U}{2} \sum_i \hat{n}_i(\hat{n}_i - 1) + \sum_i V_i \, \hat{n}_i \, , \tag{8.1}$$

where $\hat{a}_i$ ($\hat{a}_i^\dagger$) is the bosonic annihilation (creation) operator at the site i of an $L \times L$ square lattice,
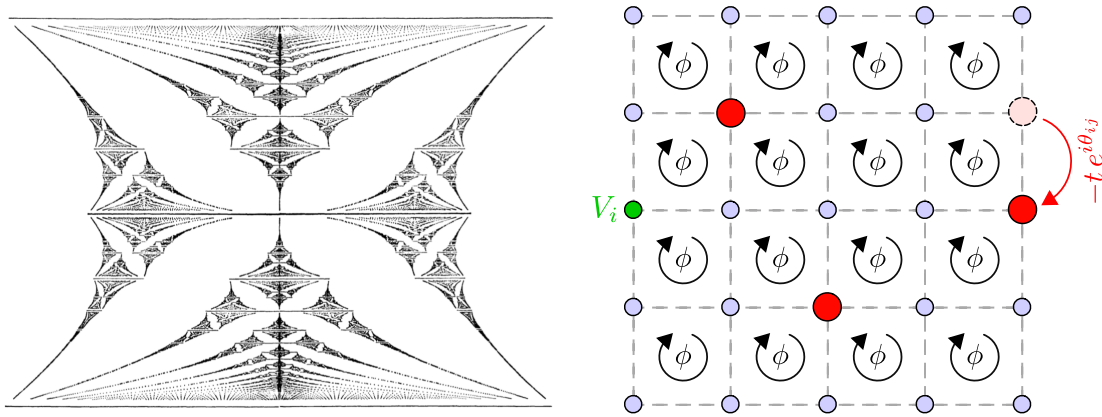
Figure 8.1: Left: Hofstadter butterfly, i.e. the energy spectrum for the Bloch electron experiencing a uniform magnetic field. The magnetic flux ϕ runs vertically from 0 to Φ_0, while energy runs horizontally. This picture has been taken from Hofstadter [1976]. Right: Schematic representation of three bosons (red circles) on a 5×5 lattice with $\phi = \alpha\Phi_0$ flux per plaquette. Picture taken from Macaluso et al. [2019b].

and where $\hat{n}_i = \hat{a}_i^\dagger \hat{a}_i$ is the on-site particle density. The hopping between neighboring sites i and j is characterized by an amplitude t and by the Peierls phase θ_{ij}, which is related to the magnetic flux passing through the system [Peierls, 1933]. We focus on the case of a uniform magnetic flux per plaquette $\phi = \alpha\Phi_0$, where $\Phi_0 = 2\pi\hbar/e$ is again the magnetic flux quantum. For a given value of the flux density α, multiple choices of the phases θ_{ij} are possible. Among them, we choose the Landau gauge considered for instance in Gerster et al. [2017], namely the one in which $\theta_{ij} = 0$ for hopping in the x direction, while $\theta_{ij} = x\phi$ for hopping in the y direction[1]. Moreover, we consider the limit of hard-core bosons (that is, with infinite on-site repulsion U), where each site can host at most one particle. The local energy offsets V_i represent additional attractive or repulsive potentials on some lattice sites [see Fig. 8.1, right], which can encode the localized impurity potentials and/or an additional trapping potential for the particles.

Even though in the following we focus only on harmonic confinements described by $V_i = \Omega|\vec{r}_i - \vec{r}_{\text{center}}|^2$, where the trap center corresponds to the center of the $L \times L$ lattice, more complicated forms could be studied with no additional difficulties. Note that the value of Ω cannot be chosen arbitrarily, since it is not guaranteed that the ground state is an FCI for *any* trapping strength. However, for all considered sets of Hamiltonian parameters (N, L, α) we identified a finite interval of Ω's for which the ground state is an FCI. Although a systematic study of the stability of such a strongly correlated phase, as a function of both the magnetic flux density α and the confining strength Ω, is certainly interesting for experimental purposes, we left it for future work.

To conclude this introductory section, we stress that different values of α correspond to different ratios between the lattice constant a and the effective magnetic length l_B. In particular, for the model under study (i.e., the HH model on a square lattice), such a ratio reads

$$\boxed{\frac{a}{l_{\text{B}}} = \sqrt{2\pi\alpha}} \; . \tag{8.2}$$

This expression of the lattice spacing in terms of the effective magnetic length is not only at the heart of the numerical method described in Sec. 8.4.1, but it will be of crucial importance for the analysis of the QH density depletions in Sec. 8.4. Note that, as shown by Liu et al. [2015], one can introduce a (model-dependent) effective magnetic length also in the case of lattice models where topologically non-trivial bands appear in the absence of a net external magnetic field [e.g., the Haldane [1988] model]. To take into account also for these models, one can consider the general definition of the effective magnetic length: $l_B = \sqrt{A/2\pi}$, where A is the area of the magnetic unit cell.

---

[1]Note that we assigned the coordinates $(x = 0, y = 0)$ to the lower left lattice site.
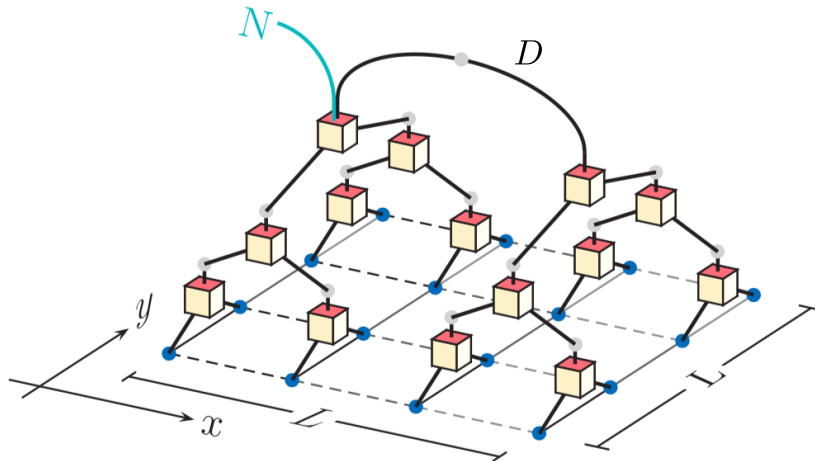

Figure 8.2: Tree Tensor Network ansatz for a $L \times L$ lattice. Blue dots represent the physical lattice sites, and in the case of hard-core interactions have local dimension $d = 2$. Each tensor (squares) links to sites to one virtual site (grey dots), leading to a hierarchical tree structure. Virtual sites in the l-th level (counting from below) have dimension given by $\min(d^{2^l}, D)$, where D denotes the bond dimension of the Tree Tensor Network. Picture taken from Gerster et al. [2017].

8.2 The Tree Tensor Network ansatz

In the presence of interactions, finding the exact ground state of a quantum many body problem is often possible only for small system sizes, by means of exact diagonalization (ED) of the Hamiltonian matrix. A more recent class of numerical techniques is based on the optimization of quantum states in the family of Tensor Network (TN) states, which is a generalization of Matrix Product States – see for instance the reviews by Orús [2014], Gerster et al. [2014], Montangero [2018] and Silvi et al. [2019]. Tensor Network states, which are distinguished by their different network topologies, notably include Projected Entangled-Pair States (PEPS) [Verstraete et al., 2006, Schuch et al., 2007], Entangled-Plaquette States (EPS) [Mezzacapo et al., 2009], the Multi-scale Entanglement Renormalization Ansatz (MERA) [Vidal, 2007, 2008], and the Tree Tensor Network (TTN) states used in the following.

This latter variational ansatz has some noticeable advantages and shortcomings compared to other TN ansatz states, all essentially related to their loop-free structure [see Fig. 8.2]. On the one hand, TTNs do not capture the entanglement area law for arbitrarily large systems (which, instead, PEPS would do by construction). On the other hand, their simple connectivity allows for very efficient computational algorithms [Shi et al., 2006, Montangero, 2018, Silvi et al., 2019]. Thus, the bond dimension D (which can be interpreted as a set of variational parameters) can be pushed to large enough values to compensate for the intrinsic weaknesses of the ansatz, yielding reliable numerical results for system sizes which are beyond reach with exact diagonalization. Finally, TTNs can be equally used to study systems with periodic boundary conditions (PBCs) and systems with experimentally more relevant open boundary conditions (OBCs).

The capability of the TTN technique to reproduce the properties of a FCI state without QH excitations, has be shown by Gerster et al. [2017] for the interacting Harper-Hofstadter model in Eq. (8.1). These properties include the correct topological degeneracy when the system is placed on a torus, the many-body Chern number, the behavior of correlation functions, and the entanglement-entropy scaling laws. For the case of a FCI state with QH excitations, we benchmark the validity of the TTN ansatz through a comparison to ED results, obtained for a system with a small number of particles and PBCs [see Appendix F]. The convergence analysis of the TTN results as a function of the bond dimension is instead reported in Appendix G.

8.3 The charge of lattice quasiholes

As a preliminary step before entering into the discussion of the QH braiding phase, we show that it is possible to stabilize states with either one or two (overlapping) QHs. To do so, we make use

of some localized pinning potentials with different strengths and shapes (e.g. point-like potentials acting on a single-site, plus-shaped potentials, square-shaped potentials, etc.). For systems with PBCs, it is already known that some of these potentials can select states with a single QH as the ground state of the system [Liu et al., 2015, Umucalılar, 2018, Jaworowski et al., 2019]. On the other hand, only recently Račiūnas et al. [2018] have inspected the stabilization of QHs in systems with OBCs. However, the use of exact diagonalization techniques limited their analysis to systems with small number of particles ($N = 4$), preventing them from clearly observing the predicted value of the QH fractional charge.

Charge fractionalization is known to be one of the hallmarks of FQH physics and, as such, it has been at the center of many theoretical and experimental studies. However, we would like to stress that in the present literature there was no unambiguous signature, obtained starting from a realistic lattice Hamiltonian with OBCs, that such a property can be clearly observed in experiments with relatively small number of particles. In the following, thanks to the TTN technique discussed in the previous section, we show that $N = 12$ particles are already enough to observe the $-1/2$ charge of the QHs in the interacting Harper-Hofstadter model.

8.3.1   TTN results for the quasihole charge

We consider the Hamiltonian in Eq. (8.1) with $N = 12$, $L = 16$, $\alpha = 0.15$ and traping frequency $\Omega = 1 \times 10^{-3}$ and we add a pinning potential with finite intensity V_i on each of the four sites of a plaquette at the center of the trap (squared-shaped potential). Then we compute the charge Q_l, defined as:

$$Q_l = \sum_j \delta n_j = \sum_j \left[\langle \hat{n}_j \rangle_{V_i} - \langle \hat{n}_j \rangle_{V_i=0} \right], \tag{8.3}$$

where the sum is restricted to the sites j of a $l \times l$ square at the center of the trap. For large V_i, the density on the central 2×2 plaquette tends to zero, so that (for $l = 2$) Q_l tends to $-4 \times (\alpha/2) = -0.3$, which is minus four times the bulk density in the absence of pinning potentials. This is clearly visible in the lower panel of Fig. 8.3. Note that for $\alpha = 0.25$ the plateau in Q_2 would occur exactly at $-1/2$, independently on the number of QHs pinned by the impurity potential, and this could lead to the misinterpretation of the data. The correct values for the (fractional) charge of the QH excitations are recovered for large enough l. The lower panel in Fig. 8.3 clearly shows that, by increasing the potential strength, Q_l saturates at $-1/2$ and -1, which are the expected charges for one and two QHs, respectively. Note that the exact location of the transitions between 0, 1 and 2 QHs also depends on the trapping strength Ω, on the flux density α, and on the particle number N.

Along this line, there are two important remarks we want to make. The first one concerns the robustness of the bulk against weak perturbations: While for pinning potentials strong enough to create some QH excitations, the density depleted by the QHs is displaced to the system boundary [see middle and right pictures in Fig. 8.3, top panel], weak repulsive potentials modify the systems density only around the potential position, giving an overall depleted charge $Q_l \simeq 0$ for sufficiently large values of l and no accumulated charge on the boundary [see left picture in Fig. 8.3, top panel]. Note also that the robustness of the bulk is expected to increase with the number of particles, since in the large-N limit the density depleted by the QH must be pushed much farther away to reach the system boundary.

The second point concerns the role played by harmonic confinement, which we found to be very important to efficiently stabilize the QH states. The advantage of introducing an additional harmonic trap is twofold: On the one hand, it shifts the edge modes of the FCI state to higher energies. On the other hand, it allows the system to automatically regulate its spatial extension to minimize the energy. Thus the system can adapt itself to the presence of the pinning potentials by putting QHs in correspondence with the potentials and displacing the extra density to the boundary, without the need of removing particles or modifying the flux density α. In other words, in the presence of a harmonic confinement the system automatically chooses the right amount of flux quanta in order to be an FCI at filling $\nu = 1/2$ with the most suitable number of QH excitations. Note that this behavior is completely different from what usually happens in systems with OBCs (without additional trapping potentials), where the total number N_{QH} of QH excitations is set by the fact that $\nu = (N + N_{QH}/2)/(L-1)^2\alpha$.

Even though we considered squared-shaped potentials in our analysis of the QH charge, we verified that similar results can be obtained for pinning potentials of different forms [see for instance
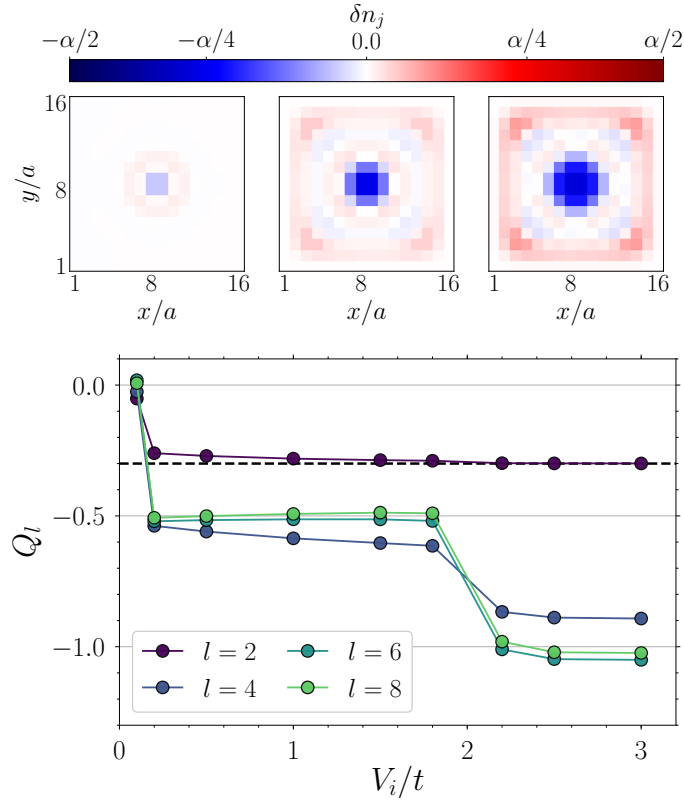
Figure 8.3: Upper panel: variation in the occupation of the different lattice sites with respect to the unperturbed state $\delta n_j = \langle \hat{n}_j \rangle_{V_i} - \langle \hat{n}_j \rangle_{V_i=0}$, induced by a 2×2 pinning potential of strength V_i ($V_i/t = 0.1$, 1.0, and 2.5, from left to right) placed in the center of the lattice. Lower panel: Charge Q_l induced by a square-shaped pinning potential with intensity V_i on the central plaquette (i.e. on the central 2×2 lattice sites). For large enough l, the charge saturates to the expected values for one and two QHs, namely $Q_l = -1/2$ and $Q_l = -1$. The charge is computed as in Eq. (8.3), for the values of l indicated in the legend. The horizontal dashed line corresponds to $-4 \times (\alpha/2) = -0.3$, that is, minus four times the bulk density of the unperturbed FCI state. The TTN bond dimension is $D = 350$ for all data points. In both panels the considered Hamiltonian parameters are $N = 12$, $L = 16$, $\alpha = 0.15$ and $\Omega = 1 \times 10^{-3}$. Taken from Macaluso et al. [2019b].

the single-site and the plus-shaped potentials used in Sec. 8.4 to stabilize one and two QHs, respectively]. The discussion about the pros and cons of the different pinning potentials, and the effects they have on the QH properties, is postponed to the next section.

8.4   The statistics of lattice quasiholes

From the theoretical point of view, the statistical properties of the QH excitations on top of a FCI have been largely inspected in the past, for both Abelian and non-Abelian QHs. However, all these studies have been carried on by considering either abstract periodic structures (i.e., systems with PBCs) [Liu et al., 2015, Jaworowski et al., 2019, Kapit et al., 2012], or analytic ansatz wave functions with complicated parent Hamiltonians [Nielsen, 2015, Nielsen et al., 2018, Manna et al., 2018].

On the contrary, in this section we evaluate the braiding phase of the QHs hosted by the FCI state with Hamiltonian (8.1) in the case of OBCs. For this purpose we use a lattice version of Eq. (7.23) and we consider two different sets of Hamiltonian parameters: $N = 12$ particles on a 16×16 lattice with flux density $\alpha = 0.15$ and an addition harmonic trap of strength $\Omega = 1 \times 10^{-3}$ (Case I) or $N = 18$ particles on a 16×16 lattice with $\alpha = 0.25$ and $\Omega = 3 \times 10^{-3}$ (Case II). Note that these two choices for α correspond to $a/l_B \simeq 0.97$ and $a/l_B \simeq 1.25$, respectively [see Eq. (8.2)]. The two sets of parameters used in the numerical calculations are summarized in Table 8.1.

Considering different values of α allows us to modify N in a significant way without changing the

	N	L	α	Ω/t
Case I	12	16	0.15	1×10^{-3}
Case II	18	16	0.25	3×10^{-3}

Table 8.1: Parameters of the Harper-Hofstadter model used in this section.

size of the lattice, and it also gives us the opportunity to inspect discretization and flux-dependent effects. Note also that for Case II we choose $\alpha = 0.25$, which is one of the most appealing flux densities for realizing (almost-)flat topological bands in realistic experiments [Aidelsburger et al., 2014, Tai et al., 2017, Roushan et al., 2016, Owens et al., 2018].

Finally, concerning the TTN ansatz, we use bond dimensions as large as $D = 500$ (for the largest N), and we verify that the systematic error in the relevant observables is negligible [see Appendix G].

8.4.1   An auxiliary method: sampling of discretized Laughlin quasiholes

Even though the TTN approach allows us to capture a very close approximation of the true ground state of the Harper-Hofstadter model, there is a practical limit on the lattice size and particle number that can be treated [see discussion in Appendix G].

To address more technical questions related to the effect of the lattice grid, rather than of the system size [see Sec. 8.4.3], we employ an auxiliary method which provides more flexibility. This consists in the Monte Carlo sampling of a discretized version of the Laughlin-like wave functions presented in Chapter 3, which are evaluated on the sites of a two-dimensional grid, as done for instance by Hafezi et al. [2007]. As we know, at filling $\nu = 1/2$, the wave function for N particles and κ QHs reads

$$\Psi_{\kappa\mathrm{QH}}(\eta; z) = \left[\prod_{i=1}^{N} \prod_{\mu=1}^{\kappa} (z_i - \eta_\mu) \right] \Psi_{\mathrm{L}}(z) \tag{8.4}$$

where $\Psi_{\mathrm{L}}(z)$ is again the Laughlin wave function in Eq. (3.5) and, on a lattice, the position of the j-th particle $z_j = x_j + iy_j$ in the complex plane only takes discrete values (that is, with x_j/a and y_j/a integer).

The use of the Laughlin wave function as a reference state for Harper-Hofstadter systems in the limit of low flux density α is common in literature [Sørensen et al., 2005, Hafezi et al., 2007]. In this work, we use the wave functions in Eq. (8.4) to study the properties of QH excitations, and to provide a comparison with the HH model. The usefulness of this comparison relies on the study by Liu et al. [2015], which proves that the density profile around FCI QHs is a discretized version of the one of Laughlin QHs in continuum space, up to a proper rescaling of the length units. Of course, for a given flux density α, a proper comparison with the HH model requires that the lattice spacing of the discretization grid satisfies Eq. (8.2).

For a discretized Laughlin-like wave function, it is straightforward to generalize the Monte Carlo technique presented in Appendix E. Moreover, by changing the discretization of $\Psi(\eta; z)$ (that is, by tuning the lattice constant a), we have access to different values of a/l_{B}. This is valuable to have a one-to-one comparison with HH systems [where this ratio is set by α – see Eq. (8.2)], but also to perform a more systematic study of the convergence towards the continuum limit ($a/l_{\mathrm{B}} \to 0$).

Note, to conclude, that other ansatz wave functions are available for the lattice version of Laughlin state, see for instance the one proposed by Nielsen [2015], and we expect that similar results can be obtained for all of them.

8.4.2   The lattice generalization of the depletion protocol

While in Secs. 7.2.2 and 7.2.3 we presented the theory relating the anyonic statistics of QHs to their depletion profiles in a continuum geometry, here we discuss how these relations [Eqs. (7.19) and (7.23)] change in the case of lattice systems.

The mean square radius $\langle r^2 \rangle$ now reads

$$\langle r^2 \rangle = \frac{1}{N} \sum_j \langle \hat{n}_j \rangle |\vec{r}_j|^2, \tag{8.5}$$

$a/l_{\rm B}$	$\varphi_{\rm br}/(2\pi)$	α
0.5605	0.53 ± 0.04	0.05
0.9708	0.55 ± 0.04	0.15
1.2533	0.57 ± 0.04	0.25
1.7725	0.56 ± 0.04	0.50

Table 8.2: Quasihole braiding phase $\varphi_{\rm br}$ for a discretized Laughlin-like wave function (with $N = 40$ particles), for different values of the grid spacing a. Numerical results (listed in the second column, with their statistical uncertainty) are obtained via Eq. (8.6) and Monte Carlo sampling of the discretized Laughlin wave functions. In the third column, we list the value of α that would correspond, in the HH model, to the chosen lattice spacing $a/l_{\rm B}$ [see Eq. (8.2)].

where $\vec{r}_j$ is the position of the j-th site. With this definition, it is straightforward to generalize Eq. (7.19) to the lattice case:

$$\boxed{\frac{\varphi_{\rm br}}{2\pi} = \frac{1}{2l_{\rm B}^2} \sum_j \left[\langle \hat{n}_j \rangle_{|\eta_1|=|\eta_2|} - \langle \hat{n}_j \rangle_{\eta_1 = \eta_2} \right] |\vec{r}_j|^2 }. \tag{8.6}$$

In a similar way we define the depletions $d_{1\rm QH}(\vec{\rho}_j)$ and $d_{2\rm QH}(\vec{\rho}_j)$ as

$$d_{k\rm QH}(\vec{\rho}_j) = \langle \hat{n}_j \rangle_{0\rm QH} - \langle \hat{n}_j \rangle_{\kappa\rm QH}, \qquad \kappa = 1, 2, \tag{8.7}$$

where $\langle \hat{n}_j \rangle_{\kappa\rm QH}$ is the average density on site j for a state with κ QHs at position $\vec{\eta}$, and where $\vec{r}_j = \vec{\eta} + \vec{\rho}_j$. Thus Eq. (7.23) becomes

$$\boxed{\frac{\varphi_{\rm br}}{2\pi} = \frac{1}{2l_{\rm B}^2} \sum_j \left[d_{2\rm QH}(\vec{\rho}_j) - 2d_{1\rm QH}(\vec{\rho}_j) \right] |\vec{\rho}_j|^2 }, \tag{8.8}$$

where the sum over j is restricted to sites with $|\vec{\rho}_j| < R_{\rm max}$, as for Eq. (7.23). Note that both expressions for the braiding phase $\varphi_{\rm br}$ [see Eqs. (8.6) and (8.8)] explicitly depend on the effective magnetic length $l_{\rm B}$, defined in Eq. (8.2).

Before moving on, we need to stress that the angular momentum operator is not properly defined on a lattice, and therefore the relation between the QH braiding phase and the density profile [Eqs. (8.6) and (8.8)] is not mathematically rigorous in this case[2]. However, the idea of generalizing Eqs. (7.19) and (7.23) to the case of FCIs on a lattice is motivated (and partially justified) by two observations:

First, the study by Liu et al. [2015] clearly shows that, for systems with periodic boundary conditions (PBCs), the density profile close to a single FCI QH is a discrete sampling of the continuum case, once a suitable (model-dependent) effective magnetic length is introduced. In Sec. 8.4.3, we explicitly extend this result to the case of the interacting HH model with OBC, both for a single and a double QH.

Second, we perform a complementary analysis of the lattice case, based on the discretized Laughlin-like wave functions described in Sec. 8.4.1. This flexible ansatz allows us to scan different values of the grid spacing a, and to compute the braiding phase through the discretized versions of Eqs. (7.19) and (7.23). In Table 8.2, we report the numerical results obtained via Eq. (8.6). We find that the braiding phase of the QH excitations of the discretized Laughlin state is in full agreement –up to some small deviations mainly due to discretization effects– with the expected value $\varphi_{\rm br}/(2\pi) = 1/2$, within the statistical uncertainties of the Monte Carlo method. It is remarkable that this still holds true for $a/l_{\rm B} \simeq 1.77$, which corresponds to the maximum flux density that can be realized in the HH model, i.e. $\alpha = 1/2$. The behavior of the braiding phase as a function of the cut-off radius $R_{\rm max}$, entering in Eq. (8.8), in shown in Fig. 8.4 instead. Although for small values of $R_{\rm max}$ the discretization effects are clearly visible (especially for $a \geq l_B$), the behavior characterizing the braiding phase of the Laughlin QHs in the continuum is recover at larger values of the cut-off for all considered lattice spacings.

---

[2]Note that in Sec. 7.1 we assumed the rotational invariance of the system Hamiltonian without pinning potentials, which is of course explicitly broken for a lattice system.
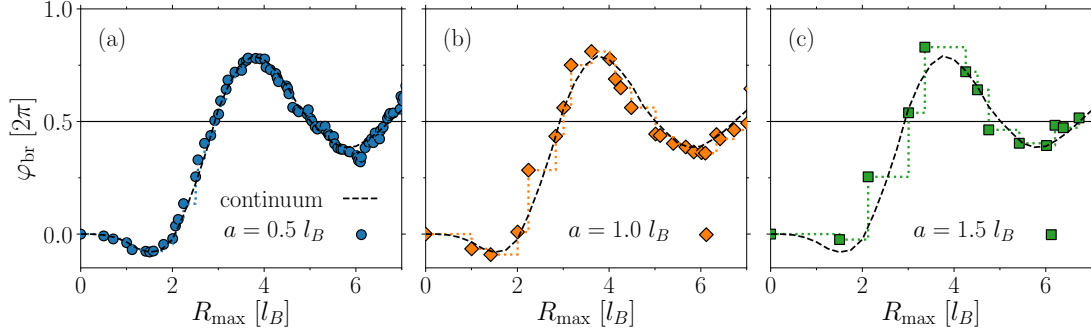

Figure 8.4: (a)-(c): Quasihole braiding phase evaluate with Eq. (8.8), as a function of the cutoff radius $R_{\max}$, obtained by sampling the Laughlin quasihole wave functions with different discretization grids: $a/l_B = 0.5, 1.0$ and 1.5 for (a), (b) and (c), respectively. For all panels we considered $N = 40$, $\nu = 1/M = 1/2$ and quasiholes pinned at the $\eta_\mu = 0$.

Marker	Parameters	1QH pinning	2QH pinning
○	Case I	single-site $(V_i/t = 2.0)$	plus-shaped $(V_i/t = 1.0)$
□	Case II	single-site $(V_i/t = 4.0)$	plus-shaped $(V_i/t = 0.7)$
◇	Case II	single-site $(V_i/t = 4.0)$	plus-shaped $(V_i/t = 1.0)$
⬡	Case II	square-shaped $(V_i/t = 0.4)$	square-shaped $(V_i/t = 2.0)$

Table 8.3: Hamiltonian and pinning potential parameters considered in the TTN calculations of the quasihole braiding phase [see Figs. 8.6 and 8.7].

8.4.3 TTN results for the quasihole statistics

The method proposed in Sec. 7.2.3 has the great advantage of allowing us to determine the QH braiding phase in a set-up that would be prohibitive for the more traditional schemes involving real braiding and interference. By lifting the needs of an explicit rotation of the QHs, and of their spatial separation, this method allows us to work with trapped samples with OBCs (rather than with abstract periodic structures) also when the number of particles is relatively small [3]. On this basis, we decided to apply the lattice generalization of that protocol (derived in the previous section) to the FCI QHs under study [see parameter sets in Table 8.1]. We stress that both in Case I and in Case II, the system size is too small to accommodate two QHs far enough from each other and from the system boundary to apply the usual braiding schemes.

Quasihole density depletions

The key ingredients to measure the QH braiding phase, through the protocol described by Eq. (8.8), are the density depletions $d_{1QH}(\vec{\rho}_j)$ and $d_{2QH}(\vec{\rho}_j)$. To take advantage of Eq. (8.8), the set of vectors $\{\vec{\rho}_j\}$, i.e. the distances between the lattice sites and the QH center, must be the same for both d_{1QH} and d_{2QH}. As a consequence, both the single QH and the two overlapping QHs must be centered at the same position. To satisfy this constraint we identified two possible configurations: (i) a single-site potential to pin the single QH and a plus-shaped potential (centered on the same site and spread over five sites) to pin the two overlapping QHs; (ii) a 2×2 square-shaped potential with different strengths to selectively pin one or two QHs.

In order to extract the depletions $d_{1QH}(\vec{\rho}_j)$ and $d_{2QH}(\vec{\rho}_j)$, one needs the density profiles $\langle \hat{n}_j \rangle_{\kappa QH}$ characterizing states without QHs ($\kappa = 0$), with a single QH ($\kappa = 1$), and with $\kappa = 2$ overlapping QHs [see Eq. (8.7)]. We evaluated these density profiles by means of the TTN technique [see

---

[3]The presence of the system boundary dramatically reduces the available flat-density region, where the QHs must be pinned (far from each other) and eventually braided to address their statistical properties through the traditional methods.
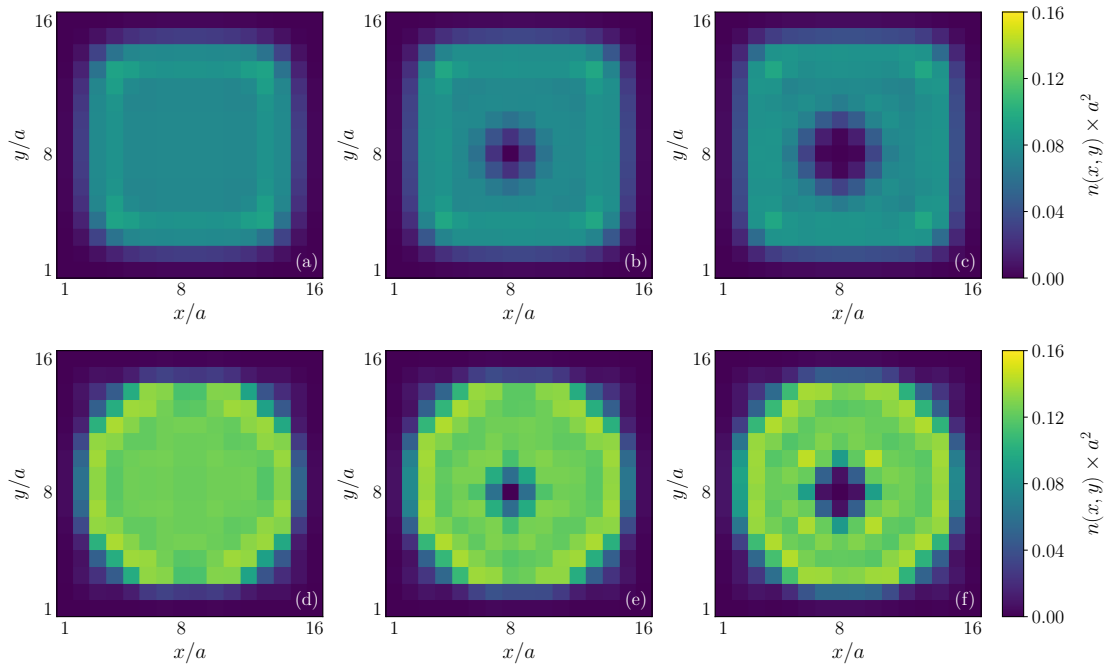
Figure 8.5: Two-dimensional density profiles for Case I [panels (a), (b) and (c)] and Case II [panels (d), (e) and (f)], obtained by TTN calculations. Panels from left to right represent states with zero, one or two QHs pinned at site $(8, 8)$. For Case I we used a single-site pinning potential of strength $V_i/t = 2.0$ located at $(8, 8)$, to pin the single QH [panel (b)], and a plus-shaped potential of strength $V_i/t = 1.0$ acting on the sites $(7, 8)$, $(8, 7)$, $(8, 8)$, $(8, 8)$ and $(9, 8)$, to pin the two overlapping QHs [panel (c)]. For Case II we used a single-site pinning potential of strength $V_i/t = 4.0$, still at $(8, 8)$, for the single QH [panel (e)], and the same plus-shaped potential as before, for the two overlapping QHs [panel (f)]. The TTN bond dimension is $D = 350$ for Case I and $D = 500$ for Case II. Picture taken from Macaluso et al. [2019b].

examples in Fig. 8.5], and the resulting QH density depletions $d_{1\text{QH}}(\vec{\rho}_j)$ and $d_{2\text{QH}}(\vec{\rho}_j)$ are shown in panel (a) of Fig. 8.6 and in panels (a) and (b) of Fig. 8.7.

To simplify the interpretation of these figures, we introduce the following marker notation: First, blue (orange) markers denote the data obtained through the TTN technique for the depletion due to a single (double) QH. Second, the different marker shapes are associated with different physical parameters and/or pinning potentials, as summarized in Table 8.3. Finally, regarding the results for the QH braiding phase [panel (b) of Fig. 8.6 and panels (c) and (d) of Fig. 8.7], red markers indicate the TTN results for the interacting HH model, the black crosses refer to the data obtained through the sampling of the discretized Laughlin-like wave functions, while the black dashed line corresponds to the behavior of φ_{br} for the Laughlin QHs in the continuum.

The comparison of the QH density depletions obtained through the TTN technique with those characterizing the Laughlin QHs is in general very good [see panel (a) in Fig. 8.6 and panels (a) and (b) in Fig. 8.7], up to small deviations. At large distances there are discrepancies due to finite-size effects which affect both $d_{1\text{QH}}(\vec{\rho}_j)$ and $d_{2\text{QH}}(\vec{\rho}_j)$. To be precise, these are caused by the presence of the density bump close to system boundary, which modifies the tail of the depletions. Note that this bump in the system density is not a particular feature of the lattice system under study, but it is common to all FQH states in geometries with OBCs [see for instance the density profiles in Fig. 7.3].

To mitigate this problem, we restrict the plotted data to distances for which the depletions behave smoothly and the QH charges are close to the predicted values (i.e., -0.5 and -1 for the single and the double QH, respectively). Concerning small and intermediate distances instead, the reason why the QH density depletions in these regions appear slightly different with respect to their continuum counterparts is twofold. On the one hand, there is the effect of the pinning potentials [see for instance the radial profiles of the 2QH density depletions reported in panel (a) of Fig. 8.7], which is more evident for $\alpha = 0.25$ than for $\alpha = 0.15$. This dependence on the flux density is due to the fact that larger α's correspond to larger values of the ratio a/l_{B}.
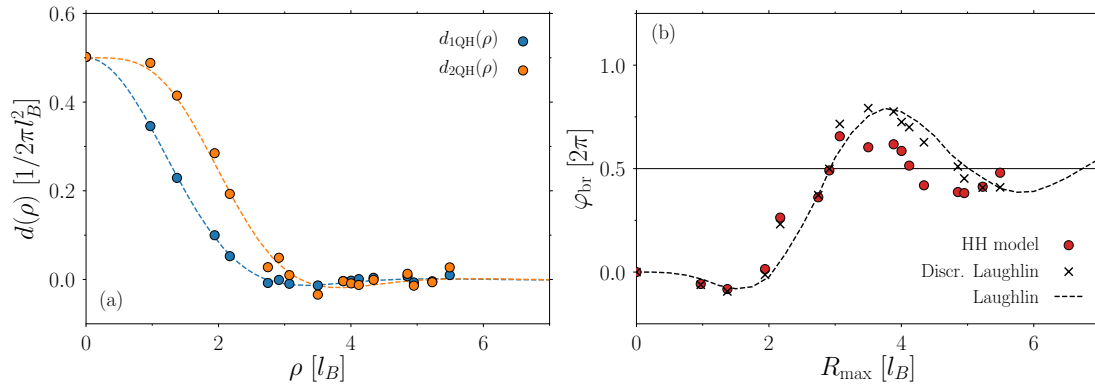
Figure 8.6: Panel (a): Comparison between the density depletions created by a single QH (blue dots) and two overlapping QHs (orange dots) in the interacting HH model and in the continuum $\nu = 1/2$ Laughlin state (blue and orange dashed lines). Panel (b): Comparison between the quasihole braiding phase, as a function of the cutoff radius $R_{\max}$, for the interacting HH model (red dots), for the discretized quasihole wave functions in Eq. (8.4) with $a \simeq 0.97\,l_{\mathrm{B}}$ (black crosses), and for their continuum version (black dashed line). The Hamiltonian parameters are those of Case I and the properties –shape and strength– of the pinning potentials considered in the TTN calculations are reported in Table 8.3. The TTN bond dimension is $D = 350$ for all data sets. Picture taken from Macaluso et al. [2019b].

As a consequence, in the case of $\alpha = 0.25$, the same (finite-width) pinning potential used for $\alpha = 0.15$ effectively acts at larger distances from the center of the QH, where the system density is higher and the potential has stronger effects on the QH depletions $d_{1\mathrm{QH}}$ and $d_{2\mathrm{QH}}$. On the other hand, there are unexpected deformations which are present also in the density depletion of the single QH pinned by a single-site potential [see blue squares and blue diamonds in panel (a) of Fig. 8.7 at short and intermediate distances]. Zero-range pinning potentials should not deform the QH density depletions and therefore we consider the observed discrepancies as model-dependent effects, probably due to the specific properties of the HH bands for a given value of α. This would explain why this behavior is more evident for Case II ($\alpha = 0.25$) than for Case I ($\alpha = 0.15$).

Quasihole anyonic statistics

Finally, we used the method described in the previous section to extract the braiding phase φ_{br} of the lattice QHs, as a function of the cutoff radius $R_{\max}$ [see Figs. 8.6 (b) and 8.7 (c) and (d)]. We compare it with the results obtained for both the QHs of the continuum-space Laughlin state and their discretized counterparts. We recall that for the sampling of the discretized QH wave functions one needs a different discretization grid for Case I and Case II, since they are characterized by a different value of the ratio a/l_{B} [see Eq. (8.2)].

For Case I, the behavior of φ_{br} obtained for the QHs of the interacting HH model is extremely similar to the one predicted by the Monte Carlo sampling of the discretized Laughlin QHs up to a certain value of $R_{\max}$ [see Fig. 8.6, panel (b)]. After that, at larger cutoff radii, we observe small deviations between the two data sets, reflecting the deformations in the depletion $d_{2\mathrm{QH}}(\vec{\rho}_j)$ caused by the plus-shaped pinning potential. However, the results shown in Fig. 8.6(b) clearly indicate that for Case I the anyonic nature of the QHs in the interacting HH model can be probed through simple density measurements.

The interpretation of the QH braiding phase obtained for Case II is more subtle. As we have already discussed, for $\alpha = 0.25$ the density depletions of the lattice QHs display more visible discrepancies, with respect to their continuum counterparts, than for $\alpha = 0.15$. Moreover, due to the $|\vec{\rho}_j|^2$ factor in Eq. (8.8), these discrepancies in the depletions translate into even stronger effects affecting the behavior of $\varphi_{\mathrm{br}}(R_{\max})$. This is clearly visible in panel (c) of Fig. 8.7. Despite discrepancies in the profile of the density depletions, the method proposed in Eq. (8.8) is still valid and the correct results for $\varphi_{\mathrm{br}}(R_{\max})$ are recovered for large enough integration regions – where the deformations in the density depletions are damped. We attribute this behavior to the topological robustness[4] of the QH braiding properties and we expect further confirmation of this

---

[4]The robustness of Laughlin properties on the lattice has been already seen by explicit computation of many-body
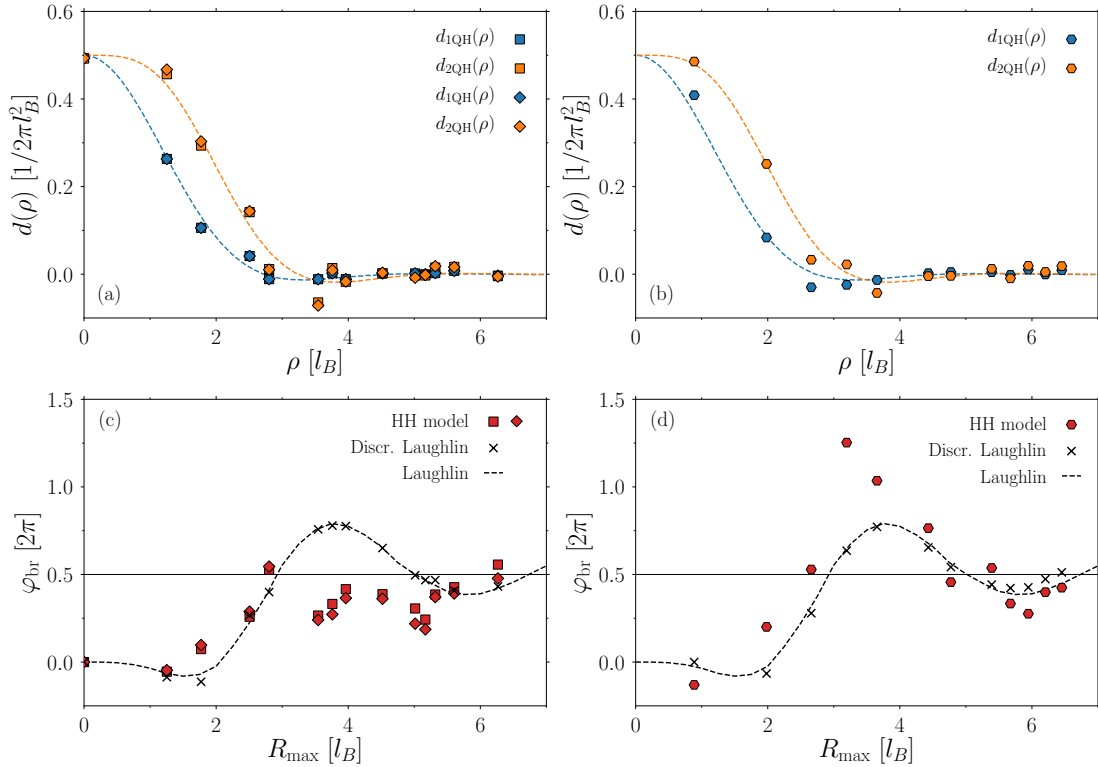
Figure 8.7: Panels (a) and (b): Comparison between the density depletions created by a single QH (blue markers) and two overlapping QHs (orange markers) in the interacting HH model and in the continuum $\nu = 1/2$ Laughlin state (blue and orange dashed lines). Different markers indicate the use of different pinning potentials [see Table 8.3] to create the quasiholes in a system with Case II parameters. Panels (c) and (d): Comparison between the quasihole braiding phase, as a function of the cutoff radius $R_{\max}$, obtained for the interacting HH model with different pinning potentials (red markers), for the discretized quasihole wave functions in Eq. (8.4) with $a \simeq 1.25\, l_B$ (black crosses), and for their continuum version (black dashed line). In panels (a) and (c) quasiholes are centered on a lattice site, while in (b) and (d) they are located at the center of a plaquette. The TTN bond dimension is $D = 500$ for all data sets. Taken from Macaluso et al. [2019b].

interpretation from future studies of of larger systems. In spite of these additional difficulties, the results obtained for Case II confirm that the anyonic nature of the QHs can be inspected through simple density-profile measurements also in the experimentally promising $\alpha = 0.25$ case.

Even though our method to measure QH braiding phase seems to be robust against the deformations induced by extended pinning potentials in the depletion profiles, such deformations affect the behavior of $\varphi_{\mathrm{br}}(R_{\max})$ at small and intermediate values of the cutoff radius. To get rid of these effects, one could in principle create multiple QHs at the same position by locally inserting the suitable amount of flux quanta, in the presence of a single-site potential able to pin a single QH, as suggested in Grusdt et al. [2014], Wang et al. [2018a] and Račiūnas et al. [2018]. Despite being experimentally feasible, in the theoretical framework this flux-insertion procedure requires time-dependent simulations of the interacting HH Hamiltonian, which at the moment go beyond the capabilities of our TTN technique. Along this line, a recent application of the TTN ansatz for time-dependent simulations by Kohn et al. [2019] opens interesting perspectives.

8.5   Conclusions and remarks

In this last Chapter we have used a Tree Tensor Network ansatz to study the properties of the quasiholes of the bosonic fractional Chern insulator described by the Harper-Hofstadter Hamiltonian with hardcore interactions. The loop-free geometry of the Tree Tensor Network ansatz has

Chern number Sørensen et al. [2005], Gerster et al. [2017].

allowed us to study systems with open boundary conditions, far beyond the typical system sizes manageable by exact diagonalization calculations.

As a first step, we have showed that it is possible to use localized potentials to stabilize states hosting either a single or two overlapping quasiholes, and that the expected fractional charge of these excitations is already clearly visible in systems made of a dozen particles. In this respect, we have discovered that superimposing an additional harmonic confinement to the lattice greatly simplifies the stabilization of the quasihole states.

Then, to characterize the statistics of the quasiholes, we have applied a lattice version of the expression derived in the previous Chapter, relating the quasihole braiding phase to the depletions induced by such excitations in the system density. This has allowed us to show that these excitations are anyons and that their braiding phase is very close to the predicted one. Note that since on a lattice the angular momentum operator is not properly defined, such an expression can not be rigorously derived as done in Chapter 7 for systems in continuum geometries. This opens the interesting question whether it is possible to find a deeper and more general explanation of the link between the statistical properties of the QHs and their density profiles, which seems to be valid also for lattice systems.

To conclude, we would like to stress that the Tree Tensor Network results presented in this Chapter have been obtained by solving an experimentally feasible Hamiltonian, and as such they do now rely on any ansatz wave functions. As a consequence, the present study provides numerical evidence that the quasihole anyonic statistics can be observed through simple density measurements in near-future experiments with ultracold atoms and superconducting qubits: First of all, the flux densities we have considered in this work are already within the current experimental capabilities. The case of $\alpha = 0.25$, in particular, minimizes the ratio between the width of the lowest band and its separation from the higher ones, and it is therefore the most appealing flux-density value for the experimental realization of (almost-)flat topological bands. At the same time, adding an overall harmonic confinement to the system should be possible both for ultracold atoms in optical lattice and for platforms based on superconducting qubits. Finally, while the hard-core limit describes well the on-site interactions in superconducting qubits, it is typically difficult to reach with ultracold atoms. However, in the light of several studies present in the literature [see for instance the papers by Račiūnas et al. [2018], Rosson et al. [2019] and Hudomal et al. [2019]], we strongly believe that considering finite-strength interactions instead of the hard-core ones should not modify our results in a considerable way. A detailed study in this direction is a natural follow-up of this work.

Conclusions and outlooks.

$\widehat{\mathbb{T}}$his Thesis was devoted to the analysis of the quasihole and the edge excitations of some bosonic fractional quantum Hall and fractional Chern insulator states.

In the first part, we have studied the behavior of a $\nu = 1/2$ Laughlin-like fractional quantum Hall droplet in the presence of cylindrically symmetric hard-wall potentials by means of exact diagonalization calculations. We have shown that, already in the presence of a single hard-wall potential confining the system in a disk-shaped region, the obtained many-body spectra display much richer structures with respect to those characterizing harmonically-confined Laughlin droplets. While in the latter edge states with the same angular momentum are degenerate and their energy dispersion is linear in L_z, as predicted by Wen's chiral Luttinger liquid theory, the hard-wall potential removes this degeneracy and the many-body state organized themselves into energy branches and sub-branches which can be fully interpreted in terms of Jack polynomials, highlighting a very precise one-to-one correspondence between them and the Hamiltonian eigenstates. After that we have explored the case of ring-shaped fractional quantum Hall droplets confined within two concentric hard-wall potentials. For this kind of confinements we have found even more complex energy spectra, all characterized by a non-degenerate ground state presenting several quasihole excitations (whose number can be predicted from the knowledge of the potential parameters) at the center of the Laughlin droplet. On top of that, we have proposed an extension of the Jack polynomial formalism to properly describe the presence of two different edges in ring-shaped systems. This allowed us to classify the excited states of ring-shaped droplets and to show the persistence of the one-to-one correspondence between numerically-obtained Hamiltonian eigenstates and the Jack trial wave functions.

Umucalılar and Carusotto [2017] have recently proposed an incoherent pumping scheme for the stabilization of a photonic Laughlin state, which relies on the single hard-wall potential considered in this Thesis. This, together with our analysis of the case of two concentric hard-wall potentials, suggests that ring-shaped geometries obtained in this way could be used in the driven-dissipative photonic context to stabilize fractional quantum Hall fluids with an arbitrary number of quasiholes at the origin. From the theoretical point of view instead, we believe that an exciting future direction would be the extension of our study to the edge excitations of more exotic fractional quantum Hall states, such as the Moore-Read and Read-Rezayi ones [Moore and Read, 1991, Read and Rezayi, 1999]. Although the Jack polynomials formalism for the description of the edge modes of these states has been already developed in Jiang and Hu [2016], the effects of a hard-wall potential on these systems remain totally unexplored.

In the second part of this Thesis, we have proposed a novel scheme to detect anyons in many-body systems. By considering system configurations in which the anyons can be exchanged through rigid rotations of the external potentials creating and pinning them, we were able to express the geometric contributions to the time-evolution of the system in terms of the matrix elements of the rotation and the angular-momentum operators on the states forming the ground-state manifold at initial time. Remarkably, this has been done by using only time-dependent perturbation theory. After that we have focused our attention on the quasihole excitations of fractional quantum Hall states in the lowest Landau level, by showing that part of their statistical properties are encoded in the density profile of the system and, in particular, in the shapes of the depletions they induce

in the bulk density. These theoretical results were tested for the quasihole excitations of the paradigmatic Laughlin and Moore-Read states. On the one hand, this has demonstrated that the quasihole anyonic statistics can be experimentally probed without performing any interference measurement, but just by looking at the system density profile. On the other hand, by considering the quasiholes of the Moore-Read state, we have proved that our method, giving access to the different fusion channels, can be used to characterize also non-Abelian anyons.

An obvious but exciting outlook of this theoretical study is its practical application in next-future experiments with ultracold atoms and photons. In both set-ups indeed, density-profile measurements can be easily performed, and this could lead to the first unambiguous detection of particles with anyonic statistics. In the theoretical context, natural extensions of our analysis include the anyonic excitations of other states in the lowest Landau level, as for instance the Read-Rezayi state whose quasiholes are known to be parafermions, or the Majorana zero modes of the $p_x + ip_y$ superconductor, closely related to the Moore-Read quasiholes studied here. Another interesting question is whether the link between anyonic statistics and angular momentum (or system density) remains valid also for the so-called anisotropic fractional quantum Hall states [Qiu et al., 2012], where the rotational symmetry is explicitly broken.

Finally, in the last part of the Thesis we have extended our investigation to the properties of the quasihole excitations above a bosonic $\nu = 1/2$ fractional Chern insulator state, i.e. in a lattice geometry. For this purpose we have employed a sophisticated Tree Tensor Network technique which allowed us to find the ground state of the Harper-Hofstadter Hamiltonian with hard-core interactions. To be precise, we have considered up to $N = 18$ particles on a 16×16 lattice with open boundary conditions, in the presence of both an additional harmonic confinement and some impurity potentials creating and pinning the quasiholes. As a first step, we have observed the quantization of the quasihole charge at the predicted fractional value and its robustness against small changes in the potential parameters. Then, we have numerically characterized the quasihole anyonic statistics by applying a discretized version of the previously-obtained expression relating such a quantity to the depletion induced in the system density by the quasiholes. The results obtained in this way have clearly shown that these excitations are anyons, as expected, and that the quasihole braiding phase is very close to the predicted one, i.e. $\varphi_{\text{br}} = 2\pi\nu$. At the same time, our study have provided numerical evidence that also in the case of fractional Chern insulators (i.e., the lattice counterparts of fractional quantum Hall states) the anyonic nature of quasiholes can be observed through simple density measurements, and that this can be done in state-of-the-art experiments with ultracold atoms and superconducting qubits.

The analysis we have performed in the last part of this Thesis indicates several interesting directions for future theoretical works. Among them we would like to highlight the extension of this study to other fractional Chern insulator states, and in particular to those hosting non-Abelian excitations [Mazza et al., 2010, Hafezi et al., 2014]. Most of the present literature on this subjects is indeed based either on exact diagonalization calculations or on ansatz wave functions. However, while in the former case one is limited to very small number of particles and/or to unphysical systems with periodic boundary conditions, in the latter case one typically has to deal with complex parent Hamiltonians. As a consequence, we strongly believe that a Tree-Tensor-Network-based investigation of non-Abelian fractional Chern insulators would set the new state-of-the-art. To conclude, we would like to stress that the most thrilling outlook of our proposal is again its experimental implementation. Indeed, in virtue of its simplicity, we strongly believe that our detection scheme would lead to the first observation of anyons in the forthcoming experiments with atomic and photonic quantum simulators.

Appendices

Appendix A

Exact diagonalization technique.

Here we present an efficient method to properly choose the basis for the diagonalization of the Hamiltonian matrix describing a $\nu = 1/r$ FQH liquid in a ring-shaped geometry. It is mainly inspired by the following observations: (i) The number of QHs in the system ground state can be predicted from the knowledge of the $\mathcal{U}_m$ potentials, (ii) the Hamiltonian eigenstates are in general well-described by Jack polynomials[1], and (iii) given two partitions λ and μ of the same integer $L = L_{\mathrm{L}} + \Delta L$, such that $\lambda \succeq \mu$, the associated squeezed Hilbert spaces are related by Eq. (5.8), i.e. $\mathcal{H}_{\mathrm{sq}}(\lambda) \subseteq \mathcal{H}_{\mathrm{sq}}(\mu)$.

Found the number κ of QHs in the system ground state, the monotonically increasing behavior of the $\mathcal{U}_m$ potentials, with respect to their minimum, gives us information on the energetic ordering of states presenting an higher or lower number of QHs,

$$E_{\kappa \mathrm{QH}} < E_{(\kappa-1)\mathrm{QH}} < E_{(\kappa-2)\mathrm{QH}} < \dots \tag{A.1}$$

$$E_{\kappa \mathrm{QH}} < E_{(\kappa+1)\mathrm{QH}} < E_{(\kappa+2)\mathrm{QH}} < \dots, \tag{A.2}$$

but also on the energy costs of different edge excitations sharing the same total angular momentum ΔL. To be precise, for a given angular momentum sector, the lowest-energy eigenstates will be those described by Jacks having root partitions which can be obtained from the ground state one by moving particles only by a few orbitals. Therefore, points (i) and (ii) mentioned above allows us to have a coarse idea of the energetic ordering of Jacks within a given angular momentum sector.

Before moving on, we would like to better explain what we mean by "coarse idea of the energetic ordering". As discussed for instance in Sec. 6.4.2, the energy shifts induced by the confining Hamiltonian H_{conf} depend on the details of the $\mathcal{U}_m$ potentials, but also on the particular values of the mean occupation numbers $\bar{n}_m$ taken on the different Jacks. Therefore, the exact energetic ordering of Jacks with similar root partitions is in general very difficult to predict. For instance, if we consider Jacks with partitions $\lambda_1 = \Omega + \sigma^\kappa + [1,1] - [1] = \Omega + [\kappa+1, \kappa+1, \kappa, \dots, \kappa, \kappa-1]$ and $\lambda_2 = \Omega + \sigma^\kappa + [1,1,1] - [1,1] = \Omega + [\kappa+1, \kappa+1, \kappa+1, \kappa, \dots, \kappa, \kappa-1, \kappa-1]$, their energies will be almost the same and we cannot be sure of which Jack will have the lowest one. However, both of them will certainly have much lower energies than the Jack polynomial of root partition $\lambda_3 = \Omega + \sigma^{\kappa-1} + [N+2] = \Omega + [\kappa+N+1, \kappa-1, \dots, \kappa-1]$. The latter has indeed a non-vanishing occupation of larger-m single-particle orbitals and, as a consequence, its energy will take contributions from $\mathcal{U}_m$ potentials with much higher values.

At this point we can take advantage of the relations between the so-called squeezed Hilbert spaces. Root partitions labelling the lowest-energy states, i.e. those obtained from the ground-state one by moving particles only few orbitals, are in general dominated by those labelling the higher-energy ones, indeed. As a consequence, relation (5.8) tell us that the lowest energy states of a given angular momentum sector generally belong to a sub-space of the squeezed Hilbert space

---

[1]The fact that one describes the Hamiltonian eigenstates with Jack polynomials of the form $J^\alpha_{\Omega+\gamma}$, instead of the more accurate product of Jacks $J^\nu_\gamma J^\alpha_\Omega$, is completely irrelevant in this context since both of them belong to the same squeezed Hilbert space $\mathcal{H}_{sq}(\Omega + \gamma)$.
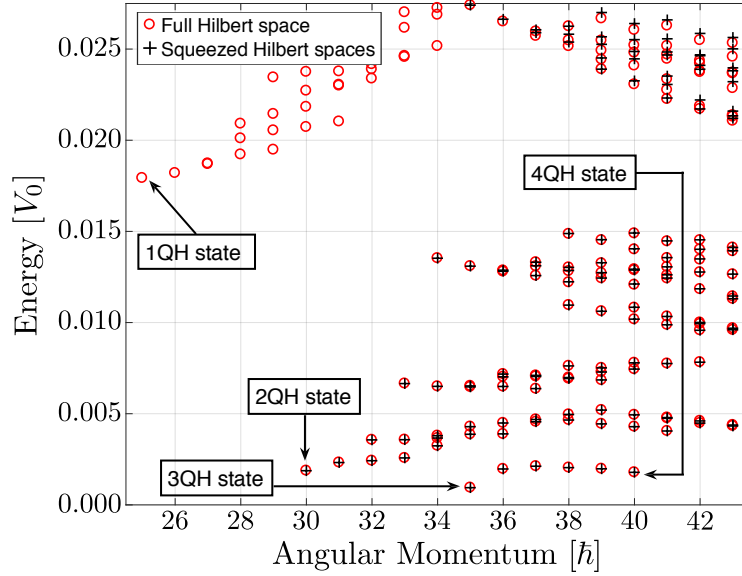
Figure A.1: Energy spectrum for an $N = 5$ particle system experiencing a confinement potential of parameters $V_{in}/V_0 = 2$, $R_{in}/\sqrt{2}\,l_B = 0.5$, $V_{ext}/V_0 = 10$, and $R_{ext}/\sqrt{2}\,l_B = 5.4$. We compare the eigenvalues obtained by diagonalizing the system Hamiltonian on the full Hilbert space $\mathcal{H}_{full}$ (red circles) with those obtained by restricting the system Hamiltonian to the squeezed Hilbert spaces $\mathcal{H}_{sq}(\bar\lambda)$ (black pluses). To be precise, for $\mathcal{H}_{full}$ a single-particle angular momentum cutoff $m = 15$ has been chosen, while for the different $\mathcal{H}_{sq}(\bar\lambda)$ partitions of the form $\bar\lambda = \Omega + \sigma^2 + \rho$, where ρ is the dominant configuration among those of the integer $L - L_L - 2N$ which satisfy $\rho_1 \leq 5$, have been considered. As we can see, the agreement between the different spectra is excellent and small deviations only appear for the highest-energy states. This picture has been taken from Macaluso and Carusotto [2018].

associated with the root partition of Jacks describing states with higher energies. Therefore, in order to obtain the lowest-energy part of the spectrum, one only has to identify (for each angular momentum sector of interest) a Jack polynomial of partition $\bar\lambda$ with sufficiently high energy and then diagonalize the Hamiltonian matrix on the squeezed Hilbert space $\mathcal{H}_{sq}(\bar\lambda)$.

To test our method we compare the energy spectra for $\nu = 1/2$ bosonic FQH droplet made of $N = 5$ particles experiencing an external potential of parameters $V_{in} = 2V_0$, $R_{in} = 0.5\sqrt{2}l_B$, $V_{ext} = 10V_0$, and $R_{ext} = 5.4\sqrt{2}l_B$, obtained by considering the full Hilbert space or properly chosen squeezed Hilbert spaces [see Fig. A.1].

To be precise, for the full Hilbert space we choose $m = 15$ as the cutoff for the single-particle angular momenta. The dimension of such a Hilbert space is $d(\mathcal{H}_{full}) = 20349$. Concerning the squeezed Hilbert spaces instead, we consider partitions of the form $\bar\lambda = \Omega + \sigma^2 + \rho$. In particular, for a given angular momentum sector, we choose $\rho = [\rho_1, \rho_2, \dots]$ as the dominant partition among those of the integer $L - L_L - 2N$ which fulfill the condition we imposed on the maximum single-particle angular momentum for the full Hilbert space. Note that in terms of the elements of the partition rho, such a constraint corresponds to $\rho_1 \leq 5$. The sum of the dimensions of the Hilbert spaces obtained in this way is $\sum_{\bar\lambda} d(\mathcal{H}_{sq}(\bar\lambda)) = 2846$, which is almost one order of magnitude smaller than $d(\mathcal{H}_{full})$.

Actually an even smarter choice for the cutoff on the ρ_1 value is possible if one looks at the $\mathcal{U}_m$ potentials associated with the considered potentials parameter [see Fig. 6.11(a)]. The previous choice of $\bar\lambda$ does not take into account of all states with a non-vanishing occupation of the $m = 1$ orbital. Therefore, since $\mathcal{U}_1$ and $\mathcal{U}_{15}$ are of the same order of magnitude, the same should be done with the states taking contributions from the $m = 15$ orbital by imposing $\rho_1 \leq 4$. In this way we would correctly reproduce only those states whose energies in Fig. A.1 are lower than $0.015V_0$.

Before concluding this appendix we would like to make some remarks. First of all, we would like to hihglight that the relation

$$E(\lambda) > E(\mu) \implies \lambda \succeq \mu \tag{A.3}$$

is not true in general, especially when one considers states with total angular momentum quite

different from the ground state one. What instead holds is that

$$E(\lambda) \gg E(\mu) \implies \lambda \succeq \mu. \tag{A.4}$$

This means that the choice of $\bar{\lambda}$ must be made in a proper way. Second, it is important to stress that the approximation introduced by diagonalizing the Hamiltonian on the squeezed Hilbert space $\mathcal{H}_{\mathrm{sq}}(\bar{\lambda})$ is only good when the effects of the confinement are weak and the mixing with states lying above the many-body gap is negligible. If this condition is not satisfied, the squeezed Hilbert space $\mathcal{H}_{\mathrm{sq}}(\bar{\lambda})$ may be missing some physical states.

Appendix B

Pierced geometry with a harmonic confinement.

In this Appendix we briefly discuss the situation in which a FQH liquid in the so-called pierced geometry experiences an additional external confinement in the form of a harmonic potential.

If we restrict ourselves to the LLL, the second quantized form of such a confining potential simply gives an energy shift proportional to the total angular momentum

$$\Delta E_{\text{harm}} \propto \upsilon \hat{L}_z \tag{B.1}$$

and does not modify the Hamiltonian eigenstates [Cazalilla, 2003]. Therefore, one can use this scheme to remove the degeneracy between the κ-QH states and their OEEs lying in the same energy branch, obtaining in this way a non-degenerate ground state with a given number of QHs (see Fig. B.1). As already discussed many times in Chapter 6, the number κ of QHs in the ground state depends on the parameters of the piercing potential and, in this particular case, on the strength υ of the external harmonic potential. As a consequence, although a quite precise fine-tuning of both of them may be still needed, selecting a well-defined number of QHs in the ground state with a harmonic confinement is definitely simpler than in the ring geometry where one would have to properly set four parameters and even small changes of each of them, especially the radii $R_{\text{in,ext}}$, may strongly affect the ordering of the Hamiltonian eigenstates.

In conclusion, exactly as one can remove the macroscopic degeneracy characterizing an unconfined FQH liquid to obtain a non-degenerate ground state in a Laughlin form, one can add an
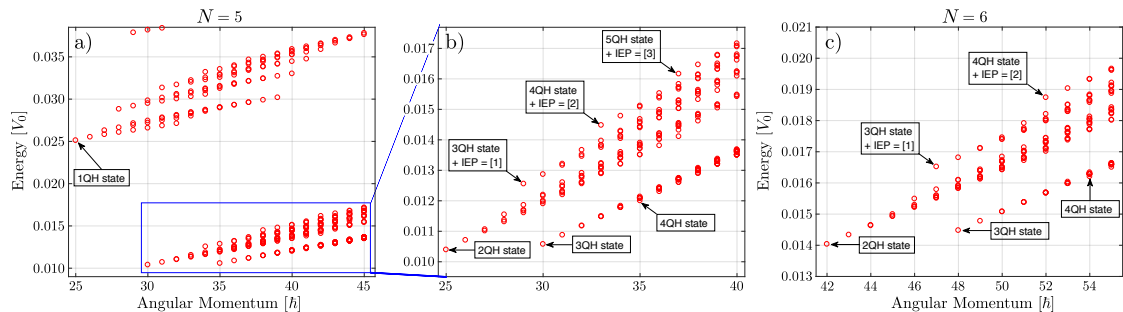
Figure B.1: Many-body spectra for $N = 5$ (a) and b)) and $N = 6$ (c)) particle systems experiencing to a piercing potential of parameters $V_{\text{in}}/V_0 = 2$ and $R_{\text{in}}/\sqrt{2}\,l_B = 0.5$ and a harmonic potential characterized by $\upsilon = 3 \times 10^{-4} V_0/\hbar$. The addition of a harmonic confinement preserves the organization of many-body energy levels into branches and subbranches as in the pierced geometry, but, at the same time, it leads to a non-degenerate ground state corresponding to a QH state. Taken from Macaluso and Carusotto [2018].

external harmonic potential to a FQH liquid in the pierced geometry to obtain a non-degenerate ground state in the form of an κ-QH state.

On the other hand, the addition of the harmonic confinement preserves the energy branch and subbranch structure distinctive of the pierced geometry [compare Figs. 6.9 and B.1]. This means that most of the OEEs of a given κ-QH state remain very difficult to resolve. Therefore, such a confinement of the FQH liquid is the most suitable if one wants to study states containing a different number of QHs but it is not suitable to study the edge excitations of the system.

Appendix C

Aharonov-Bohm contribution to $\langle \hat{L}_z \rangle$.

In the following we explicitly compute the non-topological (NT) contribution to the Berry phase $\varphi_{\mathrm{B}} = \theta_f \mathcal{L}/\hbar$ acquired by the Moore-Read state with two non-Abelian QHs, after a 2π-rotation of the anyons. After that, we extend this result to the simpler case of the QHs hosted by the Laughlin state.

Since in the PR basis φ_{B} can be expressed in terms of the angular momentum expectation value taken on the 2QH state [see Sec. 7.1], one can write in general

$$\varphi_{\mathrm{B}}(\eta_1, \eta_2) = \frac{2\pi}{\hbar} \langle \hat{L}_z \rangle_{\eta_1,\eta_2} = \varphi_{\mathrm{NT}}(\eta_1, \eta_2) + \varphi_{\mathrm{br}}, \tag{C.1}$$

in which $\varphi_{\mathrm{NT}}(\eta_1, \eta_2)$ is the aforementioned non-topological contribution to φ_{B}, while η_1, η_2 and φ_{br} denote as usual the coordinates of the QHs and their braiding phase, respectively.

To find an analytic expression for $\varphi_{\mathrm{NT}}(\eta_1, \eta_2)$, we consider a generic state with far apart QHs at positions η_1, η_2 (with $|\eta_1| < |\eta_2|$), for a large number of particles $N \gg 1$. Within this approximation we can assume that:

(i) The density $n(\mathbf{r})$ of the FQH cloud is a constant $n_{\mathrm{b}} = 1/2\pi M l_B^2$ in the interval $0 \leq |\mathbf{r}| \leq R_{\mathrm{cl}}$, where $R_{\mathrm{cl}} = R_{\mathrm{cl}}(N)$ denotes the semi-classical radius of the cloud, and it is equal to 0 elsewhere. In other words, we are neglecting the density bump at the cloud boundary.

(ii) The QH size is negligible, and therefore each QH can be seen as an additional magnetic flux $\Phi_{\mathrm{QH}} = \pi\hbar/e = \Phi_0/2$, where $\Phi_0 = 2\pi\hbar/e$ is the quantum flux, located at the QH position [1].

As a consequence of (ii), the QH positions η_1 and η_2 divide the FQH cloud in three regions: A circular region S_1 of radius $|\eta_1|$; a ring-shaped region S_2 with inner radius $|\eta_1|$ and outer radius $|\eta_2|$; and a ring-shaped region S_3 extending from $|\eta_2|$ to R_{cl} [see Fig. C.1].

For adiabatic processes in which charged objects move in presence of magnetic fields, the non-topological phase φ_{NT} acquired by the many-body wave function is an Aharonov-Bohm (AB) phase [Aharonov and Bohm, 1959]. Therefore equation (C.1) becomes

$$\frac{2\pi}{\hbar} \langle \hat{L}_z \rangle_{\eta_1,\eta_2} = \varphi_{\mathrm{AB}}(\eta_1, \eta_2) + \varphi_{\mathrm{br}}. \tag{C.2}$$

where $\varphi_{\mathrm{AB}}(\eta_1, \eta_2)$ is not the AB phase associated with the rotation of the QHs, but rather the one due to the rotation of the particles forming the MR state. This is a consequence of working in the PR basis, in which anyons are fixed and particles move [see Fig. 7.2].

For the simplest case of a charged particle moving along a closed path in presence of a constant magnetic field, the AB phase is $q\Phi/\hbar$, where q and Φ denote the particle charge and the magnetic flux passing through the surface enclosed by the particle path, respectively. Here we consider

---

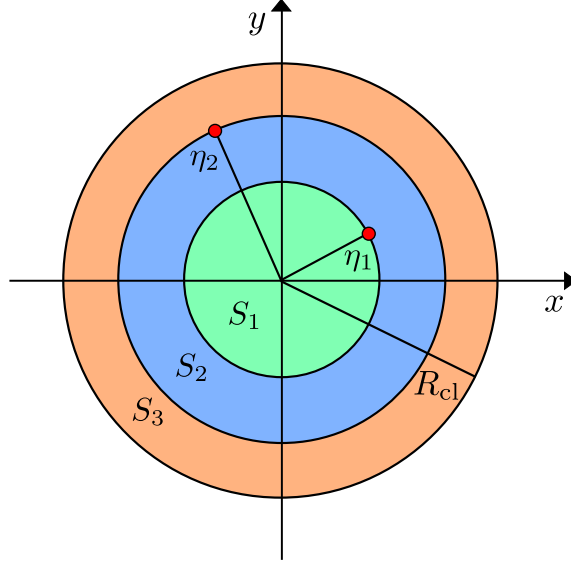[1]Note that in the case of Laughlin QHs $\Phi_{\mathrm{QH}} = 2\pi\hbar/e = \Phi_0$.

Figure C.1: Schematic picture of the regions S_1, S_2 and S_3 of the FQH cloud defined by the quasihole positions η_1, η_2 (red dots) in the large N limit. Picture taken from the supplemental material of Macaluso et al. [2019a].

a charge density distributed over the FQH cloud, rather than individual particles. Under our previous assumption that the density is constant for all $r \leq R_{\rm cl}$, the AB phase $\varphi_{\rm AB}(\eta_1, \eta_2)$ is $\int_0^{R_{cl}} [2\pi r \, q n_{\rm b} \Phi(r)/\hbar] \, dr$, where $q n_{\rm b}$ is the charge density and where the flux $\Phi(r)$ seen at radius r depends on the region S_i to which r belongs. Particles in S_1 only feel the flux $\Phi_{S_1}(r) = \pi r^2 \rho_B \Phi_0$ due to the external magnetic field, where πr^2 is the surface enclosed by the ring and $\rho_{\rm B} = 1/2\pi l_B^2$ is the flux density. Particles in S_2 feel the external-field flux plus an additional magnetic flux $\Phi_{\rm QH}$ due to the fact they encircle a QH. Particles in S_3 encircle two QHs, and thus they feel two additional fluxes: $\Phi_{S_3}(r) = \pi r^2 \rho_B \Phi_0 + 2\Phi_{\rm QH}$. Therefore, the AB phases associated with the rotation of the charge density in the three different regions are

$$\varphi_{\rm AB}^{S_1}(\eta_1) = \frac{q n_{\rm b}}{\hbar} \int_0^{|\eta_1|} dr \, 2\pi r \, \Phi_{S_1}(r) = \frac{q n_{\rm b} 2\pi^2 B}{\hbar} \frac{|\eta_1|^4}{4}, \tag{C.3}$$

$$\varphi_{\rm AB}^{S_2}(\eta_1, \eta_2) = \frac{q n_{\rm b}}{\hbar} \int_{|\eta_1|}^{|\eta_2|} dr \, 2\pi r \Phi_{S_2}(r) = \frac{q n_{\rm b} 2\pi^2 B}{\hbar} \left(\frac{|\eta_2|^4}{4} - \frac{|\eta_1|^4}{4} \right) + \frac{q n_{\rm b} \pi \Phi_0}{\hbar} \left(\frac{|\eta_2|^2}{2} - \frac{|\eta_1|^2}{2} \right), \tag{C.4}$$

$$\varphi_{\rm AB}^{S_3}(\eta_2) = \frac{q n_{\rm b}}{\hbar} \int_{|\eta_2|}^{R_{cl}} dr \, 2\pi r \Phi_{S_3}(r) = \frac{q n_{\rm b} 2\pi^2 B}{\hbar} \left(\frac{R_{\rm cl}^4}{4} - \frac{|\eta_2|^4}{4} \right) + \frac{q n_{\rm b} 2\pi \Phi_0}{\hbar} \left(\frac{R_{\rm cl}^2}{2} - \frac{|\eta_2|^2}{2} \right), \tag{C.5}$$

and the global AB phase reads

$$\begin{aligned} \varphi_{\rm AB}(\eta_1, \eta_2) &= \varphi_{\rm AB}^{S_1}(\eta_1) + \varphi_{\rm AB}^{S_2}(\eta_1, \eta_2) + \varphi_{\rm AB}^{S_3}(\eta_2) \\ &= \frac{q n_{\rm b} 2\pi^2 B}{\hbar c} \frac{R_{\rm cl}^4}{4} + \frac{q n_{\rm b} 2\pi \Phi_0}{\hbar c} \frac{R_{\rm cl}^2}{2} - \frac{q n_{\rm b} \pi \Phi_0}{\hbar c} \left(\frac{|\eta_1|^2}{2} + \frac{|\eta_2|^2}{2} \right) \\ &= K(M, N) - 2\pi \frac{1}{2M} \left(\frac{|\eta_1|^2}{2 l_B^2} + \frac{|\eta_2|^2}{2 l_B^2} \right), \end{aligned} \tag{C.6}$$

where in the last equality we used $n_{\rm b} = 1/2\pi M l_B^2$, $\Phi_0 = 2\pi l_B^2 B$ and $q = e$. Here $K(M, N)$ is a constant which does not depend on η_1 and η_2. The second term on the right-hand side of equation (C.6) is the AB phase associated with the rotation of the two QHs [Bonderson et al., 2011], which means that the dependence of $\langle \hat{L}_z \rangle_{\eta_1, \eta_2}$ on the QH positions allows one to compute the fractional charge of MR QHs. This is also an indication of the correctness of our reasoning: particle and QH rotations are indeed related.

The prediction for $K(M, N)$, however, is not reliable. This is easily understood by observing that in the large-N approximation the semi-classical radius of the FQH cloud R_{cl} does not depend on the number N_{QH} of QH excitations. If our expression for $K(M, N)$ were correct, then also the mean angular momentum of the MR state with $\eta_1 = \eta_2 = 0$ would not depend on N_{QH}, but we know that this is not the case.

The issue is solved by rewriting equation (C.2) for the case of $\eta_1 = \eta_2 = 0$, since in this case the particle rotation does not induce any exchange of the QHs and so $\varphi_{\text{br}} = 0$. We find

$$\frac{2\pi}{\hbar} \langle \hat{L}_z \rangle_{0,0} = \varphi_{\text{AB}}(0,0) + \varphi_{\text{br}} = \varphi_{\text{AB}}(0,0), \tag{C.7}$$

which implies that $K(M, N)$ must be computed as the mean angular momentum of the MR state having both QHs located in the origin: $K(M, N) = (2\pi/\hbar)\langle \hat{L}_z \rangle_{0,0}$. Equation (C.2) then becomes

$$\frac{2\pi}{\hbar} \langle \hat{L}_z \rangle_{\eta_1, \eta_2} = \frac{2\pi}{\hbar} \langle \hat{L}_z \rangle_{0,0} - 2\pi \frac{1}{2M} \left(\frac{|\eta_1|^2}{2l_B^2} + \frac{|\eta_2|^2}{2l_B^2} \right) + \varphi_{\text{br}}, \tag{C.8}$$

and the braiding phase of MR non-Abelian QHs is related to the angular momentum via

$$\boxed{\varphi_{\text{br}} = \frac{2\pi}{\hbar} \langle \hat{L}_z \rangle_{\eta_1, \eta_2} - \frac{2\pi}{\hbar} \langle \hat{L}_z \rangle_{0,0} + 2\pi \frac{1}{2M} \left(\frac{|\eta_1|^2}{2l_B^2} + \frac{|\eta_2|^2}{2l_B^2} \right)}. \tag{C.9}$$

Note that the mean angular momentum of a Moore-Read state with QHs at $\eta_1 = \eta_2 = 0$ depends on the parity of N, in particular:

$$\langle \hat{L}_z \rangle_{0,0} = \hbar \left[\frac{MN(N-1)}{2} + \frac{N}{2} - \frac{P_N}{2} \right]. \tag{C.10}$$

Finally, we notice that if we consider a state with QH at positions η_1, η_2 such that $|\eta_1| = |\eta_2|$, the last two terms on the right-hand side of equation (C.9) correspond to the mean angular momentum of the state with QHs on top of each other at distance $|\eta_i|$ from the center of the cloud. So we have

$$\boxed{\varphi_{\text{br}} = \frac{2\pi}{\hbar} \langle \hat{L}_z \rangle_{|\eta_1| = |\eta_2|} - \frac{2\pi}{\hbar} \langle \hat{L}_z \rangle_{\eta_1 = \eta_2}}, \tag{C.11}$$

which corresponds to Eq. (7.17).

The calculations of this section are easily generalized to the QHs of the Laughlin state, with the only difference that the corresponding QH magnetic flux is $\Phi_{\text{QH}} = \Phi_0$ instead of $\Phi_0/2$. Therefore, in this case we obtain

$$\boxed{\varphi_{\text{br}} = \frac{2\pi}{\hbar} \langle \hat{L}_z \rangle_{\eta_1, \eta_2} - \frac{2\pi}{\hbar} \langle \hat{L}_z \rangle_{0,0} + 2\pi \frac{1}{M} \left(\frac{|\eta_1|^2}{2l_B^2} + \frac{|\eta_2|^2}{2l_B^2} \right)}, \tag{C.12}$$

which can be again rewritten as Eq. (7.17).

Appendix D

Derivation of the phase-depletion relation.

In this Appendix we show how to express the QH braiding phase in terms of the QH density depletions [see Eq. (7.23)], starting from its expression in term of the mean square radii [see Eq. (7.19)].

As discussed in Sec. 7.2.3 we can rewrite Eq. (7.19) as

$$
\begin{aligned}
\frac{\varphi_{\mathrm{br}}}{2\pi} &= \frac{N}{2l_B^2} \left[\langle r^2 \rangle_{|\eta_1|=|\eta_2|} - \langle r^2 \rangle_{\eta_1=\eta_2} \right] \\
&= \frac{N}{2l_B^2} \frac{1}{N} \int_{\mathbb{R}^2} r^2 \left[n_{|\eta_1|=|\eta_2|}(\vec{r}) - n_{\eta_1=\eta_2}(\vec{r}) \right] d\vec{r} \\
&= \frac{1}{2l_B^2} \int_{A_1, A_2} r^2 \left[n_{|\eta_1|=|\eta_2|}(\vec{r}) - n_{\eta_1=\eta_2}(\vec{r}) \right] d\vec{r},
\end{aligned}
\tag{D.1}
$$

where we recall that the last equivalence is justified the fact that the densities $n_{|\eta_1|=|\eta_2|}(\vec{r})$ and $n_{\eta_1=\eta_2}(\vec{r})$ are equal over the whole 2D plane, except for the surfaces A_1 and A_2 surrounding the QHs [see red circles in Fig. 7.3 (a) and (b)]. Densities $n_{|\eta_1|=|\eta_2|}(\vec{r})$ and $n_{\eta_1=\eta_2}(\vec{r})$ in the regions A_1 and A_2 can be rewritten as

$$
\begin{aligned}
n_{|\eta_1|=|\eta_2|}(\vec{r}) &= n_{\mathrm{b}} - d_{\mathrm{1QH}}(\vec{r} - \eta_j) \quad \forall \vec{r} \in A_j, \, j = 1, 2 \\
n_{\eta_1=\eta_2}(\vec{r}) &= n_{\mathrm{b}} - d_{\mathrm{2QH}}(\vec{r} - \eta_1) \quad \forall \vec{r} \in A_1, \\
n_{\eta_1=\eta_2}(\vec{r}) &= n_{\mathrm{b}} \quad\quad\quad\quad\quad\quad\quad \forall \vec{r} \in A_2,
\end{aligned}
\tag{D.2}
$$

where $n_{\mathrm{b}} = 1/2\pi M l_B^2$ is the bulk density, and $d_{\mathrm{1QH}}(\vec{r})$ and $d_{\mathrm{2QH}}(\vec{r})$ are the widely discussed QH density depletions. By inserting these expressions in the previous integral one obtains

$$
\begin{aligned}
\frac{\varphi_{\mathrm{br}}}{2\pi} &= \frac{1}{2l_B^2} \left\{ \int_{A_1} r^2 \left[d_{\mathrm{2QH}}(\vec{r} - \eta_1) - d_{\mathrm{1QH}}(\vec{r} - \eta_1) \right] d\vec{r} - \int_{A_2} r^2 \, d_{\mathrm{1QH}}(\vec{r} - \eta_2) \, d\vec{r} \right\} \\
&= \frac{1}{2l_B^2} \int_{A_1} r^2 \left[d_{\mathrm{2QH}}(\vec{r} - \eta_1) - 2 d_{\mathrm{1QH}}(\vec{r} - \eta_1) \right] d\vec{r},
\end{aligned}
\tag{D.3}
$$

where we used the facts that $|\eta_1| = |\eta_2|$ and that the integrals do not depend on the angle distinguishing A_1 and A_2. By changing variables to $\vec{\rho} \equiv \vec{r} - \eta_1$, we obtain

$$
\begin{aligned}
\frac{\varphi_{\mathrm{br}}}{2\pi} &= \frac{1}{2l_B^2} \int_{A_1} (\vec{\rho} - \eta_1)^2 \left[d_{\mathrm{2QH}}(\vec{\rho}) - 2 d_{\mathrm{1QH}}(\vec{\rho}) \right] d\vec{\rho} \\
&= \frac{1}{2l_B^2} \int_0^{2\pi} d\theta \int_0^{R_{\max}} d\rho \, \rho \, (\rho^2 - 2\rho |\eta_1| \cos\theta + |\eta_1|^2) \left[d_{\mathrm{2QH}}(\rho) - 2 d_{\mathrm{1QH}}(\rho) \right],
\end{aligned}
\tag{D.4}
$$

where $R_{\max}$ is the radius of the disk-shaped surface A_1. This radius must be small enough to avoid the overlap between the different A_i regions and the spurious contributions from the density

deformations at the FQH cloud boundary, but large enough to ensure an appropriate damping of the density oscillations induced by the QHs on top of the bulk density.

Finally, we note that (as long as $R_{\max}$ is large enough) the integrate density depletion for two QHs on top of each other and for two QHs far away is the same, i.e.

$$\int_0^{2\pi} d\theta \int_0^{R_{\max}} d\rho\, \rho\, [d_{2\mathrm{QH}}(\rho) - 2d_{1\mathrm{QH}}(\rho)] = 0, \tag{D.5}$$

and that the integral of $\cos\theta$ vanishes in the interval $[0, 2\pi]$. Therefore, the previous expression for the braiding phase simplifies and becomes Eq. (7.23).

We stress that the reasoning in this Appendix applies to all QH excitations of FQH states in the LLL, since it only requires the validity of the expression (7.18), relating the mean angular momentum of a state in the LLL to its mean square radius.

Appendix E

Monte Carlo sampling of Laughlin and Moore-Read states.

$\mathcal{M}$any of the results we reported in this Thesis, especially those in Chapters 7 and 8, required the evaluation of the expectation values of some spatial-dependent observables $\mathcal{O}(\vec{r})$ on different FQH states. In the following we briefly explain how one can do that without using (numerically expensive) exact diagonalization calculations.

The expectation values of observables of this kind can be rewritten as averages over the probability distribution given by the squared modulus of the wave functions of interest, i.e.

$$\frac{\langle \Psi | \mathcal{O}(\vec{r}) | \Psi \rangle}{\langle \Psi | \Psi \rangle} = \frac{\int \mathcal{O}(\vec{r}) \, |\Psi(z_1, \ldots, z_N)|^2 \, dz_1 \ldots dz_N}{\int |\Psi(z_1, \ldots, z_N)|^2 \, dz_1 \ldots dz_N}. \tag{E.1}$$

After that one can these integrals through the Metropolis et al. [1953] Monte Carlo technique [see also the book by Krauth [2006] for more details], leading to results which are exact within statistical errors.

Despite being developed for other purposes, this method has been widely used also in the FQH context, where the possibility to construct ansatz wave functions allowed physicists to inspect many properties of these systems (e.g., density profiles and pair correlation functions) without solving exactly the many-body problem; see for instance the works by Morf and Halperin [1986] and by Kjønsberg and Myrheim [1999]. As we have seen in Chapter 3, not only one can construct analytic ansatz wave functions describing states in the same universality class of those experimentally observed, but the square modulus of some of them (e.g., those describing the Laughlin state and its QH excitations) can be interpreted as the Boltzmann factor $e^{i\beta U(z,\eta)}$ of a classical 2D one-component plasma [see Eqs. (3.23) and (3.45)]. This further simplifies the numerical evaluation of $\langle \Psi | \mathcal{O}(\vec{r}) | \Psi \rangle$.

Now there is a final remark we want to make, and it regards the results we obtained for the Moore-Read states with two non-Abelian QHs [see Eq. (4.8)]. In Bonderson et al. [2011] the authors proposed a plasma representation for the wave functions associated with the Moore-Read state and its QH excitations. Differently from the plasma describing the squared modulus of the Laughlin state, the one introduced by Bonderson et al. [2011] (and then numerically studied by Herland et al. [2012, 2013]) is a two-component plasma, where the need of the second component is due to the presence of the Pfaffian term. Even though this plasma has already been used successfully in the past, for instance to estimate the overlaps $G_{\alpha\beta} = \langle \Psi_\alpha | \Psi_\beta \rangle$ between the Moore-Read 4-QH wave functions $\Psi_{0,1}(\eta; z)$ [see Eqs. (4.13) and (4.14)], we treat the Pfaffian factor directly, i.e. without making use of its integral representation introduced by Gurarie and Nayak [1997]. We use the usual one-component plasma for the description of the Laughlin-like part of the Moore-Read wave functions. This choice is mainly motivated by the fact that we limit ourselves to the non-degenerate case of two Moore-Read QHs. In this case there are no overlaps of the form $G_{\alpha\beta}$ and we only need to compute the squared modulus of ground state wave function $|\Psi_{2\mathrm{QH}}^{e/4}(\eta; z)|^2$. As a

consequence the probability distributions entering in our Metropolis algorithm never contain the Pfaffian term $\text{Pf}(W)$, but only its squared modulus which can be efficiently computed through the relation $|\text{Pf}(W)|^2 = |\det(W)|$. Note also that this brute-force approach allows one to treat both states with even and odd number of particles, while it is not clear if the two-component plasma discussed in Bonderson et al. [2011] safely applies also in the odd N case.

For your information, Comparin and Macaluso provide an open-source version of the code implementing the Metropolis algorithm to sample the probability density associated with the Laughlin state presenting an arbitrary number of quasiholes.

Appendix F

ED benchmark of the TTN ansatz.

To perform a systematic benchmark of the TTN results against exact diagonalization (ED) calculations, we consider $N = 3$ particles on a 8×8 lattice with periodic boundary conditions (PBCs), and with flux density $\alpha = 1/8$. For these system parameters, the magnetic filling $\nu = (N + N_{\text{QH}}/2)/(L)^2\alpha$ is such that the system hosts two QHs. Note that since we are dealing with PBCs the number of fluxes N_Φ is given by $L^2\alpha$ instead of $(L-1)^2\alpha$, as for the case of OBCs. To localize these two QHs at the same position, we also include a five-sites plus-shaped impurity potential centered at site $(4,4)$, with intensity $V_i/t = 1$ on each site.

Differently from the OBC cases treated in Chapter 8, the toroidal geometry of a PBC system induces a $1/\nu$ topological degeneracy of the ground state Wen and Niu [1990], that is, a twofold degeneracy for the case treated in this work. This degeneracy is preserved when the system hosts localized Abelian QHs (up to finite-size effects), in contrast to the general case of non-Abelian or non-localized QHs, in which the number of (quasi-)degenerate states is typically larger [Regnault and Bernevig, 2011, Umucalılar, 2018].

For $N = 3$ and $L = 8$, the Hilbert space dimension is $\approx 4.2 \times 10^4$, and we can obtain the three lowest-energy states Ψ_0, Ψ_1 and Ψ_2 through the ED technique (via the Lanczos algorithm). The corresponding energies [see Table F.1] display a signature of the (quasi-)degeneracy of Ψ_0 and Ψ_1, while the state Ψ_2 has a larger energy gap – a similar study has been done in Gerster et al. [2017] for larger systems.

For this small system, the TTN ansatz has moderate requirements in terms of the bond dimensions of its tensors. In general, within the hierarchical tree structure of a loop-free TTN state, the bonds of a tensor on the l-th layer may have dimension up to d^{2^l} [Gerster et al., 2014, Silvi et al., 2019], where d is the dimension of the local Hilbert space. To make this ansatz tractable, one typically introduces a cutoff D on the bond dimension, so that the dimension of each bond becomes $\min(d^{2^l}, D)$. For $L = 8$, the root tensor (i.e. the one at the top of the tree structure) has a maximum bond dimension of $\min(d^{2^5}, D) = \min(d^{32}, D)$.

For the hard-core Bose-Hubbard model treated in this work, the local dimension is $d = 2$. By considering a fixed number N of bosons, the number of states is reduced, and we can compute the bond-dimension D_{exact} needed to span the entire many-body Hilbert space. For $N = 3$ and $L = 8$, a TTN state with $D \geq D_{\text{exact}} = 66$ can reproduce an arbitrary many-body state. We then set $D = 66$ in this Appendix, and show that the optimization of the TTN parameters yields the same

State	E/t
Ψ_0	-9.865430303
Ψ_1	-9.860769293
Ψ_2	-9.828784649

Table F.1: Total energy of the three lowest-energy states of $N = 3$ particles on a 8×8 periodic lattice with $\alpha = 1/8$, in the presence of a plus-shaped pinning potential.
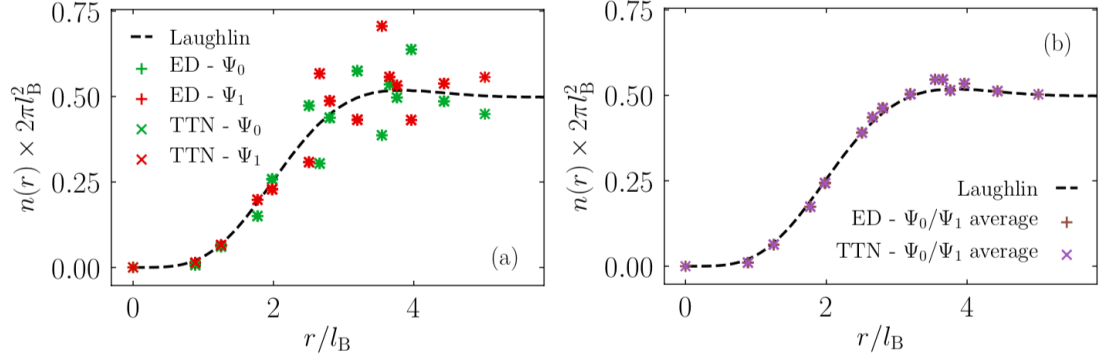
Figure F.1: (a) Density profiles for the two states Ψ_0 and Ψ_1 [see text], computed via ED and TTN. (b) Density profiles averaged over Ψ_0 and Ψ_1, both for TTN and ED. In both panels, the dashed black line is the result for a Laughlin QH state in continuum space. Picture taken from Macaluso et al. [2019b].

physical results as ED.

First of all, the TTN energies for Ψ_0, Ψ_1 and Ψ_2 perfectly match with the ED values in Table F.1, up to the precision reported therein. We also compute the density profile close to the pinned QHs, as shown in Fig. F.1 for Ψ_0 and Ψ_1. These two degenerate states have different profiles, but once we average over the two states we obtain a smooth curve, as shown for instance by Liu et al. [2015]. Also for the profiles, as for the energies, we observe full agreement between ED and TTN results. This further validates the TTN method, also in the presence of a localized QH excitation.

Appendix G

Convergence analysis of the TTN results.

In App. F, we showed that for a small system one can reach the saturation of the bond-dimension cutoff ($D = D_{\text{exact}}$), which makes the TTN ansatz a general parametrization for any state in the Hilbert space. The computational cost of this task, however, becomes prohibitively large for larger systems. For the $N = 12$ and the $N = 18$ particles systems considered in Chapter 8, such saturation would require a bond dimension $D \gtrsim 6 \times 10^9$ ($D \gtrsim 2 \times 10^{13}$). Since this is clearly beyond reach, the TTN ansatz can only represent states in the subset of Hilbert space with low to moderate entanglement content, which introduces a bias in the computed observables.

As a representative example, in this Appendix we consider a $N = 18$ particles system on a 16×16 lattice with OBCs and with flux density $\alpha = 0.25$, supplemented with a plus-shaped pinning potential of intensity $V_i/t = 1$. In this set-up the system has a localized double QH – see orange diamonds in Fig. 8.7 (a). We first look at the energy, for bond dimension D between 100 and 500 – see data in Table G.1. Even if the large-D convergence is not reached, the energies for the two largest bond dimensions are very close, with a relative energy difference as small as 1.5×10^{-4}. This suggests that the TTN ansatz with the currently available bond dimension may be sufficiently accurate to represent the ground state of the model under study. Note that the relative energy differences reached in this work are comparable with the TTN analysis for the case of a homogeneous FCI, done in Gerster et al. [2017].

Furthermore, we look at how the depletion profile around a QH (the key observable in the current work) depends on the TTN bond dimension. We look again at the same case, and compute the depletion profile $d_{2\text{QH}}^{(D)}(\rho)$ for different values of D. To visualize the dependence on the bond dimension, we take $D = 500$ as a reference case and define the depletion-profile deviation as

$$\Delta d_{2\text{QH}}(\rho) = d_{2\text{QH}}^{(D)}(\rho) - d_{2\text{QH}}^{(500)}(\rho). \tag{G.1}$$

This quantity is shown in Fig. G.1, for D between 100 and 400. We observe that its fluctuations decrease for increasing bond dimension, and that the curve for $D = 400$ is barely distinguishable from 0, on this scale. We conclude that for a TTN with $D = 500$ (the bond dimension used for Case II in the main text) the systematic error in the depletion profile is negligible.

D (bond dim.)	E/t
100	-47.508
200	-47.616
300	-47.631
400	-47.654
500	-47.661

Table G.1: Dependence of the total energy E on the bond dimension D, for a double QH in Case II – see text.

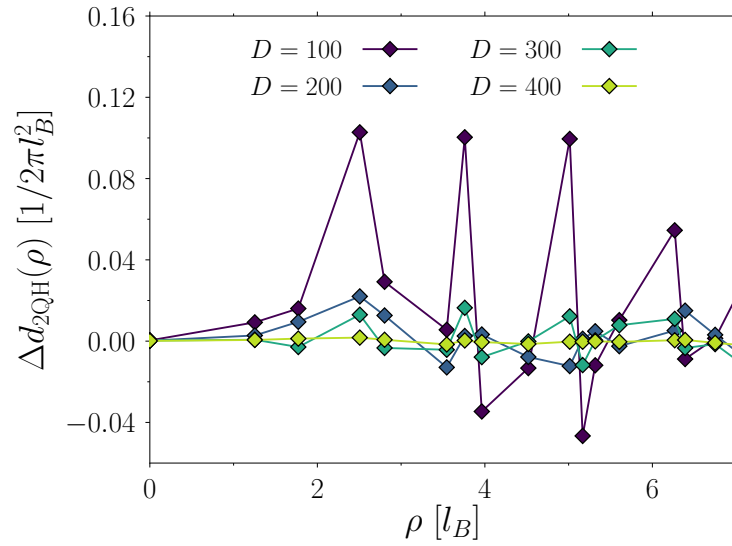Figure G.1: Finite-D deviations in the depletion profile of a double QH in a system with $N = 18$, $L = 16$ and $\alpha = 0.25$ – see Eq. (G.1). The reference value $\Delta d_{2\text{QH}}(\rho) = 0$ corresponds to $D = 500$ [see orange diamonds in Fig. 8.7 (a)]. Picture taken from Macaluso et al. [2019b].

Bibliography

Y. Aharonov and D. Bohm. Significance of Electromagnetic Potentials in the Quantum Theory. *Phys. Rev.*, 115:485–491, Aug 1959. doi: 10.1103/PhysRev.115.485. URL https://link.aps.org/doi/10.1103/PhysRev.115.485. (cited on pp. 13, 48, 95, and 127)

M. Aidelsburger, M. Atala, M. Lohse, J. T. Barreiro, B. Paredes, and I. Bloch. Realization of the Hofstadter Hamiltonian with Ultracold Atoms in Optical Lattices. *Phys. Rev. Lett.*, 111:185301, Oct 2013. doi: 10.1103/PhysRevLett.111.185301. URL https://link.aps.org/doi/10.1103/PhysRevLett.111.185301. (cited on p. 33)

M. Aidelsburger, M. Lohse, C. Schweizer, M. Atala, J. T. Barreiro, S. Nascimbène, N. R. Cooper, I. Bloch, and N. Goldman. Measuring the Chern number of Hofstadter bands with ultracold bosonic atoms. *Nature Physics*, 11:162–166, 12 2014. doi: 10.1038/nphys3171. URL https://doi.org/10.1038/nphys3171. (cited on pp. 105 and 110)

D. Arovas, J. R. Schrieffer, and F. Wilczek. Fractional Statistics and the Quantum Hall Effect. *Phys. Rev. Lett.*, 53:722–723, Aug 1984. doi: 10.1103/PhysRevLett.53.722. URL https://link.aps.org/doi/10.1103/PhysRevLett.53.722. (cited on pp. 7, 46, 47, and 55)

F. Arute, K. Arya, R. Babbush, D. Bacon, J. C. Bardin, R. Barends, R. Biswas, S. Boixo, F. G. S. L. Brandao, D. A. Buell, B. Burkett, Y. Chen, Z. Chen, B. Chiaro, R. Collins, W. Courtney, A. Dunsworth, E. Farhi, B. Foxen, A. Fowler, C. Gidney, M. Giustina, R. Graff, K. Guerin, S Habegger, M. P. Harrigan, M. J. Hartmann, A. Ho, M. Hoffmann, T. Huang, T. S. Humble, S. V. Isakov, E. Jeffrey, Z. Jiang, D. Kafri, K. Kechedzhi, J. Kelly, P. V. Klimov, S. Knysh, A. Korotkov, F. Kostritsa, D. Landhuis, M. Lindmark, E. Lucero, D. Lyakh, S. Mandrà, J. R. McClean, M. McEwen, A. Megrant, X. Mi, K. Michielsen, M. Mohseni, J. Mutus, O. Naaman, M. Neeley, C. Neill, M. Y. Niu, E. Ostby, A. Petukhov, J. C. Platt, C. Quintana, E. G. Rieffel, P. Roushan, N. C. Rubin, D. Sank, K. J. Satzinger, V. Smelyanskiy, K. J. Sung, M. D. Trevithick, A. Vainsencher, B. Villalonga, T. White, Z. J. Yao, P. Yeh, A. Zalcman, H. Neven, and J. M. Martinis. Quantum supremacy using a programmable superconducting processor. *Nature*, 574(7779):505–510, 2019. doi: 10.1038/s41586-019-1666-5. URL https://doi.org/10.1038/s41586-019-1666-5. (cited on p. 36)

A. Aspuru-Guzik and P. Walther. Photonic quantum simulators. *Nature Physics*, 8(4):285–291, 2012. doi: 10.1038/nphys2253. URL https://doi.org/10.1038/nphys2253. (cited on p. 31)

W. S. Bakr, J. I. Gillen, A. Peng, S. Fölling, and M. Greiner. A quantum gas microscope for detecting single atoms in a Hubbard-regime optical lattice. *Nature*, 462:74–77, 11 2009. doi: 10.1038/nature08482. URL https://doi.org/10.1038/nature08482. (cited on p. 32)

M. Banerjee, M. Heiblum, V. Umansky, D. E. Feldman, Y. Oreg, and A. Stern. Observation of half-integer thermal Hall conductance. *Nature*, 559(7713):205–210, 2018. doi: 10.1038/s41586-018-0184-1. URL https://doi.org/10.1038/s41586-018-0184-1. (cited on p. 52)

M. Baraban, G. Zikos, N. Bonesteel, and S. H. Simon. Numerical Analysis of Quasiholes of the Moore-Read Wave Function. *Phys. Rev. Lett.*, 103:076801, Aug 2009. doi:

10.1103/PhysRevLett.103.076801. URL https://link.aps.org/doi/10.1103/PhysRevLett.
103.076801. (cited on p. 54)

M. S. Baraban. *Low Energy Excitations in Quantum Condensates.* PhD thesis, 01 2010.
(cited on pp. 51, 53, 55, 101, and 103)

M. Barkeshli, N. Y. Yao, and C. R. Laumann. Continuous Preparation of a Fractional Chern
Insulator. *Phys. Rev. Lett.*, 115:026802, Jul 2015. doi: 10.1103/PhysRevLett.115.026802. URL
https://link.aps.org/doi/10.1103/PhysRevLett.115.026802. (cited on p. 31)

M. C. Beeler, R. A. Williams, K. Jiménez-García, L. J. LeBlanc, A. R. Perry, and I. B.
Spielman. The spin Hall effect in a quantum gas. *Nature*, 498(7453):201–204, 2013. doi:
10.1038/nature12185. URL https://doi.org/10.1038/nature12185. (cited on p. 33)

B. A. Bernevig and F. D. M. Haldane. Generalized clustering conditions of Jack polyno-
mials at negative Jack parameter α. *Phys. Rev. B*, 77:184502, May 2008a. doi: 10.
1103/PhysRevB.77.184502. URL https://link.aps.org/doi/10.1103/PhysRevB.77.184502.
(cited on pp. 57, 58, and 60)

B. A. Bernevig and F. D. M. Haldane. Model Fractional Quantum Hall States
and Jack Polynomials. *Phys. Rev. Lett.*, 100:246802, Jun 2008b. doi: 10.1103/
PhysRevLett.100.246802. URL https://link.aps.org/doi/10.1103/PhysRevLett.100.
246802. (cited on pp. 57, 58, and 60)

B. A. Bernevig and F. D. M. Haldane. Properties of Non-Abelian Fractional Quan-
tum Hall States at Filling $\nu = k/r$. *Phys. Rev. Lett.*, 101:246806, Dec 2008c. doi:
10.1103/PhysRevLett.101.246806. URL https://link.aps.org/doi/10.1103/PhysRevLett.
101.246806. (cited on pp. 57 and 61)

B. A. Bernevig and N. Regnault. Anatomy of Abelian and Non-Abelian Fractional Quantum Hall
States. *Phys. Rev. Lett.*, 103:206801, Nov 2009. doi: 10.1103/PhysRevLett.103.206801. URL
https://link.aps.org/doi/10.1103/PhysRevLett.103.206801. (cited on p. 57)

M. V. Berry. Quantal phase factors accompanying adiabatic changes. *Proc. R. Soc. London A*,
392(1802):45–57, 1984. doi: 10.1098/rspa.1984.0023. (cited on pp. 12 and 13)

E. Bettelheim, Alexander G. Abanov, and P. Wiegmann. Nonlinear Quantum Shock Waves
in Fractional Quantum Hall Edge States. *Phys. Rev. Lett.*, 97:246401, Dec 2006. doi:
10.1103/PhysRevLett.97.246401. URL https://link.aps.org/doi/10.1103/PhysRevLett.
97.246401. (cited on p. 77)

R. Bhat, M. Krämer, J. Cooper, and M. J. Holland. Hall effects in Bose-Einstein condensates in a
rotating optical lattice. *Phys. Rev. A*, 76:043601, Oct 2007. doi: 10.1103/PhysRevA.76.043601.
URL https://link.aps.org/doi/10.1103/PhysRevA.76.043601. (cited on p. 31)

R. Blatt and C. F. Roos. Quantum simulations with trapped ions. *Nature Physics*, 8(4):277–284,
2012. doi: 10.1038/nphys2252. URL https://doi.org/10.1038/nphys2252. (cited on p. 31)

I. Bloch, J. Dalibard, and W. Zwerger. Many-body physics with ultracold gases. *Rev. Mod. Phys.*,
80:885–964, Jul 2008. doi: 10.1103/RevModPhys.80.885. URL https://link.aps.org/doi/
10.1103/RevModPhys.80.885. (cited on p. 32)

I. Bloch, J. Dalibard, and S. Nascimbène. Quantum simulations with ultracold quantum gases.
Nature Physics, 8(4):267–276, 2012. doi: 10.1038/nphys2259. URL https://doi.org/10.1038/
nphys2259. (cited on p. 31)

B. Blok and X.-G. Wen. Effective theories of the fractional quantum Hall effect at generic filling
fractions. *Phys. Rev. B*, 42:8133–8144, Nov 1990a. doi: 10.1103/PhysRevB.42.8133. URL
https://link.aps.org/doi/10.1103/PhysRevB.42.8133. (cited on p. 28)

B. Blok and X.-G. Wen. Effective theories of the fractional quantum Hall effect: Hierarchy con-
struction. *Phys. Rev. B*, 42:8145–8156, Nov 1990b. doi: 10.1103/PhysRevB.42.8145. URL
https://link.aps.org/doi/10.1103/PhysRevB.42.8145. (cited on p. 28)

O. Boada, A. Celi, J. I. Latorre, and M. Lewenstein. Quantum Simulation of an Extra Dimension. *Phys. Rev. Lett.*, 108:133001, Mar 2012. doi: 10.1103/PhysRevLett.108.133001. URL https://link.aps.org/doi/10.1103/PhysRevLett.108.133001. (cited on p. 32)

P. Bonderson, A. Kitaev, and K. Shtengel. Detecting Non-Abelian Statistics in the $\nu = 5/2$ Fractional Quantum Hall State. *Phys. Rev. Lett.*, 96:016803, Jan 2006a. doi: 10.1103/PhysRevLett.96.016803. URL https://link.aps.org/doi/10.1103/PhysRevLett.96.016803. (cited on p. 91)

P. Bonderson, K. Shtengel, and J. K. Slingerland. Probing Non-Abelian Statistics with Quasiparticle Interferometry. *Phys. Rev. Lett.*, 97:016401, Jul 2006b. doi: 10.1103/PhysRevLett.97.016401. URL https://link.aps.org/doi/10.1103/PhysRevLett.97.016401. (cited on p. 91)

P. Bonderson, V. Gurarie, and C. Nayak. Plasma analogy and non-Abelian statistics for Ising-type quantum Hall states. *Phys. Rev. B*, 83:075303, Feb 2011. doi: 10.1103/PhysRevB.83.075303. URL https://link.aps.org/doi/10.1103/PhysRevB.83.075303. (cited on pp. 12, 54, 55, 94, 103, 104, 128, 133, and 134)

M. Born and V. Fock. Beweis des Adiabatensatzes. *Zeitschrift für Physik*, 51(3):165–180, Mar 1928. ISSN 0044-3328. doi: 10.1007/BF01343193. URL https://doi.org/10.1007/BF01343193. (cited on pp. 12 and 93)

M. Bukov, L. D'Alessio, and A. Polkovnikov. Universal high-frequency behavior of periodically driven systems: from dynamical stabilization to Floquet engineering. *Advances in Physics*, 64(2):139–226, 2015. doi: 10.1080/00018732.2015.1055918. URL https://doi.org/10.1080/00018732.2015.1055918. (cited on p. 33)

J. M. Caillol, D. Levesque, J. J. Weis, and J. P. Hansen. A Monte Carlo study of the classical two-dimensional one-component plasma. *Journal of Statistical Physics*, 28(2):325–349, Jun 1982. ISSN 1572-9613. doi: 10.1007/BF01012609. URL https://doi.org/10.1007/BF01012609. (cited on p. 47)

G. Campagnano, O. Zilberberg, I. V. Gornyi, D. E. Feldman, A. C. Potter, and Y. Gefen. Hanbury Brown–Twiss Interference of Anyons. *Phys. Rev. Lett.*, 109:106802, Sep 2012. doi: 10.1103/PhysRevLett.109.106802. URL https://link.aps.org/doi/10.1103/PhysRevLett.109.106802. (cited on p. 91)

I. Carusotto and C. Ciuti. Quantum fluids of light. *Rev. Mod. Phys.*, 85:299–366, Feb 2013. doi: 10.1103/RevModPhys.85.299. URL https://link.aps.org/doi/10.1103/RevModPhys.85.299. (cited on p. 34)

M. A. Cazalilla. Surface modes of ultracold atomic clouds with a very large number of vortices. *Phys. Rev. A*, 67:063613, Jun 2003. doi: 10.1103/PhysRevA.67.063613. URL https://link.aps.org/doi/10.1103/PhysRevA.67.063613. (cited on pp. 43, 59, 67, and 125)

M. A. Cazalilla, N. Barberán, and N. R. Cooper. Edge excitations and topological order in a rotating Bose gas. *Phys. Rev. B*, 71:121303, Mar 2005. doi: 10.1103/PhysRevB.71.121303. URL https://link.aps.org/doi/10.1103/PhysRevB.71.121303. (cited on pp. 43, 59, and 67)

A. Celi, P. Massignan, J. Ruseckas, N. Goldman, I. B. Spielman, G. Juzeliūnas, and M. Lewenstein. Synthetic Gauge Fields in Synthetic Dimensions. *Phys. Rev. Lett.*, 112:043001, Jan 2014. doi: 10.1103/PhysRevLett.112.043001. URL https://link.aps.org/doi/10.1103/PhysRevLett.112.043001. (cited on p. 32)

A. M. Chang. Chiral Luttinger liquids at the fractional quantum Hall edge. *Rev. Mod. Phys.*, 75:1449–1505, Nov 2003. doi: 10.1103/RevModPhys.75.1449. URL https://link.aps.org/doi/10.1103/RevModPhys.75.1449. (cited on pp. 15 and 42)

A. M. Chang, L. N. Pfeiffer, and K. W. West. Observation of Chiral Luttinger Behavior in Electron Tunneling into Fractional Quantum Hall Edges. *Phys. Rev. Lett.*, 77:2538–2541, Sep 1996. doi: 10.1103/PhysRevLett.77.2538. URL https://link.aps.org/doi/10.1103/PhysRevLett.77.2538. (cited on p. 42)

C. Chin, R. Grimm, P. Julienne, and E. Tiesinga. Feshbach resonances in ultracold gases. *Rev. Mod. Phys.*, 82:1225–1286, Apr 2010. doi: 10.1103/RevModPhys.82.1225. URL https://link.aps.org/doi/10.1103/RevModPhys.82.1225. (cited on p. 32)

J. Cho, D. G. Angelakis, and S. Bose. Fractional Quantum Hall State in Coupled Cavities. *Phys. Rev. Lett.*, 101:246809, Dec 2008. doi: 10.1103/PhysRevLett.101.246809. URL https://link.aps.org/doi/10.1103/PhysRevLett.101.246809. (cited on p. 31)

S. B. Chung and M. Stone. Proposal for reading out anyon qubits in non-Abelian $\nu = 12/5$ quantum Hall state. *Phys. Rev. B*, 73:245311, Jun 2006. doi: 10.1103/PhysRevB.73.245311. URL https://link.aps.org/doi/10.1103/PhysRevB.73.245311. (cited on p. 91)

L. W. Clark, N. Schine, C. Baum, N. Jia, and J. Simon. Observation of Laughlin states made of light. *arXiv e-prints*, Jul 2019. URL https://arxiv.org/abs/1907.05872. (cited on pp. 35, 67, 68, 91, and 96)

J. Clarke and F. K. Wilhelm. Superconducting quantum bits. *Nature*, 453(7198):1031–1042, 2008. doi: 10.1038/nature07128. URL https://doi.org/10.1038/nature07128. (cited on p. 36)

C. Cohen-Tannoudji, B. Diu, and F. Laloe. *Quantum Mechanics, Volume 1: Basic Concepts, Tools, and Applications, 2nd Edition*. Wiley, 2019. (cited on p. 19)

T. Comparin and E. Macaluso. tcompa/Laughlin-Metropolis. URL https://zenodo.org/record/1193694. publicy available at https://zenodo.org/record/1193694. (cited on p. 134)

N. R. Cooper. Rapidly rotating atomic gases. *Advances in Physics*, 57(6):539–616, 2008. doi: 10.1080/00018730802564122. URL https://doi.org/10.1080/00018730802564122. (cited on pp. 33 and 43)

N. R. Cooper and S. H. Simon. Signatures of Fractional Exclusion Statistics in the Spectroscopy of Quantum Hall Droplets. *Phys. Rev. Lett.*, 114:106802, Mar 2015. doi: 10.1103/PhysRevLett.114.106802. URL https://link.aps.org/doi/10.1103/PhysRevLett.114.106802. (cited on pp. 44 and 91)

N. R. Cooper and N. K. Wilkin. Composite fermion description of rotating Bose-Einstein condensates. *Phys. Rev. B*, 60:R16279–R16282, Dec 1999. doi: 10.1103/PhysRevB.60.R16279. URL https://link.aps.org/doi/10.1103/PhysRevB.60.R16279. (cited on p. 67)

N. R. Cooper, N. K. Wilkin, and J. M. F. Gunn. Quantum Phases of Vortices in Rotating Bose-Einstein Condensates. *Phys. Rev. Lett.*, 87:120405, Aug 2001. doi: 10.1103/PhysRevLett.87.120405. URL https://link.aps.org/doi/10.1103/PhysRevLett.87.120405. (cited on pp. 52 and 67)

N. R. Cooper, J. Dalibard, and I. B. Spielman. Topological bands for ultracold atoms. *Rev. Mod. Phys.*, 91:015005, Mar 2019. doi: 10.1103/RevModPhys.91.015005. URL https://link.aps.org/doi/10.1103/RevModPhys.91.015005. (cited on pp. 32 and 105)

J. Dalibard, F. Gerbier, G. Juzeliūnas, and P. Öhberg. Colloquium: Artificial gauge potentials for neutral atoms. *Rev. Mod. Phys.*, 83:1523–1543, Nov 2011. doi: 10.1103/RevModPhys.83.1523. URL https://link.aps.org/doi/10.1103/RevModPhys.83.1523. (cited on pp. 32 and 33)

S. Das Sarma, M. Freedman, and C. Nayak. Topologically Protected Qubits from a Possible Non-Abelian Fractional Quantum Hall State. *Phys. Rev. Lett.*, 94:166802, Apr 2005. doi: 10.1103/PhysRevLett.94.166802. URL https://link.aps.org/doi/10.1103/PhysRevLett.94.166802. (cited on p. 91)

C. de C. Chamon, D. E. Freed, S. A. Kivelson, S. L. Sondhi, and X. G. Wen. Two point-contact interferometer for quantum Hall systems. *Phys. Rev. B*, 55:2331–2343, Jan 1997. doi: 10.1103/PhysRevB.55.2331. URL https://link.aps.org/doi/10.1103/PhysRevB.55.2331. (cited on p. 91)

R. de Picciotto, M. Reznikov, M. Heiblum, V. Umansky, G. Bunin, and D. Mahalu. Direct observation of a fractional charge. *Nature*, 389:162–164, 09 1997. URL https://doi.org/10.1038/38241. (cited on p. 46)

M. H. Devoret and J. M. Martinis. Implementing Qubits with Superconducting Integrated Circuits. *Quantum Information Processing*, 3(1):163–203, Oct 2004. ISSN 1573-1332. doi: 10.1007/s11128-004-3101-5. URL https://doi.org/10.1007/s11128-004-3101-5. (cited on p. 36)

X.-Y. Dong, A. G. Grushin, J. Motruk, and F. Pollmann. Charge Excitation Dynamics in Bosonic Fractional Chern Insulators. *Phys. Rev. Lett.*, 121:086401, Aug 2018. doi: 10.1103/PhysRevLett.121.086401. URL https://link.aps.org/doi/10.1103/PhysRevLett.121.086401. (cited on p. 31)

R. Dum and M. Olshanii. Gauge Structures in Atom-Laser Interaction: Bloch Oscillations in a Dark Lattice. *Phys. Rev. Lett.*, 76:1788–1791, Mar 1996. doi: 10.1103/PhysRevLett.76.1788. URL https://link.aps.org/doi/10.1103/PhysRevLett.76.1788. (cited on p. 33)

I. Dumitriu, A. Edelman, and G. Shuman. MOPS: Multivariate orthogonal polynomials (symbolically). *Journal of Symbolic Computation*, 42(6):587 – 620, 2007. ISSN 0747-7171. doi: https://doi.org/10.1016/j.jsc.2007.01.005. URL http://www.sciencedirect.com/science/article/pii/S0747717107000090. (cited on p. 58)

A. Eckardt, C. Weiss, and M. Holthaus. Superfluid-Insulator Transition in a Periodically Driven Optical Lattice. *Phys. Rev. Lett.*, 95:260404, Dec 2005. doi: 10.1103/PhysRevLett.95.260404. URL https://link.aps.org/doi/10.1103/PhysRevLett.95.260404. (cited on p. 33)

A. Eckardt, M. Holthaus, H. Lignier, A. Zenesini, D. Ciampini, O. Morsch, and E. Arimondo. Exploring dynamic localization with a Bose-Einstein condensate. *Phys. Rev. A*, 79:013611, Jan 2009. doi: 10.1103/PhysRevA.79.013611. URL https://link.aps.org/doi/10.1103/PhysRevA.79.013611. (cited on p. 33)

Z. F. Ezawa and A. Iwazaki. Chern-Simons gauge theories for the fractional-quantum-Hall-effect hierarchy and anyon superconductivity. *Phys. Rev. B*, 43:2637–2641, Feb 1991. doi: 10.1103/PhysRevB.43.2637. URL https://link.aps.org/doi/10.1103/PhysRevB.43.2637. (cited on p. 28)

K. Fang, Z. Yu, and S. Fan. Realizing effective magnetic field for photons by controlling the phase of dynamic modulation. *Nature Photonics*, 6(11):782–787, 2012. doi: 10.1038/nphoton.2012.236. URL https://doi.org/10.1038/nphoton.2012.236. (cited on p. 36)

D. E. Feldman. Comment on "Interpretation of thermal conductance of the $\nu = 5/2$ edge". *Phys. Rev. B*, 98:167401, Oct 2018. doi: 10.1103/PhysRevB.98.167401. URL https://link.aps.org/doi/10.1103/PhysRevB.98.167401. (cited on p. 52)

R. Fern and S. H. Simon. Quantum Hall edges with hard confinement: Exact solution beyond Luttinger liquid. *Phys. Rev. B*, 95:201108, May 2017. doi: 10.1103/PhysRevB.95.201108. URL https://link.aps.org/doi/10.1103/PhysRevB.95.201108. (cited on pp. 60, 62, 63, 68, 69, 70, 71, 72, 74, 75, and 76)

R. Fern, R. Bondesan, and S. H. Simon. Effective edge state dynamics in the fractional quantum Hall effect. *Phys. Rev. B*, 98:155321, Oct 2018. doi: 10.1103/PhysRevB.98.155321. URL https://link.aps.org/doi/10.1103/PhysRevB.98.155321. (cited on pp. 43 and 77)

R. P. Feynman. Simulating physics with computers. *International Journal of Theoretical Physics*, 21(6):467–488, Jun 1982. ISSN 1572-9575. doi: 10.1007/BF02650179. URL https://doi.org/10.1007/BF02650179. (cited on p. 31)

J. Fröhlich and A. Zee. Large scale physics of the quantum hall fluid. *Nuclear Physics B*, 364(3):517 – 540, 1991. ISSN 0550-3213. doi: https://doi.org/10.1016/0550-3213(91)90275-3. URL http://www.sciencedirect.com/science/article/pii/0550321391902753. (cited on p. 28)

A. L. Gaunt, T. F. Schmidutz, I. Gotlibovych, R. P. Smith, and Z. Hadzibabic. Bose-Einstein Condensation of Atoms in a Uniform Potential. *Phys. Rev. Lett.*, 110:200406, May 2013. doi: 10.1103/PhysRevLett.110.200406. URL https://link.aps.org/doi/10.1103/PhysRevLett.110.200406. (cited on p. 67)

N. Gemelke, E. Sarajlic, and S. Chu. Rotating Few-body Atomic Systems in the Fractional Quantum Hall Regime. *arXiv e-prints*, Jul 2010. URL https://arxiv.org/abs/1007.2677. (cited on pp. 33, 34, 91, and 97)

I. M. Georgescu, S. Ashhab, and Franco Nori. Quantum simulation. *Rev. Mod. Phys.*, 86:153–185, Mar 2014. doi: 10.1103/RevModPhys.86.153. URL https://link.aps.org/doi/10.1103/RevModPhys.86.153. (cited on pp. 15 and 31)

M. Gerster, P. Silvi, M. Rizzi, R. Fazio, T. Calarco, and S. Montangero. Unconstrained tree tensor network: An adaptive gauge picture for enhanced performance. *Phys. Rev. B*, 90:125154, Sep 2014. doi: 10.1103/PhysRevB.90.125154. URL https://link.aps.org/doi/10.1103/PhysRevB.90.125154. (cited on pp. 107 and 135)

M. Gerster, M. Rizzi, P. Silvi, M. Dalmonte, and S. Montangero. Fractional quantum Hall effect in the interacting Hofstadter model via tensor networks. *Phys. Rev. B*, 96:195123, Nov 2017. doi: 10.1103/PhysRevB.96.195123. URL https://link.aps.org/doi/10.1103/PhysRevB.96.195123. (cited on pp. 31, 106, 107, 115, 135, and 137)

S. M. Girvin. The quantum hall effect: novel excitations and broken symmetries. In *Aspects topologiques de la physique en basse dimension. Topological aspects of low dimensional systems*, pages 53–175. Springer, 1999. (cited on p. 23)

S. M. Girvin, A. H. MacDonald, and P. M. Platzman. Magneto-roton theory of collective excitations in the fractional quantum Hall effect. *Phys. Rev. B*, 33:2481–2494, Feb 1986. doi: 10.1103/PhysRevB.33.2481. URL https://link.aps.org/doi/10.1103/PhysRevB.33.2481. (cited on p. 45)

M. O. Goerbig. Quantum Hall Effects. *arXiv e-prints*, Sep 2009. URL https://arxiv.org/abs/0909.1998. (cited on pp. 7, 23, 24, and 28)

N. Goldman, G. Juzeliūnas, P. Öhberg, and I. B. Spielman. Light-induced gauge fields for ultracold atoms. *Reports on Progress in Physics*, 77(12):126401, nov 2014. doi: 10.1088/0034-4885/77/12/126401. URL https://iopscience.iop.org/article/10.1088/0034-4885/77/12/126401. (cited on p. 32)

S. Golkar, D. X. Nguyen, and D. T. Son. Spectral sum rules and magneto-roton as emergent graviton in fractional quantum Hall effect. *Journal of High Energy Physics*, 2016(1):21, Jan 2016. ISSN 1029-8479. doi: 10.1007/JHEP01(2016)021. URL https://doi.org/10.1007/JHEP01(2016)021. (cited on p. 45)

M. Greiter, X.-G. Wen, and F. Wilczek. Paired Hall state at half filling. *Phys. Rev. Lett.*, 66: 3205–3208, Jun 1991. doi: 10.1103/PhysRevLett.66.3205. URL https://link.aps.org/doi/10.1103/PhysRevLett.66.3205. (cited on p. 52)

M. Greiter, X.-G. Wen, and F. Wilczek. Paired Hall states. *Nuclear Physics B*, 374(3):567 – 614, 1992. ISSN 0550-3213. doi: 10.1016/0550-3213(92)90401-V. URL http://www.sciencedirect.com/science/article/pii/055032139290401V. (cited on p. 52)

F. Grusdt, F. Letscher, M. Hafezi, and M. Fleischhauer. Topological Growing of Laughlin States in Synthetic Gauge Fields. *Phys. Rev. Lett.*, 113:155301, Oct 2014. doi: 10.1103/PhysRevLett.113.155301. URL https://link.aps.org/doi/10.1103/PhysRevLett.113.155301. (cited on pp. 31 and 115)

A. G. Grushin, Á. Gómez-León, and T. Neupert. Floquet Fractional Chern Insulators. *Phys. Rev. Lett.*, 112:156801, Apr 2014. doi: 10.1103/PhysRevLett.112.156801. URL https://link.aps.org/doi/10.1103/PhysRevLett.112.156801. (cited on p. 31)

X. Gu, A. F. Kockum, A. Miranowicz, Y. Liu, and F. Nori. Microwave photonics with superconducting quantum circuits. *Physics Reports*, 718-719:1–102, 2017. ISSN 0370-1573. doi: https://doi.org/10.1016/j.physrep.2017.10.002. URL http://www.sciencedirect.com/science/article/pii/S0370157317303290. (cited on p. 36)

V. Gurarie and C. Nayak. A plasma analogy and Berry matrices for non-abelian quantum Hall states. *Nuclear Physics B*, 506(3):685 – 694, 1997. ISSN 0550-3213. doi: 10.1016/S0550-3213(97) 00612-3. URL http://www.sciencedirect.com/science/article/pii/S0550321397006123. (cited on p. 133)

M. Hafezi, A. S. Sørensen, E. Demler, and M. D. Lukin. Fractional quantum Hall effect in optical lattices. *Phys. Rev. A*, 76:023613, Aug 2007. doi: 10.1103/PhysRevA.76.023613. URL https://link.aps.org/doi/10.1103/PhysRevA.76.023613. (cited on pp. 31 and 110)

M. Hafezi, S. Mittal, J. Fan, A. Migdall, and J. M. Taylor. Imaging topological edge states in silicon photonics. *Nature Photonics*, 7(12):1001–1005, 2013. doi: 10.1038/nphoton.2013.274. URL https://doi.org/10.1038/nphoton.2013.274. (cited on pp. 34 and 35)

M. Hafezi, P. Adhikari, and J. M. Taylor. Engineering three-body interaction and Pfaffian states in circuit QED systems. *Phys. Rev. B*, 90:060503, Aug 2014. doi: 10.1103/PhysRevB.90.060503. URL https://link.aps.org/doi/10.1103/PhysRevB.90.060503. (cited on p. 118)

F. D. M. Haldane. Fractional Quantization of the Hall Effect: A Hierarchy of Incompressible Quantum Fluid States. *Phys. Rev. Lett.*, 51:605–608, Aug 1983. doi: 10.1103/PhysRevLett.51. 605. URL https://link.aps.org/doi/10.1103/PhysRevLett.51.605. (cited on p. 40)

F. D. M. Haldane. Model for a Quantum Hall Effect without Landau Levels: Condensed-Matter Realization of the "Parity Anomaly". *Phys. Rev. Lett.*, 61:2015–2018, Oct 1988. doi: 10.1103/PhysRevLett.61.2015. URL https://link.aps.org/doi/10.1103/PhysRevLett.61.2015. (cited on pp. 30 and 106)

F. D. M. Haldane. Geometrical Description of the Fractional Quantum Hall Effect. *Phys. Rev. Lett.*, 107:116801, Sep 2011. doi: 10.1103/PhysRevLett.107.116801. URL https://link.aps.org/doi/10.1103/PhysRevLett.107.116801. (cited on p. 45)

F. D. M. Haldane and S. Raghu. Possible Realization of Directional Optical Waveguides in Photonic Crystals with Broken Time-Reversal Symmetry. *Phys. Rev. Lett.*, 100:013904, Jan 2008. doi: 10.1103/PhysRevLett.100.013904. URL https://link.aps.org/doi/10.1103/PhysRevLett.100.013904. (cited on p. 34)

F. D. M. Haldane and E. H. Rezayi. Finite-Size Studies of the Incompressible State of the Fractionally Quantized Hall Effect and its Excitations. *Phys. Rev. Lett.*, 54:237–240, Jan 1985. doi: 10.1103/PhysRevLett.54.237. URL https://link.aps.org/doi/10.1103/PhysRevLett.54.237. (cited on p. 29)

B. I. Halperin. Statistics of Quasiparticles and the Hierarchy of Fractional Quantized Hall States. *Phys. Rev. Lett.*, 52:1583–1586, Apr 1984. doi: 10.1103/PhysRevLett.52.1583. URL https://link.aps.org/doi/10.1103/PhysRevLett.52.1583. (cited on pp. 7 and 46)

P. G. Harper. Single Band Motion of Conduction Electrons in a Uniform Magnetic Field. *Proceedings of the Physical Society. Section A*, 68(10):874–878, oct 1955. doi: 10.1088/0370-1298/68/10/304. (cited on p. 105)

M. Z. Hasan and C. L. Kane. Colloquium: Topological insulators. *Rev. Mod. Phys.*, 82:3045–3067, Nov 2010. doi: 10.1103/RevModPhys.82.3045. URL https://link.aps.org/doi/10.1103/RevModPhys.82.3045. (cited on p. 15)

A.-L. He, W.-W. Luo, Y.-F. Wang, and C.-D. Gong. Wave functions for fractional Chern insulators in disk geometry. *New Journal of Physics*, 17(12):125005, dec 2015. doi: 10.1088/1367-2630/17/12/125005. URL https://iopscience.iop.org/article/10.1088/1367-2630/17/12/125005. (cited on p. 58)

Y.-C. He, F. Grusdt, A. Kaufman, M. Greiner, and A. Vishwanath. Realizing and adiabatically preparing bosonic integer and fractional quantum Hall states in optical lattices. *Phys. Rev. B*, 96:201103, Nov 2017. doi: 10.1103/PhysRevB.96.201103. URL https://link.aps.org/doi/10.1103/PhysRevB.96.201103. (cited on p. 31)

E. V. Herland, E. Babaev, P. Bonderson, V. Gurarie, C. Nayak, and A. Sudbø. Screening properties and phase transitions in unconventional plasmas for Ising-type quantum Hall states. *Phys. Rev. B*, 85:024520, Jan 2012. doi: 10.1103/PhysRevB.85.024520. URL https://link.aps.org/doi/10.1103/PhysRevB.85.024520. (cited on p. 133)

E. V. Herland, E. Babaev, P. Bonderson, V. Gurarie, C. Nayak, L. Radzihovsky, and A. Sudbø. Freezing of an unconventional two-dimensional plasma. *Phys. Rev. B*, 87:075117, Feb 2013. doi: 10.1103/PhysRevB.87.075117. URL https://link.aps.org/doi/10.1103/PhysRevB.87.075117. (cited on p. 133)

T.-L. Ho and E. J. Mueller. Rotating Spin-1 Bose Clusters. *Phys. Rev. Lett.*, 89:050401, Jul 2002. doi: 10.1103/PhysRevLett.89.050401. URL https://link.aps.org/doi/10.1103/PhysRevLett.89.050401. (cited on p. 96)

D. R. Hofstadter. Energy levels and wave functions of Bloch electrons in rational and irrational magnetic fields. *Phys. Rev. B*, 14:2239–2249, Sep 1976. doi: 10.1103/PhysRevB.14.2239. URL https://link.aps.org/doi/10.1103/PhysRevB.14.2239. (cited on pp. 30, 105, and 106)

A. A. Houck, H. E. Türeci, and J. Koch. On-chip quantum simulation with superconducting circuits. *Nature Physics*, 8(4):292–299, 2012. doi: 10.1038/nphys2251. URL https://doi.org/10.1038/nphys2251. (cited on p. 31)

K. Huang. *Statistical Mechanics, 2nd Edition*. Wiley, 2019. URL https://www.wiley.com/en-us/Statistical+Mechanics%2C+2nd+Edition-p-9780471815181. (cited on p. 26)

J. Hubbard. Electron correlations in narrow energy bands. *Proceedings of the Royal Society of London. Series A. Mathematical and Physical Sciences*, 276(1365):238–257, 1963. doi: 10.1098/rspa.1963.0204. URL https://royalsocietypublishing.org/doi/abs/10.1098/rspa.1963.0204. (cited on p. 31)

A. Hudomal, N. Regnault, and I. Vasić. Bosonic fractional quantum Hall states in driven optical lattices. *Phys. Rev. A*, 100:053624, Nov 2019. doi: 10.1103/PhysRevA.100.053624. URL https://link.aps.org/doi/10.1103/PhysRevA.100.053624. (cited on pp. 31 and 116)

D. A. Ivanov. Non-Abelian Statistics of Half-Quantum Vortices in p-Wave Superconductors. *Phys. Rev. Lett.*, 86:268–271, Jan 2001. doi: 10.1103/PhysRevLett.86.268. URL https://link.aps.org/doi/10.1103/PhysRevLett.86.268. (cited on pp. 7 and 52)

J. K. Jain. *Composite Fermions*. Cambridge University Press, 2007. doi: 10.1017/CBO9780511607561. (cited on p. 52)

D. Jaksch and P. Zoller. Creation of effective magnetic fields in optical lattices: the Hofstadter butterfly for cold neutral atoms. *New Journal of Physics*, 5:56–56, may 2003. doi: 10.1088/1367-2630/5/1/356. URL https://iopscience.iop.org/article/10.1088/1367-2630/5/1/356/meta. (cited on p. 33)

D. Jaksch and P. Zoller. The cold atom Hubbard toolbox. *Annals of Physics*, 315(1):52–79, 2005. ISSN 0003-4916. doi: https://doi.org/10.1016/j.aop.2004.09.010. URL http://www.sciencedirect.com/science/article/pii/S0003491604001782. Special Issue. (cited on p. 32)

B. Jaworowski, N. Regnault, and Z. Liu. Characterization of quasiholes in two-component fractional quantum Hall states and fractional Chern insulators in $|C|=2$ flat bands. *Phys. Rev. B*, 99:045136, Jan 2019. doi: 10.1103/PhysRevB.99.045136. URL https://link.aps.org/doi/10.1103/PhysRevB.99.045136. (cited on pp. 31, 98, 108, and 109)

N. Jia, N. Schine, A. Georgakopoulos, A. Ryou, L. W. Clark, A. Sommer, and J. Simon. A strongly interacting polaritonic quantum dot. *Nature Physics*, 14(6):550–554, 2018. doi: 10.1038/s41567-018-0071-6. URL https://doi.org/10.1038/s41567-018-0071-6. (cited on pp. 34 and 36)

N. Jiang and Z.-X. Hu. Identification of the fractional quantum Hall edge modes by density oscillations. *Phys. Rev. B*, 94:125116, Sep 2016. doi: 10.1103/PhysRevB.94.125116. URL https://link.aps.org/doi/10.1103/PhysRevB.94.125116. (cited on pp. 60, 90, and 117)

G. Jotzu, M. Messer, M. Desbuquois, R. Lebrat, T. Uehlinger, D. Greif, and T. Esslinger. Experimental realization of the topological Haldane model with ultracold fermions. *Nature*, 515(7526): 237–240, 2014. doi: 10.1038/nature13915. URL https://doi.org/10.1038/nature13915. (cited on p. 33)

G. Juzeliūnas and P. Öhberg. Slow Light in Degenerate Fermi Gases. *Phys. Rev. Lett.*, 93:033602, Jul 2004. doi: 10.1103/PhysRevLett.93.033602. URL https://link.aps.org/doi/10.1103/PhysRevLett.93.033602. (cited on p. 33)

G. Juzeliūnas, J. Ruseckas, P. Öhberg, and M. Fleischhauer. Light-induced effective magnetic fields for ultracold atoms in planar geometries. *Phys. Rev. A*, 73:025602, Feb 2006. doi: 10.1103/PhysRevA.73.025602. URL https://link.aps.org/doi/10.1103/PhysRevA.73.025602. (cited on p. 33)

E. Kapit and E. Mueller. Exact Parent Hamiltonian for the Quantum Hall States in a Lattice. *Phys. Rev. Lett.*, 105:215303, Nov 2010. doi: 10.1103/PhysRevLett.105.215303. URL https://link.aps.org/doi/10.1103/PhysRevLett.105.215303. (cited on p. 31)

E. Kapit, P. Ginsparg, and E. Mueller. Non-Abelian Braiding of Lattice Bosons. *Phys. Rev. Lett.*, 108:066802, Feb 2012. doi: 10.1103/PhysRevLett.108.066802. URL https://link.aps.org/doi/10.1103/PhysRevLett.108.066802. (cited on p. 109)

E. Kapit, M. Hafezi, and S. H. Simon. Induced Self-Stabilization in Fractional Quantum Hall States of Light. *Phys. Rev. X*, 4:031039, Sep 2014. doi: 10.1103/PhysRevX.4.031039. URL https://link.aps.org/doi/10.1103/PhysRevX.4.031039. (cited on p. 31)

A. Y. Kitaev. Fault-tolerant quantum computation by anyons. *Annals of Physics*, 303(1):2 – 30, 2003. ISSN 0003-4916. doi: https://doi.org/10.1016/S0003-4916(02)00018-0. URL http://www.sciencedirect.com/science/article/pii/S0003491602000180. (cited on pp. 7, 11, and 102)

H. Kjnsberg and J. Myrheim. Numerical study of charge and statistics of Laughlin quasiparticles. *International Journal of Modern Physics A*, 14(04):537–557, 1999. doi: 10.1142/S0217751X99000270. URL https://doi.org/10.1142/S0217751X99000270. (cited on p. 133)

L. Kohn, P. Silvi, M. Gerster, M. Keck, R. Fazio, G. E. Santoro, and S. Montangero. Superfluid to Mott transition in a Bose-Hubbard ring: Persistent currents and defect formation. *arXiv e-prints*, art. arXiv:1907.00009, Jun 2019. URL https://arxiv.org/abs/1907.00009. (cited on p. 115)

W. Krauth. *Statistical Mechanics: Algorithms and Computations*. Oxford University Press, 2006. (cited on p. 133)

R. Kubo. Statistical-Mechanical Theory of Irreversible Processes. I. General Theory and Simple Applications to Magnetic and Conduction Problems. *Journal of the Physical Society of Japan*, 12 (6):570–586, 1957. doi: 10.1143/JPSJ.12.570. URL https://doi.org/10.1143/JPSJ.12.570. (cited on p. 24)

T. Lahaye, C. Menotti, L. Santos, M. Lewenstein, and T. Pfau. The physics of dipolar bosonic quantum gases. *Reports on Progress in Physics*, 72(12):126401, nov 2009. doi: 10.1088/0034-4885/72/12/126401. URL https://iopscience.iop.org/article/10.1088/0034-4885/72/12/126401. (cited on p. 32)

L. D. Landau and E. M. Lifshitz. *Quantum mechanics: non-relativistic theory*, volume 3. Elsevier, 2013. (cited on p. 16)

R. B. Laughlin. Anomalous Quantum Hall Effect: An Incompressible Quantum Fluid with Fractionally Charged Excitations. *Phys. Rev. Lett.*, 50:1395–1398, May 1983. doi: 10.1103/PhysRevLett.50.1395. URL https://link.aps.org/doi/10.1103/PhysRevLett.50.1395. (cited on pp. 25, 37, 40, and 41)

R. B. Laughlin. Elementary theory: the incompressible quantum fluid. In *The quantum Hall effect*, pages 233–301. Springer, 1987. URL https://link.springer.com/chapter/10.1007/978-1-4612-3350-3_7. (cited on p. 47)

J. Lebreuilly and I. Carusotto. Quantum simulation of zero-temperature quantum phases and incompressible states of light via non-Markovian reservoir engineering techniques. *Comptes Rendus Physique*, 19(6):433 – 450, 2018. ISSN 1631-0705. doi: https://doi.org/10.1016/j.crhy.2018.07.001. URL http://www.sciencedirect.com/science/article/pii/S1631070518300513. (cited on p. 34)

K. H. Lee, Z.-X. Hu, and X. Wan. Construction of edge states in fractional quantum Hall systems by Jack polynomials. *Phys. Rev. B*, 89:165124, Apr 2014. doi: 10.1103/PhysRevB.89.165124. URL https://link.aps.org/doi/10.1103/PhysRevB.89.165124. (cited on pp. 59, 60, 62, and 63)

S.-S. Lee, S. Ryu, C. Nayak, and M. P. A. Fisher. Particle-Hole Symmetry and the $\nu = \frac{5}{2}$ Quantum Hall State. *Phys. Rev. Lett.*, 99:236807, Dec 2007. doi: 10.1103/PhysRevLett.99.236807. URL https://link.aps.org/doi/10.1103/PhysRevLett.99.236807. (cited on pp. 52 and 54)

J. M. Leinaas and J. Myrheim. On the theory of identical particles. *Il Nuovo Cimento B Series 11*, 37(1):1–23, jan 1977. doi: 10.1007/bf02727953. URL https://doi.org/10.1007/bf02727953. (cited on pp. 7 and 9)

M. Levin, B. I. Halperin, and B. Rosenow. Particle-Hole Symmetry and the Pfaffian State. *Phys. Rev. Lett.*, 99:236806, Dec 2007. doi: 10.1103/PhysRevLett.99.236806. URL https://link.aps.org/doi/10.1103/PhysRevLett.99.236806. (cited on pp. 52 and 54)

M. Lewenstein, A. Sanpera, V. Ahufinger, B. Damski, A. Sen(De), and U. Sen. Ultracold atomic gases in optical lattices: mimicking condensed matter physics and beyond. *Advances in Physics*, 56(2):243–379, 2007. doi: 10.1080/00018730701223200. URL https://doi.org/10.1080/00018730701223200. (cited on p. 32)

Y. J. Lin, R. L. Compton, K. Jiménez-García, J. V. Porto, and I. B. Spielman. Synthetic magnetic fields for ultracold neutral atoms. *Nature*, 462(7273):628–632, 2009. doi: 10.1038/nature08609. URL https://doi.org/10.1038/nature08609. (cited on p. 33)

S.-F. Liou, F. D. M. Haldane, K. Yang, and E. H. Rezayi. Chiral Gravitons in Fractional Quantum Hall Liquids. *Phys. Rev. Lett.*, 123:146801, Sep 2019. doi: 10.1103/PhysRevLett.123.146801. URL https://link.aps.org/doi/10.1103/PhysRevLett.123.146801. (cited on p. 45)

Z. Liu, R. N. Bhatt, and N. Regnault. Characterization of quasiholes in fractional Chern insulators. *Phys. Rev. B*, 91:045126, Jan 2015. doi: 10.1103/PhysRevB.91.045126. URL https://link.aps.org/doi/10.1103/PhysRevB.91.045126. (cited on pp. 31, 98, 106, 108, 109, 110, 111, and 136)

K. K. W. Ma and D. E. Feldman. The sixteenfold way and the quantum Hall effect at half-integer filling factors. *Phys. Rev. B*, 100:035302, Jul 2019a. doi: 10.1103/PhysRevB.100.035302. URL https://link.aps.org/doi/10.1103/PhysRevB.100.035302. (cited on p. 52)

K. K. W. Ma and D. E. Feldman. Partial equilibration of integer and fractional edge channels in the thermal quantum Hall effect. *Phys. Rev. B*, 99:085309, Feb 2019b. doi: 10.1103/PhysRevB.99.085309. URL https://link.aps.org/doi/10.1103/PhysRevB.99.085309. (cited on p. 52)

R. Ma, B. Saxberg, C. Owens, N. Leung, Y. Lu, J. Simon, and D. I. Schuster. A dissipatively stabilized Mott insulator of photons. *Nature*, 566(7742):51–57, 2019. doi: 10.1038/s41586-019-0897-9. URL https://doi.org/10.1038/s41586-019-0897-9. (cited on p. 36)

E. Macaluso and I. Carusotto. Hard-wall confinement of a fractional quantum Hall liquid. *Phys. Rev. A*, 96:043607, Oct 2017. doi: 10.1103/PhysRevA.96.043607. URL https://link.aps.org/doi/10.1103/PhysRevA.96.043607. (cited on pp. 2, 57, 60, 63, 67, 68, 69, 70, 71, 73, 75, 76, 77, 78, and 79)

E. Macaluso and I. Carusotto. Ring-shaped fractional quantum Hall liquids with hard-wall potentials. *Phys. Rev. A*, 98:013605, Jul 2018. doi: 10.1103/PhysRevA.98.013605. URL https://link.aps.org/doi/10.1103/PhysRevA.98.013605. (cited on pp. 2, 57, 60, 62, 63, 64, 67, 68, 69, 80, 82, 84, 85, 87, 88, 89, 92, 122, and 125)

E. Macaluso, T. Comparin, L. Mazza, and I. Carusotto. Fusion Channels of Non-Abelian Anyons from Angular-Momentum and Density-Profile Measurements. *Phys. Rev. Lett.*, 123:266801, Dec 2019a. doi: 10.1103/PhysRevLett.123.266801. URL https://link.aps.org/doi/10.1103/PhysRevLett.123.266801. (cited on pp. 3, 11, 91, 94, 96, 98, 101, 102, and 128)

E. Macaluso, T. Comparin, R. O. Umucalılar, M. Gerster, S. Montangero, M. Rizzi, and I. Carusotto. Charge and statistics of lattice quasiholes from density measurements: a Tree Tensor Network study. 2019b. URL https://arxiv.org/abs/1910.05222. (cited on pp. 3, 31, 105, 106, 109, 113, 114, 115, 136, and 138)

Y. Makhlin, G. Schön, and A. Shnirman. Quantum-state engineering with Josephson-junction devices. *Rev. Mod. Phys.*, 73:357–400, May 2001. doi: 10.1103/RevModPhys.73.357. URL https://link.aps.org/doi/10.1103/RevModPhys.73.357. (cited on p. 36)

S. Manna, J. Wildeboer, G. Sierra, and A. E. B. Nielsen. Non-Abelian quasiholes in lattice Moore-Read states and parent Hamiltonians. *Phys. Rev. B*, 98:165147, Oct 2018. doi: 10.1103/PhysRevB.98.165147. URL https://link.aps.org/doi/10.1103/PhysRevB.98.165147. (cited on p. 109)

S. Manna, N. S. Srivatsa, J. Wildeboer, and A. E. B. Nielsen. Quasiparticles as Detector of Topological Quantum Phase Transitions. *arXiv e-prints*, art. arXiv:1909.02046, Sep 2019. URL https://arxiv.org/abs/1909.02046. (cited on p. 31)

L. Mazza, M. Rizzi, M. Lewenstein, and J. I. Cirac. Emerging bosons with three-body interactions from spin-1 atoms in optical lattices. *Phys. Rev. A*, 82:043629, Oct 2010. doi: 10.1103/PhysRevA.82.043629. URL https://link.aps.org/doi/10.1103/PhysRevA.82.043629. (cited on p. 118)

M. McDonald, J. Trisnadi, K.-X. Yao, and C. Chin. Superresolution Microscopy of Cold Atoms in an Optical Lattice. *Phys. Rev. X*, 9:021001, Apr 2019. doi: 10.1103/PhysRevX.9.021001. URL https://link.aps.org/doi/10.1103/PhysRevX.9.021001. (cited on p. 32)

N. Metropolis, A. W. Rosenbluth, M. N. Rosenbluth, A. H. Teller, and E. Teller. Equation of State Calculations by Fast Computing Machines. *The Journal of Chemical Physics*, 21(6):1087–1092, 1953. doi: 10.1063/1.1699114. URL https://doi.org/10.1063/1.1699114. (cited on p. 133)

F. Mezzacapo, N. Schuch, M. Boninsegni, and J. I. Cirac. Ground-state properties of quantum many-body systems: entangled-plaquette states and variational Monte Carlo. *New Journal of Physics*, 11(8):083026, aug 2009. doi: 10.1088/1367-2630/11/8/083026. URL https://doi.org/10.1088. (cited on p. 107)

M. Milovanović and N. Read. Edge excitations of paired fractional quantum Hall states. *Phys. Rev. B*, 53:13559–13582, May 1996. doi: 10.1103/PhysRevB.53.13559. URL https://link.aps.org/doi/10.1103/PhysRevB.53.13559. (cited on pp. 51, 53, and 102)

H. Miyake, G. A. Siviloglou, C. J. Kennedy, W. C. Burton, and W. Ketterle. Realizing the Harper Hamiltonian with Laser-Assisted Tunneling in Optical Lattices. *Phys. Rev. Lett.*, 111:185302, Oct 2013. doi: 10.1103/PhysRevLett.111.185302. URL https://link.aps.org/doi/10.1103/PhysRevLett.111.185302. (cited on p. 33)

S. Montangero. *Introduction to Tensor Network Methods.* Springer International Publishing, 2018. doi: 10.1007/978-3-030-01409-4. (cited on p. 107)

G. Moore and N. Read. Nonabelions in the fractional quantum Hall effect. *Nuclear Physics B*, 360(2):362 – 396, 1991. ISSN 0550-3213. doi: 10.1016/0550-3213(91)90407-O. URL http://www.sciencedirect.com/science/article/pii/055032139190407O. (cited on pp. 7, 51, 52, 54, and 117)

R. Morf and B. I. Halperin. Monte Carlo evaluation of trial wave functions for the fractional quantized Hall effect: Disk geometry. *Phys. Rev. B*, 33:2221–2246, Feb 1986. doi: 10.1103/PhysRevB.33.2221. URL https://link.aps.org/doi/10.1103/PhysRevB.33.2221. (cited on p. 133)

R. H. Morf. Transition from Quantum Hall to Compressible States in the Second Landau Level: New Light on the $\nu = 5/2$ Enigma. *Phys. Rev. Lett.*, 80:1505–1508, Feb 1998. doi: 10.1103/PhysRevLett.80.1505. URL https://link.aps.org/doi/10.1103/PhysRevLett.80.1505. (cited on p. 52)

O. Morsch and M. Oberthaler. Dynamics of Bose-Einstein condensates in optical lattices. *Rev. Mod. Phys.*, 78:179–215, Feb 2006. doi: 10.1103/RevModPhys.78.179. URL https://link.aps.org/doi/10.1103/RevModPhys.78.179. (cited on p. 32)

J. Motruk and F. Pollmann. Phase transitions and adiabatic preparation of a fractional Chern insulator in a boson cold-atom model. *Phys. Rev. B*, 96:165107, Oct 2017. doi: 10.1103/PhysRevB.96.165107. URL https://link.aps.org/doi/10.1103/PhysRevB.96.165107. (cited on p. 31)

V. Mourik, K. Zuo, S. M. Frolov, S. R. Plissard, E. P. A. M. Bakkers, and L. P. Kouwenhoven. Signatures of Majorana Fermions in Hybrid Superconductor-Semiconductor Nanowire Devices. *Science*, 336(6084):1003, 2012. ISSN 0036-8075. doi: 10.1126/science.1222360. URL http://science.sciencemag.org/content/336/6084/1003. (cited on p. 7)

D. F. Mross, Y. Oreg, A. Stern, G. Margalit, and M. Heiblum. Theory of Disorder-Induced Half-Integer Thermal Hall Conductance. *Phys. Rev. Lett.*, 121:026801, Jul 2018. doi: 10.1103/PhysRevLett.121.026801. URL https://link.aps.org/doi/10.1103/PhysRevLett.121.026801. (cited on p. 52)

J. Nakamura, S. Fallahi, H. Sahasrabudhe, R. Rahman, S. Liang, G. C. Gardner, and M. J. Manfra. Aharonov–Bohm interference of fractional quantum Hall edge modes. *Nature Physics*, 15(6):563–569, 2019. doi: 10.1038/s41567-019-0441-8. URL https://doi.org/10.1038/s41567-019-0441-8. (cited on p. 91)

C. Nayak and F. Wilczek. $2n$-quasihole states realize 2^{n-1}-dimensional spinor braiding statistics in paired quantum Hall states. *Nuclear Physics B*, 479(3):529 – 553, 1996. ISSN 0550-3213. doi: 10.1016/0550-3213(96)00430-0. URL http://www.sciencedirect.com/science/article/pii/0550321396004300. (cited on pp. 52, 54, 55, and 56)

C. Nayak, S. H. Simon, A. Stern, M. Freedman, and S. Das Sarma. Non-Abelian anyons and topological quantum computation. *Rev. Mod. Phys.*, 80:1083–1159, Sep 2008. doi: 10.1103/RevModPhys.80.1083. URL https://link.aps.org/doi/10.1103/RevModPhys.80.1083. (cited on pp. 7, 10, 11, 13, 15, 52, 54, 95, and 102)

T. Neupert, L. Santos, C. Chamon, and C. Mudry. Fractional Quantum Hall States at Zero Magnetic Field. *Phys. Rev. Lett.*, 106:236804, Jun 2011. doi: 10.1103/PhysRevLett.106.236804. URL https://link.aps.org/doi/10.1103/PhysRevLett.106.236804. (cited on pp. 30 and 31)

A. E. B. Nielsen. Anyon braiding in semianalytical fractional quantum Hall lattice models. *Phys. Rev. B*, 91:041106, Jan 2015. doi: 10.1103/PhysRevB.91.041106. URL https://link.aps.org/doi/10.1103/PhysRevB.91.041106. (cited on pp. 109 and 110)

A. E. B. Nielsen, I. Glasser, and I. D. Rodríguez. Quasielectrons as inverse quasiholes in lattice fractional quantum Hall models. *New Journal of Physics*, 20(3):033029, mar 2018. doi: 10.1088/1367-2630/aab5d0. URL https://iopscience.iop.org/article/10.1088/1367-2630/aab5d0. (cited on pp. 31 and 109)

R. Orús. A practical introduction to tensor networks: Matrix product states and projected entangled pair states. *Annals of Physics*, 349:117–158, oct 2014. doi: 10.1016/j.aop.2014.06.013. URL https://doi.org/10.1016/j.aop.2014.06.013. (cited on p. 107)

C. Owens, A. LaChapelle, B. Saxberg, B. M. Anderson, R. Ma, J. Simon, and D. I. Schuster. Quarter-flux Hofstadter lattice in a qubit-compatible microwave cavity array. *Phys. Rev. A*, 97:013818, Jan 2018. doi: 10.1103/PhysRevA.97.013818. URL https://link.aps.org/doi/10.1103/PhysRevA.97.013818. (cited on pp. 105 and 110)

T. Ozawa and H. M. Price. Topological quantum matter in synthetic dimensions. *Nature Reviews Physics*, 1(5):349–357, 2019. doi: 10.1038/s42254-019-0045-3. URL https://doi.org/10.1038/s42254-019-0045-3. (cited on p. 32)

T. Ozawa, H. M. Price, A. Amo, N. Goldman, M. Hafezi, L. Lu, M. C. Rechtsman, D. Schuster, J. Simon, O. Zilberberg, and I. Carusotto. Topological photonics. *Rev. Mod. Phys.*, 91:015006, Mar 2019. doi: 10.1103/RevModPhys.91.015006. URL https://link.aps.org/doi/10.1103/RevModPhys.91.015006. (cited on pp. 32, 34, and 105)

R. N. Palmer and D. Jaksch. High-Field Fractional Quantum Hall Effect in Optical Lattices. *Phys. Rev. Lett.*, 96:180407, May 2006. doi: 10.1103/PhysRevLett.96.180407. URL https://link.aps.org/doi/10.1103/PhysRevLett.96.180407. (cited on p. 31)

S. A. Parameswaran, R. Roy, and S. L. Sondhi. Fractional quantum Hall physics in topological flat bands. *Comptes Rendus Physique*, 14(9):816 – 839, 2013. ISSN 1631-0705. doi: https://doi.org/10.1016/j.crhy.2013.04.003. URL http://www.sciencedirect.com/science/article/pii/S163107051300073X. Topological insulators / Isolants topologiques. (cited on p. 31)

B. Paredes, P. Fedichev, J. I. Cirac, and P. Zoller. $\frac{1}{2}$-anyons in small atomic bose-einstein condensates. *Phys. Rev. Lett.*, 87:010402, Jun 2001. doi: 10.1103/PhysRevLett.87.010402. URL https://link.aps.org/doi/10.1103/PhysRevLett.87.010402. (cited on p. 92)

R. Peierls. Zur Theorie des Diamagnetismus von Leitungselektronen. *Zeitschrift für Physik*, 80(11): 763–791, Nov 1933. doi: 10.1007/BF01342591. URL https://doi.org/10.1007/BF01342591. (cited on p. 106)

L. E. Picasso. *Lectures in Quantum Mechanics.* Springer International Publishing, 2016. doi: 10.1007/978-3-319-22632-3. URL https://doi.org/10.1007/978-3-319-22632-3. (cited on p. 93)

L. Pitaevskii and S. Stringari. *Bose-Einstein Condensation and Superfluidity.* Oxford University Press, 2016. doi: 10.1093/acprof:oso/9780198758884.001.0001. URL https://doi.org/10.1093/acprof:oso/9780198758884.001.0001. (cited on pp. 32 and 92)

J. Preskill. Lecture notes for physics 229: Quantum information and computation. *California Institute of Technology*, 16, 1998. (cited on p. 10)

E. Prodan and F. D. M. Haldane. Mapping the braiding properties of the Moore-Read state. *Phys. Rev. B*, 80:115121, Sep 2009. doi: 10.1103/PhysRevB.80.115121. URL https://link.aps.org/doi/10.1103/PhysRevB.80.115121. (cited on pp. 92 and 101)

X.-L. Qi and S.-C. Zhang. Topological insulators and superconductors. *Rev. Mod. Phys.*, 83: 1057–1110, Oct 2011. doi: 10.1103/RevModPhys.83.1057. URL https://link.aps.org/doi/10.1103/RevModPhys.83.1057. (cited on p. 15)

R.-Z. Qiu, F. D. M. Haldane, X. Wan, K. Yang, and S. Yi. Model anisotropic quantum Hall states. *Phys. Rev. B*, 85:115308, Mar 2012. doi: 10.1103/PhysRevB.85.115308. URL https://link.aps.org/doi/10.1103/PhysRevB.85.115308. (cited on p. 118)

S. Raghu and F. D. M. Haldane. Analogs of quantum-Hall-effect edge states in photonic crystals. *Phys. Rev. A*, 78:033834, Sep 2008. doi: 10.1103/PhysRevA.78.033834. URL https://link.aps.org/doi/10.1103/PhysRevA.78.033834. (cited on p. 34)

M. Račiūnas, F. N. Ünal, E. Anisimovas, and A. Eckardt. Creating, probing, and manipulating fractionally charged excitations of fractional Chern insulators in optical lattices. *Phys. Rev. A*, 98:063621, Dec 2018. doi: 10.1103/PhysRevA.98.063621. URL https://link.aps.org/doi/10.1103/PhysRevA.98.063621. (cited on pp. 31, 108, 115, and 116)

N. Read. Excitation structure of the hierarchy scheme in the fractional quantum Hall effect. *Phys. Rev. Lett.*, 65:1502–1505, Sep 1990. doi: 10.1103/PhysRevLett.65.1502. URL https://link.aps.org/doi/10.1103/PhysRevLett.65.1502. (cited on p. 28)

N. Read and N. R. Cooper. Free expansion of lowest-Landau-level states of trapped atoms: A wavefunction microscope. *Phys. Rev. A*, 68:035601, Sep 2003. doi: 10.1103/PhysRevA.68.035601. URL https://link.aps.org/doi/10.1103/PhysRevA.68.035601. (cited on p. 96)

N. Read and D. Green. Paired states of fermions in two dimensions with breaking of parity and time-reversal symmetries and the fractional quantum Hall effect. *Phys. Rev. B*, 61:10267–10297, Apr 2000. doi: 10.1103/PhysRevB.61.10267. URL https://link.aps.org/doi/10.1103/PhysRevB.61.10267. (cited on pp. 7 and 52)

N. Read and E. Rezayi. Beyond paired quantum Hall states: Parafermions and incompressible states in the first excited Landau level. *Phys. Rev. B*, 59:8084–8092, Mar 1999. doi: 10.1103/PhysRevB.59.8084. URL https://link.aps.org/doi/10.1103/PhysRevB.59.8084. (cited on pp. 7, 55, and 117)

M. C. Rechtsman, J. M. Zeuner, Y. Plotnik, Y. Lumer, D. Podolsky, F. Dreisow, S. Nolte, M. Segev, and A. Szameit. Photonic Floquet topological insulators. *Nature*, 496(7444): 196–200, 2013. doi: 10.1038/nature12066. URL https://doi.org/10.1038/nature12066. (cited on pp. 34 and 35)

N. Regnault and B. A. Bernevig. Fractional Chern Insulator. *Phys. Rev. X*, 1:021014, Dec 2011. doi: 10.1103/PhysRevX.1.021014. URL https://link.aps.org/doi/10.1103/PhysRevX.1.021014. (cited on pp. 31 and 135)

N. Regnault and Th. Jolicoeur. Quantum Hall Fractions in Rotating Bose-Einstein Condensates. *Phys. Rev. Lett.*, 91:030402, Jul 2003. doi: 10.1103/PhysRevLett.91.030402. URL https://link.aps.org/doi/10.1103/PhysRevLett.91.030402. (cited on p. 67)

C. Repellin and N. Goldman. Detecting Fractional Chern Insulators through Circular Dichroism. *Phys. Rev. Lett.*, 122:166801, Apr 2019. doi: 10.1103/PhysRevLett.122.166801. URL https://link.aps.org/doi/10.1103/PhysRevLett.122.166801. (cited on p. 31)

E. H. Rezayi and F. D. M. Haldane. Incompressible Paired Hall State, Stripe Order, and the Composite Fermion Liquid Phase in Half-Filled Landau Levels. *Phys. Rev. Lett.*, 84:4685–4688, May 2000. doi: 10.1103/PhysRevLett.84.4685. URL https://link.aps.org/doi/10.1103/PhysRevLett.84.4685. (cited on p. 52)

E. H. Rezayi, N. Read, and N. R. Cooper. Incompressible Liquid State of Rapidly Rotating Bosons at Filling Factor 3/2. *Phys. Rev. Lett.*, 95:160404, Oct 2005. doi: 10.1103/PhysRevLett.95.160404. URL https://link.aps.org/doi/10.1103/PhysRevLett.95.160404. (cited on p. 52)

G. Rigolin and G. Ortiz. Adiabatic theorem for quantum systems with spectral degeneracy. *Phys. Rev. A*, 85:062111, Jun 2012. doi: 10.1103/PhysRevA.85.062111. URL https://link.aps.org/doi/10.1103/PhysRevA.85.062111. (cited on pp. 12 and 93)

P. Rosson, M. Lubasch, M. Kiffner, and D. Jaksch. Bosonic fractional quantum Hall states on a finite cylinder. *Phys. Rev. A*, 99:033603, Mar 2019. doi: 10.1103/PhysRevA.99.033603. URL https://link.aps.org/doi/10.1103/PhysRevA.99.033603. (cited on pp. 31 and 116)

P. Roushan, C. Neill, A. Megrant, Y. Chen, R. Babbush, R. Barends, B. Campbell, Z. Chen, B. Chiaro, A. Dunsworth, A. Fowler, E. Jeffrey, J. Kelly, E. Lucero, J. Mutus, P. J. J. O'Malley, M. Neeley, C. Quintana, D. Sank, A. Vainsencher, J. Wenner, T. White, E. Kapit, H. Neven, and J. Martinis. Chiral ground-state currents of interacting photons in a synthetic magnetic field. *Nature Physics*, 13:146–151, 10 2016. doi: 10.1038/nphys3930. URL https://doi.org/10.1038/nphys3930. (cited on pp. 36, 68, 105, and 110)

P. Roushan, C. Neill, J. Tangpanitanon, V. M. Bastidas, A. Megrant, R. Barends, Y. Chen, Z. Chen, B. Chiaro, A. Dunsworth, A. Fowler, B. Foxen, M. Giustina, E. Jeffrey, J. Kelly, E. Lucero, J. Mutus, M. Neeley, C. Quintana, D. Sank, A. Vainsencher, J. Wenner, T. White, H. Neven, D. G. Angelakis, and J. Martinis. Spectroscopic signatures of localization with interacting photons in superconducting qubits. *Science*, 358(6367):1175–1179, 2017. ISSN 0036-8075. doi: 10.1126/science.aao1401. URL https://science.sciencemag.org/content/358/6367/1175. (cited on p. 36)

N. Schine, A. Ryou, A. Gromov, A. Sommer, and J. Simon. Synthetic Landau levels for photons. *Nature*, 534:671–675, 06 2016. doi: 10.1038/17943. URL https://doi.org/10.1038/nature17943. (cited on pp. 35, 67, 68, and 96)

N. Schuch, M. M. Wolf, F. Verstraete, and J. I. Cirac. Computational Complexity of Projected Entangled Pair States. *Phys. Rev. Lett.*, 98:140506, Apr 2007. doi: 10.1103/PhysRevLett.98.140506. URL https://link.aps.org/doi/10.1103/PhysRevLett.98.140506. (cited on p. 107)

D. N. Sheng, Z.-C. Gu, K. Sun, and L. Sheng. Fractional quantum Hall effect in the absence of Landau levels. *Nature Communications*, 2:389, 07 2011. doi: 10.1038/ncomms1380. URL https://doi.org/10.1038/ncomms1380. (cited on p. 30)

J. F. Sherson, C. Weitenberg, M. Endres, M. Cheneau, I. Bloch, and S. Kuhr. Single-atom-resolved fluorescence imaging of an atomic Mott insulator. *Nature*, 467(7311):68–72, 2010. doi: 10.1038/nature09378. URL https://doi.org/10.1038/nature09378. (cited on p. 32)

Y.-Y. Shi, L.-M. Duan, and G. Vidal. Classical simulation of quantum many-body systems with a tree tensor network. *Phys. Rev. A*, 74:022320, Aug 2006. doi: 10.1103/PhysRevA.74.022320. URL https://link.aps.org/doi/10.1103/PhysRevA.74.022320. (cited on p. 107)

P. Silvi, F. Tschirsich, M. Gerster, J. Jünemann, D. Jaschke, M. Rizzi, and S. Montangero. The Tensor Networks Anthology: Simulation techniques for many-body quantum lattice systems. *SciPost Phys. Lect. Notes*, page 8, 2019. doi: 10.21468/SciPostPhysLectNotes.8. URL https://scipost.org/10.21468/SciPostPhysLectNotes.8. (cited on pp. 107 and 135)

S. H. Simon. Interpretation of thermal conductance of the $\nu = \mathbf{5/2}$ edge. *Phys. Rev. B*, 97:121406, Mar 2018a. doi: 10.1103/PhysRevB.97.121406. URL https://link.aps.org/doi/10.1103/PhysRevB.97.121406. (cited on p. 52)

S. H. Simon. Reply to "Comment on 'Interpretation of thermal conductance of the $\nu = 5/2$ edge' ". *Phys. Rev. B*, 98:167402, Oct 2018b. doi: 10.1103/PhysRevB.98.167402. URL https://link.aps.org/doi/10.1103/PhysRevB.98.167402. (cited on p. 52)

S. H. Simon. Fractional oscillations. *Nature Physics*, 15(6):527–528, 2019. doi: 10.1038/s41567-019-0461-4. URL https://doi.org/10.1038/s41567-019-0461-4. (cited on p. 91)

S. H. Simon, M. Ippoliti, M. P. Zaletel, and E. H. Rezayi. Energetics of Pfaffian-AntiPfaffian Domains. *arXiv e-prints*, Sep 2019. URL https://arxiv.org/abs/1909.12844. (cited on p. 52)

D. T. Son. Is the Composite Fermion a Dirac Particle? *Phys. Rev. X*, 5:031027, Sep 2015. doi: 10.1103/PhysRevX.5.031027. URL https://link.aps.org/doi/10.1103/PhysRevX.5.031027. (cited on p. 52)

A. S. Sørensen, E. Demler, and M. D. Lukin. Fractional Quantum Hall States of Atoms in Optical Lattices. *Phys. Rev. Lett.*, 94:086803, Mar 2005. doi: 10.1103/PhysRevLett.94.086803. URL https://link.aps.org/doi/10.1103/PhysRevLett.94.086803. (cited on pp. 31, 110, and 115)

R. P. Stanley. Some combinatorial properties of Jack symmetric functions. *Advances in Mathematics*, 77(1):76 – 115, 1989. ISSN 0001-8708. doi: https://doi.org/10.1016/0001-8708(89)90015-7. URL http://www.sciencedirect.com/science/article/pii/0001870889900157. (cited on p. 58)

A. Sterdyniak, N. Regnault, and G. Möller. Particle entanglement spectra for quantum Hall states on lattices. *Phys. Rev. B*, 86:165314, Oct 2012. doi: 10.1103/PhysRevB.86.165314. URL https://link.aps.org/doi/10.1103/PhysRevB.86.165314. (cited on p. 31)

A. Stern. Anyons and the quantum Hall effect–A pedagogical review. *Annals of Physics*, 323(1):204 – 249, 2008. ISSN 0003-4916. doi: 10.1016/j.aop.2007.10.008. URL http://www.sciencedirect.com/science/article/pii/S0003491607001674. January Special Issue 2008. (cited on p. 7)

A. Stern and B. I. Halperin. Proposed Experiments to Probe the Non-Abelian $\nu = 5/2$ Quantum Hall State. *Phys. Rev. Lett.*, 96:016802, Jan 2006. doi: 10.1103/PhysRevLett.96.016802. URL https://link.aps.org/doi/10.1103/PhysRevLett.96.016802. (cited on p. 91)

M. Stone. *Quantum Hall Effect*. WORLD SCIENTIFIC, 1992. doi: 10.1142/1584. URL https://www.worldscientific.com/doi/abs/10.1142/1584. (cited on p. 47)

J. Struck, C. Ölschläger, M. Weinberg, P. Hauke, J. Simonet, A. Eckardt, M. Lewenstein, K. Sengstock, and P. Windpassinger. Tunable Gauge Potential for Neutral and Spinless Particles in Driven Optical Lattices. *Phys. Rev. Lett.*, 108:225304, May 2012. doi: 10.1103/PhysRevLett.108.225304. URL https://link.aps.org/doi/10.1103/PhysRevLett.108.225304. (cited on p. 33)

S. Subhankar, Y. Wang, T-C. Tsui, S. L. Rolston, and J. V. Porto. Nanoscale Atomic Density Microscopy. *Phys. Rev. X*, 9:021002, Apr 2019. doi: 10.1103/PhysRevX.9.021002. URL https://link.aps.org/doi/10.1103/PhysRevX.9.021002. (cited on p. 32)

K. Sun, Z. Gu, H. Katsura, and S. Das Sarma. Nearly Flatbands with Nontrivial Topology. *Phys. Rev. Lett.*, 106:236803, Jun 2011. doi: 10.1103/PhysRevLett.106.236803. URL https://link.aps.org/doi/10.1103/PhysRevLett.106.236803. (cited on pp. 30 and 31)

M. E. Tai, A. Lukin, M. Rispoli, R. Schittko, T. Menke, D. Borgnia, P. M. Preiss, F. Grusdt, A. M. Kaufman, and M. Greiner. Microscopy of the interacting Harper–Hofstadter model in the two-body limit. *Nature*, 546:519–523, 06 2017. doi: 10.1038/nature22811. URL https://doi.org/10.1038/nature22811. (cited on pp. 33, 34, 36, 105, and 110)

E. Tang, J.-W. Mei, and X.-G. Wen. High-Temperature Fractional Quantum Hall States. *Phys. Rev. Lett.*, 106:236802, Jun 2011. doi: 10.1103/PhysRevLett.106.236802. URL https://link.aps.org/doi/10.1103/PhysRevLett.106.236802. (cited on pp. 30 and 31)

R. Thomale, B. Estienne, N. Regnault, and B. A. Bernevig. Decomposition of fractional quantum Hall model states: Product rule symmetries and approximations. *Phys. Rev. B*, 84:045127, Jul 2011. doi: 10.1103/PhysRevB.84.045127. URL https://link.aps.org/doi/10.1103/PhysRevB.84.045127. (cited on pp. 57, 58, and 59)

D. J. Thouless, M. Kohmoto, M. P. Nightingale, and M. den Nijs. Quantized Hall Conductance in a Two-Dimensional Periodic Potential. *Phys. Rev. Lett.*, 49:405–408, Aug 1982. doi: 10.1103/PhysRevLett.49.405. URL https://link.aps.org/doi/10.1103/PhysRevLett.49.405. (cited on pp. 15, 24, and 30)

D. Tong. *Lectures on the Quantum Hall Effect*. June 2016. (cited on pp. 18, 19, 22, 23, 28, 40, 42, 46, 52, 56, and 97)

D. C. Tsui, H. L. Stormer, and A. C. Gossard. Two-Dimensional Magnetotransport in the Extreme Quantum Limit. *Phys. Rev. Lett.*, 48:1559–1562, May 1982. doi: 10.1103/PhysRevLett.48.1559. URL https://link.aps.org/doi/10.1103/PhysRevLett.48.1559. (cited on pp. 15 and 25)

R. O. Umucalılar. Real-space probe for lattice quasiholes. *Phys. Rev. A*, 98:063629, Dec 2018. doi: 10.1103/PhysRevA.98.063629. URL https://link.aps.org/doi/10.1103/PhysRevA.98.063629. (cited on pp. 31, 108, and 135)

R. O. Umucalılar and I. Carusotto. Many-body braiding phases in a rotating strongly correlated photon gas. *Physics Letters A*, 377(34):2074 – 2078, 2013. ISSN 0375-9601. doi: https://doi.org/10.1016/j.physleta.2013.06.011. URL http://www.sciencedirect.com/science/article/pii/S0375960113005860. (cited on p. 35)

R. O. Umucalılar and I. Carusotto. Generation and spectroscopic signatures of a fractional quantum Hall liquid of photons in an incoherently pumped optical cavity. *Phys. Rev. A*, 96:053808, Nov 2017. doi: 10.1103/PhysRevA.96.053808. URL https://link.aps.org/doi/10.1103/PhysRevA.96.053808. (cited on pp. 67, 68, 90, 91, and 117)

R. O. Umucalılar, E. Macaluso, T. Comparin, and I. Carusotto. Time-of-Flight Measurements as a Possible Method to Observe Anyonic Statistics. *Phys. Rev. Lett.*, 120:230403, Jun 2018. doi: 10.1103/PhysRevLett.120.230403. URL https://link.aps.org/doi/10.1103/PhysRevLett.120.230403. (cited on pp. 3, 91, 92, 96, and 98)

F. Verstraete, M. M. Wolf, D. Perez-Garcia, and J. I. Cirac. Criticality, the Area Law, and the Computational Power of Projected Entangled Pair States. *Phys. Rev. Lett.*, 96:220601, Jun 2006. doi: 10.1103/PhysRevLett.96.220601. URL https://link.aps.org/doi/10.1103/PhysRevLett.96.220601. (cited on p. 107)

G. Vidal. Entanglement Renormalization. *Phys. Rev. Lett.*, 99:220405, Nov 2007. doi: 10.1103/PhysRevLett.99.220405. URL https://link.aps.org/doi/10.1103/PhysRevLett.99.220405. (cited on p. 107)

G. Vidal. Class of Quantum Many-Body States That Can Be Efficiently Simulated. *Phys. Rev. Lett.*, 101:110501, Sep 2008. doi: 10.1103/PhysRevLett.101.110501. URL https://link.aps.org/doi/10.1103/PhysRevLett.101.110501. (cited on p. 107)

K. von Klitzing, G. Dorda, and M. Pepper. New Method for High-Accuracy Determination of the Fine-Structure Constant Based on Quantized Hall Resistance. *Phys. Rev. Lett.*, 45:494–497, Aug 1980. doi: 10.1103/PhysRevLett.45.494. URL https://link.aps.org/doi/10.1103/PhysRevLett.45.494. (cited on pp. 15 and 23)

X. Wan, K. Yang, and E. H. Rezayi. Edge Excitations and Non-Abelian Statistics in the Moore-Read State: A Numerical Study in the Presence of Coulomb Interaction and Edge Confinement. *Phys. Rev. Lett.*, 97:256804, Dec 2006. doi: 10.1103/PhysRevLett.97.256804. URL https://link.aps.org/doi/10.1103/PhysRevLett.97.256804. (cited on pp. 51, 53, 92, 101, and 102)

X. Wan, Z.-X. Hu, E. H. Rezayi, and K. Yang. Fractional quantum Hall effect at $\nu = 5/2$: Ground states, non-Abelian quasiholes, and edge modes in a microscopic model. *Phys. Rev. B*, 77: 165316, Apr 2008. doi: 10.1103/PhysRevB.77.165316. URL https://link.aps.org/doi/10.1103/PhysRevB.77.165316. (cited on pp. 53, 92, 101, and 102)

B. Wang, F. N. Ünal, and A. Eckardt. Floquet Engineering of Optical Solenoids and Quantized Charge Pumping along Tailored Paths in Two-Dimensional Chern Insulators. *Phys. Rev. Lett.*, 120:243602, Jun 2018a. doi: 10.1103/PhysRevLett.120.243602. URL https://link.aps.org/doi/10.1103/PhysRevLett.120.243602. (cited on p. 115)

C. Wang, A. Vishwanath, and B. I. Halperin. Topological order from disorder and the quantized Hall thermal metal: Possible applications to the $\nu = 5/2$ state. *Phys. Rev. B*, 98:045112, Jul 2018b. doi: 10.1103/PhysRevB.98.045112. URL https://link.aps.org/doi/10.1103/PhysRevB.98.045112. (cited on p. 52)

Z. Wang, Y. Chong, J. D. Joannopoulos, and M. Soljačić. Observation of unidirectional backscattering-immune topological electromagnetic states. *Nature*, 461(7265):772–775, 2009. doi: 10.1038/nature08293. URL https://doi.org/10.1038/nature08293. (cited on p. 34)

X.-G. Wen. An Introduction of Topological Orders. *Unpublished.* URL https://web.archive.org/web/20170829201814/http://dao.mit.edu/~wen/topartS3.pdf. (cited on pp. 26 and 27)

X.-G. Wen. Vacuum degeneracy of chiral spin states in compactified space. *Phys. Rev. B*, 40: 7387–7390, Oct 1989. doi: 10.1103/PhysRevB.40.7387. URL https://link.aps.org/doi/10.1103/PhysRevB.40.7387. (cited on pp. 15, 26, and 42)

X.-G. Wen. Chiral Luttinger liquid and the edge excitations in the fractional quantum Hall states. *Phys. Rev. B*, 41:12838–12844, Jun 1990a. doi: 10.1103/PhysRevB.41.12838. URL https://link.aps.org/doi/10.1103/PhysRevB.41.12838. (cited on pp. 43, 67, 68, and 75)

X.-G. Wen. Electrodynamical properties of gapless edge excitations in the fractional quantum Hall states. *Phys. Rev. Lett.*, 64:2206–2209, Apr 1990b. doi: 10.1103/PhysRevLett.64.2206. URL https://link.aps.org/doi/10.1103/PhysRevLett.64.2206. (cited on p. 43)

X.-G. Wen. Gapless boundary excitations in the quantum Hall states and in the chiral spin states. *Phys. Rev. B*, 43:11025–11036, May 1991a. doi: 10.1103/PhysRevB.43.11025. URL https://link.aps.org/doi/10.1103/PhysRevB.43.11025. (cited on p. 43)

X.-G. Wen. Edge transport properties of the fractional quantum Hall states and weak-impurity scattering of a one-dimensional charge-density wave. *Phys. Rev. B*, 44:5708–5719, Sep 1991b. doi: 10.1103/PhysRevB.44.5708. URL https://link.aps.org/doi/10.1103/PhysRevB.44.5708. (cited on p. 43)

X.-G. Wen. THEORY OF THE EDGE STATES IN FRACTIONAL QUANTUM HALL EFFECTS. *International Journal of Modern Physics B*, 06(10):1711–1762, 1992. doi: 10.1142/S0217979292000840. URL https://doi.org/10.1142/S0217979292000840. (cited on pp. 43, 60, and 75)

X.-G. Wen. Topological orders and edge excitations in fractional quantum Hall states. *Advances in Physics*, 44(5):405–473, 1995. doi: 10.1080/00018739500101566. URL https://doi.org/10.1080/00018739500101566. (cited on pp. 28, 43, 51, 53, and 102)

X.-G. Wen. Colloquium: Zoo of quantum-topological phases of matter. *Rev. Mod. Phys.*, 89: 041004, Dec 2017. doi: 10.1103/RevModPhys.89.041004. URL https://link.aps.org/doi/10.1103/RevModPhys.89.041004. (cited on p. 26)

X.-G. Wen. Choreographed entanglement dances: Topological states of quantum matter. *Science*, 363(6429), 2019. ISSN 0036-8075. doi: 10.1126/science.aal3099. URL https://science.sciencemag.org/content/363/6429/eaal3099. (cited on pp. 15 and 28)

X.-G. Wen and Q. Niu. Ground-state degeneracy of the fractional quantum Hall states in the presence of a random potential and on high-genus Riemann surfaces. *Phys. Rev. B*, 41:9377–9396, May 1990. doi: 10.1103/PhysRevB.41.9377. URL https://link.aps.org/doi/10.1103/PhysRevB.41.9377. (cited on pp. 28 and 135)

X.-G. Wen and A. Zee. Classification of Abelian quantum Hall states and matrix formulation of topological fluids. *Phys. Rev. B*, 46:2290–2301, Jul 1992. doi: 10.1103/PhysRevB.46.2290. URL https://link.aps.org/doi/10.1103/PhysRevB.46.2290. (cited on p. 28)

E. Wigner. On the Interaction of Electrons in Metals. *Phys. Rev.*, 46:1002–1011, Dec 1934. doi: 10.1103/PhysRev.46.1002. URL https://link.aps.org/doi/10.1103/PhysRev.46.1002. (cited on p. 29)

F. Wilczek. Magnetic Flux, Angular Momentum, and Statistics. *Phys. Rev. Lett.*, 48:1144–1146, Apr 1982a. doi: 10.1103/PhysRevLett.48.1144. URL https://link.aps.org/doi/10.1103/PhysRevLett.48.1144. (cited on pp. 7 and 9)

F. Wilczek. Quantum Mechanics of Fractional-Spin Particles. *Phys. Rev. Lett.*, 49:957–959, Oct 1982b. doi: 10.1103/PhysRevLett.49.957. URL https://link.aps.org/doi/10.1103/PhysRevLett.49.957. (cited on p. 7)

F. Wilczek and A. Zee. Appearance of Gauge Structure in Simple Dynamical Systems. *Phys. Rev. Lett.*, 52:2111–2114, Jun 1984. doi: 10.1103/PhysRevLett.52.2111. URL https://link.aps.org/doi/10.1103/PhysRevLett.52.2111. (cited on p. 12)

N. K. Wilkin and J. M. F. Gunn. Condensation of "Composite Bosons" in a Rotating BEC. *Phys. Rev. Lett.*, 84:6–9, Jan 2000. doi: 10.1103/PhysRevLett.84.6. URL https://link.aps.org/doi/10.1103/PhysRevLett.84.6. (cited on pp. 40, 52, and 67)

R. Willett, J. P. Eisenstein, H. L. Störmer, D. C. Tsui, A. C. Gossard, and J. H. English. Observation of an even-denominator quantum number in the fractional quantum Hall effect. *Phys. Rev. Lett.*, 59:1776–1779, Oct 1987. doi: 10.1103/PhysRevLett.59.1776. URL https://link.aps.org/doi/10.1103/PhysRevLett.59.1776. (cited on p. 25)

R. L. Willett, L. N. Pfeiffer, and K. W. West. Measurement of filling factor 5/2 quasiparticle interference with observation of charge e/4 and e/2 period oscillations. *Proceedings of the National Academy of Sciences*, 106(22):8853, 2009. ISSN 0027-8424. doi: 10.1073/pnas.0812599106. URL https://www.pnas.org/content/106/22/8853. (cited on p. 7)

Y.-L. Wu, B. A. Bernevig, and N. Regnault. Zoology of fractional Chern insulators. *Phys. Rev. B*, 85:075116, Feb 2012. doi: 10.1103/PhysRevB.85.075116. URL https://link.aps.org/doi/10.1103/PhysRevB.85.075116. (cited on p. 31)

Y.-L. Wu, B. Estienne, N. Regnault, and B. A. Bernevig. Braiding Non-Abelian Quasiholes in Fractional Quantum Hall States. *Phys. Rev. Lett.*, 113:116801, Sep 2014. doi: 10.1103/PhysRevLett.113.116801. URL https://link.aps.org/doi/10.1103/PhysRevLett.113.116801. (cited on p. 98)

Y.-S. Wu. General Theory for Quantum Statistics in Two Dimensions. *Phys. Rev. Lett.*, 52: 2103–2106, Jun 1984. doi: 10.1103/PhysRevLett.52.2103. URL https://link.aps.org/doi/10.1103/PhysRevLett.52.2103. (cited on p. 7)

D. Yoshioka. *The Quantum Hall Effect.* Springer Berlin Heidelberg, 2002. doi: 10.1007/978-3-662-05016-3. URL https://doi.org/10.1007/978-3-662-05016-3. (cited on p. 40)

Y. Zhang, G. J. Sreejith, N. D. Gemelke, and J. K. Jain. Fractional Angular Momentum in Cold-Atom Systems. *Phys. Rev. Lett.*, 113:160404, Oct 2014. doi: 10.1103/PhysRevLett.113.160404. URL https://link.aps.org/doi/10.1103/PhysRevLett.113.160404. (cited on p. 91)

Y. Zhang, G. J. Sreejith, and J. K. Jain. Creating and manipulating non-Abelian anyons in cold atom systems using auxiliary bosons. *Phys. Rev. B*, 92:075116, Aug 2015. doi: 10.1103/PhysRevB.92.075116. URL https://link.aps.org/doi/10.1103/PhysRevB.92.075116. (cited on p. 91)